The Phosphate Vibration as a Sensor for Ion-Pair Formation Studied by Nonlinear Time-Resolved Vibrational Spectroscopy

Dissertation

zur Erlangung des akademischen Grades

doctor rerum naturalium

(Dr. rer. nat.)

im Fach Physik

eingereicht an der

Mathematisch-Naturwissenschaftlichen Fakultät

der Humboldt-Universität zu Berlin

von

M. Sc. Jakob Schauss

Kommissarischer Präsident der Humboldt-Universität zu Berlin

Prof. Dr. Peter Frensch

Dekanin der Mathematisch-Naturwissenschaftlichen Fakultät

Prof. Dr. Caren Tischendorf

Gutachter:

1. Prof. Dr. Thomas Elsässer
2. Prof. Dr. Oliver Benson
3. Prof. Dr. Peter Hildebrandt

Eingereicht am 03.02.2022
Tag der Disputation: 23.06.2022

Abstract

The structure and dynamics of biomolecules are influenced by a complex interplay with ions and water molecules in the surrounding hydration shell. The underlying interactions are poorly understood, partly because of a lack of experimental probes that can access the molecular scale. Local vibrations of the RNA backbone provide non-invasive probes, that are sensitive to the first few hydration layers of the RNA solvation shell via the imposed electric field on the (biomolecular) surface. This thesis exploits this sensitivity in femtosecond 2D-IR spectroscopy experiments on the asymmetric phosphate stretch vibration $\nu_{AS}(PO_2^-)$ to investigate the role of positively charged ions, particularly the magnesium cation Mg^{2+}, in counteracting the negatively charged phosphate backbone, thus stabilizing the tertiary structure of the RNA molecule.

Initial experiments with the model system dimethyl phosphate in combination with theoretical calculations report an ion-dependent frequency blue-shift due to the formation of contact ion pairs. In such geometries, particularly short distances between Mg^{2+} and phosphate lead to exchange repulsion interactions that strongly perturb the potential energy surface of the vibration. Extending the approach to double helical RNA, a strong dependence of the $\nu_{AS}(PO_2^-)$ vibrational mode on the local hydration structure of the phosphate group is found. Three distinct vibrational peaks reflect three different local hydration geometries as a result of the vibrational Stark shifts. Responsible for the frequency shifts are electric fields from solvating water molecules.

Ultimately, the characteristic blue-shift of the $\nu_{AS}(PO_2^-)$ phosphate mode allows to quantitatively follow the formation of Mg^{2+}/PO_2^- contact pairs in transfer RNA systems. It could be shown that these configurations stabilize the tertiary structure of the tRNA molecule by efficiently compensating the Coulomb repulsion from negatively charged phosphate groups, particularly in highly congested regions of the tRNA molecule.

The thesis demonstrates the potential of time-resolved vibrational spectroscopy combined with theoretical descriptions on the molecular level to probe the complex interactions of biomolecular solvation environments.

Kurzfassung

Die Struktur und Dynamik von Biomolekülen wird durch ein komplexes Wechselspiel mit Ionen und Wassermolekülen der umgebenden Hydratationshülle beeinflusst. Die zu Grunde liegenden Wechselwirkungen sind kaum verstanden, zum Teil weil es an experimentellen Sonden mangelt, die das molekulare Level erfassen können. Lokale Schwingungen des RNA-Rückgrats bieten solch nicht-invasive Sonden, die empfindlich gegenüber den ersten Hydratationsschichten der RNA-Solvatationshülle sind. Die lokale Empfindlichkeit rührt von elektrischen Feldern auf der (biomolekularen) Oberfläche. Die vorliegende Dissertation nutzt diese Sensitivität aus, um mit Femtosekunden-2D-IR-Spektroskopie der asymmetrischen Phosphatstreckschwingung $\nu_{AS}(PO_2^-)$ die Rolle positiv geladener Ionen zu untersuchen, die die negativ geladenen Phosphatgruppen des Rückgrats kompensieren. Insbesondere das Magnesium-Kation Mg^{2+} spielt eine wichtige Rolle dabei, die Tertiärstruktur des RNA-Moleküls zu stabilisieren.
Erste Experimente am Modellsystem Dimethylphosphat in Kombination mit theoretischen Berechnungen zeigen eine ionenabhängige Blauverschiebung der $\nu_{AS}(PO_2^-)$-Mode aufgrund der Bildung von Kontaktionenpaaren. In solchen Geometrien führen kurze Abstände zwischen Mg^{2+} und dem Phosphat zu repulsiven Austauschwechselwirkungen, die die Potentialfläche der Schwingung stark stören. Eine Erweiterung der Methode auf doppelsträngige RNA zeigt eine starke Abhängigkeit der $\nu_{AS}(PO_2^-)$ Schwingungsmode von lokalen Hydratationsstrukturen der Phosphatgruppe. Frequenzverschiebungen durch den Starkeffekt führen zu drei klar getrennten Schwingungsbanden, die drei unterschiedliche lokale Hydratationsgeometrien widerspiegeln. Elektrische Felder von solvatisierenden Wassermolekülen beeinflussen direkt das Bindungspotential und verursachen so Frequenzverschiebungen in der Größenordnung von $\sim 20\,\mathrm{cm}^{-1}$.
Abschließend erlaubt es die für Kontaktgeometrien charakteristische Blauverschiebung der $\nu_{AS}(PO_2^-)$ Phosphatmode, die Bildung von Mg^{2+}/PO_2^- Kontaktionenpaaren in Transfer-RNA Systemen (tRNA) quantitativ zu verfolgen. Es konnte gezeigt werden, dass diese Konfigurationen die Tertiärstruktur der tRNA stabilisieren, indem sie die Coulombabstoßung zwischen negativ geladenen Phosphatgruppen kompensieren, insbesondere in stark verdichteten Regionen des tRNA-Moleküls.
Die Dissertation demonstriert das Potential zeitaufgelöster Schwingungsspektroskopie, kombiniert mit theoretischen Beschreibungen auf molekularer Ebene, um die komplexen Interaktionen biomolekularer Solvatationsumgebungen zu erforschen.

Contents

List of Abbreviations

biological and chemical acronyms

- 8-HQS 8-hydroxyquinoline-5-sulfonic acid
- bp base pairs
- CIP contact ion pair
- DNA deoxyribonucleic acid
- DMP dimethyl phosphate
  - *gg* gauche-gauche
  - *gt* gauche-trans
- EDTA ethylene diamine tetraacetic acid
- RNA ribonucleic acid
  - dsRNA double-stranded RNA
  - mRNA messenger RNA
  - rRNA ribosomal RNA
  - ssRNA single-stranded RNA
  - tRNA transfer RNA
  - $tRNA^{phe}$ phenylalanine specific transfer RNA
- SSIP solvent-separated ion pair

methodological acronyms

theoretical

- ALMO-EDA absolutely localized molecular orbital energy decomposition analysis
- DFT density functional theory
- FFCF frequency fluctuation correlation function
- MD molecular dynamics
- (NL)PB (nonlinear) Poisson-Boltzmann
- QM/MM quantum mechanics/molecular mechanics

experimental

- $\nu_{AS}(PO_2^-)$ asymmetric phosphate stretch vibration
- 2D-IR two-dimensional infrared
- (A)SAXS (anomalous) small-angle x-ray scattering
- BBO beta-barium borate
- CD circular dichroism
- DFG difference frequency generation
- ESA excited state absorption
- FTIR Fourier-transform infrared
- FWHM full width at half maximum
- GSB ground state bleach
- ICP-OES inductively coupled plasma optical emission spectroscopy
- LO local oscillator
- MCT mercury cadmium telluride
- NMR nuclear magnetic resonance
- OPA optical parametric amplification
- PP pump-probe
- SE stimulated emission
- UV-vis ultraviolet-visible

1

RNA and its versatile role in biochemistry

Ribonucleic acid (RNA) is one of the most relevant molecules in the biological world. It is best known for its role in the central dogma of molecular biology that states that genetic information stored in long-lived *DNA* molecules (deoxyribonucleic acid) is *transcribed* onto short-lived messenger RNA (mRNA) in the cell's nucleus [1]. mRNA is then read out by the ribosome and *translated* into an amino acid chain, the protein. The human body is estimated to contain 80000-400000 different proteins, all of which are encoded by roughly 20000 DNA genes and transported from the nucleus to the cell by mRNA. mRNA has come into focus for medical applications, most prominently during the recent SARS-CoV 2 pandemic. mRNA encoding a specific virus protein is part of several vaccines that allow the human body to synthesise the protein and subsequently stimulate the vaccinee's immune system to produce antibodies against it. [2, 3]
A variety of RNA molecules perform a number of functional roles, non-coding RNA, as opposed to the coding mRNA that carries genetic information. The most prominent examples for non-coding RNA are ribosomal RNA (rRNA) and transfer RNA (tRNA). Together with ribosomal proteins, rRNA forms the ribosome, the molecular machine that performs protein synthesis. tRNA links the mRNA sequences read out by the ribosome to an amino acid that is then added to the growing polypeptide chain. tRNA and rRNA differ fundamentally in size: tRNA is generally made up of ≈ 80 base pairs (bp), rRNA is 1500-5000 bp in length, exemplary x-ray structures are shown in figure 1.1. Other non-coding RNA fragments perform regulatory function in transcription and translation processes, as recently discovered. One such example is the riboswitch shown in figure 1.1 (35-200 bp). The function of all these RNA molecules is strongly influenced by their macromolecular structure, the surrounding water shell and the ion environment.

The general biochemical structure of RNA molecules follows the universal principles shown in figure 1.2. Negatively charged phosphate groups $(PO_4)^-$ link ribose sugars $(C_5H_{10}O_5)$ to form a backbone chain. The phosphate groups are the major hydration site of RNA. The genetic information is encoded in the sequence of the bases connected to the ribose. A nucleotide, consisting of a phosphate group, a sugar molecule, and a base is considered the basic building block of every RNA molecule. Four types of bases are most common for RNA molecules, the purines adenine (A) and guanine (G), and the pyrimidines uracil (U) and cytosine (C). Less common bases are typically modifications of these four, such as $O^{2\prime}$-methyl-guanosine, a methylation modification important in stabilizing the anticodon loop of $tRNA^{Phe}$. [7]

RNA exists in a multitude of single- and double-stranded geometries. In double strands as well as helical regions of single-stranded RNA opposing bases link to each other using

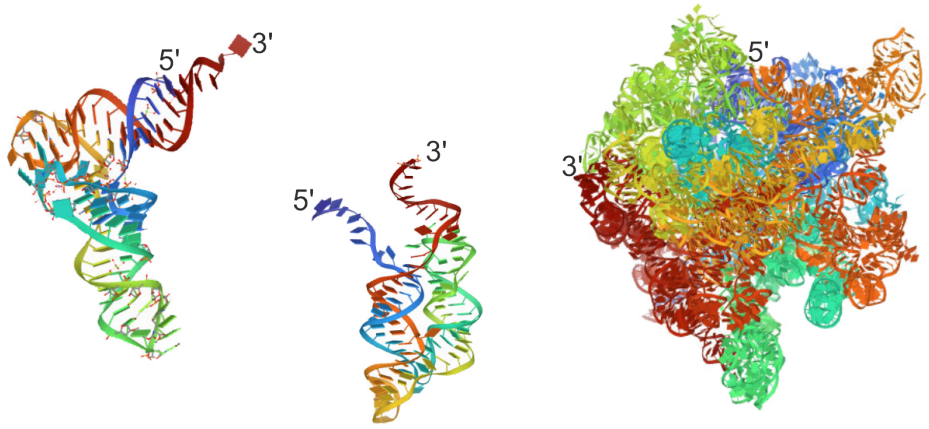

Figure 1.1: Different functional RNAs consist of a single RNA strand but assume different three-dimensional structures. Shown here from left to right, not to scale, are crystal structures of $tRNA^{phe}$ (protein data base 1EHZ, [4]), a tetrahydrofolate-binding riboswitch (pdb: 3SUY [5]), and a 50S-rRNA (pdb: 1NJN [6]). The ribbon structures show the sugar-phosphate backbone, the rectangular plates symbolize nucleobases. Color coding follows the primary base sequence of each RNA molecule from the 5′ end (blue) to the 3′ end (red).

hydrogen bonding. G and C share three hydrogen bonds, making GC-rich RNA geometries particularly stable. A and U share two hydrogen bonds in a weaker arrangement. Watson-Crick hydrogen bonding is shown in figure 1.2. Alternative pairing geometries, such as Hoogsteen pairs or water mediated G-U (similarly U-C or U-U) pairs, occur less frequently [8]. In the latter, one of the direct hydrogen bonds in Watson-Crick geometry is replaced by a mediating water molecule [9].

RNA shares the common biochemical structure, a sugar-phosphate backbone linking nucleobases, with DNA. Three major differences, however, result in significantly different properties:

- DNA contains thymine (T) instead of U. The extra methyl group of T provides better resistance against mutations [10].
- The ribose sugar is replaced by deoxyribose in DNA by removing the 2′-OH group. This specific hydroxide group is the docking point for enzymes that degrade RNA (RNAses), deoxyribose effectively protects DNA from degradation by cleavage. Consequently, the lifetime of DNA is prolonged by orders of magnitude, RNA degrades after minutes to hours, DNA persists for centuries [11–13].
- The sugar pucker, i.e. out-of-plane behaviour of the ribose ring as shown in fig. 1.2, switches from a $C_{3'}$ conformation in RNA to a $C_{2'}$ conformation in fully hydrated DNA. In the $C_{3'}$ conformation, the distance between adjacent phosphate groups is reduced from 7 Å to 5.9 Å. Fully hydrated DNA consequently forms an elongated, narrow double helix (B-helix geometry), whereas a double-stranded RNA is compressed to a shorter and wider A-type double helix, as shown in fig. 1.3.

Experimental and theoretical work comparing the hydration of DNA and RNA found that both the additional OH-group and the changed sugar pucker result in a more ordered local

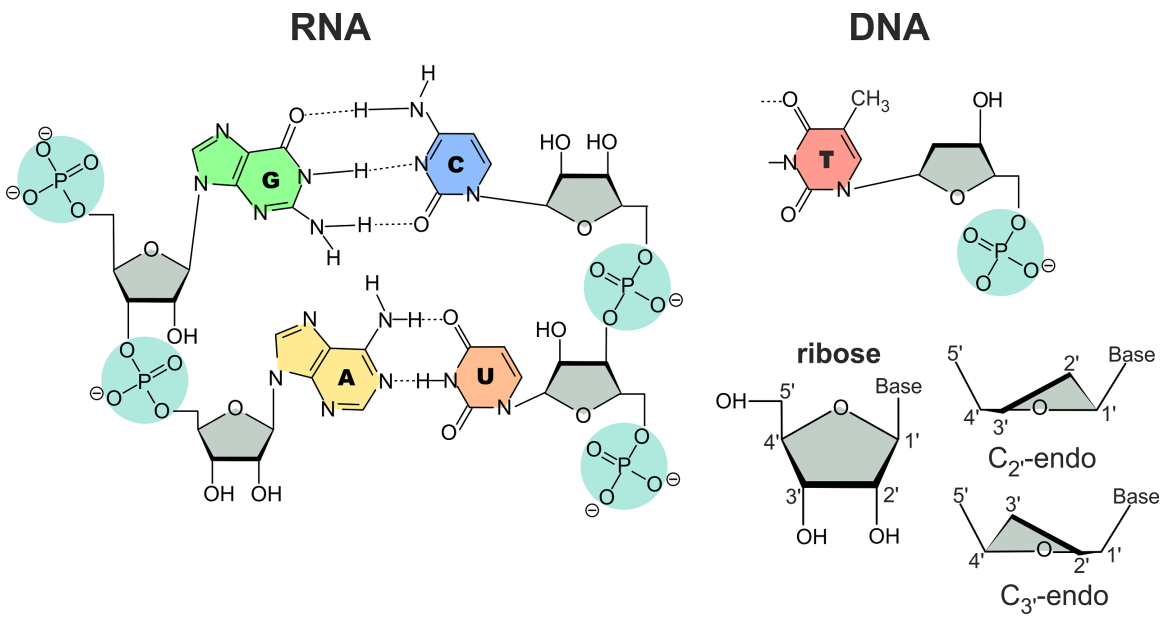

Figure 1.2: General biochemical structure of RNA. Phosphate groups (light blue) and ribose sugars (grey) form the RNA backbone, to which the nucleobases are attached. RNA generally contains guanine (G, green), cytosine (C, blue), adenine (A, yellow), and uracil (U, orange), shown here in Watson-Crick pairing with their predominant counterpart. DNA contains thymine (T, red) instead of uracil, and deoxyribose instead of ribose. Deoxyribose lacks the 2′-OH hydroxide group, cf. the prime notation (1′-5′) of the sugar carbons in the bottom right. The sugar pucker, i.e. the out-of-plane behaviour of the ribose ring, can adopt a $C_{2'}$-endo or $C_{3'}$-endo conformation.

hydration environment around RNA [14–16].

The molecule shown in figure 1.3 represents double-stranded RNA (dsRNA). This is a special case in biology, only certain RNA viruses are known to use dsRNA instead of DNA to store their genetic information [18, 19]. Artificially introducing synthetical or viral dsRNA in cells has recently been found to stimulate cellular immune systems [20]. Most RNA, however, is present as a single-strand that folds in on itself to form the complex structures shown in fig. 1.1. Helical domains with B-type helical geometry play important roles also in these functional structures, but only $\approx 50\%$ of bases are arranged helically [21]. A second recurring structural motif is a loop, where a number of bases do not pair, but rather create a circular element. One RNA molecule, where the loop structures are particularly important is tRNA, shown in fig. 1.4.

tRNA is a cornerstone of protein synthesis. It connects the genetic information of mRNA to the amino acid sequence of proteins. Its cloverleaf secondary structure (cf. fig. 1.4(a)) is conserved for all tRNA species and consists of three loop regions connected by helices. Most important for the reading out of mRNA is the anti-codon loop with the three anti-codon bases in red ($O^{2'}$-methyl-guanosine—adenine—adenine, G_mAA in the case of $tRNA^{phe}$). Each base triplet encodes one of twenty amino acids (phenylalanine in the case of $tRNA^{phe}$), the corresponding amino acids is attached to the 3′ end, the acceptor stem of the tRNA molecule. The D-loop is particularly important in the recognition process of linking amino

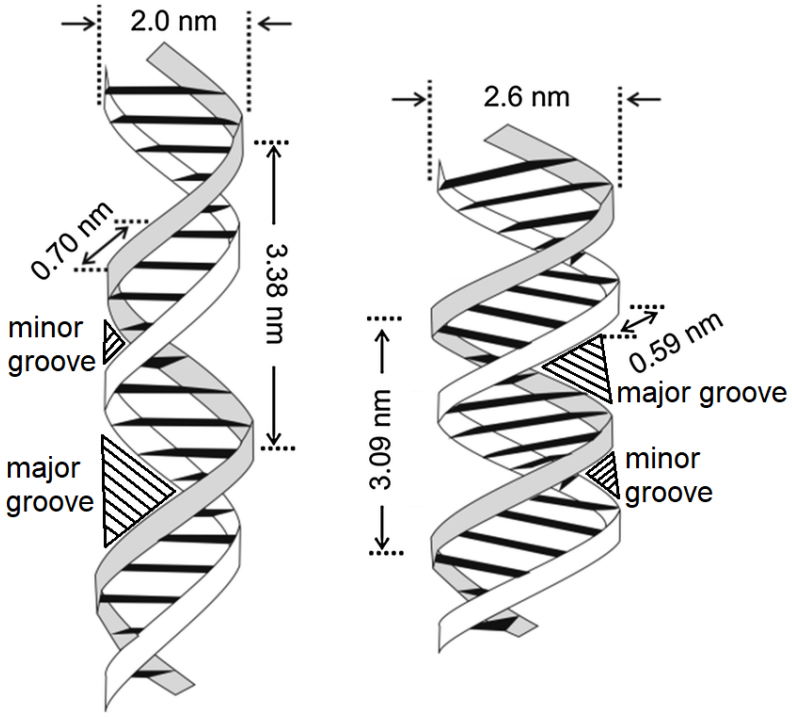

Figure 1.3: Fully hydrated DNA adopts a B-helix geometry (left), RNA and underhydrated DNA adopt an A-helix geometry (right). Shown are typical helix diameters, typical phosphate-phosphate distances and the total length of a single helical turn. The reduced P—P distance results in the compressed A-helix geometry. Major and minor groove are indicated as shaded regions. Image modified from [17]

acids to their correct tRNA molecule. The folded tertiary, functional, structure of tRNA has an upside-down L-shape shown in fig. 1.4(b), with the highlighted regions showing equivalent regions in secondary and tertiary structure.

The folding process of RNA takes place on timescales ranging from $10^{-2} - 10^{3}$ s and is hierarchically organized [22]. The initial step of a folding process is base-pairing to form a secondary structure of helical regions linking various loops (see fig. 1.4 (a)). This occurs relatively fast, secondary structure formation for tRNA has been observed in 10^{-4}-10^{-5} s. In a second step these domains associate to form the native tertiary structure, allowing RNA to perform its function. Tertiary structure formation in tRNA is associated with timescales around 10^{-2}-10^{-1} s (measured *in vitro* in NaCl solution, [23]). Larger molecules, such as the group I-intron of *Tetrahymena thermophila* (>400 nucleotides), show folding timescales on the order of seconds to minutes (measured *in vitro* in $MgCl_2$ solution, [24]). Several independently folding sub-domains lead to the formation of intermediate structures which slows down the folding process compared to tRNA.

A major challenge in the folding of RNA molecules is set by the negative charge of the backbone phosphate groups. Coulomb repulsion makes it unfavourable for phosphate groups to be in close proximity. However, this close proximity is exactly what is observed in functional RNA molecules. The typical distance of 5.9 Å between adjacent phosphates is significantly reduced in some arrangements, in tRNA particularly in the vicinity of the D-loop. Posi-

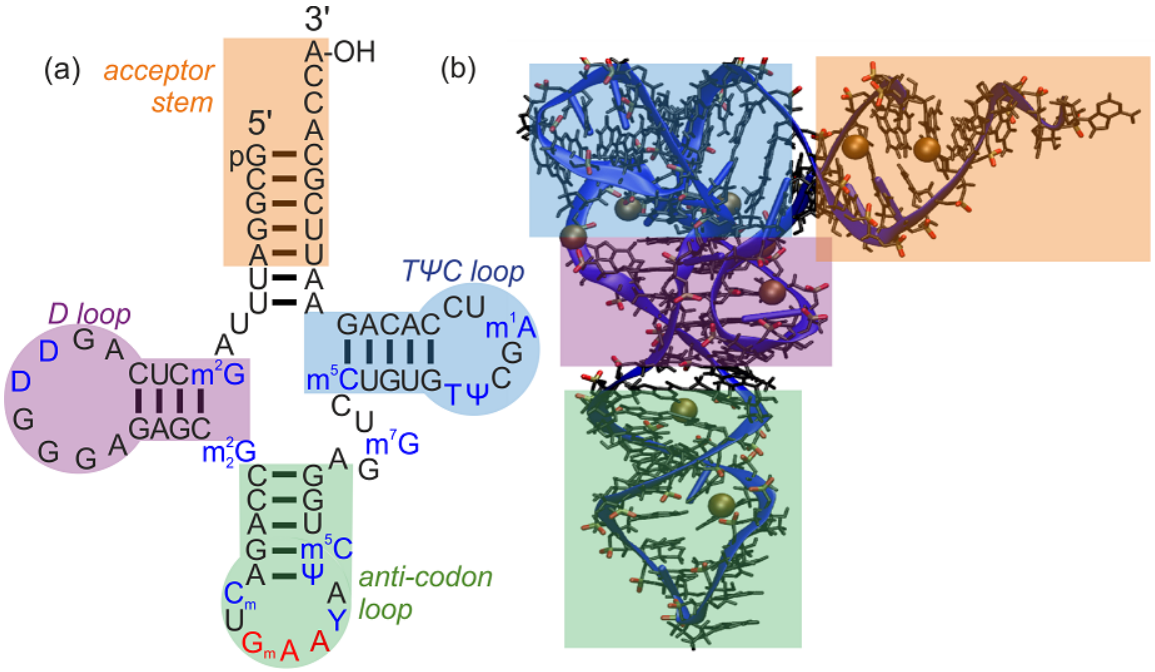

Figure 1.4: Secondary (a) and tertiary (b) structure of $tRNA^{phe}$ from yeast (modified bases in blue lettering, see [4]). The anticodon sequence encoding phenylalanine (G_mAA: $O^{2'}$-methyl-guanosine—adenine—adenine) in red lettering. Color coded boxes show equivalent regions in secondary and tertiary structure of $tRNA^{phe}$. Secondary structure is formed in a first folding step by basepairing. Tertiary, native, structure is then formed by a rearrangement of the structural groups.

tively charged metal ions, in particular magnesium (Mg^{2+}), have been found to stabilize RNA geometries by counteracting this Coulomb repulsion [25–27]. Mg^{2+} ions also mediate a comparably fast (≈ms) compaction of the secondary structure helical domains of large RNAs [28, 29].

How Mg^{2+} affects RNA structure and dynamics is still largely unresolved at a molecular level. The surface of RNA and of biomolecules in general is the playfield of interactions between various ionic molecular groups, charged counterions and the dipolar water molecules of the cellular environment. Hydration involves long-range electrostatic interactions, specific short-range interactions and inductive many-body interactions [30]. It is becoming more and more clear, that the first few hydration layers are crucial in determining structural stability and dynamics of biomolecules, e.g. by mediating the folding of proteins [31, 32].

Phosphate groups, as the major hydration site of RNA, are affected by fluctuating electric fields from surrounding water molecules and counterions. However, the role of counterions is disputed in literature. Mean-field theories, such as Poisson-Boltzmann theory, predict a stabilization of tRNA via long-range electrostatic interactions with ions that retain a complete solvation shell [33]. X-ray diffraction and quantum chemical calculations on large RNAs, on the other hand, see a strong contribution from ions directly bound to the RNA [34, 35]. A key problem is that the interaction of RNA with its hydration shell, including counterions, has not been experimentally accessible on a local, molecular level. Vibrations of the RNA

backbone, i.e., vibrations of the phosphate group, diester linkage vibrations, or vibrations of the ribose main chain, could provide noninvasive molecular probes. Collectively, they are carriers of energy transport, vital in the dissipation of excess energy both within the helix and to the aqueous solvent. Vibrations of the phosphate group in particular have been shown to strongly depend on the molecular hydration level [36]. Their vibrational frequency depends on the electric field exerted on the phosphate group by the solvent environment [37, 38]. A particularly useful technique is two-dimensional infrared spectroscopy (2D-IR), which allows to identify coupling between vibrational modes and reveal the influence of solvent fluctuations on spectral lineshapes. This thesis employs the asymmetric stretch vibration of the phosphodioxy moiety $\nu_{AS}(PO_2^-)$ to combine the sensitivity of the backbone vibrations with the spectral information provided by 2D-IR spectroscopy. We ultimately intend to answer the question, to what extent ions directly bound to RNA are present in solution and how they contribute to the stabilization of RNA structure.

Outline

The thesis is structured as follows: Chapter 2 will review the current knowledge about the hydration shell of RNA and the role metal ions play within this hydration shell. Both theoretical and experimental methods that contribute to the current understanding are presented. The vibrations of the phosphate group will be introduced as sensitive reporters of their surrounding electric field, a property that makes them predestined to report on the hydration environment and surrounding ions. Chapter 3 will then discuss the particular spectroscopic methods employed in this thesis, both linear and nonlinear, with an emphasis on the theoretical foundations of these methods. Chapter 4 focuses on the peculiarities of working with biological samples. Preparation and characterization of the aqueous sample used in the thesis, particularly the RNA solutions, will be explained in detail.
The results of the thesis are presented in a step-wise approach in chapters 5-7. We first consider interactions of positively charged alkali and alkaline earth metal ions with negatively charged phosphate groups of the dimethyl phosphate anion (DMP^-), a common model system of the RNA backbone. Linear and ultrafast IR spectra of DMP^- monitoring the behaviour of $\nu_{AS}(PO_2^-)$ under different ion environments are presented in chapter 5. We find that the formation of DMP/ion contact pairs results in the emergence of a characteristically blue-shifted vibrational mode, independent of the original $\nu_{AS}(PO_2^-)$ mode. Chapter 6 then investigates the local solvation shell of synthetical short double-helical RNA (dsRNA) by combining IR spectroscopy with heat-induced changes in RNA structure. We discern three typical types of local phosphate hydration geometry and assign them to the respective contributions to vibrational spectra of $\nu_{AS}(PO_2^-)$. The final step is the analysis of Mg^{2+}/RNA interactions in dsRNA and biologically relevant tRNA in chapter 7. The combination of linear and nonlinear, time-resolved infrared spectroscopy with theoretical calculations on a molecular level allows to quantify direct interactions of the RNA backbone phosphate groups with Mg^{2+} ions.
Chapter 8 summarizes the results presented in this thesis and provides an outlook into activities that could be pursued using the newly gained knowledge.

2
RNA-ion interactions

2.1 Defining RNA-ion interactions

2.1.1 The RNA hydration shell

It is impossible to discuss the interactions of RNA and its surrounding ions without considering their water environment. The RNA hydration shell, generally defined as the number of water molecules surrounding RNA whose properties differ from bulk water, contributes to the stabilization of secondary and tertiary RNA structure [8]. Water molecules as polar molecules help to some degree shield Coulomb repulsion between the negatively charged phosphate groups of the RNA backbone. Moreover, secondary structure formation, where base pairing and stacking occurs, is partly due to hydrophobic interactions [39].

The definition of water molecules in the hydration shell versus in bulk water naturally depends on what properties are considered and consequently the method used to observe them [40]. Early experiments on DNA distinguished two distinct layers of hydration [8, 41]. The first hydration shell contains about 20 water molecules per nucleotide. Five to six water molecules bind at the phosphate groups, 4-6 waters less tightly at the sugar and the bases. These 11-12 water molecules can still be observed at reduced hydration levels (<65% relative hydration levels), at such reduced hydration levels DNA assumes an A-type helical geometry similar to RNA. Further 8-9 binding water molecules appear at higher hydration levels and hydrate the bases. Ultrafast measurements of reorientation dynamics found that the second hydration layer extends to ≤ 7Å away from the biomolecule and is characterized mainly by structural distortions compared to bulk water [42].

Current knowledge specifically of RNA hydration is mainly the result of x-ray diffraction data from crystallized RNA [15] and theoretical molecular dynamics (MD) simulations, with diffraction data restricted to the first hydration shell. Figure 2.1 shows data of first hydration shell MD simulations [16]. 22 hydration sites are occupied by ≈20 water molecules, again the phosphate group is found to be the major hydration site. Up to three water molecules hydrogen bond to the two free oxygens in each phosphate group to form a tetrahedral arrangement. The water structure around RNA is generally found to be more stable and less dynamic than around DNA. High resolution X-ray experiments confirm this higher structural order for RNA and show a strong increase in hydration along the sugar-phosphate backbone [15]. The additional hydroxy group in RNA helps form a stable ring-like hydration structure in the minor and, less pronounced, the major groove. The reduced phosphate-phosphate distance additionally allows single water molecules to bridge the distance between neighbouring phosphates with strong hydrogen bonds [14, 15].

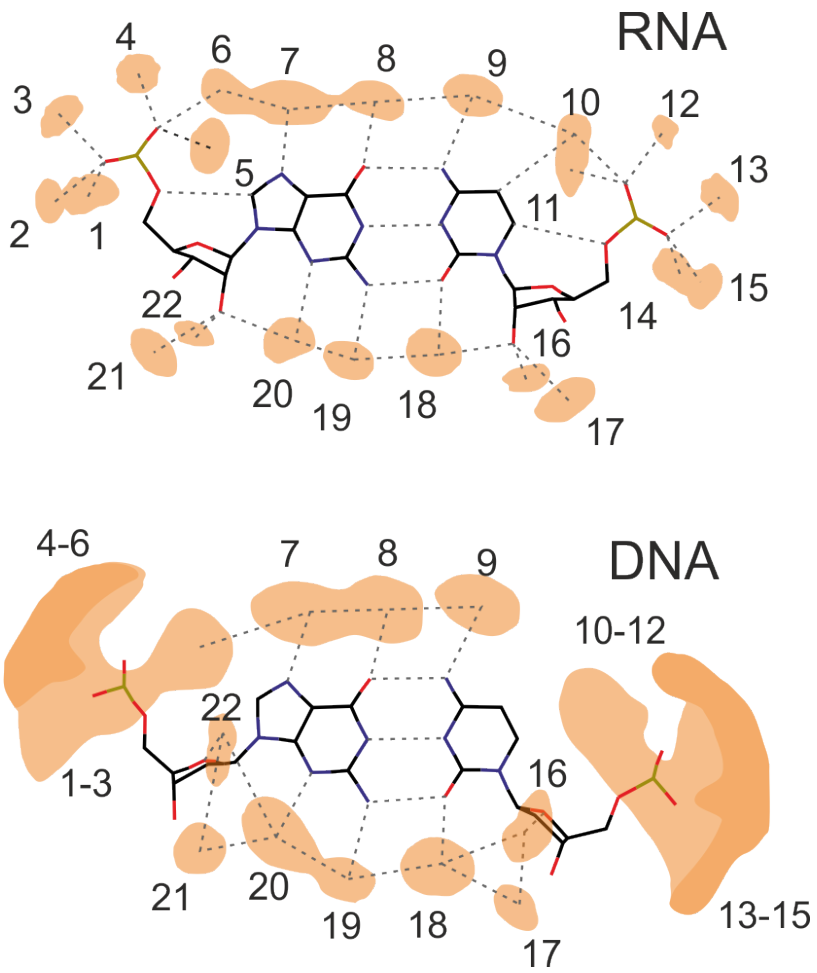

Figure 2.1: Molecular Dynamics simulation of the hydration shell around a single C-G base pair of RNA and DNA, adapted from ref. [16]. Blue: nitrogen (N); red: oxygen (O); black: carbon (C); ochre: phosphorous (P). Qualitative isodensity contours (orange) symbolize the distribution of water molecules around RNA and DNA. The 22 hydration sites surrounding the RNA are clearly distinguishable, while the DNA hydration shell is less ordered, especially around the phosphate groups. Potential hydrogen bonds are shown as dashed lines. The predominant hydration site in both systems is the phosphate group (12 of 22 sites), where water molecules form a tetrahedral arrangement around each phosphate oxygen. Four hydration sites are situated at the ribose ring, the remaining 6-8 sites link to the nucleobases.

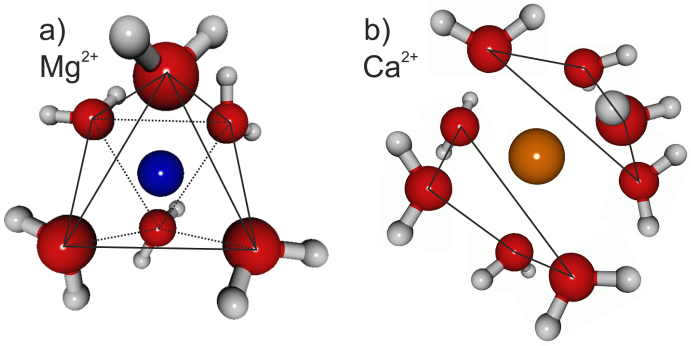

Figure 2.2: Hydration shell around Mg^{2+} and Ca^{2+}. Mg^{2+} is surrounded by six water molecules in a rigid, octahedral hydration shell, Ca^{2+} by eight water molecules in a distorted square antiprismatic configuration. Structures adapted from refs. [44, 45]

The hydration shell around the phosphate group of nucleic acids has been shown to be responsible for local electric field strengths up to 100 MV/cm [43]. RNA hydration is a topic of ongoing research and will be the focus of chapter 6 of this thesis.

2.1.2 Biologically relevant ions and their hydration

The introduction briefly discussed the importance of cations in reducing Coulomb repulsion in RNA molecules. Table 2.1 gives an overview over the most abundant ions present in mammals together with relevant properties of the ions. The monovalent alkali metals potassium (K^+) and sodium (Na^+) are present at the highest concentrations, K^+ mostly in the cell, Na^+ in the extracellular fluid. Divalent alkaline earth metals Mg^{2+} and calcium (Ca^{2+}) are present at lower concentrations, with Mg^{2+} predominantly in the cellular fluid, Ca^{2+} in the extracellular [21]. The predominant anion in mammalian cells is chlorine (Cl^-), concentrations depend on the cell type, from 5 mM in skeletal cells to 80 mM in red blood cells [46].

Ion	Hydration number	Ionic radius	Ion-Water distance	Water exchange rate	Physiological concentration intracellular	extracellular
		Å		s^{-1}	mM	
K^+	6	1.38	2.65	$\approx 10^9$	140	5
Na^+	6	1.02	2.34	$\approx 10^9$	10	145
Mg^{2+}	6	0.72	2.1	$< 10^6$	30	1
Ca^{2+}	8	1.12	2.46	$\approx 10^8$	1	4
Cl^-	6	1.67	2.2	$\approx 10^{11}$	5-80	115

Table 2.1: Properties of relevant ions. Hydration number refers to the number of H_2O molecules in the first shell, the hydration shell of divalent ions usually extends further. The ion-water distance is taken from radial distribution functions, that show predominant cation–water oxygen and Cl^-–water hydrogen distances in the first hydration shell. From refs. [21, 44, 46–48]

Mg^{2+} has a particularly rigid hydration shell, as evident from the low water exchange rate [21]. This correlates with the important role that Mg^{2+} plays in many biological processes. Figure 2.2 compares the first hydration shell of Mg^{2+} and Ca^{2+}. Mg^{2+} is surrounded by six water molecules in a tight octahedral structure, Ca^{2+} is hydrated by eight water molecules that form a more cubic structure. The comparably small ionic radius of Mg^{2+} results in a high charge density, strengthening the hydrogen bonds and resulting in a particularly low distance to the nearest water molecule (in the cation case, this is the ion-water oxygen distance). Typical ion-water distances shown in table 2.1 are taken from the first maximum of respective radial distribution functions, calculated in MD simulations and experimentally confirmed by NMR spectroscopy [21, 46]. Mg^{2+} is closest to its surrounding water shell, Ca^{2+} and Na^{+} are comparable, but the divalent Ca^{2+} also forms a second hydration shell, that Na^{+} does not have. The chlorine anion also has a comparably close first hydration shell. In this case, the distance is measured to one of the hydrogen atoms, the distance is therefore highly susceptible to fluctuations. In fact, this can be seen in the water exchange rate, which is significantly higher than for any of the cations.

2.1.3 Binding Modes

The ions listed in table 2.1 can interact with RNA molecules in a number of ways that follow universal rules. The first important distinction is that between directly and diffusely bound ions, both of which are present around RNA. Directly bound ions are characterized by their direct, specific interaction with phosphate groups in the RNA backbone, as shown in fig. 2.3**A**. In inner sphere coordination, the Mg^{2+} ion is in direct contact with a phosphate group, one water in its hydration shell is substituted by a phosphate oxygen. In outer sphere coordination Mg^{2+} retains its full first hydration shell, one of the water molecules bridges the distance between Mg^{2+} and PO_2^-. Inner sphere coordination always forms a contact ion pair (CIP), while up to three water molecules separate phosphate and ion in solvent-separated ion pairs (SSIP, [49]). Ions that are further away are termed diffusely bound ions. They interact with the RNA via long-range electrostatic interactions. Figure 2.3**B** shows three interactions of directly bound ions that are relevant for RNA when Mg^{2+} ions bridge the distance between two phosphate groups. In that case, both phosphate groups can interact with the Mg^{2+} ion either in inner or outer sphere coordination or in a combination of both. In this thesis we mainly differentiate between CIPs, SSIPs, and diffusely bound ions.

The process of n Mg^{2+} ions binding to RNA can be seen as a set of binding reactions in equilibrium [51, 52]

$$\begin{aligned}
\mathrm{RNA}_0 + \mathrm{Mg}^{2+} &\overset{K_1}{\longleftrightarrow} \mathrm{RNA} \cdot \mathrm{Mg}^{2+} \\
\mathrm{RNA}_0 + 2\mathrm{Mg}^{2+} &\overset{K_2}{\longleftrightarrow} \mathrm{RNA} \cdot \mathrm{Mg}_2^{2+} \\
&\vdots \\
\mathrm{RNA}_0 + n\mathrm{Mg}^{2+} &\overset{K_n}{\longleftrightarrow} \mathrm{RNA} \cdot \mathrm{Mg}_n^{2+}
\end{aligned}$$

with RNA_0 the nucleic acid without bound Mg^{2+} and K_i the macroscopic equilibrium constant associated with binding i Mg^{2+}. The sum of all binding modes can then be described

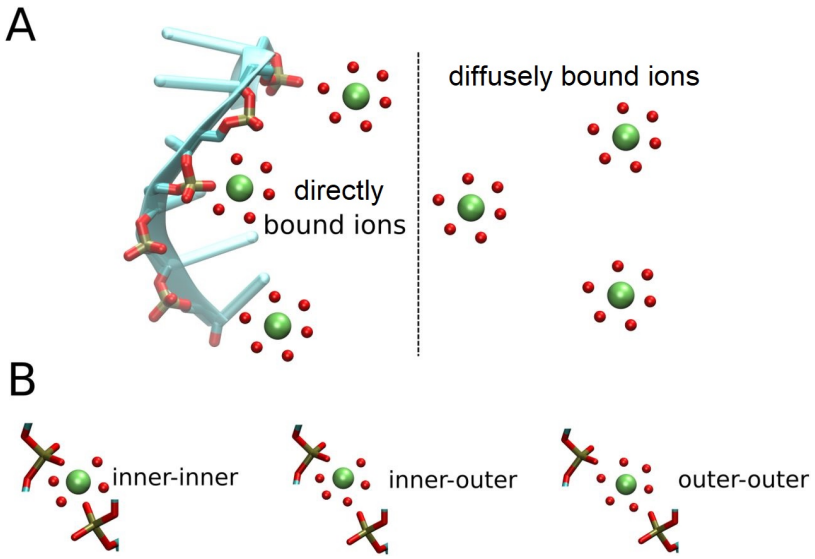

Figure 2.3: Schematic of Mg^{2+} binding to RNA. Binding occurs in different schemes, **A** shows the general distinction between bound ions that interact with phosphate groups of the backbone in a direct, specific manner, and diffusely bound ions, that interact via non-specific, long-range Coulomb interactions. **B** further distinguishes directly bound ions according to the hydration level of the Mg^{2+} ion. This correlates with the RNA/ion distance. Adapted from ref. [50]

by a binding partition function as a function of the total Mg^{2+} concentration $c_{Mg^{2+}}$. This binding polynomial has the form

$$Q = 1 + K_1 c_{Mg^{2+}} + K_2 c_{Mg^{2+}}^2 + ... + K_n c_{Mg^{2+}}^n \tag{2.1}$$

from which the number v of bound Mg^{2+} ions per RNA can be derived

$$v = \frac{\partial \ln Q}{\partial \ln c_{Mg^{2+}}} = \frac{c_{Mg^{2+}}}{Q} \frac{\partial Q}{\partial c_{Mg^{2+}}}. \tag{2.2}$$

For a single class of n independent binding sites with binding constant K the partition function takes the form $Q = (1 + K c_{Mg^{2+}})^n$, the number of ions bound per RNA molecule is then

$$v = \frac{n K c_{Mg^{2+}}}{1 + K c_{Mg^{2+}}}. \tag{2.3}$$

A Scatchard plot visualizes the data by plotting the ratio of bound ion to ligand concentration as a function of bound ion concentration $v/c_{Mg^{2+}}$ vs. v [54]. The corresponding Scatchard curve is linear with a negative slope (see fig. 2.4, dashed lines), following

$$\frac{v}{c_{Mg^{2+}}} = nK - vK.$$

The Scatchard plot allows to conveniently determine both binding constant and number of binding sites from slope and intersection with the x-axis, respectively.

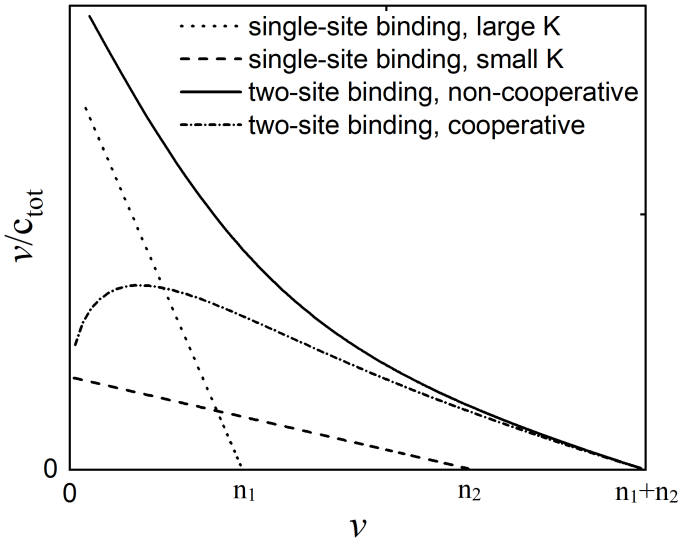

Figure 2.4: Scatchard plots for different binding conditions. Single-site binding results in a linear Scatchard graph, the slope is determined by the equilibrium binding constant. The solid line shows non-cooperative two-site binding, similar to what has been reported for $tRNA^{phe}$ uptake of Mg^{2+} [53]. The dash-dotted line gives an example of cooperative binding to the strong binding site, which has been observed for $tRNA^{phe}$ at elevated temperatures. The number of binding sites in a system is given in a Scatchard graph directly as the intersection with the x-axis.

The distinction between tightly and diffusely bound ions in the case of RNA requires a model that accounts for two classes of binding sites:

$$Q = (1 + K_1 c_{\mathrm{Mg^{2+}}})^{n_1} + (1 + K_2 c_{\mathrm{Mg^{2+}}})^{n_2}$$
$$v = \frac{n_1 K_1 c_{\mathrm{Mg^{2+}}}}{1 + K_1 c_{\mathrm{Mg^{2+}}}} + \frac{n_2 K_2 c_{\mathrm{Mg^{2+}}}}{1 + K_2 c_{\mathrm{Mg^{2+}}}}$$

$n_{1/2}$ is the number of ions associated with each binding site and $K_{1/2}$ the binding constant. In the case of two classes of independent binding sites the Scatchard plot shows a hyperbolic curve that asymptotically approaches the linear functions of its constituents. Certain systems of macromolecules may exhibit cooperative binding, where the binding of ligands (not necessarily only ions) facilitates the binding of additional ligands. A classic example is the binding of oxygen to hemoglobin. Conversely, anti-cooperative binding impedes future ion binding should ions already bind to the macromolecules. Cooperative binding can significantly alter the shape of a Scatchard plot, as has been observed for mixtures of native and denatured tRNA.

In an experimental framework, where the total Mg^{2+} concentration can be separated in bound and free ions ($c_{tot} = c_{bnd} + c_{fr}$), the number of bound ions can be indirectly quantified by measuring the concentration of free Mg^{2+}

$$v = \frac{c_{tot} - c_{fr}}{c_{\mathrm{RNA}}} \tag{2.4}$$

One approach to measure the concentration of free Mg^{2+} is the fluorescence spectroscopy of 8-hydroxyquinoline-5-sulfonic acid (8-HQS) [55]. Mg^{2+} is added to aqueous solutions of 8-HQS with and without RNA, titration curves allow to infer c_{fr}. The method will be explained in more detail in section 3.1, as we use it in chapter 7 of this thesis to quantify binding of Mg^{2+} to our RNA samples.

So far, we have considered ion binding to RNA purely from the viewpoint of fundamental equilibrium equations. This approach allows to differentiate different binding modes but lacks information on the microscopic structure. In the following we will present the prevalent theoretical methods to understand RNA-ion interactions in the molecular context.

2.1.4 Theoretical approaches in describing RNA-ion interactions

Earliest theories linking nucleic acids and their counterions originated from polyelectrolyte theory that initially studied the general properties of charged polymer chains in solution. Expanding the Debye-Hückel theory for solvated ions, Manning developed a theory of **counterion condensation** around polyelectrolytes, including DNA [58]. The polymer is simplified to a rod where charges are separated by a constant distance $d_{charge} = L/P$, with the total length L of the nucleic acid and P the number of basepairs with valency $z_P = 2$. Under this assumption, the statistical-mechanical integral over configuration space diverges until enough counterions of valency z_i condense around, i.e., bind to, the RNA to fulfill the critical condition

$$\xi = \frac{\lambda_B}{d_{charge}} > \frac{1}{N} \tag{2.5}$$

where ξ is the Manning parameter, $N = |z_i z_P|$ the absolute product of the two valencies, and $\lambda_B = e^2/(4\pi\varepsilon_0\varepsilon k_B T)$ the Bjerrum length, the distance between two monovalent charges at which their Coulomb energy and their thermodynamic kinetic energies are the same. ε denotes the dielectric constant of the solvent. The fraction of phosphate pairs with condensed ions is given by $1 - 1/N\xi$, the charge of the polyphosphate is reduced to $1/\mathrm{N}\xi$. In the case of monovalent cations around RNA in water, where $\varepsilon = 80$ and $d_{charge} = 0.28\,\mathrm{nm}$ (cf. fig. 1.3) the Manning parameter is $\xi = 2.48$. For this choice of parameters, 80% of phosphate groups are binding counterions (comp. fig. 2.5(a)), the effective charge of a basepair reduces to -0.2e.
The theory was later extended to account for competition of different counterion species [59]. Mixtures of counterions with different valencies, e.g. Na^+ and Mg^{2+}, showed complete selectivity towards the higher valent ion. The nucleic acid would always bind the divalent species until those ions were depleted. If the condition from eq. (2.5) was not yet met at that point, monovalent ions would condense until stability was restored.
Apart from its simplistic ansatz that neglects local solvation effects and individual ion properties, one major drawback of Manning theory is the unphysical spatial distribution of counterions. As shown in fig. 2.5(d) ions are predicted to accumulate mainly within a certain distance from the helical axis with sharp, step-like transitions between bound and free ions. Two major methods were developed that correct for the artificial behaviour: Poisson-Boltzmann (PB) and Molecular Dynamics (MD) simulations.

The PB method relies on the solutions of the **Poisson-Boltzmann** equation to predict the electrostatic potential around a nucleic acid. Several properties can then be deduced, such

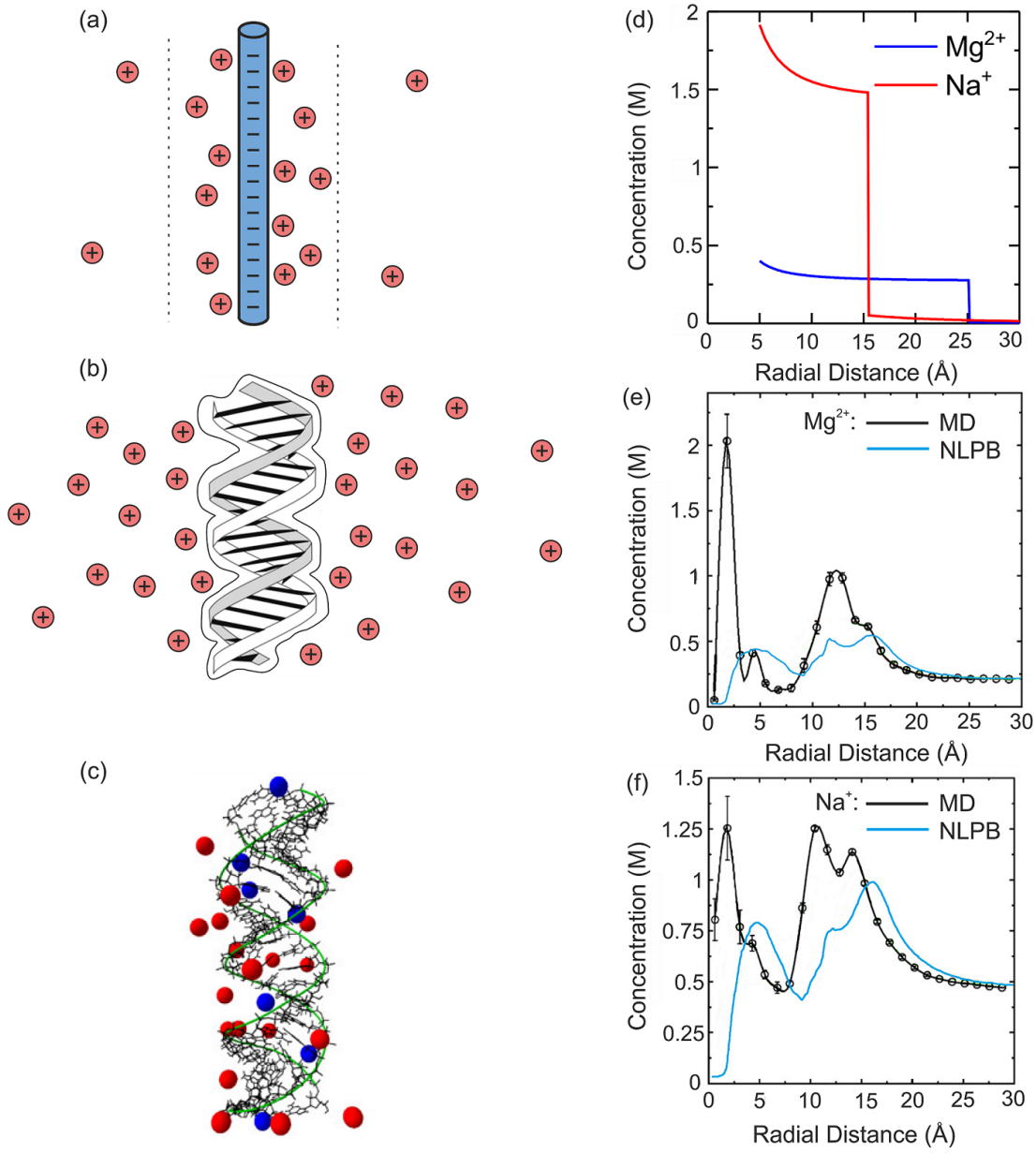

Figure 2.5: Schematic of findings from the three predominant theoretical methods used in RNA-ion characterization. (a) Counterion condensation theory treats the nucleic acid as a rod of uniform linear charge density. Positive counterions accumulate at a cylindrical volume around the RNA. Outside the condensation volume, ion concentrations rapidly approaches bulk ion concentrations. (b) NLPB theory treats the nucleic acid as a three-dimensional charge density distribution $\rho(\vec{r})$. The solution of the nonlinear Poisson-Boltzmann equation gives the electrostatic potential around the nucleic acid, from which ion distributions and thermodynamic parameters can be inferred. (c) Atomistic model of an RNA double helix used in MD simulations (water not shown). The negative charge is compensated in this simulation by Na^+ ions in the grooves of the RNA (blue spheres) and on the outer surface of the RNA (red spheres). (d) Counterion condensation: radial concentration profile of Na^+ (red) or Mg^{2+} (blue) around an RNA rod of 5Å radius, calculated acc. to ref. [56]. (e,f) Radial concentration profile of Mg^{2+} (e) and Na^+ (f) around a 25-mer dsRNA molecule according to MD simulations (black) and NLPB calculations (blue), adapted from ref. [57].

as the number density of surrounding ions, or thermodynamic properties relevant for the folding process. The Poisson-Boltzmann equation describes the spatial distribution of the electrostatic potential governed by a charge distribution $\rho(\vec{r})$, here, the negatively charged sugar-phosphate double helix of RNA. The potential is modified by the surrounding ions i, characterized by their valency z_i and their concentration c_{0i} according to [40]

$$\nabla \cdot [\varepsilon_0 \varepsilon(\vec{r}) \nabla V(\vec{r})] = -\left[\rho(\vec{r}) + \sum_i c_{0i} z_i e \exp\left(\frac{-z_i e V(\vec{r})}{k_B T}\right)\right] \tag{2.6}$$

The solvent is approximated as a continuum with a constant dielectric constant ε, typically $\varepsilon = 80$ in water. In proximity of the nucleic acid ε is reduced to < 4 [40], the transition can be simulated with a sharp step function [60] or a smoother sigmoidal function $\varepsilon(r)$ [57]. Early theory work relied on linearizing the exponential of eq. (2.6), but computational progress allows to calculate the non-linear equation at low computational cost for a variety of systems [61].

PB simulations were the first to introduce the concept of the ion atmosphere: ions that are not directly bound to the negative phosphate charges, but have been attributed a major contribution to stabilizing RNA structure and function through cumulative electrostatic interactions. Work on RNA has focused mainly on short double-helical RNA. The blue curve in fig. 2.5(f) shows the concentration curve of Na^+ around a 25-mer duplex RNA at high Na^+ concentration (0.4 M, [57]). The major contribution to counterion concentration is predicted 10-20 Å away from the RNA molecule, with a portion of counterions around 5Å [57]. PB simulations predict on average 0.65 Na^+ ions per nucleotide to be associated with duplex RNA at such high bulk Na^+ concentrations [60]. Lower Na^+ concentrations lead to more ion binding to the RNA, reaching up to 0.81 Na^+ per nucleotide for 10 mM NaCl concentration.

In the case of Mg^{2+} the predicted concentration curve looks similar to Na^+ (cf. fig. 2.5(e), [57]), 0.46 Mg^{2+} ions per nucleotide are predicted [60]. Simulations of counterion competition predict a strong preference for Mg^{2+} binding. In mixtures containing a fixed amount of Mg^{2+}, more than 10-fold the concentration of Na^+ was required to displace Mg^{2+}, so that the same absolute numbers of both Mg^{2+} and Na^+ were associated with the RNA molecule. More than 30-fold concentration is necessary for Na^+ binding to dominate. For both Mg^{2+} and Na^+ the ion atmosphere extends up to 30Å from the RNA helical axis, where concentrations approach bulk limits.

Misra and Draper extended the use of the nonlinear Poisson-Boltzmann equation to study the binding of Mg^{2+} ions to $tRNA^{phe}$ [33]. Within the premise of NLPB they treated the Mg^{2+} as an ensemble of ions distributed according to a Boltzmann weighted average of the mean electrostatic potential around the RNA [62]. The simulations reproduced experimental Scatchard plots, albeit primarily for high values of $v > 15$ ions bound per RNA molecule. Solvent-dependent shifts in the pK_a value of fluorescent reporters also allowed them to access the thermodynamical change in free energy upon addition of Mg^{2+}. They concluded that the Mg^{2+}-tRNA interplay is governed by long-range electrostatic interactions, since their model does not require any specifically coordinated Mg^{2+} ions to stabilize the tRNA tertiary structure. Binding of Mg^{2+} occurs purely via electrostatic trapping, additionally

helped by the thermodynamic loss of entropy upon releasing previously attached monovalent counterions.

Poisson-Boltzmann theory, however, suffers from systemic limitations: ions, RNA, and the water solvent are approximated in a continuum model that neglects local interactions. Continuum models do not account for dehydration effects that occur due to steric constraints, or ion-ion correlations that dominate electrostatics on short distances. This has been tried to be rectified, e.g. by the *tightly bound ion* model [63]. Here, ions are inserted in the vicinity of the RNA after the PB equation has been solved. Calculated electrostatic free energies determine whether the included ions are diffusely or tightly bound to the RNA molecule.

The simplification of the solvent water as a continuum also ignores the dipole properties of the water molecules. The method therefore neglects the strong local electric fields from the water dipoles and does not reflect the polarizability of water molecules by ions or the RNA itself. PB theory has been argued to be accurate for long distances, where the sum of all molecules efficiently shields the electric fields at the RNA surface [43, 57]. Short-range interactions, especially near strong electric fields, are inherently misrepresented.

MD simulations improve on a number of these limitations, albeit at a significantly larger computational cost. They simulate complex molecular systems at an atomistic level. The molecules of interest are considered together with solvent molecules and any additional ions in an appropriate simulation volume. Using analytical functions, the force fields, the potential at every coordinate is calculated. This allows to track step-wise the dynamics of the system. After an initial equilibration time, MD simulations can track the configuration space due to thermal fluctuations at room temperature on timescales up to several microseconds.

The results highly depend on the force field used, for nucleic acids AMBER (Assisted Model Building with Energy Refinement, [64]) and CHARMM (Chemistry at Harvard Macromolecular Mechanics, [65]) are the most commonly used. These quantify the system using Coulomb interaction, the atomic Lennard-Jones potential, as well as intramolecular parameters, such as bond lengths and angles, or torsion angles. These parametrizations are constantly re-evaluated with regards to experimental benchmark results [66, 67]. Standard MD force fields are not able to factor in the electronic polarization of atoms and molecules in the calculation of the dynamics [68]. This considerably impeded simulating nucleic acid-ion interactions due to the strong electric fields present. Polarizable force fields improve on this, but are costly and very recent [69]. A less costly walkaround is a re-parametrization of charges. Strong polarization effects are reduced by numerically downscaling ion charges. This improves accuracy in the simulation, e.g. of $MgCl_2$ ion pairing, but still has limitations when it comes to MD simulations of biomolecules [70, 71].

On this basis, a range of RNA molecules has been examined. For long distances to the helical axis (> 16Å [72]) predicted ion concentrations around an RNA duplex agree well with populations predicted by PB theory. MD simulations however predict significantly larger concentrations in close vicinity to the RNA molecule with distinct differences between monovalent and divalent cations [57, 72–74]. Characteristic distance-dependent concentration curves are shown in fig. 2.5(e,f) [57]. The atomistic detail of MD simulations allows

for precise analysis of ion positions. (Most) locally interacting ions show stability in their specific location. The non-esterified oxygens of the backbone phosphate groups in particular are the binding sites of these locally interacting ions. Na^+ also has shown binding to the N7 nitrogen atom of guanine and adenine [72]. In mixtures of Mg^{2+} and Na^+, a clear preference for Mg^{2+} binding is predicted [73, 74].

MD simulations were also performed to extend the Hofmeister series to RNA [75]. The Hofmeister series is an empirical sequence of ions according to the influence on biological macromolecules. The original idea was conceptualized for proteins and captured salt-dependent differences in protein solubility [76]. Strong Hofmeister ions shape the local water structure around the biomolecules, based on charge density and ion size. In ref. [75] eight different cations are considered in MD simulations together with an RNA dinucleotide (guanine-guanine) and sorted according to their binding free energies with the phosphate backbone. Mg^{2+} ions show the strongest binding affinity, preferably forming a contact ion pair with the phosphate group by inner-sphere coordination. K^+ ions show the weakest binding, mainly as a solvent-separated ion pair. The full sequence for the biologically relevant ions of table 2.1 reads $Mg^{2+} > Ca^{2+} > Na^+ > K^+$. Interestingly, the above Hofmeister series is reversed when it comes to ions binding to the nucleobases.

Newer approaches include the combination of Debye-Hückel bulk properties with a reference interaction site model (3D-RISM) that calculates short-range ion-RNA interactions based on the density distribution of these ions. It was used to study Mg^{2+} binding to ribosomal RNA, predicting stabilization of tertiary structure by bridging Mg^{2+} that bind to more than one phosphate group [50].

All in all, PB theory is the most widely used method when it comes to simulating nucleic acids, due to its computational efficiency. It predicts stabilization of RNA structures by long-range interactions of ions with a diffuse ion atmosphere. The mean-field approach is inaccurate especially at the level of local interactions, however, since the approach neglects the dipolar field of water molecules, polarization effects, as well as ion-ion correlations. MD simulations are computationally more expensive, but better capture the discrete nature of solvent molecules and ions. They predict stronger local interactions than PB, most notably with regards to Mg^{2+} binding to the phosphate group of the RNA backbone.

2.1.5 Experimental approaches and their limitations

We reviewed the different theoretical approaches and their predictions regarding RNA-ion interactions. Various experimental methods have been developed over the years to substantiate these predictions. Focus will be on interactions of RNA with divalent ions, such as Mg^{2+}, as those have been shown to affect RNA the most. The list is not complete, but serves as an overview over experimental advances.

First attempts to quantify stabilizing RNA-ion interactions used **equilibrium dialysis** methods on ribosomal RNA, the principle is displayed in figure 2.6. RNA is dialysed in a buffer with excess ion concentrations. The system is allowed to equilibrate and ion concentrations are measured both inside and outside the dialysis membrane. Cation attraction and anion exclusion around the RNA molecule can then be quantified. From these first experiments statistically every other RNA phosphate has a Mg^{2+} ion associated with it, with

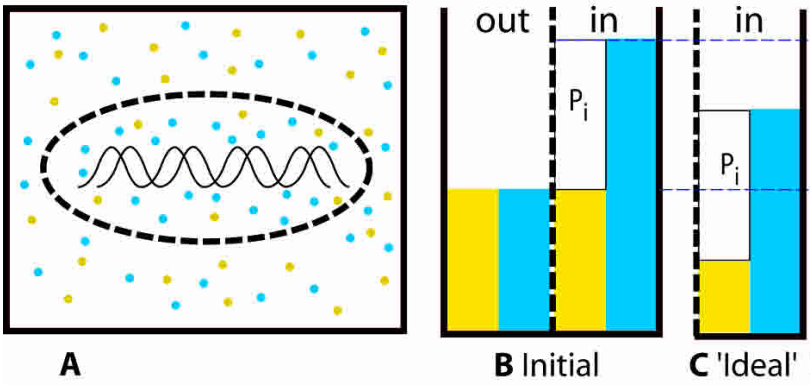

Figure 2.6: Schematic representation of equilibrium dialysis to determine bound ion concentrations to RNA (here K^+ and Cl^-). Initially, RNA in a dialysis bag is placed in a solvent with higher ion concentration. After some time, ion concentrations equilibrate and the corresponding concentration associated with RNA can be computed from concentration measurements. Adapted from ref. [80]

some evidence for Mg^{2+} ions confined to a specific site in the ribosome [77]. These specific sites were deemed essential to RNA function, similar to ligands binding to proteins [78,79].

The stabilizing influence of Mg^{2+} also shifts transition temperatures in **UV melting** experiments, explained in detail in section 3. Römer and Hach combined melting experiments with a fluorescent indicator to identify two classes of binding sites around $tRNA^{phe}$ from hyperbolic Scatchard plots [53]: 18 sites showed weak binding (K= $6 \cdot 10^3 M^{-1}$), 5 showed strong binding (K$\approx 10^5\, M^{-1}$).

Electrostatic theories, such as NL-PB became increasingly important, so experiments focused more on detailing the electrostatic interactions from diffusely bound ions around the RNA molecule. Experiments using **fluorescent indicators** were refined to report RNA-ion interactions over a wide concentration range [55,81,82]. The method exploits chelate formation of Mg^{2+} with the fluorophore 8-HQS. Details of this method are given in section 3.1, it relies on measuring the concentration of free Mg^{2+} to estimate the concentration of bound Mg^{2+}, as in eq. (2.4), but can generally not differentiate diffuse from direct binding [83]. In these experiments, a saturation of 0.3-0.4 Mg^{2+} ions per nucleotide was measured [55]. Binding of Mg^{2+} to folded and unfolded configurations of a riboswitch showed higher affinity towards the native, folded RNA. Up to 20-50% more Mg^{2+} were associated, the difference appears to saturate at 0.04 Mg^{2+} per nucleotide well before saturation of the ion atmosphere is observed [81,82].

A second method to probe the diffuse ion atmosphere is **small-angle x-ray scattering** (SAXS), the principle is displayed in fig. 2.7 [84,85]. The angular distribution of scattered x-ray radiation contains information on size and shape of RNA molecules. Regular SAXS can only passively observe ion-induced RNA/RNA interactions. Anomalous SAXS (ASAXS) goes beyond that and is capable of probing the interactions of RNA with mono-, di-, and trivalent cations [84]. Key to ASAXS is the tuning of x-ray energies to match the electronic transition of the ion in question and contrast this resonant scattering to an off-resonance measurement. The restrictions of electronic transitions limit the method to

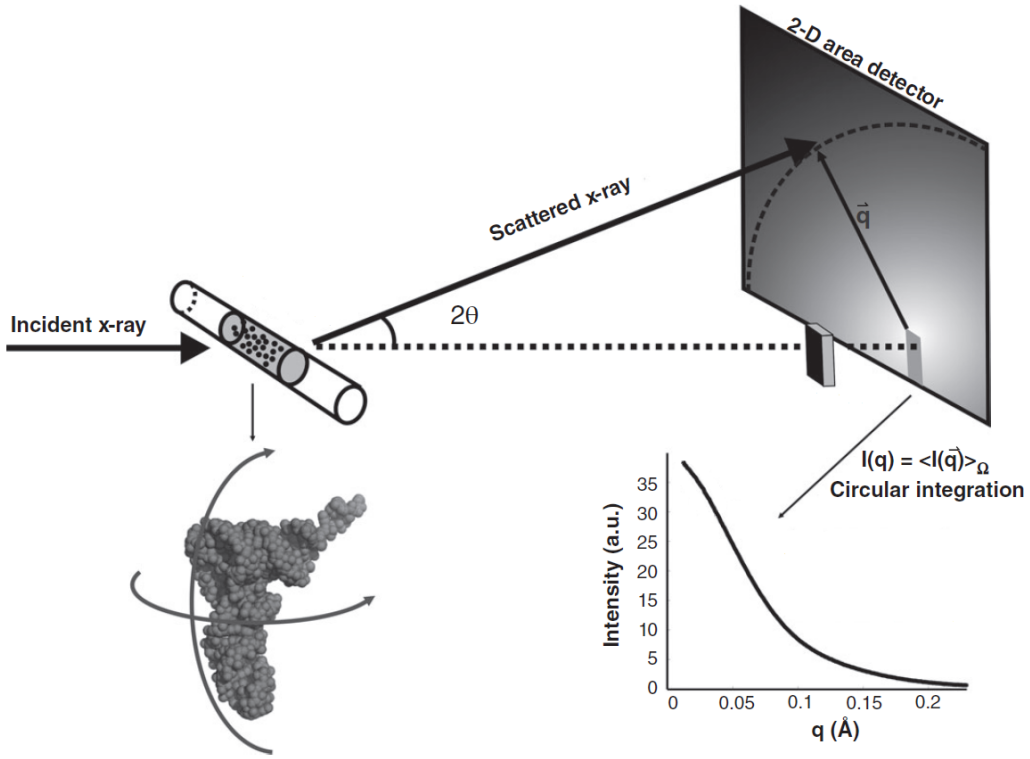

Figure 2.7: Schematic of small angle X-ray scattering (SAXS) to determine RNA properties. X-ray radiation is scattered by the liquid sample containing RNA molecules in random orientation. Scattered radiation is detected and integrated over the radial axis. From the resultant intensity distribution structural parameters of the molecule can be concluded. Tuning the x-ray energy to resonances of metal ions additionally allows insight into RNA-ion binding under certain restrictions (Anomalous SAXS). Figure adapted from ref. [85]

Mg^{2+}-substitutes such as strontium Sr^{2+}. ASAXS can then provide information on the number and distribution of cations in the diffuse ion atmosphere. Kirmizialtin et al. used the method to validate MD simulations and counted 20 Sr^{2+} ions in the atmosphere surrounding a 25-mer duplex RNA, 0.4 ions per phosphate group [86]. They were also able to quantify the radius of the ion atmosphere, i.e. the radius of the sphere where Sr^{2+} concentration is larger than in the bulk, to be 18Å. Similar experiments with monovalent rubidium Rb^{+} count 35±3 ions in a radius of 28Å.

A third method to quantify the ion atmosphere relies on **ion counting**. Buffer equilibration similar to equilibrium dialysis (fig. 2.6) is used to create an excess of divalent ions around the RNA. The concentration of ions is then determined using atomic emission spectroscopy [87]. The Herschlag group used this method to specifically study competition between different ion species that bind to nucleic acids [60, 88]. Among other results, they could quantify the increased effectiveness of divalent ions in neutralizing the negative charges of the RNA. A bulk concentration of 100 mM Na^{+} was required to replace half of the ion atmosphere generated by 6 mM bulk Mg^{2+} concentration, in agreement with Poisson-Boltzmann level theory. Ref. [60] counted 22 Mg^{2+} ions surrounding a 24-mer duplex RNA, 0.46 ions per phosphate.

A valuable contribution to the study of directly bound ions came from Shi&Moore with a 1.93Å resolution x-ray structure of $tRNA^{phe}$, where older studies only achieved 3Å [4]. In fact, **x-ray diffraction methods** were historically one of the first experimental methods to investigate RNA-Mg^{2+} geometries [89, 90]. They observed three to four Mg^{2+} ions strongly bound to $tRNA^{phe}$. The low resolution, however, made it difficult to differentiate signatures from water oxygens (O^{2-}), Na^{+}, and Mg^{2+} in solution, since all three have ten electrons. Mg^{2+} is mainly identified in x-ray diffraction spectra via their characteristic hydration geometry, Na^{+} and water oxygens are indistinguishable even at 1.93Å resolution. Shi& Moore find 11 divalent cation binding sites, 7 of which were binding Mg^{2+}. They also discussed the hydration of RNA in detail. They observe water molecules that bridge adjacent phosphate groups both in helical and loop regions. Ring-like hydration structures that link the 2'-OH group with the phosphate oxygen on the 3' side were found in loop regions.

Few other methods to investigate the direct binding are currently in practice. While NMR has the potential to see ion-RNA interactions in shifts and broadenings of resonance peaks [91], it is mostly dealing in Mg^{2+} substitutes, such as cobalt ($Co(NH_3)_6^{3+}$) or europium (Eu^{3+}). $Co(NH_3)_6^{3+}$ is supposed to resemble $Mg(H_2O)_6^{2+}$, but can not replicate a dehydrated Mg^{2+} shell [92–94].

In summary, recent literature mainly investigated the diffuse ion atmosphere around RNA. They assert that the collective long-range electrostatic interactions of these diffusely bound ions are most important in stabilizing RNA structure, with site-bound ions playing a role only in particularly condensed structural elements. The study of site-bound ions has so far been limited by the lack of an experimental technique that allows the study of RNA in solution to directly measure the interaction of RNA with Mg^{2+}. Vibrations of the RNA backbone, particularly the asymmetric phosphate stretch vibration $\nu_{AS}(PO_2^-)$, are sensitive reporters of the direct solvent environment and promise to overcome this lack of experimental accessibility.

2.2 Phosphate vibrations as reporters of ion and hydration environments

This thesis presents infrared spectra of the phosphate group. Section 2.1.1 pointed out the major role of the phosphate group in RNA hydration, the previous section emphasized that positively charged cations strongly interact with the negatively charged phosphate group. In fact, researchers early on found correlations between phosphate properties and nucleic acid structure [36, 95, 96]. In this section, we want to take a closer look at what comprises the phosphate group and what vibrational signatures can be exploited to gain an insight into RNA-ion interactions.

Figure 2.8 shows the phosphate group, consisting of a phosphodioxy (O=P–O^-, PO_2^-) and a phosphodiester (O—P—O) moiety. The oxygen atoms form a tetrahedron. This arrangement is present in nucleic acids, phospholipids, i.e. cell membranes, as well as smaller molecules, e.g. adenosine diphosphate (ADP), adenosine triphosphate (ATP) or guanosine triphosphate (GTP), that play a crucial role in cellular energy cycles. Depending on the system of interest the ester residuals commonly are single hydrogen atoms (phosphoric

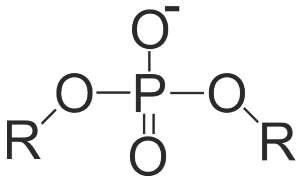

Figure 2.8: Chemical structure of the phosphate group. It consists of the phosphodioxy moiety O=P–O$^-$ and the phosphodiester moiety O—P—O. The residuals differ depending on the system.

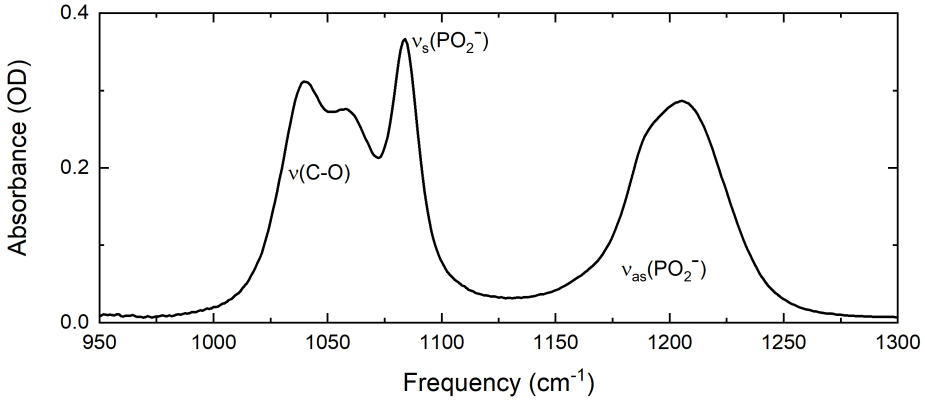

Figure 2.9: Infrared absorption spectrum of dimethyl phosphate in water, the librational background absorption of water is subtracted. Symmetric and asymmetric phosphate stretch vibrations absorb around 1080 and 1200 cm^{-1}, respectively. C-O stretch vibrations between the oxygens of the phosphate and the carbons of the methyl groups absorb at about 1050 cm^{-1}, congesting the spectrum around $\nu_S(PO_2^-)$. $\nu_{AS}(PO_2^-)$ shows a broad absorption, reflecting different DMP conformations in solution (cf. fig.2.10).

acid $H_2PO_4^-$), two methyl groups in dimethyl phosphate ($(CH_3)_2PO_4^-$), more complex (deoxy)ribose sugars in nucleic acids, or carbohydrate chains in lipid bilayer systems.

In solution, the negatively charged PO_2^- group is the part predominantly interacting with the solvent. The vibrations of this moiety are accessible to IR spectroscopy, shown in figure 2.9. Predominant contributions to the vibrational spectrum are the symmetric and asymmetric stretch vibration around 1000 cm^{-1} and 1200 cm^{-1}, respectively. The phosphodiester symmetric and asymmetric stretch vibrations contribute to the vibrational spectrum at 750 cm^{-1} and 820 cm^{-1}, respectively. Bending mode frequencies range from 300-500 cm^{-1} [97].

The spectrum in figure 2.9 shows dimethyl phosphate (DMP) where the ester residuals are two methyl groups. DMP has been studied extensively as a model system for the nucleic acid backbone, as it comprises the phosphate group and the initial carbon of the ribose sugar. The initial aim was to understand the link between phosphate vibrations and nucleic acid structure [97]. It is important to note that DMP takes on one of two conformations in aqueous solution: *gauche-gauche (gg)* or *gauche-trans (gt)*, see figure 2.10. They differ in torsion angle around the phosphodiester plane with *trans* denominating in-plane torsion and *gauche* out-of-plane ($\approx 70°$). They are similar in energy (≈ 1 kcal/mol), which leads to

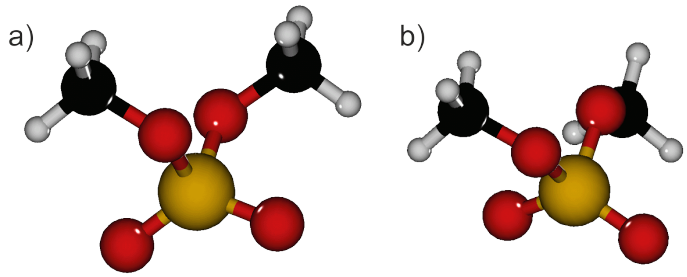

Figure 2.10: *gauche-gauche* (*gg*, a) and *gauche-trans* (*gt*, b) conformers of DMP, as determined by the torsion angle between phosphate and methyl groups. In solutions, *gg* is predominant, but both conformers occur.

a similar distribution in solution, with some preference to the *gg* conformer [98,99]. The two conformers are reflected in the broad, asymmetric absorption peak at 1200 cm^{-1}, with lower frequencies contributed by the *gt* conformer (1170-1200 cm^{-1}), and higher contributions due to the *gg* conformer [38]. Time-resolved measurements showed a lifetime of 300 fs for the asymmetric phosphate stretch vibration $\nu_{AS}(\mathrm{PO}_2^-)$, a time constant that has been shown to be universal for all phosphate systems observed so far [37, 100, 101]. The fast relaxation points to a quick energy dissipation mechanism to intra-phosphate modes, such as combination bands of bending modes. The energy is then transferred to solvent molecules on a similar, or faster timescale [37,102]. The symmetric stretch vibration $\nu_S(\mathrm{PO}_2^-)$ on the other hand has been shown to relax on a longer timescale. Times range from 300 fs in phosphoric acid [101], 700 fs in DMP [103] up to 1 ps in nucleic acids [37] and a hydration-dependent 1-1.5 ps in phospholipids [100].

A change in hydration level has also been observed to be responsible for a solvatochromic shift in vibrational spectra of DNA [43]. DNA helix geometry shifts from an A-type helix to a B-type helix with increasing hydration level. In parallel to this structural change absorption at $\nu_{AS}(\mathrm{PO}_2^-)$ shifts from $\approx 1260\,\mathrm{cm}^{-1}$ to $\approx 1220\,\mathrm{cm}^{-1}$. This shift is due to the vibrational Stark effect, whereby the frequency of an oscillator changes with an applied external field according to $\Delta\nu = -\Delta\vec{\mu}\cdot\vec{F}_{ext}$. $\Delta\nu$ is the frequency shift, $\Delta\vec{\mu}$ the Stark tuning rate, and $\vec{F}_{ext}$ the external electric field, that in this case originates from the hydrating water molecules. The main contribution to this field was shown to come from the first two to three hydration layers surrounding the phosphate [38,43].The vibrational Stark spectrum of phospholipids in a frozen glass solvent yielded values of 0.5 and 1.35 $\mathrm{cm}^{-1}/(\mathrm{MV/cm})$ for symmetric and asymmetric phosphate stretch vibration, respectively [104]. The stronger solvatochromic response of $\nu_{AS}(\mathrm{PO}_2^-)$, amongst others, makes it the preferred of the two modes for this thesis. Quantum-chemical calculations of DMP predict the value of the Stark parameter for $\nu_{AS}(\mathrm{PO}_2^-)$ to be closer to 0.5 $\mathrm{cm}^{-1}/(\mathrm{MV/cm})$, the frequency shift of 40 cm^{-1} observed above for DNA would then be caused by electrical fields in the order of 80 MV/cm. This in turn makes the phosphate vibration an ideal probe for fluctuating electric fields within these close hydration layers. Recent experiments employed $\nu_{AS}(\mathrm{PO}_2^-)$ to illuminate differences in hydration between DNA and RNA [14, 37].

Here, we will examine the changes to $\nu_{AS}(\mathrm{PO}_2^-)$ as a result of phosphate-ion interactions.

3

Experimental and Theoretical Methods

A broad range of spectroscopic methods were applied in the framework of this thesis. This chapter introduces both theoretical and experimental aspects of these techniques. We will first focus on electronic spectroscopy, well established methods in the characterization of nucleic acid samples.
Vibrational spectroscopy in the mid-infrared will be the main tool to examine RNA-ion interactions, as described in chapter 2.2. The theoretical basis of 2D-IR spectroscopy will be covered and the experimental set-up explained in detail.

3.1 Electronic spectroscopy

The electronic spectroscopy methods used in this thesis encompass light in the near ultraviolet and the visible wavelength range (UV-vis, $\approx 180\,\text{nm} < \lambda < 700\,\text{nm}$). Different methods can be used to probe the electronic structure of molecules in this range, here we employ linear absorption, circular dichroism (CD), and fluorescence spectroscopy. UV-vis absorption spectroscopy is used to measure the concentration of RNA samples, as well as observe structural changes in the RNA upon melting. CD spectroscopy probes the helicity of RNA molecules, allowing to monitor structural changes upon heating. Fluorescence spectroscopy is applied to quantify Mg^{2+} binding to RNA molecules.

UV-vis absorption spectroscopy

In linear absorption spectroscopy, the intensity of light propagating through a solution decreases exponentially. Light is absorbed by the sample, the energy is used to excite vibrational, rotational or electronic modes in the molecule in question. The transmitted light intensity I is characterized by the Lambert Beer law

$$I = I_0 \cdot 10^{-\varepsilon c l}$$

where I_0 is the intensity of incident light, ε the molar extinction coefficient, c denotes the concentration of the sample, and l is the optical path length, i.e., the thickness of the sample layer.
It is common to simplify this equation by introducing the linear absorbance A

$$A = -\lg \frac{I}{I_0} = \varepsilon \cdot c \cdot l \tag{3.1}$$

Absorption spectroscopy in the UV-vis is the most common technique to measure the concentration of nucleic acid samples. RNA exhibits a characteristic absorption maximum at 260 nm reflecting the fundamental π–π^* transition of the nucleobases. π-electrons in the aromatic rings of the bases are excited, the molar absorption coefficient ε_{260} of the RNA molecule depends on the base composition, nearest-neighbour interactions between bases (base-stacking), and interstrand interactions (base pairing) [41]. Molar absorption coefficients of single nucleotides are in the range $\varepsilon_{260} = 0.7 - 1.5 \cdot 10^4\,\mathrm{M^{-1}cm^{-1}}$ [41, 105]. When molar absorption coefficients are known or can be approximated (see section 4.2.2) the UV absorbance maximum can be used to measure the concentration of RNA in a liquid sample at room temperature via eq. (3.1). Elevating sample temperatures leads to changes in both inter- and intrastrand interactions that affect ε_{260}. UV absorbance as a function of temperature then reflects structural changes of the RNA molecule.

To measure UV-vis absorption spectra, a commercial scanning spectrophotometer was used (Perkin Elmer Lambda 950) with a spectral resolution of 1 nm. The sample cell was a Hellma TrayCell with optical path lengths between 0.1 and 1 mm. To measure temperature dependent curves of RNA, the same spectrometer was used in a modified set-up. RNA samples were held in a temperature controlled liquid cell (Harrick) in between two 1 mm thick BaF_2-windows separated by a 12 µm Teflon spacer. Temperature changes were applied at a steady rate of 2 K/min, the sample was allowed to equilibrate for 6-8 minutes before measuring a spectrum.

Circular dichroism spectroscopy

CD spectroscopy is a specific case of UV absorption spectroscopy. Chiral molecules, such as RNA and DNA, show distinct absorption properties when illuminated by circularly polarized light. The molar absorption coefficient ε differs whether the sample is exposed to left- or right-handed circularly polarized light (ε_L vs ε_R). Circular dichroism spectroscopy measures this difference:

$$\Delta A = A_L - A_R = (\varepsilon_L - \varepsilon_R) lc$$

Results are traditionally expressed as molar ellipticity in standard units [$\mathrm{deg\,cm^2\,dmol^{-1}}$]

$$[\theta] = 100 \cdot \ln(10) \frac{180}{4\pi} \cdot \frac{\Delta A}{lc} \tag{3.2}$$

when l and c are expressed in units of cm and mol/l, respectively. CD spectra carry qualitative information on nucleic acid conformation and are able to distinguish A-type from B-type helices [41]. Here, CD spectroscopy was used to monitor strong structural transitions of double helical RNA upon heating, reported in section 4.2.2.

The CD spectra shown in this thesis were recorded using a commercial CD spectrometer (Jasco model J-720) in steps of 0.5 nm over the wavelength range of 200-350 nm. Samples were held in a temperature-controlled liquid cell (Harrick). The opportunity to measure the spectra was kindly provided by the Leibniz Institute for Molecular Pharmacology (FMP) in Berlin-Buch.

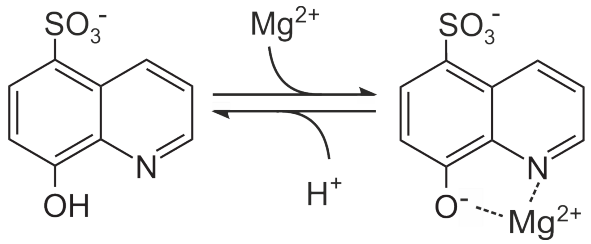

Figure 3.1: Schematic of 8-HQS and its Mg^{2+} binding complex. Upon uptake of Mg^{2+} the HQS molecule a proton is released, the complex is charge-neutral. The intrinsic binding constant K°_{HQS} is $11.3\mathrm{x}10^3\,\mathrm{M}^{-1}$, the apparent binding constant is strongly pH-dependent and is on the order of $100\,\mathrm{M}^{-1}$ at a pH of 6 in our measurements.

Fluorescence spectroscopy

Fluorescence spectroscopy is used to quantify the interactions of RNA with Mg^{2+} ions in direct vicinity and in its ion atmosphere. The technique has been used in early work on RNA-Mg^{2+} binding [53], later work systematically characterized the method [55]. It returns an accurate number of the RNA-Mg^{2+} interactions, but can not distinguish between contact and diffuse binding. Fluorescence spectroscopy is performed with 8-hydroxyquinoline-5-sulfonic acid (8-HQS, Merck) in solution. 8-HQS forms chelate complexes with a variety of multivalent metals, including Mg^{2+} [106]. Such an 8-HQS/Mg^{2+} complex is depicted in fig 3.1. Ion chelation is coupled to deprotonation of the quinoline hydroxyl group, significantly changing the electronic properties and consequently absorption and emission spectra. The solid lines in figure 3.2 show the changes in the UV-vis absorption spectrum upon addition of Mg, the isosbestic point at 330 nm indicates the formation of a 1:1 Mg^{2+}-HQS chelation complex. [55]

Upon excitation of the chelated complex the molecule shows a highly Mg^{2+} dependent fluorescence emission with an intensity maximum at 510 nm (dashed lines in fig. 3.2). The absorbance maximum of the complex is at 357 nm, but samples are excited on the edge of the absorption spectrum (see green arrow in fig. 3.2) to reduce problems with self-quenching [55].

To maintain stable pH, fluorescence samples were prepared in a buffer containing 0.1 mM 8-HQS (0.5 mM for dsRNA measurements), 10 mM sodium cacodylate and 22 mM NaCl. Buffer solutions with additional 5, 50, 250, or 1000 mM $MgCl_2$ were manually titrated in volumes of 1-20 µl to reach Mg^{2+} ion concentrations in the range of 33 µM to 400 mM.

Plotting the signal intensity at 510 nm over the added Mg^{2+} concentration yields a reference saturation curve characteristic of a single site binding isotherm (fig. 3.3 red curve, cf. equation (2.3)). At each titration step 3 – 10 fluorescence spectra were taken, the mean intensities $\bar{I}$ were normalized to lie between 0 and 1:

$$I_{norm} = \frac{\bar{I} - I_{min}}{I_{max} - I_{min}}$$

To measure Mg^{2+} ion binding to RNA, an additional titration series was performed with a sample containing both the 8-HQS buffer specified above and RNA. In samples containing both 8-HQS and RNA, added Mg^{2+} ions preferably interact with the highly negatively

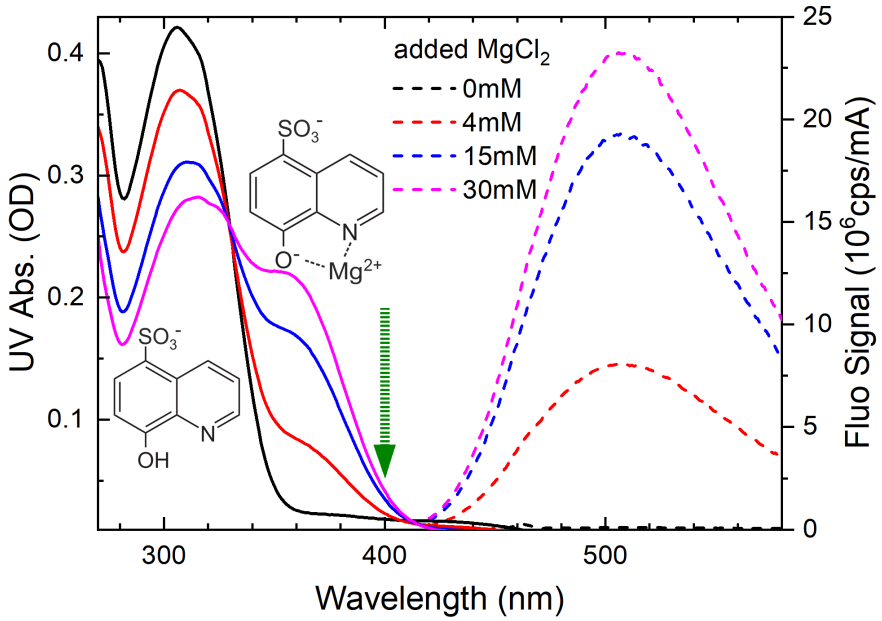

Figure 3.2: UV-vis absorption (solid) and fluorescence (dashed) of 0.1 mM 8-HQS in H_2O. Addition of Mg^{2+} leads to a decrease in absorbance around 305 nm and an increase around 370 nm due to complex formation. There is an isosbestic point at 315 nm. Excitation at 400 nm (green arrow) results in Mg^{2+} dependent fluorescence with an emission maximum at 510 nm. The lack of fluorescence in the initial, uncomplexed state has been attributed to quenching by a photoinduced proton transfer from the hydroxyl group to the nitrogen. [107]

charged RNA. This reduces the number of Mg^{2+}-HQS complexes and accordingly the detected fluorescence intensity at a given concentration of total added Mg^{2+}. A higher concentration of Mg^{2+} is necessary to achieve the same fluorescence intensity (cf. fig. 3.3). This behaviour can be exploited to determine the concentration $c_{bd\mathrm{Mg}^{2+}}$ of Mg^{2+} ions bound either directly or diffusely to the RNA sample, provided that $c_{\mathrm{HQS}} \ll c_{\mathrm{Mg}^{2+}}$:

$$c_{bd\mathrm{Mg}^{2+}} = c_{\mathrm{Mg}^{2+}}(I) - c_{free\mathrm{Mg}^{2+}}(I)$$

This allows to calculate the number v of bound ions per RNA molecule, as introduced in chapter 2.1.3

$$v = \frac{\partial \ln Q}{\partial \ln c_{\mathrm{Mg}^{2+}}} = \frac{c_{bd\mathrm{Mg}^{2+}}}{c_{RNA}}$$

An example of the binding curve as a function of the ratio of added Mg^{2+} to RNA $R = c_{\mathrm{Mg}^{2+}}/c_{RNA}$ is shown in figure 3.4.

Fluorescence spectra were recorded in a commercial fluorescence spectrometer (HORIBA Fluorolog FL3-22). Samples were excited at 400 nm, fluorescence emission was detected at 510 nm. Both emission and detection bandwidths were chosen to be 2 nm. Samples were

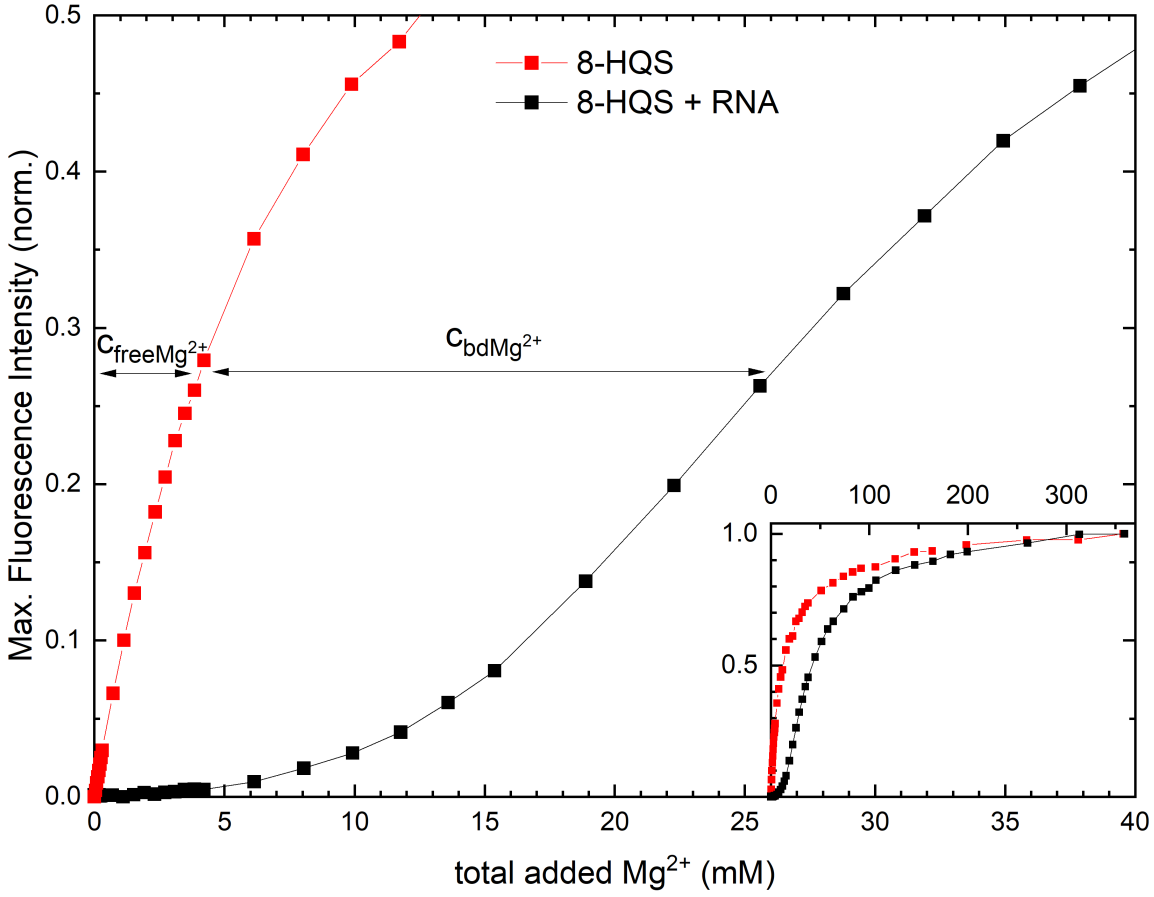

Figure 3.3: Fluorescence intensity at 510 nm taken for samples without (red) and with RNA (black). The difference in intensity increase is due to Mg^{2+} bound to RNA. By taking the concentration difference at a fixed intensity, this contribution can be quantified. Inset: The same fluorescence curve displayed over the whole concentration range. The curves start to overlap within experimental accuracy above 100 mM of added Mg^{2+}, making the difference procedure unreliable for these concentrations.

held in a fluorescence cuvette made from Suprasil Quartz Glass (QS).

3.2 Vibrational spectroscopy

This section introduces the fundamentals of two-dimensional vibrational spectroscopy. A quantum mechanical system, in our case a vibrational oscillator, can be described by its system Hamiltonian H. It is the sum of the kinetic energy T and the potential energy V, that depends on the vibration's normal coordinate r.

$$H = T + V(r) \tag{3.3}$$

The eigenstates of the Hamiltonian correspond to wavefunctions with the quantized energy levels of the oscillator, the vibrational normal modes. For a molecule with N atoms, the vibrational potential can be expanded around the normal coordinates r_i of each of the 3N-6

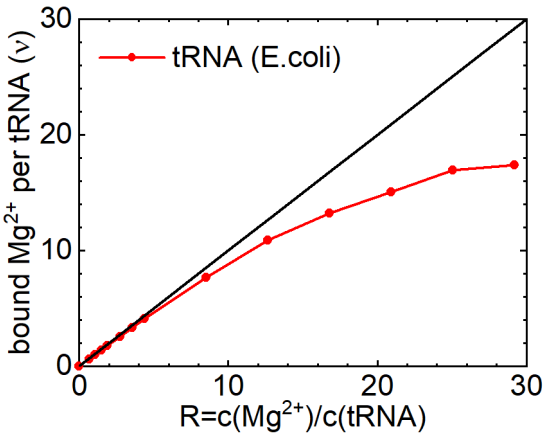

Figure 3.4: Number of bound Mg^{2+} per RNA (here: *E.coli* tRNA) determined by fluroescence titration measurements given here as a function of the ratio R. Data will be presented and discussed in detail in chapter 7.

normal modes:

$$V(r) = \underbrace{V_0}_{:=0} + \underbrace{\sum_{i}^{3N-6} \frac{\partial V}{\partial r_i} r_i}_{=0} + \frac{1}{2!} \sum_{i,j}^{3N-6} \frac{\partial^2 V}{\partial r_i \partial r_j} r_i r_j + \frac{1}{3!} \sum_{i,j,k}^{3N-6} \frac{\partial^3 V}{\partial r_i \partial r_j \partial r_k} r_i r_j r_k + \dots \tag{3.4}$$

V_0 is the equilibrium potential that is constant and can be arbitrarily set to zero. The potential is probed around the equilibrium position where the first derivative is zero. In the harmonic approximation terms of the third or higher order are neglected, so only the second order terms of equation (3.4) remain. This allows to explicitly solve the Schrödinger equation for the energy eigenvalues:

$$E_{\text{harm}}(v_1, ...v_{3N-6}) = \sum_{i}^{3N-6} \hbar\omega_i \left(v_i + \frac{1}{2}\right) \tag{3.5}$$

Here, v_i denotes the quantized energy level of the i-th vibrational mode, that vibrates with a characteristic frequency ω_i. Figure 3.5 shows the parabolic potential of a harmonic oscillator across a single normal coordinate. As a result of eq. (3.5) the energy levels are equidistant and separated by $\hbar\omega$.
In a more realistic anharmonic potential this equidistance does not hold true anymore. Higher order terms of equation (3.4) do not all disappear, resulting in anharmonicities Δ_{ij} in the energy eigenvalues

$$E_{\text{anharm}}(v_1, \dots, v_{3N-6}) = \sum_{i}^{3N-6} \hbar\omega_i \left(v_i + \frac{1}{2}\right) + \sum_{i}^{3N-6} \sum_{j \geq i}^{3N-6} \Delta_{ij} \left(v_i + \frac{1}{2}\right) \left(v_j + \frac{1}{2}\right) + \dots \tag{3.6}$$

Off-diagonal anharmonicities $\Delta_{i \neq j}$ express the pairwise potential coupling between the normal modes i and j, 2D-IR spectroscopy is one of the leading methods to detect these inter-mode couplings. Diagonal anharmonicities $\Delta_{i=j}$ offset the energy levels of the harmonic oscillator. The influence of $\Delta_{i=j}$ is seen in figure 3.5. The displayed Morse potential

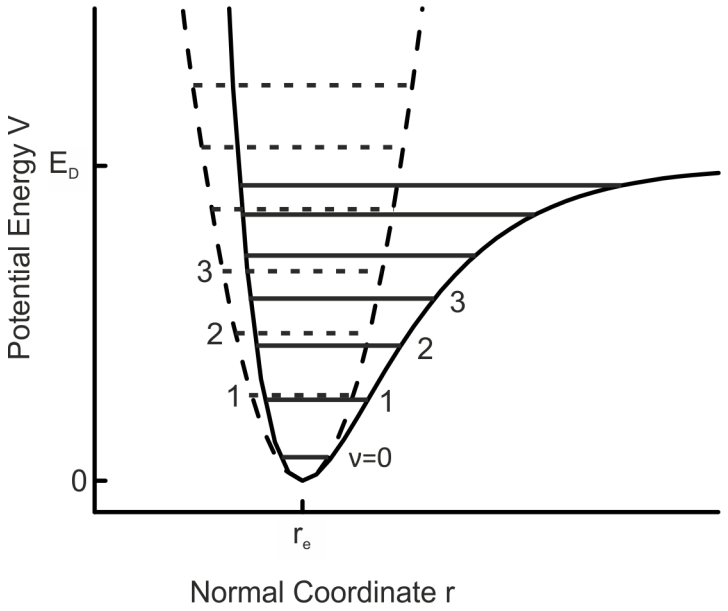

Figure 3.5: Vibrational potential of a harmonic oscillator (dashed) and of a Morse oscillator (solid). Both potentials are evaluated around the equilibrium position r_e. The harmonic potential is parabolic, the Morse potential shows a distinct asymmetry. For short distances r between the two atoms the repulsion is significantly stronger than in the harmonic case. At large distances, when the vibrational energy exceeds the dissociation energy E_D, the diatomic molecule dissociates into its constituent atoms.

models the vibrational potential of a diatomic molecule $V(r) = E_D(1 - e^{-a(r-r_e)})^2$. The equilibrium position r_e and the dissociation energy E_D are highlighted in fig. 3.5, a determines the curvature of the potential. Higher-order states are shifted to lower energy levels, because $\Delta_{i=j}$ is negative [108].

3.2.1 Density Matrix

In this thesis we do not operate with the oscillator of a single molecule, but rather with $\sim 10^{18}$ oscillators that act as a statistical ensemble. Instead of wavefunctions for each individual oscillator, this ensemble needs to be described by the density matrix ρ. The matrix dimension gives the number of considered energy eigenstates, the density matrix of a two-level system, for example, has the form $\rho = \left(\begin{smallmatrix}\rho_{00} & \rho_{01}\\ \rho_{10} & \rho_{11}\end{smallmatrix}\right)$. Diagonal elements reflect the population density of each respective state, off-diagonal elements portray coherences, i.e. coherent superposition between two states, mediated by the transition dipole. The density matrix $\rho = \frac{1}{2}\left(\begin{smallmatrix}1 & 0\\ 0 & 1\end{smallmatrix}\right)$ indicates oscillators are in ground state and first excited state with the same probability. $\rho = \frac{1}{2}\left(\begin{smallmatrix}1 & 1\\ 1 & 1\end{smallmatrix}\right)$ displays a coherent superposition between the two states.

The time evolution of the density matrix is given by the Liouville-von Neumann equation [109]

$$\frac{\mathrm{d}}{\mathrm{d}t}\rho(t) = -\frac{i}{\hbar}[H, \rho(t)].$$

In the case of an isolated molecular vibration with a time-independent Hamiltonian, the density matrix itself will not evolve. We will now look at two instances where the Hamil-

tonian does become time-dependent and significantly impacts the density matrix. First, the interaction of the density matrix with a light field that introduces a time-dependent interaction Hamiltonian. Second, fluctuations of the solvent that induce a time-dependence in the system's Hamiltonian.

3.2.2 Interaction with electric fields

Interactions of the ensemble of vibrational oscillators with the electric field of light are represented in an additional interaction Hamiltonian in eq. (3.3) linking the transition dipole moment μ with the time-dependent electric field of the interacting light $E(t)$:

$$H_{int} = -\vec{\mu} \cdot \vec{E}(t) \tag{3.7}$$

The time-dependent Hamiltonian $H(t)$ can be separated into a time-independent system Hamiltonian H_0 and the time-dependent interaction Hamiltonian $H_{int} = -\mu E(t)$. The Liouville-von Neumann equation can be rewritten entirely in the interaction picture using a basis transformation $\hat{x}_{int} = \mathrm{e}^{\frac{i}{\hbar}H_0(t-t_0)}\hat{x}\mathrm{e}^{-\frac{i}{\hbar}H_0(t-t_0)}$ on both H and ρ:

$$\frac{\mathrm{d}}{\mathrm{d}t}\rho_{int}(t) = -\frac{i}{\hbar}[H_{int}(t), \rho_{int}(t)] \tag{3.8}$$

This allows to uncouple the time-independent system contributions.

For a single interaction between ensemble and light field eq. (3.8) can be integrated to solve for $\rho(t)$

$$\rho^{(1)}(t) = \frac{i}{\hbar}\int_{t_0}^{t} [H_{int}(\tau), \rho(t_0)]\,\mathrm{d}\tau$$

which induces a linear polarization $P^{(1)}$ that is expressed by the interaction of ρ with μ

$$P^{(1)}(t) = \left\langle \mu(t)\rho^{(1)}(t) \right\rangle = \frac{i}{\hbar}\int_{t_0}^{t} E(\tau)\,\langle \mu(t)[\mu(\tau), \rho(t_0)]\rangle\,\mathrm{d}\tau \tag{3.9}$$

where $\langle \dots \rangle$ denotes the ensemble average. $P^{(1)}(t)$ emits a light field that destructively interferes with the original light field. This can be detected in linear absorption spectroscopy as an absorbance signal that depends on the square of the transition dipole moment $|\mu|^2$. Phenomenologically, linear IR spectroscopy probes single transitions on the potential energy surface, in this thesis the 0→1 transitions of the phosphate stretch vibrations introduced in section 2.2. The behaviour of IR absorption bands as a function of frequency ω is described using the Lambert-Beer law, presented in eq. (3.1)

$$A(\omega) = \varepsilon(\omega) \cdot c \cdot l$$

We generally use the angular frequency $\omega = 2\pi\nu$ for the derivations in this section, with the frequency ν of the electric field. Historically, frequencies in IR spectroscopy are given in units of cm^{-1} as wavenumber $\tilde{\nu} = \frac{\nu}{c} = \frac{1}{\lambda}$, with the speed of light c and the wavelength of the infrared radiation λ. When the frequency of the electric field is in resonance with the vibrational frequency, transitions between the sharp eigenstates along the vibrational potentials of figure 3.5 would manifest in delta distributions in the absorption spectrum. The

absorption strength is proportional to the square of the transition dipole moment $A \propto |\mu|^2$. Higher order transitions are negligible in linear spectroscopy, as the number of oscillators in the first excited state is commonly too low for excited state absorption. The transition dipole moment for excited state absorption increases as $\mu_{12} = \sqrt{2}\mu_{01}$ under the assumption of a harmonic oscillator. Non-linear techniques, such as 2D-IR spectroscopy, are sensitive to these higher-order transitions.

3.2.3 Vibrational Lineshapes

Practically, the vibrational potential is perturbed by interactions of the molecules with the environment. These perturbations modulate the absorbance around the transition frequency ω_i and can be expressed using the lineshape function g(t)

$$A_i(\omega) \propto Re \int_0^\infty \mathrm{e}^{i(\omega-\omega_i)t}\mathrm{e}^{-g(t)}\mathrm{d}t \tag{3.10}$$

Such stationary infrared spectra are presented throughout this thesis. All spectra were recorded using a commercial FTIR spectrometer (Bruker VERTEX 80v). Spectra were sampled between 800 and 6000 cm^{-1} with a resolution of 2 cm^{-1}. Samples were held in a liquid cell (Harrick), in the case of the melting experiments of chapter 6 the cell was temperature-controlled. The liquid sample was located in between two 1 mm thick BaF_2 windows separated by a 25 µm Teflon spacer.

Lineshapes observed in IR spectroscopy reflect vibrational lifetimes, as well as homogeneous and inhomogeneous broadening contributions. The aim of this section is to derive the lineshape function $g(t)$. This will allow to predict lineshapes based on assumptions about the fluctuations of transition frequencies of the oscillator induced by the molecular environment. Interactions with the solvent environment perturb the frequency of the vibrational oscillation

$$\omega(t) = \omega_0 + \delta\omega(t)$$

This in turn affects the dynamics of the off-diagonal density matrix element, that encodes coherences between the ground state and the first excited state

$$\frac{\mathrm{d}\rho_{01}}{\mathrm{d}t} = -i\omega_{01}(t)\rho_{01}(t).$$

A single integration yields

$$\rho_{01}(t) \propto e^{-i\omega_{01}t}\left\langle \exp\left(-i\int_0^t \delta\omega(\tau)\mathrm{d}\tau\right)\right\rangle. \tag{3.11}$$

In the static case, the system would simply oscillate at the transition frequency ω_{01}. The additional term, however, results in oscillations at slightly different frequencies. Statistically, all the different vibrational frequencies eventually result in purely destructive interference, i.e. dephasing. To reflect this loss of coherence the lineshape function $g(t)$ is introduced:

$$e^{-g(t)} := \left\langle \exp\left(-i\int_0^t \delta\omega(\tau)\mathrm{d}\tau\right)\right\rangle$$

The cumulant expansion allows a reordering of the ensemble average terms to yield

$$e^{-g(t)} = \left\langle \exp\left(-i\int_0^t \delta\omega(\tau)\mathrm{d}\tau\right)\right\rangle = \exp\left(-\frac{1}{2}\int_0^t\int_0^t \langle\delta\omega(\tau_1)\delta\omega(\tau_2)\rangle \mathrm{d}\tau_1\mathrm{d}\tau_2\right)$$

This expansion is exact when the fluctuations $\delta\omega$ follow Gaussian statistics, which is often the case in sample-solvent interactions [109].

In the ergodic limit, frequency fluctuations around the vibrational equilibrium are stochastic processes. When evaluating $\langle\delta\omega(\tau_1)\delta\omega(\tau_2)\rangle$, it is thus possible to shift the time origin to τ_1=0, so that the ensemble average only depends on the time difference $\tau = \|\tau_1 - \tau_2\|$. Additionally, the ergodicity of the system introduces a symmetry about the $\tau_1 = \tau_2$ axis. Both these factors allow to simplify the integral to

$$g(t) = \int_0^t\int_0^{\tau'} \langle\delta\omega(\tau'')\delta\omega(0)\rangle \mathrm{d}\tau''\mathrm{d}\tau' \tag{3.12}$$

Thus, we arrive at the most crucial part of the lineshape function, the Frequency Fluctuation Correlation Function (FFCF) as the ensemble average over the fluctuation correlations:

$$C(\tau'') := \langle\delta\omega(\tau'')\delta\omega(0)\rangle$$

The lineshape function is then a double-integral of the FFCF, allowing to connect the microscopic frequency perturbations to the experimentally observable lineshape. The form of the FFCF depends on the system that is investigated and the solvent interactions. An analytical approach for Gaussian modulations was put forward by Kubo [110], assuming an exponential behaviour characterized by the fluctuation amplitude $\Delta\omega$ and a characteristic correlation time τ_c:

$$C(\tau'') = (\Delta\omega)^2 \mathrm{e}^{-\frac{|\tau''|}{\tau_c}} \tag{3.13}$$

The corresponding Kubo lineshape function $g(t)$ is the result of the double integration of eq. (3.12)

$$g(t) = (\Delta\omega)^2\tau_c^2\left(e^{-\frac{t}{\tau_c}} + \frac{t}{\tau_c} - 1\right) \tag{3.14}$$

It is useful to examine equation (3.14) for two limiting cases: fast, or small, fluctuations ($\Delta\omega\cdot\tau_c \ll 1$, e.g. librations of surrounding water molecules) and slow, or strong, fluctuations ($\Delta\omega\cdot\tau_c \gg 1$, e.g. slow chemical reorientations).

In the former, so-called homogeneous limit, the lineshape function simplifies to

$$g(t) = (\Delta\omega)^2\tau_c t := \frac{t}{T_2^*}$$

with the pure dephasing time $T_2^* := 1/((\Delta\omega)^2\tau_c)$. The linear absorbance has a Lorentzian lineshape:

$$A(\omega) \propto \frac{1/T_2^*}{(\omega-\omega_{01})^2 + 1/T_2^*}$$

In the complementary inhomogeneous limit the FFCF $\langle \delta\omega(\tau)\delta\omega(0)\rangle = (\Delta\omega)^2$ becomes approximately constant. The lineshape function and the resulting absorption spectrum are

$$g(t) = \frac{(\Delta\omega)^2}{2}t^2$$
$$A(\omega) \propto \mathrm{e}^{-\frac{(\omega-\omega_0)^2}{2\Delta\omega^2}}.$$

The static distribution of frequencies results in a Gaussian lineshape.

Molecular vibrations are rarely subjected to only one kind of frequency fluctuation. Their FFCFs are then not mono-exponential, as in eq. (3.13), but bi- or higher order exponential, their envelope is neither Lorentzian nor Gaussian. The different lineshape contributions from all different dephasing timescales are highly convoluted in the time-averaging of linear spectroscopy. Ultrafast nonlinear spectroscopy techniques, such as 2D-IR, are required to meaningfully map the correlation function. In a 2D spectrum different lineshapes can be readily distinguished by their different characteristic two-dimensional shapes. The following section will discuss the theoretical foundations of nonlinear spectroscopy to detail these characteristic properties.

3.2.4 Nonlinear Spectroscopy

The theoretical groundwork of nonlinear spectroscopy has been established in a number of books and publications. Here we will present in brief the relevant terms, based on the works of Hamm and Zanni, as well as Mukamel. [109, 111] Two concepts are vital for the understanding of nonlinear light-matter interactions: the density matrix and the nonlinear polarization. The density matrix was introduced in section 3.2.1 and reflects the quantum states of the ensemble of oscillators. Here, we will focus on the nonlinear polarization, because knowing it allows to draw conclusions on the system's response to an external light field.

The (electric) polarization $P(t)$ describes the density of electric dipole moments generated inside matter due to an applied electric field $E(t)$, in this case the electric field of light. This relation is linear for weak electric field strengths, $P(t) = \varepsilon_0\chi^{(1)}E(t)$, with the linear electric susceptibility of the medium $\chi^{(1)}$. In the regime of nonlinear light-matter interactions, the polarization is additionally characterized by nonlinear terms of higher order:

$$\begin{aligned} P(t) &= \varepsilon_0[\chi^{(1)}E(t) + \chi^{(2)}E(t)^2 + \chi^{(3)}E(t)^3 + \dots] \\ &= P^{(1)}(t) + P^{(2)}(t) + P^{(3)}(t) + \cdots + P^{(n)}(t) \end{aligned}$$

At electric field amplitudes on the order of atomic electric fields $\chi^{(1)}|E(t)| \approx \chi^{(2)}|E(t)|^2$ [112]. This requires electric field strengths $E \approx \frac{e}{4\pi\varepsilon_0 a_0^2} \approx 5 \cdot 10^{11}\,\mathrm{V/m}$, where $a_0 = 5.29 \cdot 10^{-11}\,\mathrm{m}$ denotes the Bohr radius of a hydrogen atom. It is important to distinguish between resonant and non-resonant light-matter interactions. Non-resonant, also called parametric, processes are characterized by electric field frequencies significantly far away from any energy level transitions of the medium. They leave the quantum state of the system untouched and instead rely on virtual energy levels. Optical parametric amplification (OPA) and difference frequency generation (DFG) are examples of non-resonant nonlinear interactions. Both processes are used in this thesis to generate the mid-IR pulses employed

in the experiments, see section 3.3.

The nonlinear vibrational spectroscopy covered here is the result of resonant interactions, i.e., the frequency of the electric field is tuned to, e.g., the characteristic transition frequency of $\nu_{AS}(PO_2^-)$, the asymmetric phosphate stretch vibration, around $1200\,\mathrm{cm}^{-1}$ (8300 nm). Resonant interactions change the quantum state of the system, in this case the density matrix $\rho(t)$. Nonlinear responses at resonance frequencies occur already at lower fields, e.g. the mid-IR laser pulses used in the nonlinear experiments of this thesis had peak electric field strengths $E \sim 10^9\,\mathrm{V/m}$. Multiple interactions of the density matrix with the electric field result in higher-order perturbations of the density matrix

$$\rho_{int}(t) = \rho_{int}(t_0) + \sum_{n=1}^{\infty} \rho_{int}^{(n)}(t)$$

where n denotes the number of interactions with the electric field. The n-th order density matrix can be computed by integrating eq. (3.8) n times.

$$\begin{aligned}\rho_{int}^{(n)}(t) = &-\left(-\frac{i}{\hbar}\right)^n \int_{t_0}^{t} \mathrm{d}\tau_n \int_{t_0}^{\tau_n} \mathrm{d}\tau_{n-1} \cdots \\ &\cdots \int_{t_0}^{\tau_2} \mathrm{d}\tau_1 [H_{int}(\tau_n), [H_{int}(\tau_{n-1}), \ldots [H_{int}(\tau_1), \rho_{int}(t_0)] \cdots]]\end{aligned}$$

Here, $\rho(t_0)$ is the initial equilibrium density matrix of the system. The nonlinear polarization can be expressed by the interaction of the transition dipole moment $\mu(t)$ with the density matrix $\rho(t)$. All these elements are time-dependent because they are treated in the interaction picture. For better readability the subscript *int* is dropped.

$$P^{(n)}(t) = \mathrm{Tr}[\mu(t)\rho^{(n)}(t)] = \langle \mu(t)\rho^{(n)}(t) \rangle \tag{3.15}$$

where $\langle \ldots \rangle$ denotes the expectation value, not the ensemble average.

Inserting the definition of the n-th order density matrix and making use of the fact that $\rho(t_0) = \rho(-\infty)$ (the density matrix is time-independent up until t_0) we get

$$\begin{aligned}P^{(n)}(t) = &-\left(-\frac{i}{\hbar}\right)^n \int_{-\infty}^{t} \mathrm{d}\tau_n \int_{-\infty}^{\tau_n} \mathrm{d}\tau_{n-1} \cdots \\ &\cdots \int_{-\infty}^{\tau_2} \mathrm{d}\tau_1 \langle \mu(t)[H(\tau_n), [H(\tau_{n-1}), \ldots [H(\tau_1), \rho(-\infty)] \cdots]] \rangle.\end{aligned} \tag{3.16}$$

Inserting the interaction Hamiltonian $H(t) = -\mu(t)E(t)$:

$$\begin{aligned}P^{(n)}(t) = &-\left(-\frac{i}{\hbar}\right)^n \int_{-\infty}^{t} \mathrm{d}\tau_n \int_{-\infty}^{\tau_n} \mathrm{d}\tau_{n-1} \cdots \int_{-\infty}^{\tau_2} \mathrm{d}\tau_1 E(t-t_n)E(\tau_{n-1}) \cdots \\ &\cdots E(\tau_1) \langle \mu(t)[\mu(\tau_n), [\mu(\tau_{n-1}), \ldots [\mu(\tau_1), \rho(-\infty)] \cdots]] \rangle\end{aligned} \tag{3.17}$$

with the ensemble average $\langle \ldots \rangle$ as above. This can be reformulated by substituting the absolute times τ with time differences $t_m = \tau_{m+1} - \tau_m$ that reflect the relative time sequence of light-matter interactions. $\tau_1 = 0$ can be arbitrarily chosen as the starting point.

$$\begin{aligned}P^{(n)}(t) = &\int_0^{\infty} \mathrm{d}t_n \int_0^{\infty} \mathrm{d}t_{n-1} \cdots \int_0^{\infty} \mathrm{d}t_1 E(t-t_n)E(t-t_n-t_{n-1}) \cdots \\ &E(t-t_n-t_{n-1}-\cdots-t_1) R^{(n)}(t, t_n, t_{n-1}, \ldots, t_1)\end{aligned} \tag{3.18}$$

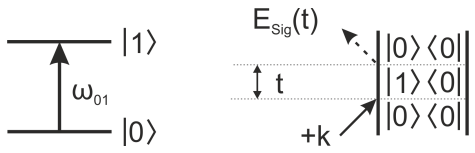

Figure 3.6: Left: Schematic energy diagram of a two-level system with transition frequency ω_{01}. Right: Double-sided Feynman diagram for the case of linear absorption in a two-level system.

where the polarization is expressed as the n-fold interaction of the electric field with an n-th order nonlinear response function $R^{(n)}$, which contains the complete microscopic information.

$$R^{(n)}(t_n, \ldots, t_1) = -\left(-\frac{i}{\hbar}\right)^n \langle \mu(t_n + \cdots + t_1)[\mu(t_{n-1} + \cdots + t_1), \ldots [\mu(0), \rho(-\infty)] \cdots]\rangle \tag{3.19}$$

It is useful for the understanding of the above equations to explicitly consider their terms in the linear case, the linear polarization was introduced in eq. (3.9). Linear absorption implies a single interaction $n = 1$ and eq. (3.19) transforms to

$$R^{(1)} \propto i\langle \mu(t_1)[\mu(0), \rho(-\infty)]\rangle$$

or explicitly

$$R^{(1)}(t_1) \propto i\mu_{01}^2 \mathrm{e}^{-i\omega_{01}t_1}\mathrm{e}^{-t_1/T_2}$$

A useful way to visualize and contextualize this and higher order response functions are double-sided Feynman diagrams. They show the time evolution of the density matrix together with relevant interactions with the light field. Such a Feynman diagram for the case of linear absorption in a two-level system is shown in fig. 3.6.

Intially, the density matrix is in its ground state $|0\rangle\langle 0|$. The interaction with the light pulse leads to the creation of a coherence $|1\rangle\langle 0|$. This interaction with the electric field adds a term proportional to the transition dipole moment μ_{01}, according to $P = \langle \mu\rho\rangle$. This coherence then oscillates at the frequency of the energy difference ω_{01} and dephases with the characteristic dephasing time T_2. T_2 is a composite term of the pure dephasing time derived in section 3.2.3 and the population relaxation time T_1. In the simplest case, $1/T_2 = 1/2T_1 + 1/T_2^*$. This dephasing contributes the term $\mathrm{e}^{-i\omega_{01}t_1}\mathrm{e}^{-t_1/T_2}$ to the response function. After this dephasing time t_1 the signal is read out, again the interaction contributes a term μ_{01}. The emitted signal is 180° phase changed with respect to the intial pulse, resulting in destructive interference. The result is a decrease in detected signal given by

$$\begin{aligned} A(\omega) &\propto \mathrm{Re}\left(\int_0^\infty iR^{(1)}(t)\mathrm{e}^{i\omega t}\mathrm{d}t\right) \\ &\propto \mathrm{Re}\left(\int_0^\infty \mu_{01}^2 \mathrm{e}^{i(\omega-\omega_{01})t_1}\mathrm{e}^{-t_1/T_2}\mathrm{d}t_1\right) \end{aligned}$$

The dephasing and lifetime dynamics discussed here are thus the microscopic origin of the lineshape function $g(t)$ in eq. (3.10).

Three-Pulse photon echo spectroscopy

Three-pulse photon echo spectroscopy relies on three field interactions with the density matrix of the sample. It is the basis for the 2D-IR set-up used in this thesis. The process can be described using the third-order polarization

$$P^{(3)}(t) = \int_0^\infty \mathrm{d}t_3 \int_0^\infty \mathrm{d}t_2 \int_0^\infty \mathrm{d}t_1 E(t-t_3)E(t-t_3-t_2)E(t-t_3-t_2-t_1)R^{(3)}(t,t_3,t_2,t_1) \tag{3.20}$$

with the third-order response function

$$R^{(3)}(t_3,t_2,t_1) = -\left(-\frac{i}{\hbar}\right)^n \langle \mu(t_3+t_2+t_1)[\mu(t_2+t_1),[\mu(t_1),[\mu(0),\rho(-\infty)]]]\rangle \tag{3.21}$$

The corresponding Feynman diagrams for a three-level system displayed in figure 3.7 are governed by three interactions of the density matrix with the light field. The three interactions are assigned to the wave vectors $\vec{k_1}, \vec{k_2}$, and $\vec{k_3}$, they are separated by the coherence time $\tau = t_1$, the waiting time $T = t_2$ and a second coherence time $t = t_3$, renamed to better distinguish them in the subsequent discussions. The experimental realization is discussed in section 3.3, the geometry used in our set-up in figure 3.15. In the case in the top left corner, the first pulse creates a coherence (contributing a term μ_{01}, as in the linear case) that then dephases for a time period τ ($\mathrm{e}^{-i\omega_{01}\tau}\mathrm{e}^{-\tau/T_2}$). The second pulse converts this coherence into a population state (μ_{01}). This population state decays with its characteristic lifetime T_1 over the time period T (e^{-T/T_1}). A third pulse creates a second coherence (μ_{01}) that again dephases ($\mathrm{e}^{-i\omega_{01}t}\mathrm{e}^{-t/T_2}$). The emitted signal then adds another μ_{01} term, so that the final response function is expressed as

$$R_1^{(3)} \propto \mu_{01}^4 \mathrm{e}^{-i\omega_{01}\tau}\mathrm{e}^{-\tau/T_2}\mathrm{e}^{-T/T_1}\mathrm{e}^{-i\omega_{01}t}\mathrm{e}^{-t/T_2}$$

This procedure can be followed for the other five relevant Feynman diagrams to yield their response functions

$$\begin{aligned}
R_2^{(3)} &\propto \mu_{01}^4 \mathrm{e}^{-i\omega_{01}\tau}\mathrm{e}^{-\tau/T_2}\mathrm{e}^{-T/T_1}\mathrm{e}^{-i\omega_{01}t}\mathrm{e}^{-t/T_2} \\
R_3^{(3)} &\propto \mu_{01}^2\mu_{12}^2 \mathrm{e}^{-i\omega_{01}\tau}\mathrm{e}^{-\tau/T_2}\mathrm{e}^{-T/T_1}\mathrm{e}^{-i\omega_{12}t}\mathrm{e}^{-t/T_2^{(12)}} \\
R_4^{(3)} &\propto \mu_{01}^4 \mathrm{e}^{+i\omega_{01}\tau}\mathrm{e}^{-\tau/T_2}\mathrm{e}^{-T/T_1}\mathrm{e}^{-i\omega_{01}t}\mathrm{e}^{-t/T_2} \\
R_5^{(3)} &\propto \mu_{01}^4 \mathrm{e}^{+i\omega_{01}\tau}\mathrm{e}^{-\tau/T_2}\mathrm{e}^{-T/T_1}\mathrm{e}^{-i\omega_{01}t}\mathrm{e}^{-t/T_2} \\
R_6^{(3)} &\propto \mu_{01}^2\mu_{12}^2 \mathrm{e}^{+i\omega_{01}\tau}\mathrm{e}^{-\tau/T_2}\mathrm{e}^{-T/T_1}\mathrm{e}^{-i\omega_{12}t}\mathrm{e}^{-t/T_2^{(12)}}
\end{aligned}$$

The Feynman diagrams in fig. 3.7 are arranged according to their physical meaning. The two leftmost diagrams describe *stimulated emission* (SE). The first two pulses create a population in the first excited state. The third pulse results in a stimulated emission of the $|1\rangle\langle 1|$ population state down to the $|1\rangle\langle 0|$ coherence. The system finally ends up in the ground state, after emitting the signal electric field.

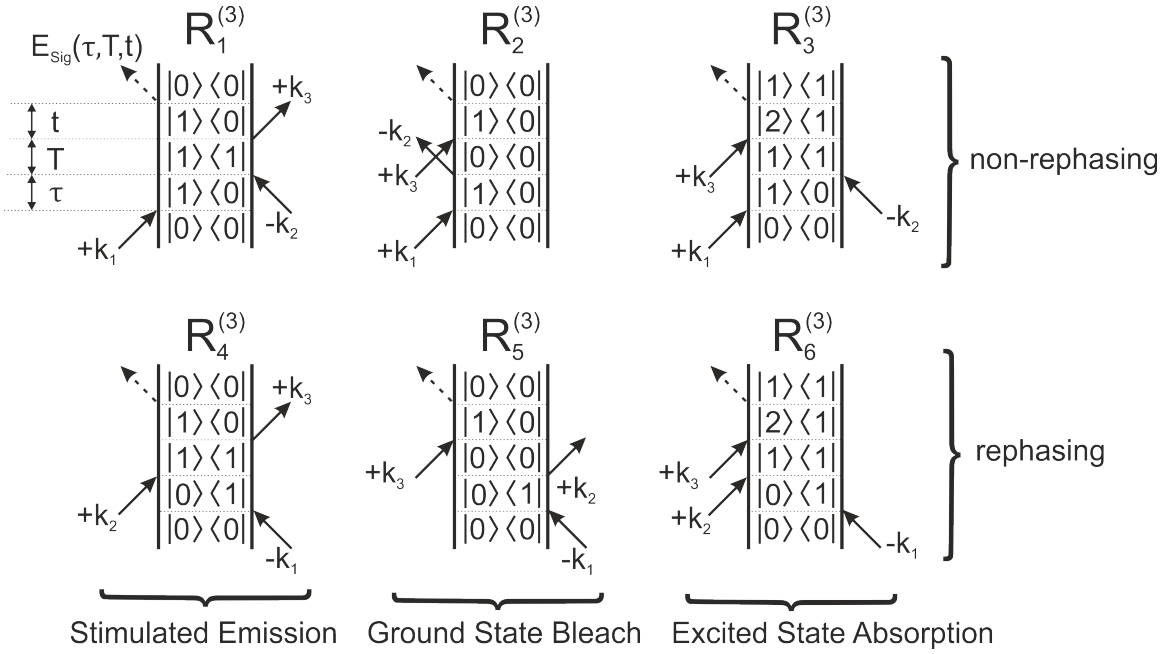

Figure 3.7: Double-sided Feynman diagrams of 2D spectroscopy for the case of a three-level system. Three pulses interact with the density matrix of the system, separated by the coherence time τ, the waiting time T, and a second coherence time t. The emitted signal E_{sig} carries information on the third-order molecular response function $R^{(3)}$

The two central diagrams show *ground-state bleach* (GSB). In this case the population state generated by the second pulse is the ground state, not the first excited state, the corresponding relaxation time refers to oscillators that need to relax back into the ground state ("bleaching" the ground state). The emitted signal is equivalent to the one from stimulated emission, consequently their response functions are also equivalent. In 2D-IR spectra GSB and SE features are indistinguishable.
The diagrams on the right side denote *excited state absorption* (ESA). k_3 acts on the $|1\rangle\langle 1|$ population state to create a coherence between first and second excited state. Correspondingly, the transition dipole moment for a transition between first and second excited state μ_{12} has to be considered, instead of μ_{01}. Within the harmonic approximation, $\mu_{12} = \sqrt{2}\mu_{01}$. The dephasing time constant T_2 is similarly affected. While the true dephasing time T_2^* is the same, the lifetime contribution from the second excited state amounts to $\frac{3}{2}T_1$.

Top and bottom diagrams are set apart by an additional factor, the phases of their coherence states. The first coherence in the three lower diagrams is $|0\rangle\langle 1|$, the second $|1\rangle\langle 0|$. A rephasing occurs in the emission of the signal (see the opposing phase in the dephasing terms of R_1, R_2, and R_3), dubbing these terms *rephasing signal*. This rephasing does not occur in the top spectra, where both coherences are in phase. The emitted signal is therefore called *non-rephasing*.

The absorptive 2D-IR spectra presented in this thesis contain rephasing and non-rephasing

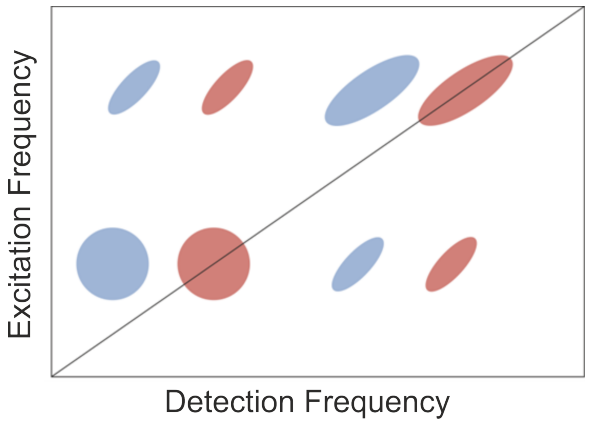

Figure 3.8: Schematic of a 2D-IR spectrum with two coupled oscillator modes. The excitation frequency axis ν_1 is set as a Fourier transform of the coherence time τ, the detection frequency axis ν_3 is a Fourier transform of t, or is established directly by passing the 2D signal through a monochromator and recording the spectrally resolved signal.

signal, the 2D-IR signal is calculated by taking the real part of their sum

$$S(\omega_1, T, \omega_3) = \mathfrak{Re}\left(\sum_{n=1}^{3} R_n(-\omega_1, T, \omega_3) + \sum_{n=4}^{6} R_n(+\omega_1, T, \omega_3)\right)$$

Here, $S(\omega_1, T, \omega_3)$ is the observed 2D-IR signal in the frequency domain, considered in the semi-impulsive limit, i.e. when the light pulses are short with respect to the characteristic timescales of the system. The 2D-IR signal is shown throughout the thesis in the frequency domain as a function of excitation frequency ω_1 and detection frequency ω_3. Evaluating the 2D-IR signal at different waiting times T gives full information on the third-order response functions [109]. The signal is transformed into the frequency domain by Fourier transformation along τ and t:

$$\begin{aligned} S(\omega_1, T, \omega_3) &= \mathfrak{Re}\left(\int_0^\infty \int_0^\infty S(\tau, T, t) \mathrm{e}^{-i\omega_1\tau} \mathrm{e}^{-i\omega_3 t} \mathrm{d}\tau \mathrm{d}t\right) \\ &= \mathfrak{Re}\left(\int_0^\infty \int_0^\infty \sum_n R_n(\tau, T, t) \mathrm{e}^{-i\omega_1\tau} \mathrm{e}^{-i\omega_3 t} \mathrm{d}\tau \mathrm{d}t\right) \end{aligned}$$

One schematic 2D-IR spectrum is presented in fig. 3.8 for two coupled vibrational modes. Along the diagonal axis contributions from GSB& SE (red) appear. ESA contributions (blue) are red-shifted on the ν_3 axis due to the anharmonicity of the vibrational potential. One vibrational mode shows a round, homogeneous signal, the other is inhomogeneously elongated along the diagonal. This difference in their lineshapes indicates fast and slow dephasing times for mode 1 and 2, respectively.
One of the prototypical problems for 2D-IR spectroscopy is the analysis of inter-mode couplings to gain information on molecular structure. These are a result of off-diagonal anharmonicities $\Delta_{i\neq j}$ in the energy eigenvalues of the oscillator (cf. eq.(3.6)) and are displayed as off-diagonal elements in fig. 3.8.

2D spectra can be simulated by explicitly calculating the 3rd order response functions. The contribution of rephasing and non-rephasing signal to the elements along the diagonal axis

is

$$R_{D1,2,3}(\tau,T,t) = \sum_{n=1}^{3} R_n^{(3)}(\tau,T,t) = \sum_i 2i\mu_{01i}^4 \left(e^{-i\omega_{01i}(t-\tau)} - e^{-i((\omega_{01i}-\Delta_i)t-\omega 01i\tau)} \right) e^{-T/T_{1i}} \times e^{-g_i(\tau)+g_i(T)-g_i(t)-g_i(\tau+T)-g_i(T+t)+g_i(\tau+T+t)} e^{-(\tau+T)/2T_{1i}}$$

$$R_{D4,5,6}(\tau,T,t) = \sum_{n=4}^{6} R_n^{(3)}(\tau,T,t) = \sum_i 2i\mu_{01i}^4 \left(e^{-i\omega_{01i}(t+\tau)} - e^{-i((\omega_{01i}-\Delta_i)t+\omega 01i\tau)} \right) e^{-T/T_{1i}} \times e^{-g_i(\tau)-g_i(T)-g_i(t)+g_i(\tau+T)+g_i(T+t)-g_i(\tau+T+t)} e^{-(\tau+T)/2T_{1i}}$$

The 2D-IR spectrum can then be computed by summing up the Fourier transforms of both signals with respect to τ and t. The parameters in such a simulation are the frequency ω_{01i} of the i-th vibrational mode, its diagonal anharmonicity Δ_i, the vibrational lifetime T_{1i} and the time-dependent lineshape function $g_i(t)$. A relative scaling factor takes into account differences between the transition dipole moments μ_{01i}. Under the assumption that the transition dipole moments are conserved, this relative scaling factor reflects differences in concentration between the underlying oscillators. The time-dependent lineshape functions $g_i(t)$ are determined by integrating the FFCF $\langle \delta\omega(\tau'')\delta\omega(0)\rangle$, which is modeled here using a double-exponential Kubo ansatz (cf. eq. (3.14)):

$$\frac{1}{4\pi}\left\langle \delta\omega(\tau'')\delta\omega(0)\right\rangle = \Delta\nu_{1i}^2 e^{-\tau''/\tau_1} + \Delta\nu_{2i}^2 e^{-\tau''/\tau_2}$$

This ansatz reflects the fast fluctuations of the water environment with the fluctuation amplitude $\Delta\nu_{1i}$, as well as slow structural re-arrangements and the inhomogeneous distribution of oscillators with the fluctuation amplitude $\Delta\nu_{2i}$. Here, the correlation decay time of the fast fluctuations $\tau_1 = 300\,\mathrm{fs}$ is on the order of the lifetime observed for $\nu_{AS}(\mathrm{PO_2^-})$. The second component can be considered static on the timescale of our experiments, values of τ_2=50 ps are assumed, as determined in similar simulations with phosphate groups [37,100]. Agreement between experimental and simulated spectra is monitored by comparing diagonal and anti-diagonal cuts, as well as simulated and experimental FTIR spectrum. Cross-peak contributions to the simulated 2D-IR spectra are not considered, since they are absent in our experimental spectra.

Pump-Probe spectroscopy

Pump-probe (PP) spectroscopy is a special case of third-order interactions. An intense pump laser pulse is used to interact twice at the same time with the density matrix of the system, effectively setting $\tau = 0$. This is schematically shown in the Feynman diagrams of fig. 3.9. The intense pump pulse quasi-instantaneously creates a population state that is then probed by a second, less intense pulse after a waiting time T. The Feynman diagrams are the same in this specific instance, carrying information on GSB& SE, and ESA. An exemplary spectrum is shown in fig. 3.9. In fact, the PP signal can be computed by integrating the 2D signal along the excitation frequency ν_1. For a purely harmonic oscillator, ESA and GSB& SE contributions have the same frequency and would cancel each other out. Pump-probe spectroscopy therefore requires some degree of anharmonicity in the oscillator's vibrational potential.

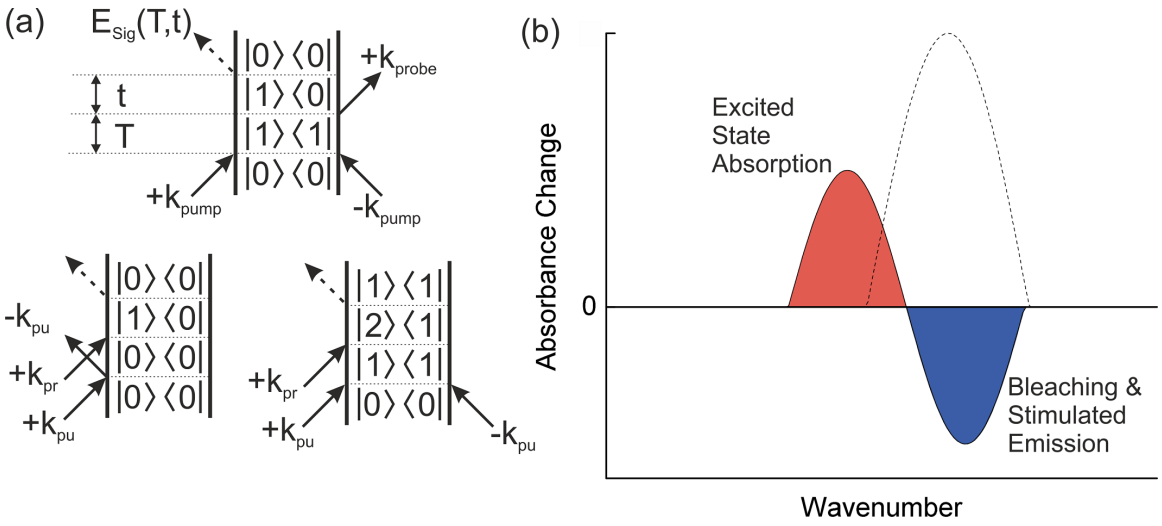

Figure 3.9: Left: Double-sided Feynman diagrams for pump-probe interactions in a three-level system. The intense pump pulse interacts twice with the density matrix, pump and probe beam are separated by a time delay T. Right: Schematic pump-probe spectrum, showing ESA and GSB&SE. The linear absorption peak is indicated as a dashed line, it should mirror the GSB&SE signal GSB should mirror, but is broader due to the overlap of GSB&SE with ESA.

3.3 Experimental set-ups for nonlinear IR spectroscopy

Two different set-ups of ultrafast nonlinear IR spectroscopy have been employed in the course of this thesis. Ultrafast pump-probe experiments are used to elucidate the vibrational lifetimes of the different phosphate vibrations. 2D-IR spectroscopy, as discussed above, enables to analyze vibrational lineshapes to understand frequency fluctuations of the environment. Off-diagonal elements in the spectra can be used to determine inter-mode anharmonic couplings. The experimental realization of both these techniques will be provided here.

Generation of femtosecond mid-IR pulses

Both set-ups employ ultrashort mid-IR pulses to excite and probe the sample of interest. These pulses are generated by parametric frequency conversion using optical parametric amplification (OPA) in beta-barium-borate (BBO) crystals followed by difference frequency generation (DFG) in gallium selenide (GaSe). The detailed generation process will be introduced here:

Figure 3.10 schematically shows the commercial laser system used to drive the experiments. It is explained here for the 2D-IR set-up, the initial 800 nm-pulse generation for the pump-probe set-up is very similar. An initial sub-100 fs laser pulse is generated in a Coherent Micra oscillator by optical pumping from a Coherent Verdi pump laser. The Verdi is a frequency-doubled Nd:YVO_4 laser in continuous wave (cw) mode reaching beam powers of 5 W at 532 nm. It is used to pump the Kerr-lens mode-locked Ti:Sapphire oscillator Micra. The Micra outputs a sub-100 fs pulse train at 800 nm with a repetition rate of 80 MHz.

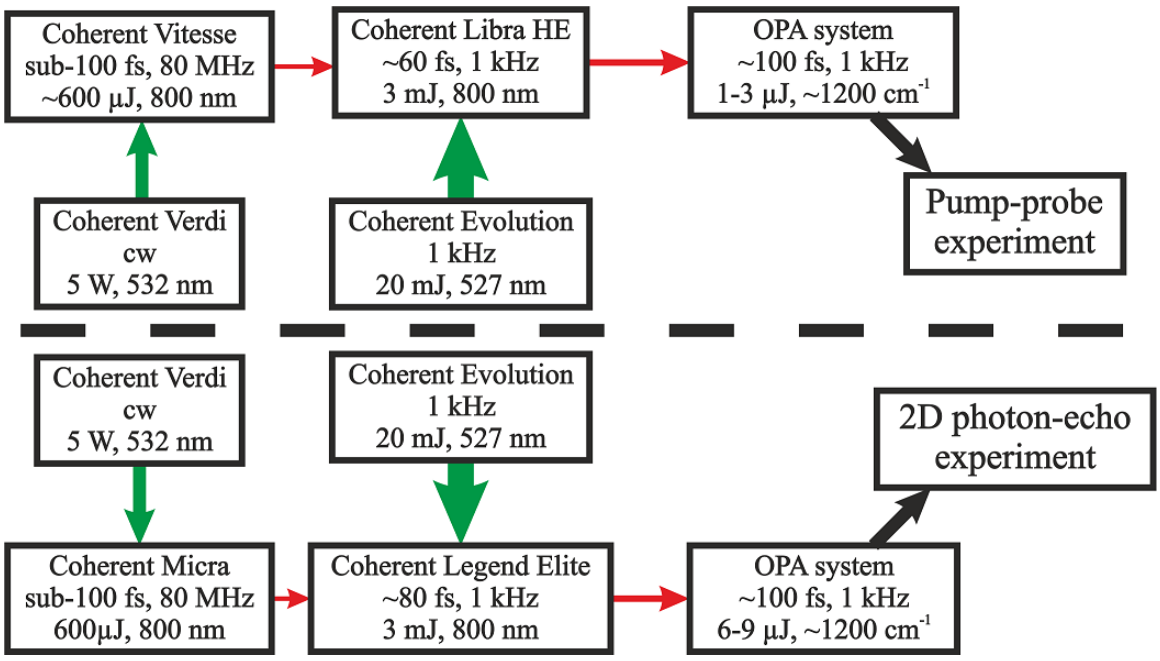

Figure 3.10: Schematic sketch of the laser systems used to feed our experiments. Intense ultrashort 800 nm laser pulses are parametrically converted into mid-IR pulses using a self-built OPA system. The 800 nm pulses are generated by commercial Coherent laser systems, where an oscillator pumped by a cw laser generates sub-100 fs pulses at a repetition rate of 80 MHz. These are then selectively amplified in a regenerative amplifier pumped by a Nd:YLF laser at 1 kHz repetition rate. Details of the OPA system are given in figure 3.11.

This pulse train is then amplified in a Coherent Legend Elite regenerative amplifier, using chirped pulse amplification (CPA). A reflective grating introduces a chirp in the pulse train, stretching the pulses to a pulse duration of 400 ps. Single pulses are singled out and coupled into the amplifier cavity via a Pockels cell, circularly polarizing them at a repetition rate of 1 kHz. These single pulses are fed into a Ti:Sapphire crystal, pumped by a Q-switched frequency doubled Nd:YLF Coherent Evolution laser. Each roundtrip amplifies this seed pulse further, until it is coupled out after $\approx 10 - 15$ roundtrips, $\approx 10^6$-fold amplified. A second Pockels cell directs the amplified pulse onto a compressor unit, where the initial chirp is reversed, compressing the pulse again to $\approx$ 80 fs and outputting pulses at 1 kHz with a power of 3 W, pulse energies are at 3 mJ.

To generate mid-IR laser pulses with femtosecond pulse duration, this output is now used to operate a multi-step optical parametric amplification process. The OPA system itself is depicted in fig. 3.11 for the case of the 2D-IR set-up. In three amplification steps, the incoming 800 nm beam is first converted into a signal pulse and an idler pulse in the near-IR. These pulses are then overlapped in a DFG crystal to generate a tunable mid-IR pulse with a pulse duration of $\approx$ 100 fs.

Initially, the 800 nm beam is split into four parts. The first part has $\approx$1 % power and is focused through a $\lambda/2$ waveplate onto a sapphire crystal (Al_2O_3). The ultra-short pulse duration leads to strong electric field strengths in the crystal and non-linear self-phase mod-

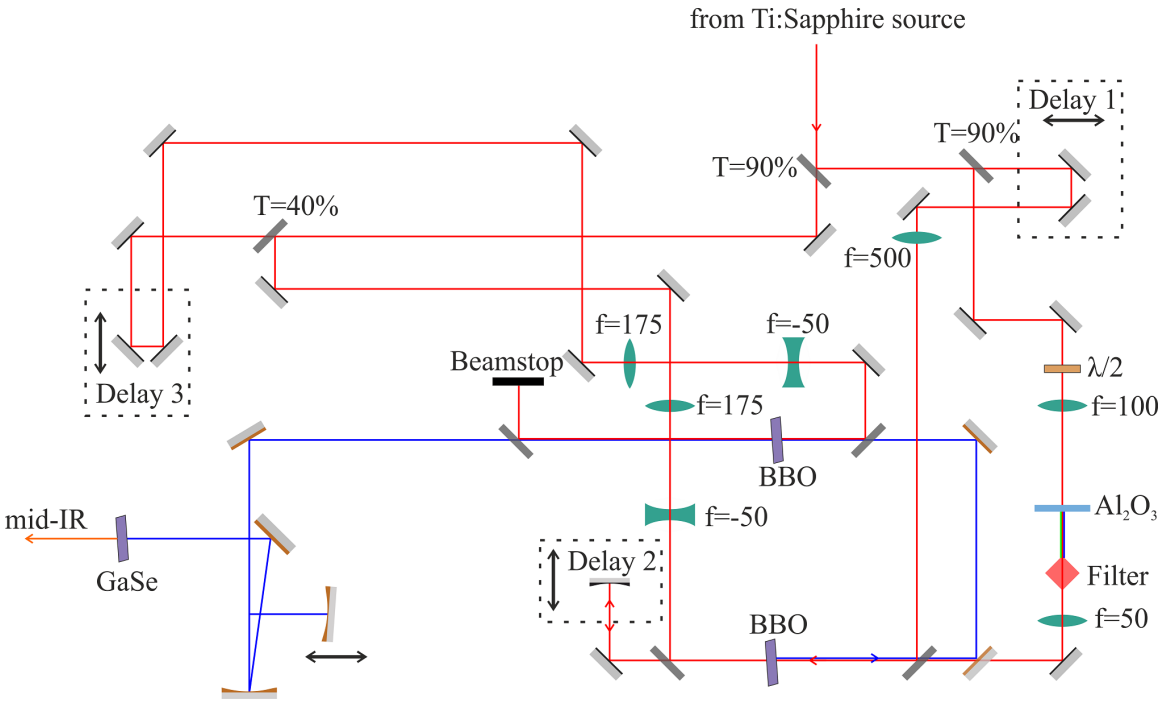

Figure 3.11: Schematic set-up of the OPA-system used to generate the mid-IR pump pulses. A white light continuum generated in Al_2O_3 is used as a signal pulse. It is parametrically amplified in BBO crystals three times resulting in near-IR signal and idler pulses with energies of 250μJ. Difference-frequency-mixing in a GaSe crystal is used to generate mid-IR pulses with an energy of 6-9 µJ at a repetition rate of 1 kHz.

ulation occurs, broadening the spectrum to a white light continuum [113]. The generated white light continuum is filtered and focused onto a BBO crystal (4 mm, $\theta = 25°$, $\phi = 0°$). There it is temporally (Delay 1) and spatially overlapped with the second part of the original pulse ($\approx 9\%$). The 800 nm pulse pumps a parametric amplification process employing type-II phase matching. The resultant signal and idler pulses are retroreflected off a second delay stage and pass through the BBO again, parallel to, but vertically displaced with respect to the first parametric amplification. The third portion of the original pulse ($\approx 55\%$) pumps the crystal and amplifies the signal to pulse energies of 250 µJ. The third amplification stage is pumped by the remaining ≈35% of the original pulse. Both signal and idler pulses pass through a second BBO crystal (2 mm, $\theta = 25°$, $\phi = 0°$) and are amplified to pulse energies of $\approx$ 300 µJ. They are then focussed onto a GaSe crystal (type-II, 0.3-0.5 mm) to generate mid-IR laser pulses via DFG. The mid-IR pulse has a pulse energy of 6 µJ after a long wave pass filter blocks the remaining near-IR portions of the beam.

The pump-probe experiment is based on a similar OPA system. Pump and probe beam have separate OPAs to independently tune their frequency. The second BBO crystal is not present in either of them, so only a two-stage parametric amplification is achieved before DFG. 90% of the original beam are used to pump the second stage to achieve 120 µJ of signal and idler pulse energies. DFG in two respective GaSe crystals leads to mid-IR pump and probe pulses with energies of 2.5 and 1.5 µJ, respectively.

Pump-probe experiment

To perform the pump-probe experiment, the two mid-IR pulses are fed into the set-up depicted in fig 3.12. The probe pulse is reflected off a BaF_2 wedge, where the wedged surfaces split the reflected signal into two pulses, weakened to about 10 nJ. Both these pulses are then focused onto the sample using a parabolic mirror. The pump pulse is also focused onto the sample and overlapped spatially and temporally with one of the two pulses generated by the wedge. Time delay is achieved by guiding the pump pulse along a delay stage T. The pulse it overlaps with serves as probe, whereas the non-interacting pulse is used as a reference, i.e., for normalization of the probe energy and, thus, to limit the impact of fluctuations. A chopper reduces the repetition rate of the pump beam to 500 Hz to measure shot-to-shot difference spectra. Both probe and reference are focused onto the detector unit after interaction with the sample. A diffraction grating spatially disperses the beams and reflects the frequency-resolved beams onto a 2x32 pixel mercury-cadmium-telluride (MCT) detector array for a frequency resolution of $2\,\mathrm{cm}^{-1}$.

After measuring both pumped and unpumped (where the pump beam is chopped) probe beam, the change in absorbance is given by [114]

$$\Delta A(T, \nu_{pr}) = -\log\left(\frac{I^{pr}(T, \nu_{pr})}{I_0^{pr}(T, \nu_{pr})} \cdot \frac{I_0^{ref}(T, \nu_{pr})}{I^{ref}(T, \nu_{pr})}\right). \tag{3.22}$$

Here I and I_0 denote the measured intensity of the pumped and unpumped beam, respectively. The superscript pr stands for the detected probe, ref for the reference beam. The measured absorbance change is a function of delay time T and frequency ν_{pr} of the probe beam. The reference term corrects for shot-to-shot intensity fluctuations.
A measure of the experimental time resolution is given by the cross-correlation of pump and probe pulses [114]:

$$I_{XC}(T) \propto \int_{-\infty}^{\infty} I_{pump}(t) I_{probe}(t - T)\mathrm{d}t \tag{3.23}$$

This quantity is measured using two-photon absorption in indium arsenide (InAs). Overlapping pump and probe beams induces this nonlinear process that gives a strong transient absorption signal, depending on the pump-probe delay. Figure 3.13 shows such a measured cross-correlation. At pulse frequencies of $\approx 1200\,\mathrm{cm}^{-1}$ the FWHM of 183 fs indicates a pulse duration of 120 fs.

Samples were held in a specific cell during the measurements to reduce coherent artifacts around time zero. This cell consists of two 100 µm thin silicon nitride (SiN_3) membranes separated by a teflon spacer, for details see [115].

Experimental 2D-IR set-up

Figure 3.14 shows the 2D-IR experimental set-up, based on the measurement of 3-pulse photon echoes with the pulse sequence shown in fig. 3.15. The OPA generated mid-IR pulse is initially split into two equal parts. One beam passes over a delay stage to introduce what will be the waiting time T in the experiment. The beam is then focused onto a reflective grating, from which the first and negative first diffraction order are used further, while

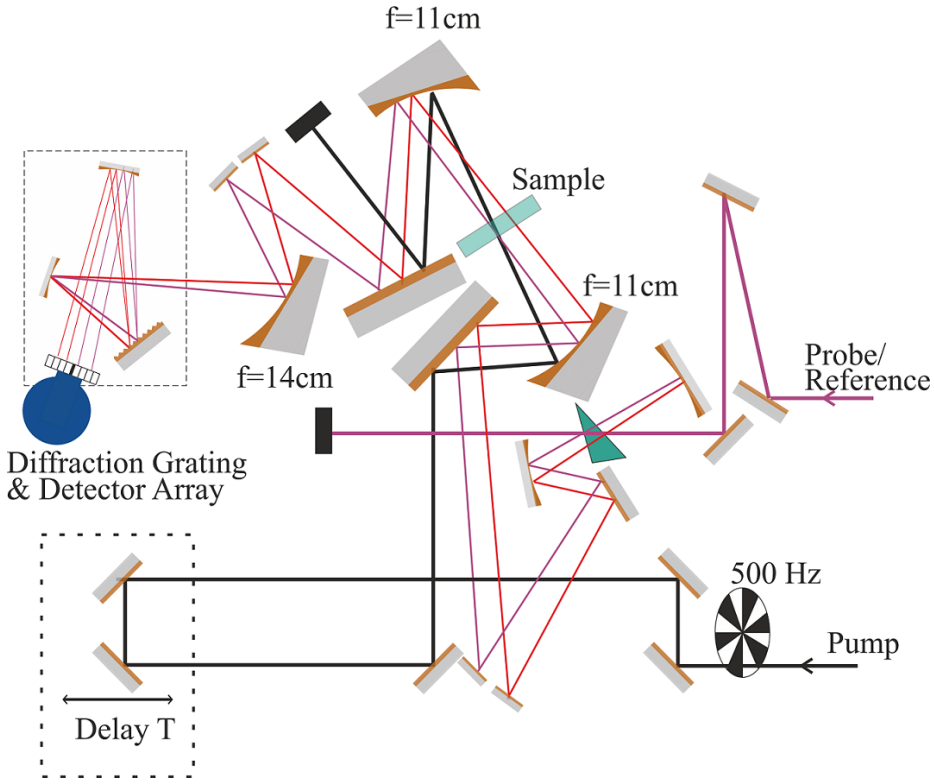

Figure 3.12: Sketch of the pulse geometry used in pump-probe measurements. The pump beam is chopped with a frequency of 500 Hz to measure shot-to-shot absorbance changes, the output of the probe OPA is split at a BaF_2 wedge. The predominant part of the beam is transmitted through the wedge and subsequently blocked. About 1% is backreflected off of one of the two edges of the wedge and used as probe and reference beam, respectively. The probe beam is overlapped spatially and temporally with the pump beam, the reference beam always interacts with an unpumped sample volume. After sample interaction both probe and reference pulses are guided into the spectrometer and onto a 2x32 MCT-detector array with $2\,\mathrm{cm}^{-1}$ resolution. Typical energies were $\approx 1\,\mu\mathrm{J}$ for pump and $\approx 10\,\mathrm{nJ}$ for probe interactions with the sample.

the zero-th order backreflection is coupled out and blocked. These two beams, which are intrinsically phase-locked, pass a set of retro-reflective mirrors and are then focused onto the sample. In the notation of our beam sequence, these beams constitute $\mathbf{k}_1$ and $\mathbf{k}_2$ (see fig. 3.15). The second half of the initial beam undergoes a similar diffractive reflection to yield the phase-locked $\mathbf{k}_3$ and $\mathbf{k}_{LO}$. An added ZnSe plate in the beampath of $\mathbf{k}_3$ delays this beam and guarantees that $\mathbf{k}_{LO}$ precedes the other three pulses by 2.6 ps. $\mathbf{k}_2$ and $\mathbf{k}_{LO}$ pass a second delay stage to introduce the coherence time τ. For $\tau > 0$ the rephasing signal is measured, for $\tau < 0$ the non-rephasing signal (cf. fig. 3.7).

All four pulses are focused onto the sample by a parabolic mirror in a box-CARS geometry, depicted in fig. 3.15. The pulses form a square so that the signal is intrinsically emitted in the direction of the local oscillator. Signal and LO are then dispersed by a reflective monochromator grating and focused onto a 64-pixel MCT detector array with a spectral resolution of $2\,\mathrm{cm}^{-1}$. Interference patterns of LO and signal are measured for a number of

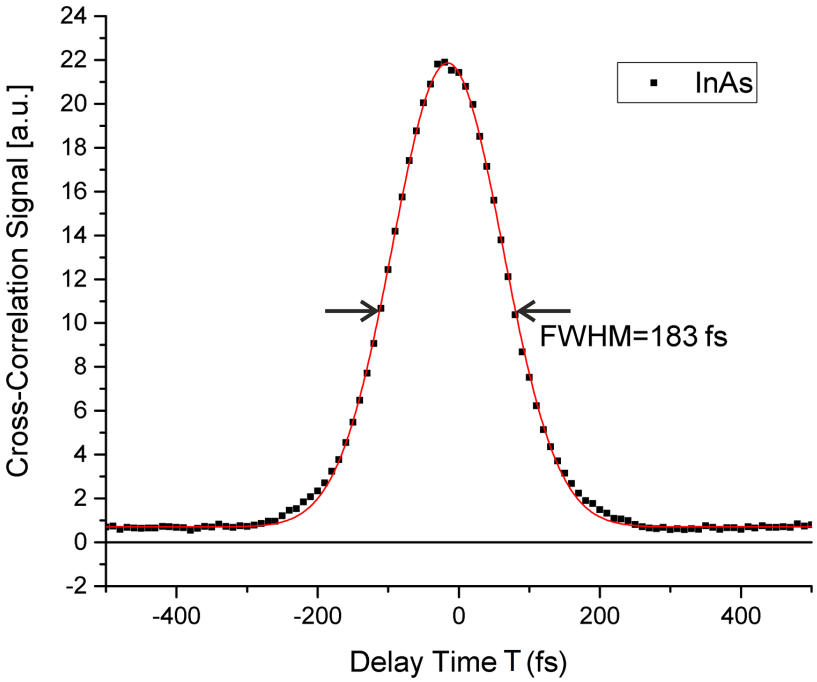

Figure 3.13: Cross-correlation measurements give the time resolution of the pump-probe experiment. Here, two-photon absorption from indium arsenide (InAs) was measured as a function of delay time between pump and probe pulse. The pulses were centered about 1200 cm^{-1}. The data were fitted with a Gaussian curve, the FWHM was 183 fs, the pulse duration after deconvolution 120 fs.

coherence times τ. The waiting time T is fixed for the duration of one τ-scan but can be varied throughout the measurement to take the time evolution of the population state into account.

The measured interference pattern consists of both LO and signal contributions:

$$I_{det}(\omega) = |E_{LO}(\omega) + E_{sig}(\omega)|^2 = |E_{LO}|^2 + 2\Re(E^*_{LO}(\omega)E_{sig}(\omega)) + |E_{sig}(\omega)|^2$$

The emitted signal field is small compared to the local oscillator, so the equation can be simplified to

$$|E_{LO}|^2 + 2|E_{LO}(\omega)||E_{sig}(\omega)| \cdot \cos(\Phi_{sig} - \Phi_{LO})$$

The contribution $|E_{LO}|^2$ needs to be removed to obtain the signal electric field. To this purpose $\mathbf{k}_3$ is chopped at a frequency of 500 Hz. Only every other pulse sequence then generates a signal electric field, allowing differential processing in the measurement program to eliminate the LO term. A second chopper chops $\mathbf{k}_2$ at 250 Hz to additionally reduce scattering from sample windows.

Tracing the phase $(\Phi_{sig} - \Phi_{LO})$ is a non-trivial problem. Φ_{sig} is a result of the three pulses $\mathbf{k}_1$, $\mathbf{k}_2$, and $\mathbf{k}_3$. The phase term can therefore be expressed as

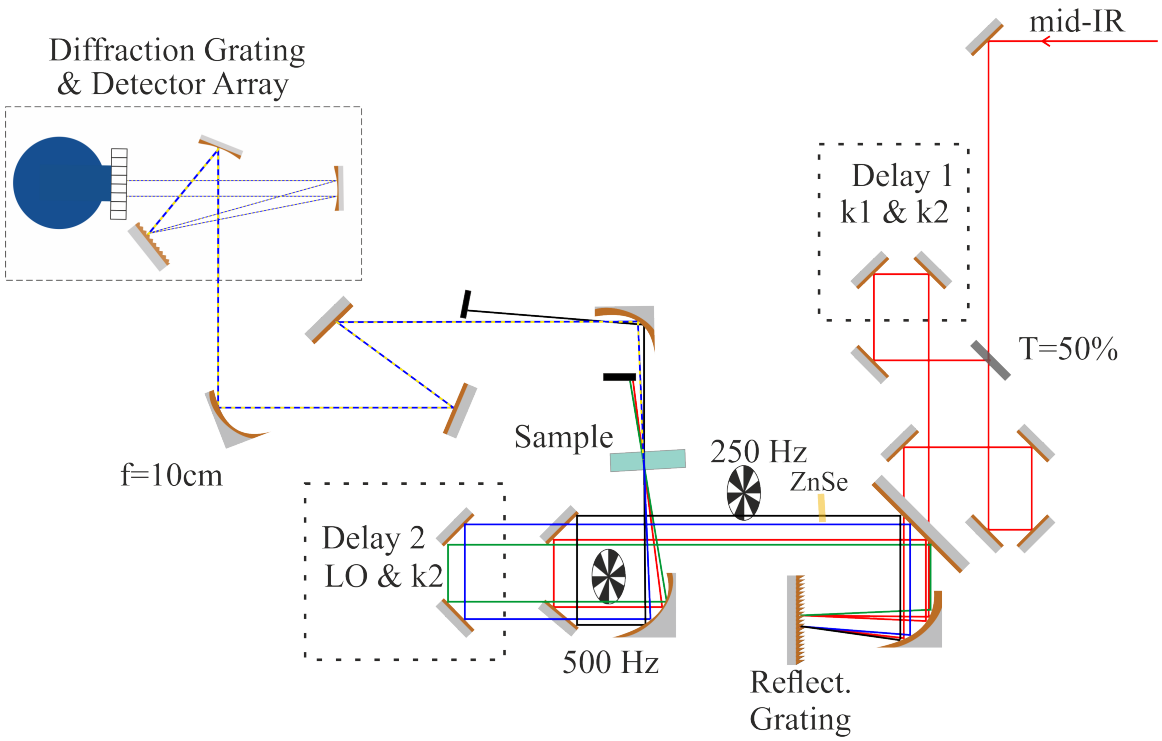

Figure 3.14: Set-up for 3-pulse photon echo measurements. The incoming beam is split into four pulses by a beamsplitter and a reflective grating. Three of these beams are required for signal generation ($\mathbf{k}_1$ to $\mathbf{k}_3$), the fourth pulse, the local oscillator (LO) is used in heterodyne detection of the signal. The pulses overlap spatially on the sample in a box-CARS geometry (see fig. 3.15). The created echo signal (yellow) propagates in the direction of the local oscillator (blue), both beams are detected simultaneously using a 64-pixel MCT detector array. Two delay stages are used to control relative time differences between the pulses (see fig. 3.15). Two choppers rotating at 250 and 500 Hz chop $\mathbf{k}_3$ and $\mathbf{k}_2$, respectively, to allow proper signal calculation in the computer.

$$\begin{aligned}\Phi_{sig} - \Phi_{LO} &= (-\Phi_1 + \Phi_2) + (\Phi_3 - \Phi_{LO}) + \phi_{sample} \\ &= (-\Phi_1 + \Phi_3) + (\Phi_2 - \Phi_{LO}) + \phi_{sample}\end{aligned}$$

Our set-up uses a diffractive grating to create inherently phase-locked pulse pairs and thus single out the phase ϕ_{sample} of the nonlinear response function. As a downside to this technique the local oscillator is also affected by moving the delay stage. This affects its phase and effectively cancels out the τ-dependency in the measured signal response. Additional phase factors need to be factored in to obtain correct 2D spectra. In our case they are determined by fitting the projection of the measured 2D data on ν_3 to a measured pump-probe spectrum. The PP spectrum is measured using the same beam geometry to ensure comparable conditions. $\mathbf{k}_2$ is used as a pump pulse, $\mathbf{k}_3$ as the probe. $\mathbf{k}_3$ and $\mathbf{k}_{LO}$ are blocked throughout the course of the PP measurement.

Pulse duration and frequency bandwidth of the pulses used in the experiment can be extracted from frequency-resolved optical gating (FROG) experiments. Here, transient grating

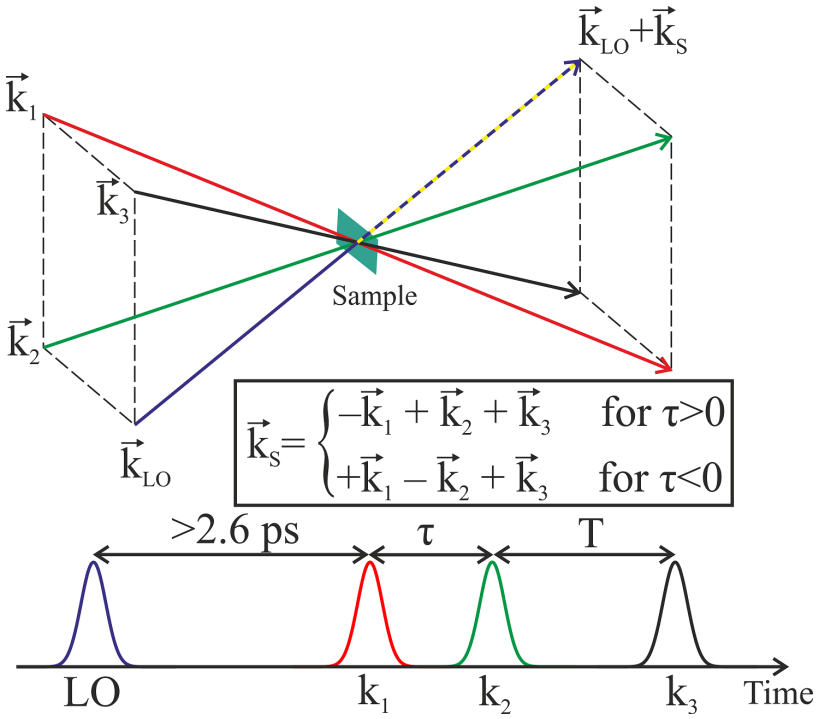

Figure 3.15: The four pulses interact with the sample in a box-CARS geometry (top). They form the corners of a square before being focused onto the sample. In this geometry, the signal is always emitted in the direction of the fourth pulse, the local oscillator, allowing for a background free detection. bottom: Time ordering of the four pulses. The time difference τ between $\mathbf{k}_1$ and $\mathbf{k}_2$ defines the coherence time, the time difference T between $\mathbf{k}_2$ and $\mathbf{k}_3$ denotes the waiting time of the system. For coherence times $\tau > 0$, the emitted signal is the rephasing signal, for $\tau < 0$ non-rephasing.

(TG)-FROG on ZnSe captured the convolution of $\mathbf{k}_1$, $\mathbf{k}_2$, and $\mathbf{k}_3$, the corresponding FROG trace is shown in fig. 3.16. The full amplitude and phase information can be extracted by complex algorithms, however a simple deconvolution helps to find the pulse duration. Assuming that all three pulses are identical and Gaussian, the pulse duration is given by $\tau_{pulse} = \frac{\Delta t}{\sqrt{3/2}}$ with Δt the FWHM of the time-dependent trace shown in fig. 3.16(b). The spectral bandwidth is 242 cm^{-1}.

3.4 Theoretical methods

The experimental results in this thesis were analyzed by theoretical simulations provided by Benjamin Fingerhut. This section does not aim to provide an in-depth explanation of these methods, but rather outline the basic principles and list the relevant parameters. The reader is referred to the original publications for further detail.

Molecular Dynamics simulations

The general principle of MD simulations was introduced in section 2.1.4. Briefly, classical MD simulates complex molecular systems at an atomistic level by calculating the potential

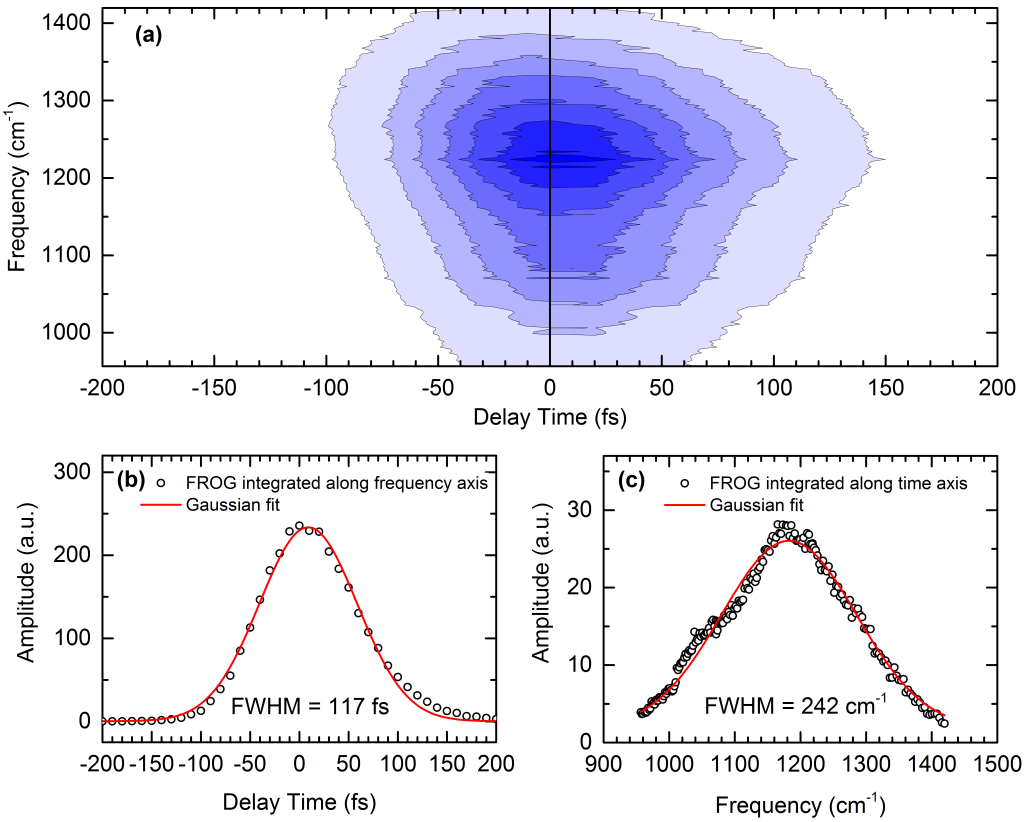

Figure 3.16: TG-FROG trace measured in the 2D-IR set-up for pulses in the region of $\nu_{AS}(PO_2^-)$. Horizontal and vertical cuts allow to deduce pulse duration and spectral bandwidth. From [115]

at every coordinate using analytical functions, so called force fields. This allows to track step-wise the dynamics of the system. For the systems at hand, AMBER software was used with the *ff99bsc0* force field that is commonly used for DNA [64,66]. For RNA systems the RNA specific χ_{LO3} extension was additionally employed. dsRNA was constructed using the AMBER nucleic acid builder and surrounded by a 10 Å H_2O buffer region (40 Å in the big simulation box) to ensure proper hydration. The $tRNA^{phe}$ structure was taken from x-ray diffraction data (protein data bank: 1ehz, [4]) and placed in an truncated octahedral solvation cell of H_2O with a total of 9 Mg^{2+} and Mn^{2+} ions placed in accordance with [4]. Na^+ ions were added for charge neutrality, water molecules were simulated using the TIP4P-fb model. Simulation runtimes after equilibration are given in table 3.1. The derived potential of mean forces (PMF) represents the free energy of the respective system.

Snapshots showing the different hydration patterns of dsRNA were taken after 160 ns. The distribution of hydrogen bonds (HB) was evaluated during six different time intervals along the 1.2 µs MD trajectory. Critical for the HB identification were the geometric criteria, i.e. an oxygen-oxygen distance $D < 3$Å and an angle $\measuredangle$ O-H...O>140°. For MD simulations of dsRNA and Mg^{2+} sample cells of two different volumes were used to explore size effects. Various amounts of Mg^{2+} were added to the dsRNA simulation cell. Results shown in this thesis were simulated using the Mg^{2+}/RNA ratio R=20 ($\approx$ 77 mM c(Mg^{2+}) in small simu-

lation box, ≈ 13 mM in big simulation box). The ion density around dsRNA was averaged over 2500 snapshots equally distributed along the whole simulation time, the ion atmosphere was obtained using volumetric integration.

The ion density around $tRNA^{phe}$ was averaged over 2500 snapshots equally distributed along the whole simulation time. Electric field and electrostatic potential around $tRNA^{phe}$ were averaged over 1600 and 3200 snapshots, respectively, taken at the last few ns of the simulation. The electric field itself is calculated at the midpoint of the O1-P-O2 bisector by projecting the total electric field onto the bisector axis.

System	Simulation time
DMP	4.7 µs (1.59 µs for each cation)
dsRNA melting	1.2 µs
dsRNA+Mg^{2+}	0.6 µs
$tRNA^{phe}$	1 µs

Table 3.1: Runtime of MD simulations for the different phosphate systems. The 4.7 µs of DMP are comprised of three independent runs, 1.59 µs each, for the three counterions Na^+, Ca^{2+}, and Mg^{2+}.

Density functional theory

Density functional theory (DFT) calculations solve the Schrödinger equation of molecular systems for only the electron density, thus highly reducing the degrees of freedom. Starting geometries are optimized iteratively to achieve equilibrium, from which molecular orbitals are computed. DFT calculations were employed in this thesis to calculate vibrational frequencies of $\nu_{AS}(PO_2^-)$ in DMP molecules as a function of DMP...cation distance. Simulated clusters contain a single DMP anion in *gg*-conformation, a single positive cation (Na^+, Ca^{2+}, or Mg^{2+}) and N water molecules. Harmonic normal mode analyses to calculate the geometry dependent frequency of the $\nu_{AS}(PO_2^-)$ vibrational mode were performed for $N = 19$. Absolutely localized molecular orbital energy decomposition analysis (ALMO-EDA) uses the calculated molecular orbitals of the same $N = 19$ clusters to sort intermolecular interaction energies into polarization contributions, charge transfer and a combined term for electrostatic and exchange repulsion interactions. To determine the molecular bonding potential, DFT cluster geometries were displaced along positive and negative directions of the $\nu_{AS}(PO_2^-)$ normal mode vector. ALMO-EDA was then performed without any further equlibration time, the molecular bonding potential was obtained via self-consistent field simulation (SCF). Minimum hydration DFT calculations were performed with $N = 11$ for DMP/Mg^{2+} and DMP/Na^+ ion pairs, and $N = 13$ for DMP/Ca^{2+} complexes. For details see the supplementary information in [116] and [117].

QM/MM calculations

QM/MM (quantum mechanics/molecular mechanics) calculations allow characterization of complex molecular systems by considering only the most relevant part under a quantum mechanical model (QM region). All other parts of the system are treated classically (MM region). QM/MM calculations were used in this thesis to calculate and assign vibrational

frequencies to phosphate groups of RNA molecules. QM/MM calculations were performed using the NWChem program package v6.3 [118]. The QM region used in calculating the vibrational frequencies consists of two neighbouring phosphate groups and the three binding ribose moieties together with first hydration shells of both phosphates and ions (Both Mg/Mn^{2+} and Na^{+}). The boundary region between QM and MM is bridged by hydrogen link atoms. The two terminating nucleotides at each end of the double helix were excluded from the calculations.

4

Sample Preparation and Characterization

This thesis examines a variety of phosphate systems in aqueous solution. This chapter gives a description of how samples were prepared and characterized prior to measurements. Figure 4.1 provides an overview of IR phosphate absorbance in the range of the asymmetric PO_2^- vibration for all samples used in this thesis. While $\nu_{AS}(PO_2^-)$ for DMP is centered around $1200\,cm^{-1}$, the RNA vibrational spectrum in this frequency region is more diverse. The two-peak structure around 1220 and $1240\,cm^{-1}$ has been attributed to the phosphate stretching vibration itself. Vibrational modes at higher frequencies have been attributed to NH vibrations of the bases, for example uracil at $1280\,cm^{-1}$ [119] or adenine at 1290, 1310, and $1330\,cm^{-1}$ [120, 121]. Theoretical simulations also predict some contribution to the absorbance spectrum at $\tilde{\nu} > 1260\,cm^{-1}$ to originate from $\nu_{AS}(PO_2^-)$ where the phosphate group is forming contact ion pairs with the naturally present Na^+/K^+-counterions [14].

4.1 DMP

The properties of the dimethyl phosphate anion have been dicussed in section 2.2. For the experiments in this thesis, the DMP sodium salt Na^+DMP^- (suppliers: ALFA Chemistry; TRC) was dissolved in ultrapure water (Roth) with a concentration of 0.2 M. To this solution, salts of alkali and alkaline earth metals were added. Concentrations of sodium chloride (NaCl, Fluka), potassium chloride (KCl, Roth), calcium chloride ($CaCl_2$ anhydrous, VWR), and magnesium chloride ($MgCl_2$ anhydrous, Alfa Aesar) ranged from 0.5 to 2 M.
Reference solutions with the same salt concentrations but without Na^+DMP^- were also prepared. This allows to subtract the librational background absorption of the solvent from all recorded FTIR spectra.

4.2 RNA

Specifically tailored single-stranded (ss) and double-stranded RNA (dsRNA) was provided as lyophilized sample (IDT DNA). All samples were 23 nucleotides in length. Two particular sequences were used: dsAU-RNA (AAUAUAUAUAUAUAUAUAUAUAA+ complementary strand) and ssA-RNA $(A)_{23}$. The lyophilized RNAs were dissolved in ultrapure water. Counterion concentrations in the initial sample were measured by inductively coupled plasma optical emission spectrometry (ICP-OES) and amounted to 51 Na^+-ions and 5 K^+-ions per RNA molecule. The ICP-OES experiments were kindly performed by the Leibniz Institute of Freshwater Ecology and Inland Fisheries (IGB).

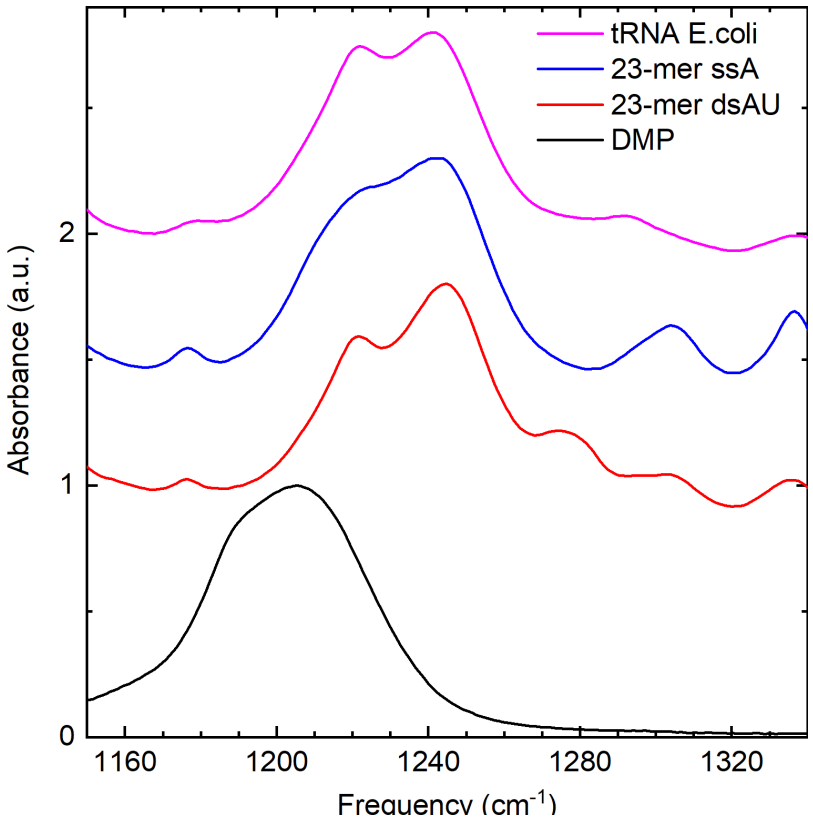

Figure 4.1: FTIR spectra of several phosphate systems in the region of the asymmetric phosphate stretch vibration $\nu_{AS}(PO_2^-)$. Spectra are normalized to the absorbance maximum.

Two kinds of tRNA samples have been used: tRNA from E.coli MRE600 (manufacturer Roche, supplier Sigma-Aldrich) which is a mix of all different amino acid encoding tRNAs in *Eschericia coli*, and $tRNA^{phe}$ from yeast (Sigma-Aldrich), which encodes the amino acid phenylalanine (anticodon sequence: G_mAA, see chap. 1). The tRNA samples were provided with initial Mg^{2+} counterions as part of the commercial extraction and purification process. ICP-OES measurements of *E.coli* tRNA samples showed 62 Na^+, 0.2 K^+, 2.1 Ca^{2+}, and 5.7 Mg^{2+} ions per tRNA molecule. Dialysis procedures detailed below allow to substitute Mg^{2+} with Na^+, ICP-OES of dialyzed tRNA samples showed 77 Na^+ per tRNA, together with 0.5 K^+, 0.6 Ca^{2+} and < 0.1 Mg^{2+}, confirming a negligible Mg^{2+} content after dialysis. For the experiments, tRNA was dissolved in ultrapure water, dialyzed and then measured. pH values of both kind of RNA samples were repeatedly monitored to be between 6.7 and 7.3.

4.2.1 Concentration determination

Linear UV absorption spectroscopy can be used to measure the concentration of an RNA sample in solution, as described in section 3.1. From the Lambert-Beer equation (eq. 3.1), absorbance is the product of sample thickness l, concentration c and the molar absorption coefficient at 260 nm ε_{260}. The concentration can be easily calculated when l and ε_{260} are known. However, ε_{260} depends on RNA composition and differs between different RNA samples.

It is well established that 1 OD UV absorption of single-stranded RNA in a 1 cm sample cell corresponds to a concentration of 40 µg/ml [122]. The molar absorption coefficient can then be calculated using the molecular weight of the specific sample. For the short ssA-RNA oligomer this corresponds to $188000\,\mathrm{M^{-1}cm^{-1}}$. For transfer RNA the average molecular weight is 25000 g/mol, so the ε_{260} is $625000\,\mathrm{M^{-1}cm^{-1}}$. There is no such established literature value for double-stranded RNA. It can be calculated according to $\varepsilon_{260} = (n_A\varepsilon_A + n_U\varepsilon_U)/H$ [123]. Here, $n_A = n_U = 23$ is the number of adenine/uracil bases in our oligomer, $\varepsilon_A = 15400\,\mathrm{M^{-1}cm^{-1}}$ and $\varepsilon_A = 9900\,\mathrm{M^{-1}cm^{-1}}$ are the absorption coefficients of the mononucleotides [124], and $H = 1.4$ the hypochromism factor [125]. This factor accounts for the reduced absorbance due to base stacking and base pairing interactions that are particularly pronounced in duplexed helices. The molar absorption coefficients together with the molecular weight of the samples are summarized in table 4.1, the RNA concentrations used for the different experiments are given in table 4.2.

sample	molecular weight	absorption coefficient ε_{260}	avg. ext. coeff. ε_{260} per nucleotide
	g/mol	$10^3\,\mathrm{M^{-1}cm^{-1}}$	$\mathrm{M^{-1}cm^{-1}}$
23-mer dsAU-RNA	14490	415	9000
23-mer ssA-RNA	7510	188	8200
tRNAs	≈ 25000	625	8000

Table 4.1: Sample data used to calculate RNA concentrations from UV absorption measurements. The molar absorption coefficient depends on the exact RNA sequence and neighbouring base-base interaction. For comparison with literature the average absorption coefficient per nucleotide is given.

sample	Experiment		
	FTIR/2D	UV/CD	Fluo
		mM	
23-mer dsAU-RNA	4.6/2.3-6.9	0.9	0.26-1.1
23-mer ssA-RNA	8.8/4.4	1.1	-
tRNAs	4	0.3-0.9	1

Table 4.2: RNA concentrations used in the various experiments as measured with UV absorption spectroscopy at 260 nm.

4.2.2 RNA melting

The absorption coefficient strongly depends on the macromolecular structure of RNA, which changes upon heating. We performed RNA melting experiments with ssA-RNA and dsRNA to track these changes as a function of sample temperature T_S. dsRNA samples were held in a temperature controlled liquid cell (Harrick) in between two 1 mm thick BaF_2-windows separated by a 12 µm Teflon spacer. Heat was applied using a metal block cylindrically surrounding the sample. Temperature changes were applied at a steady rate of 2 K/min,

the temperature accuracy was within 1 K. The sample was left to equilibrate at the target temperature for 6-8 minutes before starting a measurement.

dsRNA forms an A-type double helix in water. This type of double helix is characterized by a more compact structure compared to the predominant B-type geometry of DNA (cf. chapter 1), that is reflected in the electronic structure of the nucleic acid. Since the 260 nm-$\pi - \pi^*$ transition is influenced by both inter- and intrastrand interactions, UV spectroscopy provides a useful probe of RNA structure. Most interesting for this work is the information UV spectra can provide on the thermally induced denaturation state of RNA.

Figure 4.2 shows UV and CD absorption spectra of dsRNA together with spectra of a single-stranded RNA sample consisting purely of adenine bases. The dsAU spectrum at room temperature consists of a peak centered at 258 nm. Upon heating, UV spectra of dsRNA show a jump in absorbance. This so called hyperchromic effect is generally associated with a change in helical structure [8, 126]. It is a sign of partial or full separation of the strands, together with a destacking of the bases. The change in dipole-dipole interactions between the nucleobases' π-orbitals leads to the observed increase in absorbance [41].

The change is most clearly visible when plotting the relative increase in absorbance both for dsRNA and ssRNA (inset). Absorbance of ssA-RNA increases monotonically, whereas dsRNA shows a sigmoidal increase at temperatures between 313 and 333 K. The increase in absorbance for the case of ssRNA is dominated by a gradual transition from a single-helical structure at room-temperature to a random coil. This also occurs in the case of dsRNA, indicated by the continuing increase of absorbance at high temperatures, but is overshadowed by the jump from melting. A melting temperature can be extrapolated from the midpoint of the sigmoidal curve to be $\approx$328 K.

Circular dichroism spectra allow a closer look into the structural change upon RNA heating (figure 4.2c,d). CD spectroscopy works by measuring the difference in absorbance between left-handed and right-handed circularly polarized light. The resulting spectra carry information on the helical structure of the molecule in question (see section 3.1).
At room temperature, CD spectra of dsRNA show a distinct maximum at 258 nm together with a side peak at 230 nm. This is a characteristic spectrum of an A-type helix [127]. CD spectra for single-stranded RNA on the other hand show a maximum in ellipticity at 265 nm and a minimum at 248 nm. This spectral shape has been observed for dinucleotides [128], as well as B-type DNA helices [127]. Heating of the ssRNA sample results in a loss of ellipticity, where the shape of the spectrum is preserved. On the other hand, heating dsRNA leads to a distinctive transformation. At 348 K the CD spectrum of dsRNA shows similarities to the one of ssRNA with a maximum at 270 nm and a minimum at 245 nm.
The gradual decrease in the case of ssRNA indicates a gradual loss in helicity, agreeing with a transition to a random coil. The helicity in such a randomly oriented molecule would be zero. The stark change in spectral shape in the case of dsRNA in contrast represents a substantial reshaping of RNA structure. The shift of the ellipticity maximum with temperature is traced in the inset. A sigmoidal shift with a transition temperature around 328 K can again be observed.

All in all these are reliable indicators that dsRNA undergoes a structural transition upon heating. The influence of this structural transition on RNA hydration, reflected by $\nu_{AS}(PO_2^-)$,

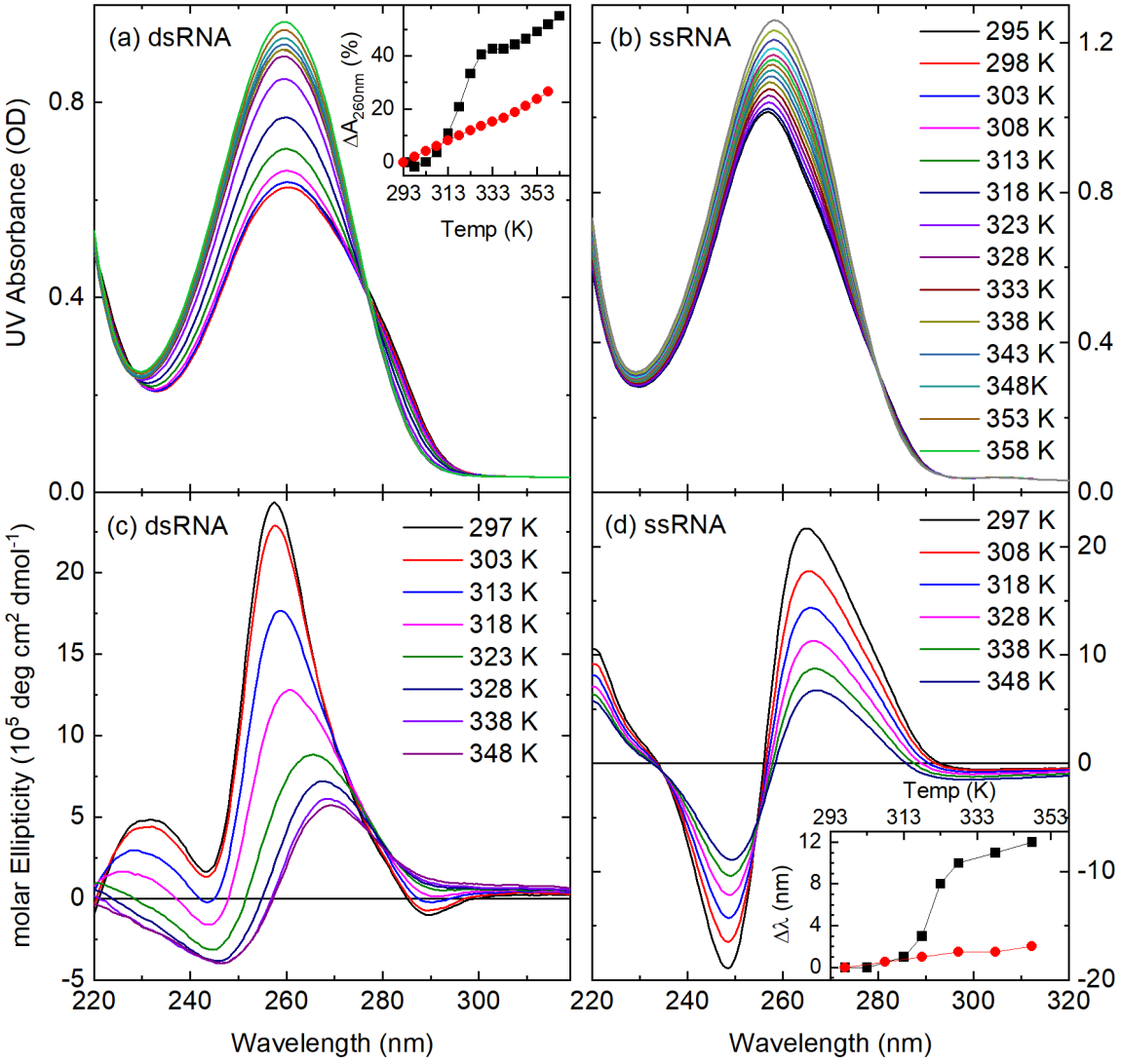

Figure 4.2: Characterization results of spectroscopic measurements in the UV. (a,b) UV absorption spectra of dsAU-RNA and ssA-RNA, respectively, for temperatures ranging from 297 K to 353 K. Inset: Relative absorption change as a function of temperature for dsAU-RNA (black) and ssA-RNA (red). A step-like behaviour is only observed in the case of dsAU-RNA. (c,d) Circular Dichroism spectra for dsAU- and ssA-RNA, respectively, for temperatures ranging from 297 K to 348 K. dsAU-RNA spectra exhibit a distinct change in spectral shape with increasing temperature. Where the spectra at room temperature is characteristic for an A helix, higher temperature spectra more closely resemble CD spectra of B helix DNA. Spectra of ssA-RNA show no change in spectral shape, but only a decrease in amplitude. Inset: relative change in wavelength for the maximum of the CD spectra. Again, a step-like behaviour is exclusive to dsAU-RNA. The transition temperature of the structural transition is at ≈320 K.

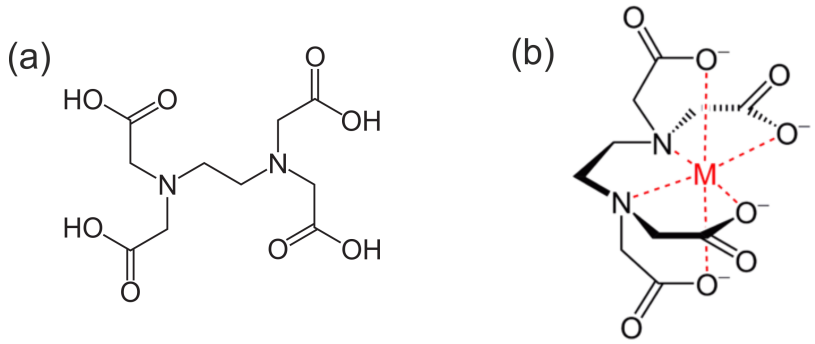

Figure 4.3: (a)Chemical structure of EDTA (b) Chemical structure of the EDTA/Mg^{2+} chelate. Binding of Mg^{2+} is linked to a four-fold deprotonation of the EDTA molecule.

will be investigated in chapter 6.

4.2.3 Dialysis

The tRNA samples were provided with initial Mg^{2+} counterions as part of the commercial extraction and purification process. ICP-OES measurements of *E.coli* tRNA samples showed 62 Na^+, 0.2 K^+, 2.1 Ca^{2+}, and 5.7 Mg^{2+} ions per tRNA molecule. This initial presence of Mg^{2+} ions is problematic for our experiments where we aim to follow the impact of Mg^{2+} on a pure, ideally Mg^{2+}-free RNA sample. It is therefore necessary to remove as much of the initial Mg as possible. The best method for the low sample volumes we are handling is desalting through dialysis. We used a combination of the methods described in literature [53, 129] employing ethylene diamine tetraacetic acid (EDTA) as Mg-binding agent. The chemical structure of EDTA is shown in figure 4.3. It forms a six-finger chelate when binding Mg^{2+}, linked to a four-fold deprotonation of the EDTA molecule. This constitutes a particularly strong binding process ($K_{EDTA/Mg^{2+}} \approx 10^{8.6}$ [130], compared to $K_{RNA/Mg^{2+}} \approx 10^4$ as given in ref. [53] for RNA binding to Mg^{2+}).

To replace the initial Mg^{2+} ions with monovalent Na^+ ions the tRNA was repeatedly dialysed in buffers containing EDTA and NaCl. tRNA was placed in µl dialysis membranes (SERVA ReadyLyzer) with a molecular weight cut-off of 12-14 kDa (mol. weight of tRNA ≈25 kDa). Dialysis was performed twice in 0.1 M NaCl (Fluka), 50 mM EDTA (SERVA, dissolved in H_2O, adjusted to pH 8 by adding NaOH), then once in 0.02 M NaCl, 10 mM EDTA, once in 0.02 M NaCl, 1mM EDTA and finally in ultrapure water (Roth). Each stage of dialysis was performed for at least two hours. Dialysis buffer was present in an excess of >500. Dialysis buffer will seep into the dialysis membrane because of osmosis, lowering the tRNA concentration of the dialyzed sample by a factor of 4. To increase the tRNA concentration after dialysis back to concentrations suitable for measuring IR spectra, some excess water was evaporated by keeping the sample at 80°C (353 K) for about 3 hours. All dialyzed samples have final pH values between 6.7 and 7.3 and contain Na^+ counterions. Using a Na^+-selective electrode (SI Analytics) ≈ 37 Na^+-ions were measured before dialysis, 46 Na^+ after dialysis. The electrode is sensitive to free ions only, so the difference to charge neutrality (78 PO_2^- groups) is likely due to Na^+ ions strongly associated with the RNA. These results were supported by ICP-OES measurements after dialysis. Per tRNA molecule 77 Na^+ ions were detected, together with 0.5 K^+ ions, 0.6 Ca^{2+} ions and < 0.1 Mg^{2+} ions,

confirming a negligible Mg^{2+} concentration after dialysis.

5
DMP as a model system

Ions in the solvation shell of nucleic acids play a central role in stabilizing macromolecular arrangements. Particularly along the negatively charged phosphate-sugar backbone, where electrostatic repulsion impedes the folding of structural elements, positively charged alkali and alkaline earth ions have been located. Structures range from ions in direct contact with the phosphate group of the backbone - here one phosphate oxygen replaces a water from the regular ion hydration shell - to ions being part of a more diffuse ion atmosphere. Ions that are separated from the phosphate group by one to three water layers form a transition region between these two cases.

Direct contact ions have so far only been reported in x-ray crystallographic experiments, it was not feasible up until now to detect these geometries in solution, as reported in chapter 2. The extent to which each ion geometry contributes to the overall stability was unclear. Poisson-Boltzmann simulations claim that long-range electrostatic contributions from the ion atmosphere collectively stabilize nucleic acid geometries [33]. Vibrational modes of the phosphate backbone reflect changes in nucleic acid hydration as a response to strong electric fields from water molecules in the first few hydration layers [36, 43]. The sensitivity to the local environment offers an opportunity to use phosphate modes, particularly the asymmetric phosphate stretch vibration $\nu_{AS}(PO_2^-)$, to investigate directly bound ions around RNA molecules.

To gain first insight into the interplay of molecular forces, we performed measurements on the dimethyl phosphate anion DMP^- in solution. Consisting of a phosphate linking two methyl groups (see fig. 5.1), DMP^- is the simplest analog both of the phosphodiester network (C-O–P–O-C) and the anionic phosphodioxy group (O=P–O^-) central to the nucleic acid backbone. The latter is known to be the major hydration site, so it will be of the most interest in our study.

5.1 Ion-dependent Steady State Infrared Absorption Spectrum

Steady-state IR absorption spectra of DMP^- in the range of $\nu_{AS}(PO_2^-)$ show the influence of various alkali and alkaline earth metals on the vibrational frequency. For the measurements, 0.2 M of DMP^- and its counterion Na^+ were dissolved in water. The corresponding FTIR absorption spectrum is shown in figure 5.2 (a-d) as a solid black line. The spectrum exhibits an absorbance maximum at $1206\,cm^{-1}$ with a shoulder at about $1190\,cm^{-1}$. These features reflect the predominant *gg* ($1206\,cm^{-1}$) and *gt* ($1190\,cm^{-1}$) conformations of DMP in solution, as explained in sec. 2.2.

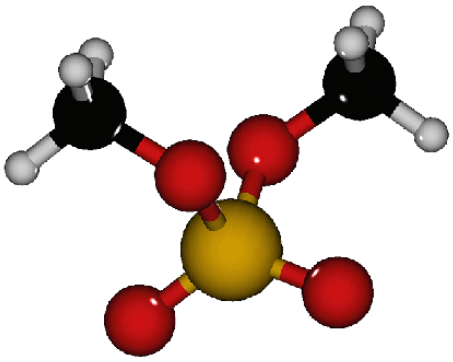

Figure 5.1: Chemical structure of a DMP^--ion in *gg* conformation. Colors are as follows: gold - phosphorous; red - oxygen; black - carbon; white - hydrogen.

Various amounts of alkali or alkaline earth metal chlorides were solvated together with DMP. They fully dissociate in metal cations and Cl^- anions in the water environment at the concentrations present. FTIR absorption spectra in the region of the asymmetric phosphate stretch vibration $\nu_{AS}(PO_2^-)$ are shown in figure 5.2(a-d). Absorption spectra of reference solutions containing only the respective salt concentrations, but no DMP, are subtracted to remove the water librational background. All spectra show a broad absorption peak, as just discussed.

With addition of ions, the peak absorption decreases for most spectra. In the case of the divalent ions calcium (Ca^{2+}) and magnesium (Mg^{2+}) an additional shoulder appears at 1242 and 1250 cm^{-1}, respectively. These changes can be followed more closely in difference absorption spectra $\Delta A = A - A_0$, figure 5.2 (e-h) (A_0: absorbance of DMP^- in neat water). In the case of the monovalent sodium (Na^+) the absorbance decrease is centered at 1195 cm^{-1}, spectra with potassium (K^+) show an absorption decrease at 1190 cm^{-1} together with an increase at 1220 cm^{-1}. For the divalent ions Ca^{2+} and Mg^{2+} the absorption decrease is strongest at 1200 and 1210 cm^{-1}, respectively. An absorption increase can be detected at 1240cm^{-1} for Ca^{2+} and 1250 cm^{-1} for Mg^{2+}.

It is possible to distinguish contributions from DMP/cation interactions using a weighted differences methods. The method works by assuming two different contributions to the total absorbance spectrum:

$$A_{total}(\nu) = \frac{c_1}{c_0} A_{DMP}(\nu) + A_{complex}(\nu) \tag{5.1}$$

Here, A_{DMP} gives the absorption of DMP without any addition of ions, and $A_{complex}$ the contribution from DMP^-/cation complexes. c_0 is the total concentration of DMP in the sample, c_1 the unknown concentration of DMP not affected by ions. The ratio c_1/c_0 thus gives the proportion of DMP not bound in ion complexes. The difference spectrum ΔA can then be expressed as:

$$\begin{aligned} \Delta A(\nu) &= \frac{c_1}{c_0} A_{DMP}(\nu) + A_{complex}(\nu) - A_{DMP}(\nu) \\ A_{complex}(\nu) &= \Delta A(\nu) - \left[-\frac{c_0 - c_1}{c_0} A_{DMP}(\nu) \right] \geq 0 \end{aligned} \tag{5.2}$$

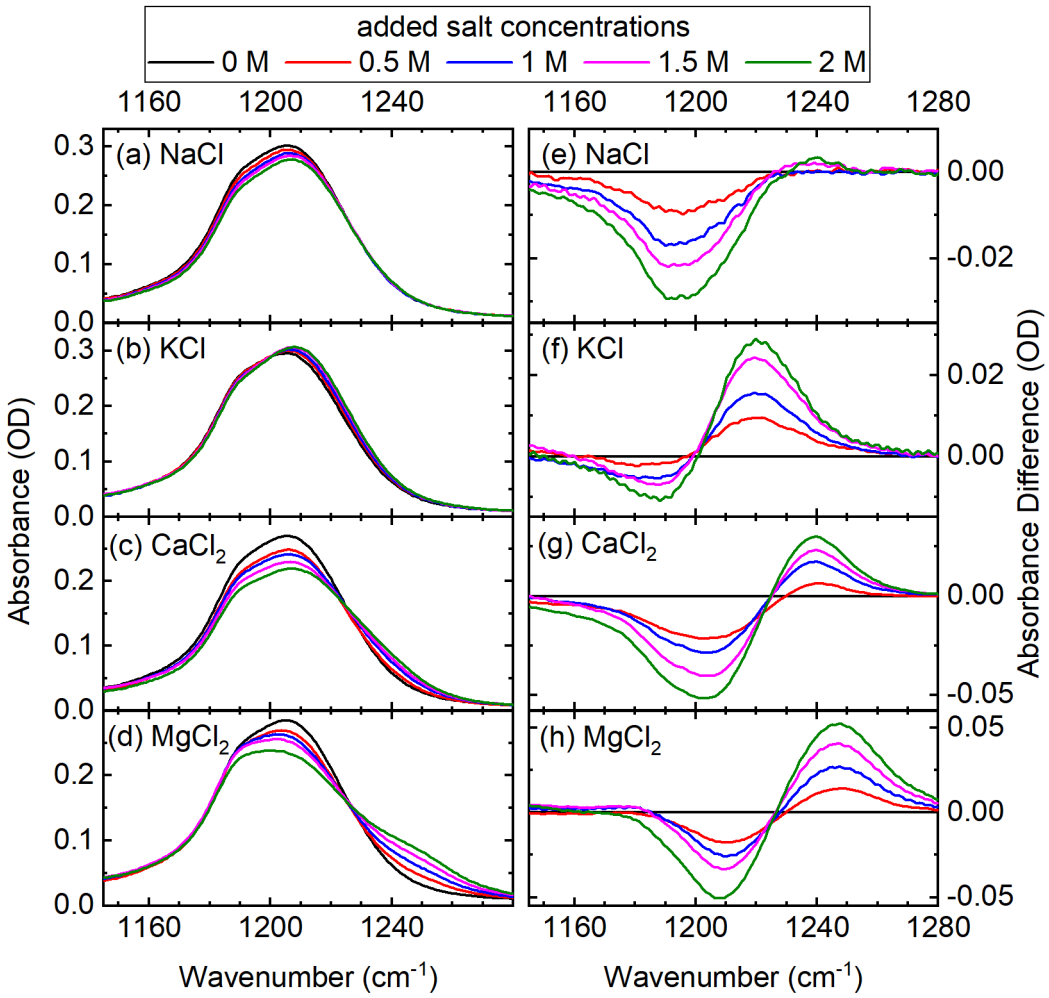

Figure 5.2: FTIR spectra in the region of the asymmetric phosphate stretch vibration $\nu_{AS}(PO_2^-)$ of DMP. (a-d) Absorption spectra of 0.2 M DMP^-Na^+ salt with added amounts of alkali or alkaline earth salts varying from 0.5 to 2 M. Absorption from a reference sample containing the respective ion concentration, but no DMP, was subtracted for all spectra to remove the librational water background. (e-h) Difference spectra for varying concentrations of metal ions, computed by subtracting the linear spectrum of pure DMP in water (black lines) from the respective spectra in (a-d).

By adjusting the unknown weighting factor $c_0 - c_1 = c_{complex}$ to the spectra at hand, with the boundary condition that $A_{complex}(\nu)$ as a physical quantity can not be negative, conclusions on the concentration of DMP/ion complexes can be drawn. The complexes that contribute to such absorption spectra include both contact ion pairs (CIP) and solvent-separated ion pairs (SSIP), as will be discussed in more detail below.

Figure 5.3 shows the decomposition into spectral components under two different assumptions. A lower limit (solid red lines) for the concentration of DMP-ion pairs $c_{complex,min}$ is set by allowing a minimum $A_{complex}(\nu) = 0$ at one frequency. In the case of Na^+ and K^+ the condition is met for $c_{complex,min} = 24\,\text{mM}$ and 12 mM, respectively (12%/6% of all DMP molecules, $A_{complex}(\nu = 1180\,\text{cm}^{-1}) = 0$). The corresponding linear absorption components

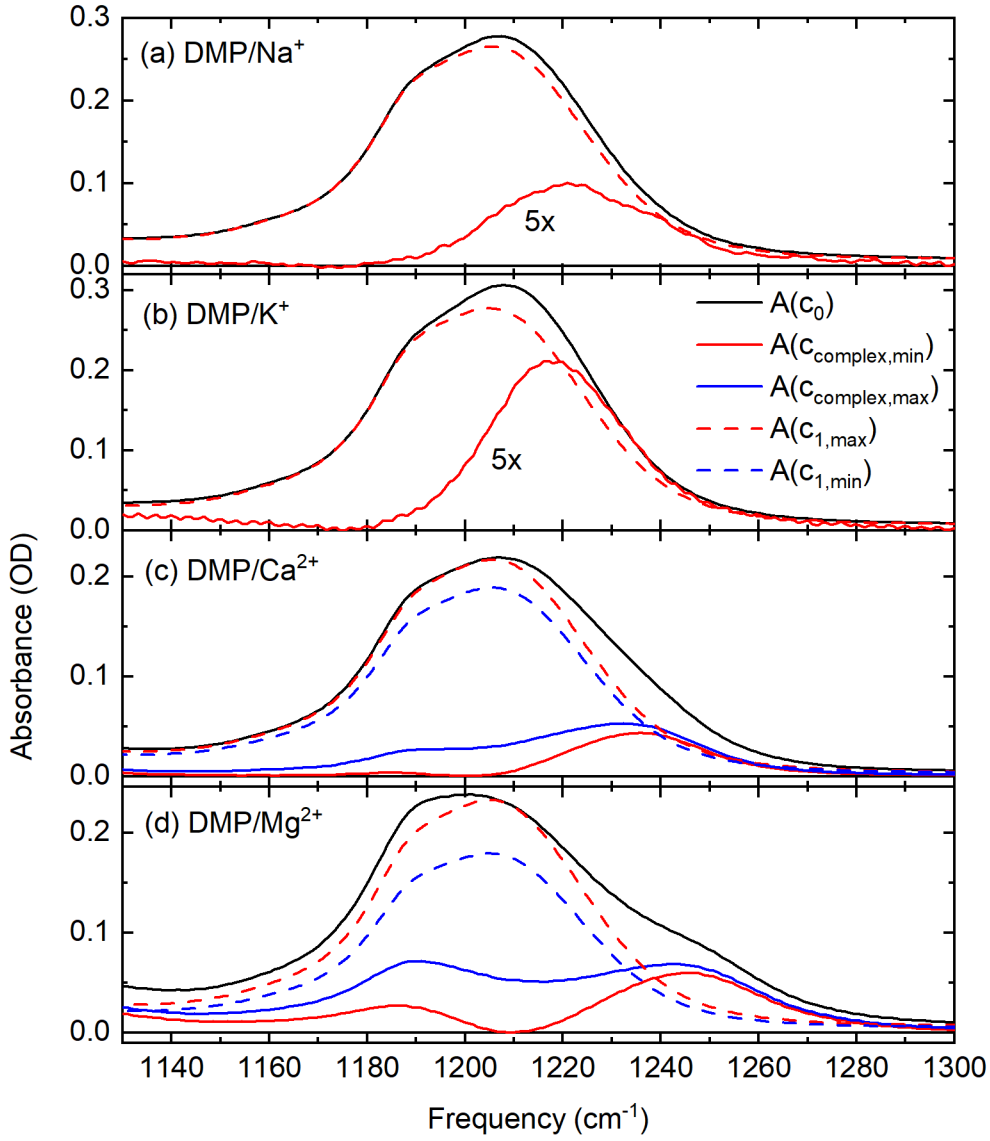

Figure 5.3: Linear absorption spectra of DMP with an added 2 M of the respective ions (black). The spectra are separated into contributions solely from ion-unaffected DMP molecules (dashed) and molecules that interact with ions in either CIP or SSIP geometry (solid red and blue, see text for details). DMP/ion complex spectra are calculated by subtracting a rescaled spectrum of DMP at 0 M added ions (see equation (5.2)). Red lines show absorption for a lower estimate of DMP/ion complex concentration, by allowing $A_{complex}(\nu) = 0$ at one frequency (1180 cm^{-1} for Na^+ and K^+, 1200 cm^{-1} for Ca^{2+}, and 1210 cm^{-1} for Mg^{2+}). Blue lines show an upper estimate by comparing linear to 2D-IR spectra.

are shown in fig. 5.3 as solid red lines, scaled up by a factor of 5. The spectra of DMP-ion complexes for both Na+ and K^+ show a single band centered at 1230 cm^{-1}. The remaining DMP molecules (176 mM for Na^+, 188 mM for K^+) do not significantly interact with the ions under this assumption. Their absorption is shown in fig. 5.3 as dashed red lines.

A larger portion of DMP molecules interacts with divalent ions. The lower boundary condition for DMP pairing with Ca^{2+} and Mg^{2+} is met at $c_{complex,min}$ = 39 mM and 36 mM, respectively ($A_{complex}(\nu) = 0$ at ν =1200 cm^{-1} for Ca^{2+}, 1210 cm^{-1} for Mg^{2+}). The spectrum with added Ca^{2+} is displayed in figure 5.3 and consists of an absorbance maximum at 1238 cm^{-1} and a small contribution at 1185 cm^{-1}. The spectral contribution of DMP/Mg^{2+} ion pairs consists of two bands at 1188 cm^{-1} and 1246 cm^{-1} separated by a minimum at 1210 cm^{-1}. All in all, 2 M bulk ion concentrations, an estimated lower boundary of 12% and 6% of DMP molecules pair with Na^+ and K^+, respectively. Ion pairing with divalent cations reaches at least 20% and 18% for Ca^{2+} and Mg^{2+}, respectively.

An upper boundary of 30% for Ca^{2+} and 37% for Mg^{2+} can be estimated by comparing linear and 2D-IR spectra and will be discussed in section 5.2.

5.2 Femtosecond spectroscopy

The spectral changes are expected to be more pronounced with nonlinear spectroscopy techniques as a result of the μ^4-dependency of the nonlinear signal on the transition dipole moment μ. PP and 2D spectroscopy, as introduced in section 3.2.4, are used here to investigate the emergent band due to DMP/ion interactions.

The DMP^- molecules are dissolved in an aqueous solution, librations of the water molecules contribute to the nonlinear signal. Figure 5.4(a) shows the pump-probe signal of pure water to establish a reference. An initial positive absorbance change for T<200 fs is followed by a negative absorbance change that decays with a lifetime longer than the 50 ps runtime of the experiment. This long-lived absorbance change is due to the formation of heated ground states of the underlying water librations [131]. This vibrational background is subtracted in all presented kinetic traces of DMP.

Spectrally resolved pump-probe data are displayed in fig. 5.4 for all cations discussed above. The PP spectrum of pure DMP in water shows two features: an increase in absorbance at 1180 cm^{-1}, as a result of excited state absorption v=1→ 2 (ESA), as well as an absorbance decrease due to ground state bleach (GSB) and stimulated emission (SE) at 1220 cm^{-1}. They intersect at 1200 cm^{-1}, the steep slope suggests an overlap of v=0→1 and v=1→ 2 vibrational bands due to the small diagonal anharmonicity of $\nu_{AS}(PO_2^-)$. The pump-probe signal mainly decays within 1 ps, the long-lived negative absorbance change reflects the solvent behaviour, as shown above.

Addition of excess ions leads to changes in the spectrum that strongly depend on the ion species. The spectrum of DMP with added Na^+ is indistinguishable from that of pure DMP. Adding Ca^{2+} results in a broadening of the GSB&SE feature, whereas the addition of Mg^{2+} leads to a side peak centered at 1255 cm^{-1}.

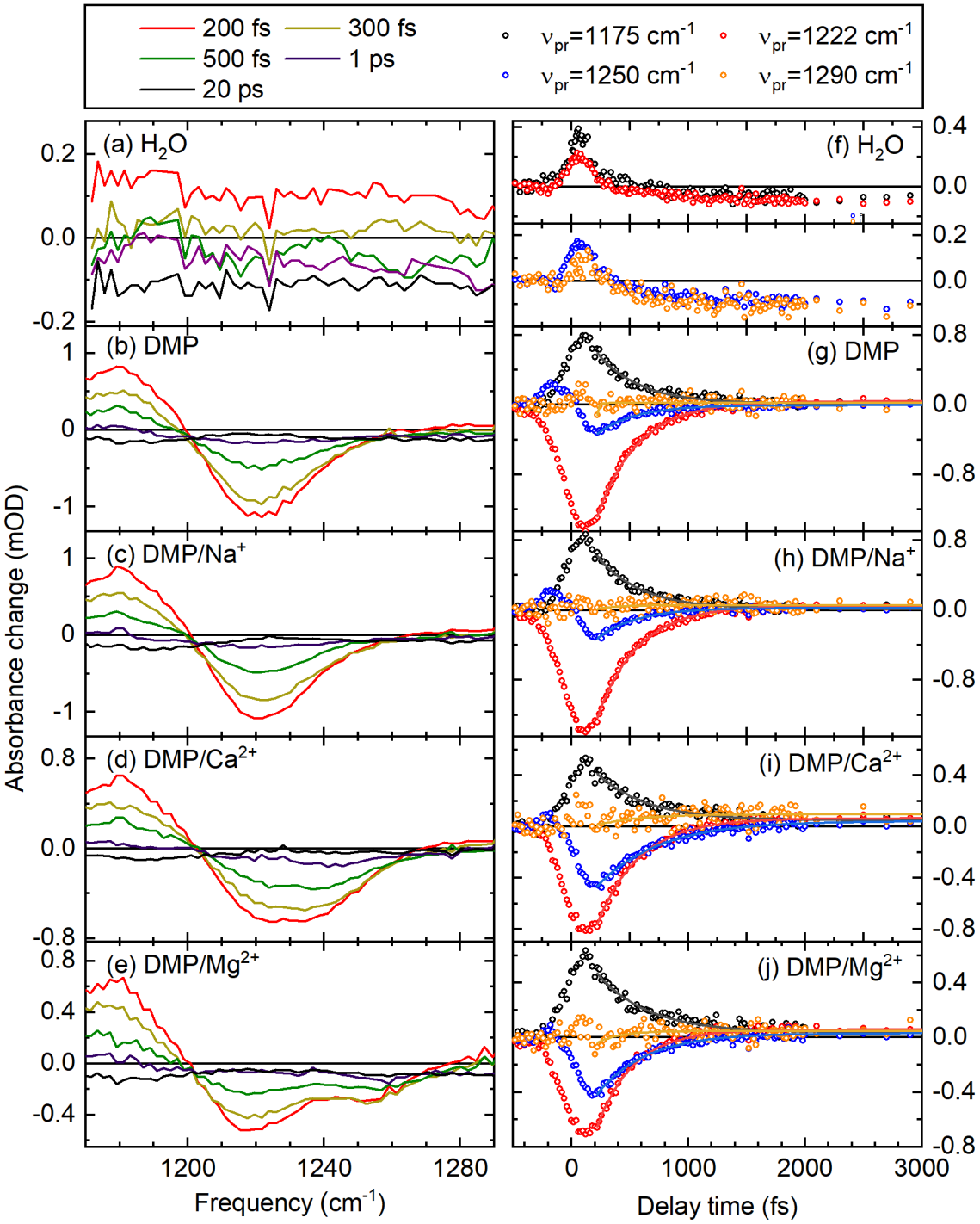

Figure 5.4: (a-d) Pump-Probe spectra of 0.2 M DMP in water with 2 M of added ions show the absorbance change as a function of wavenumber for different pump-probe delay times. Contributions from ESA result in a positive absorbance difference, GSB&SE contribute to the observed negative absorbance changes. (e-h) Absorbance change as a function pump-probe delay time at selected frequency positions. Signal from the librational water background has been subtracted. Fitting the curves using a single-exponential decay (solid lines) yields decay times on the order of 300 fs for the curves at 1175 cm^{-1} and 1222 cm^{-1}, and 500 fs at 1250 cm^{-1} for the divalent ions Ca^{2+} and Mg^{2+}.

Kinetic traces at characteristic frequencies, taken as a function of the delay T between pump and probe pulses, allow to extract the vibrational lifetimes of the underlying oscillations. The absorbance changes are plotted as a function of delay time in figure 5.4(g-j). The curve taken at 1290 cm^{-1} shows residual background signal, which is negligible after subtracting the water background of fig. 5.4(a). For -200 fs< T <200 fs the time overlap of pump and probe pulse results in coherent artifacts from interaction with the sample windows. The other kinetic traces represent ESA (1175 cm^{-1}), GSB&SE of DMP in neat water (1222 cm^{-1}), and GSB&SE in the region of the newly emergent feature (1250 cm^{-1}). For lifetime analysis the curves were fitted with a single-exponential decay curve. Fits show a ≈300 fs lifetime of the $\nu_{AS}(PO_2^-)$ vibration of DMP in neat water. This decay is slowed down for the emergent feature to ≈ 500 fs upon addition of Ca^{2+} or Mg^{2+}.

Mg^{2+} shows the strongest influence on $\nu_{AS}(PO_2^-)$. To further investigate this behaviour, figure 5.5 shows the pump-probe signal of DMP with increasing concentrations of added $MgCl_2$. The spectra (left) show the emergence of the side peak at 1255 cm^{-1} for concentrations $c_{Mg^{2+}}$ >0.5 M. Kinetic traces (right) also illustrate the shift of relative intensities from the original vibration at 1222 cm^{-1} to the new feature at 1250 cm^{-1}.

A more detailed insight into the properties of the ion-induced band is gained from 2D-IR spectroscopy. In particular, the question as to whether coupling between the new and the original mode persists, or whether the oscillators on independent molecules are probed, needs to be answered. Additionally, 2D-IR lineshapes encode interactions with the surrounding water environment. To this purpose, 2D-IR spectra were taken with the different cations, varying the ion concentration, and varying the waiting time. These spectra are presented in figures 5.6-5.10.

Figure 5.6 shows 2D spectra of 0.2 M DMP in water with 2 M of the respective salt. Since NaCl and KCl both showed a similar behaviour in the linear spectra, 2D spectra were taken only for NaCl. The 2D spectrum of DMP without addition of ions shows two dominant features. At (ν_1, ν_3)=(1206,1215) cm^{-1} yellow-red contours show a peak due to GSB and SE on the v=0→1 transition of the $\nu_{AS}(PO_2^-)$ vibrational mode. Red-shifted along the detection frequency ν_3, due to the vibrational anharmonicity, is the spectral peak from ESA on the v=1→2 transition, centered around (ν_1, ν_3)=(1206,1175) cm^{-1}. Both features are elongated along the diagonal, pointing to inhomogeneous broadening.

This spectrum is preserved upon addition of NaCl, although a slight blue shift can be observed, similar to the FTIR spectrum. The GSB&SE peak is shifted to (1208,1217) cm^{-1}, more clearly seen in a diagonal cut through the maximum of the bleaching feature (Figure 5.7, indicated by the dashed line in figure 5.6). With addition of divalent metal ions, the blue-shifted component emerges also in the 2D spectra. This is reflected in a strong shift of the GSB&SE maximum to (1224,1234) cm^{-1} in the Ca^{2+} case. For Mg^{2+}, the maximum is at (1205,1215) cm^{-1}, similar to the case without additional ions, but a new shoulder emerges, centered around (1237,1253) cm^{-1}. The new frequency component shifts more for Mg^{2+}, as in the FTIR spectra of figure 5.2, but the signal amplitude is larger for Ca^{2+}. Diagonal cuts through the GSB&SE maximum shown in figure 5.7 reflect this behaviour clearly.

The diagonal cuts also allow to estimate an upper boundary for the concentration of DMP/ion pairs, by comparing the spectral position of the emerging band in FTIR and

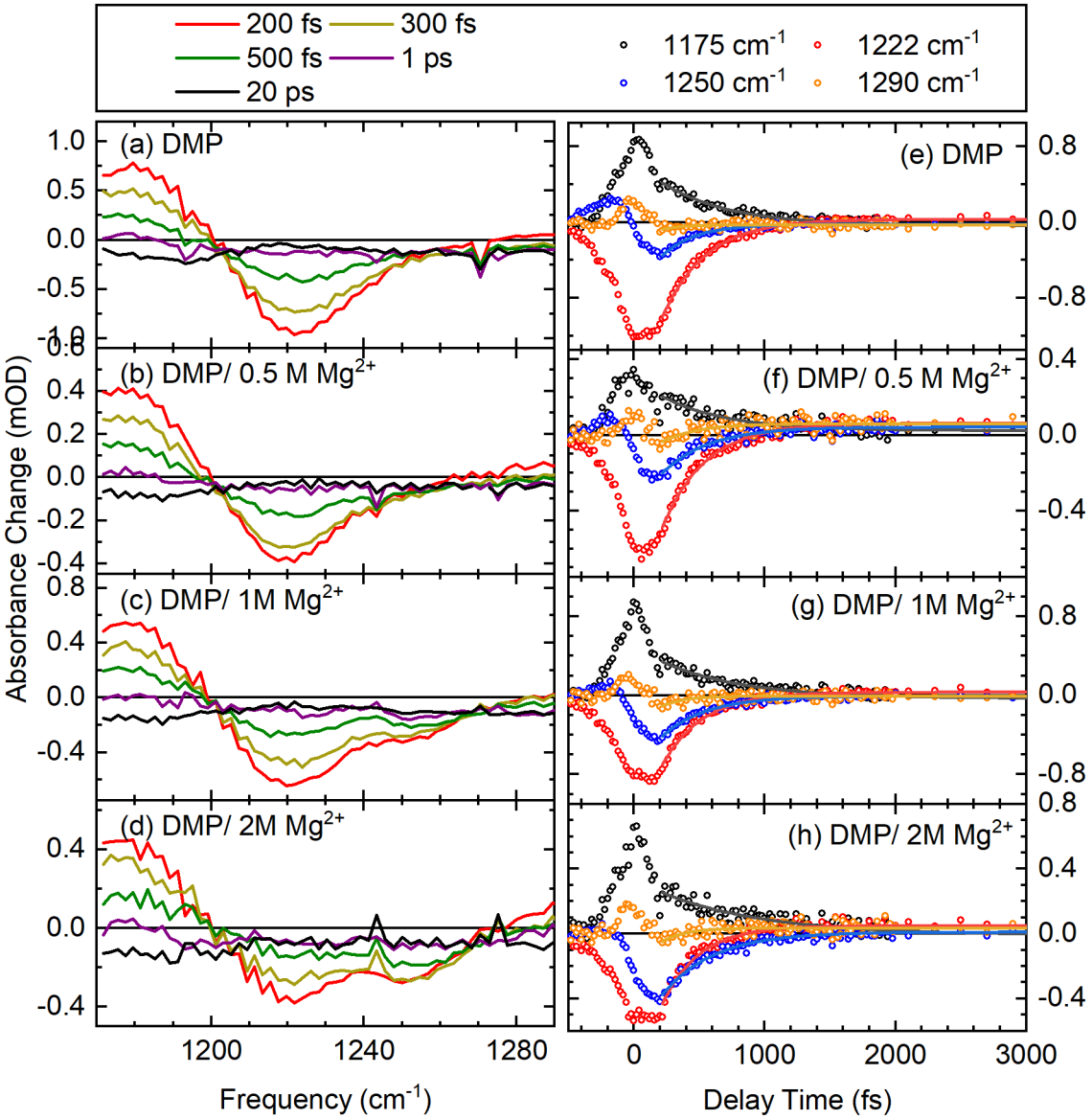

Figure 5.5: (a-d) Pump-Probe spectra of 0.2 M DMP with added excess Mg^{2+} show the absorbance change as a function of wavenumber for different pump-probe delay times. Contributions from ESA result in a positive absorbance difference, GSB&SE contribute to the observed negative absorbance changes. (e-h) Absorbance change as a function pump-probe delay time at selected frequency positions. Signal from the librational water background has been subtracted. Fitting the curves using a single-exponential decay (solid lines) yields decay times on the order of 300 fs for the curves at 1175 and 1222 cm^{-1} and 500 fs at 1250 cm^{-1}.

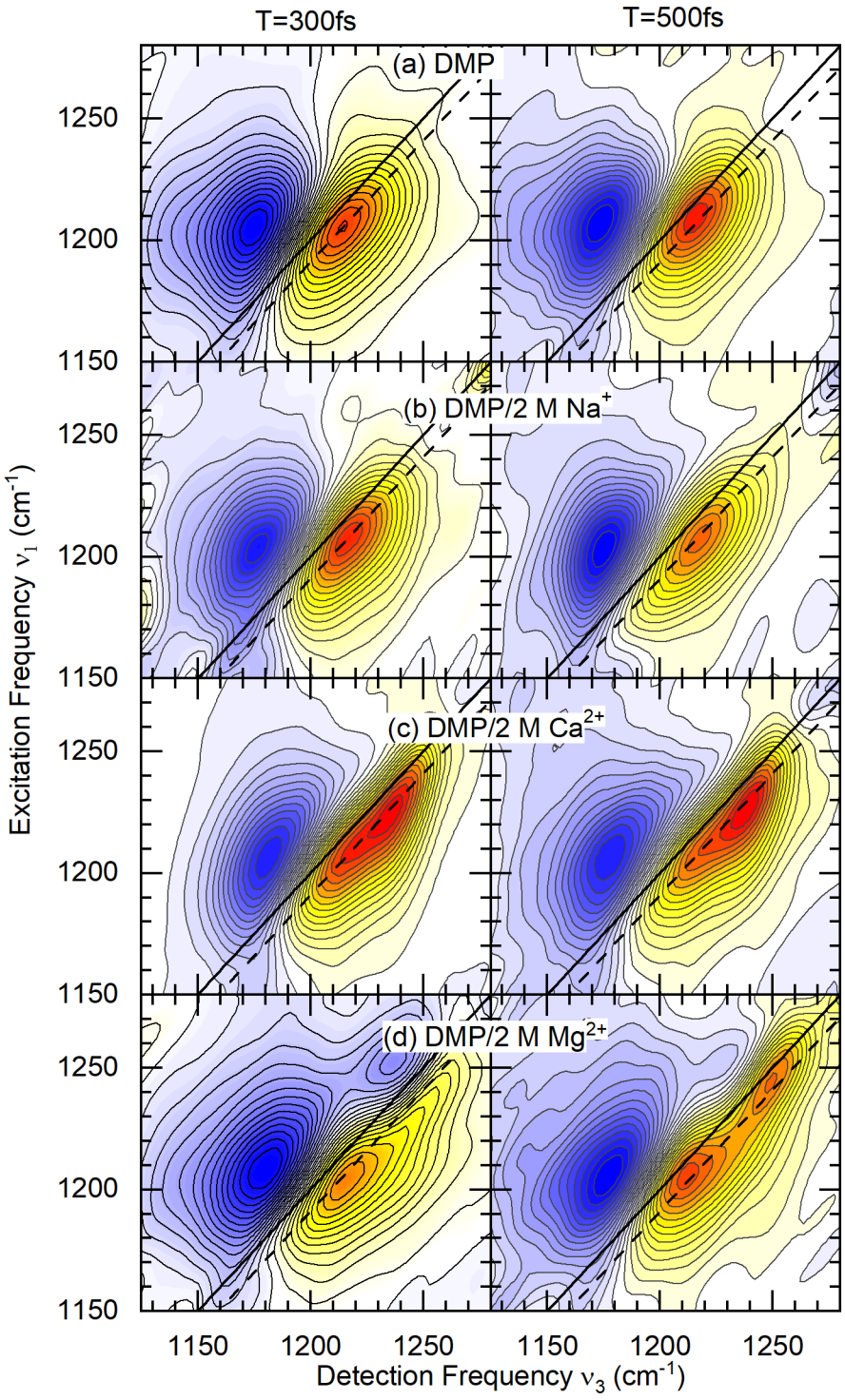

Figure 5.6: Absorptive 2D-IR spectra taken for 0.2 M $DMP^{-}Na^{+}$ in H_2O without excess salt (a), as well as with 2 M of NaCl (b), 2 M of $CaCl_2$ (c), and 2 M of $MgCl_2$ (d). Spectra were taken at waiting times of T=300 fs (left) and T=500 fs (right). As described in section 3.2.4 yellow-red contours show ground-state bleach and stimulated emission signals, whereas the blue contours depict the signal from excited state absorption, shifted to lower frequencies due to the diagonal anharmonicity of the vibrational oscillator. Neighboring contour lines are separated by 7.5% of the total signal.

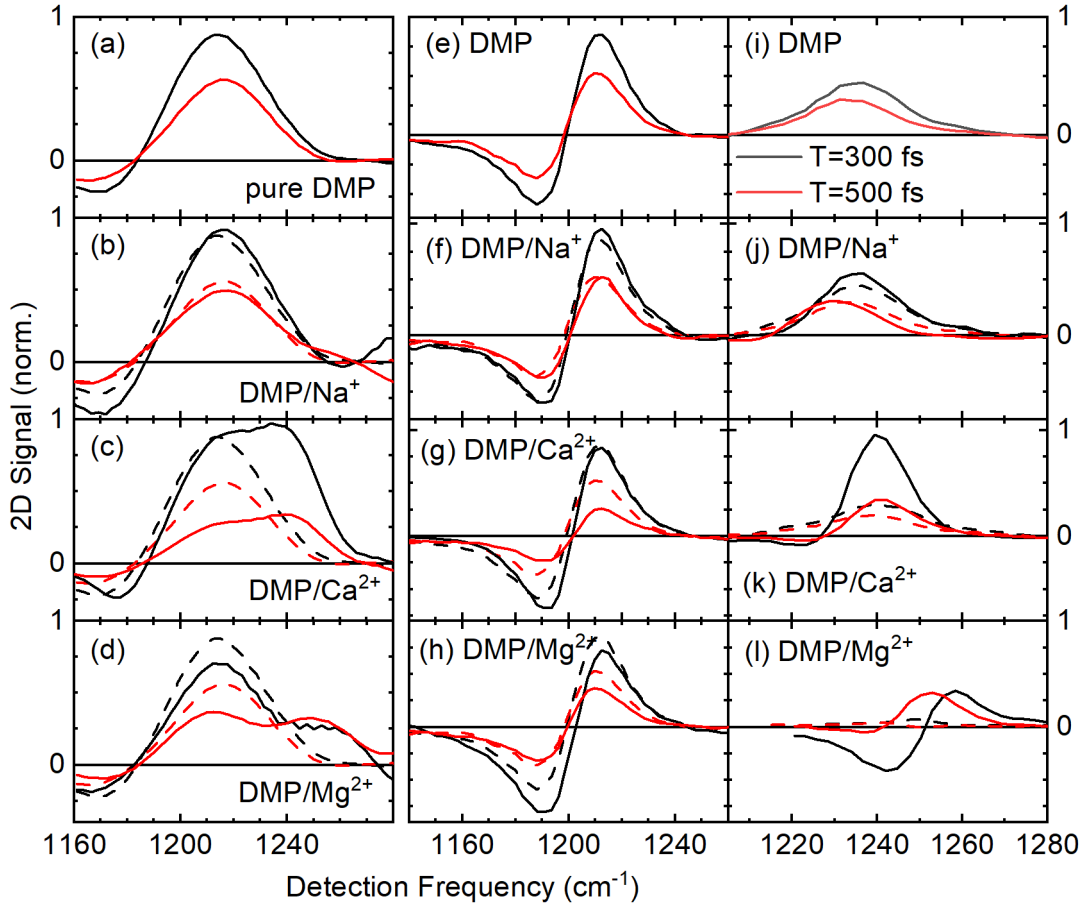

Figure 5.7: Cuts taken through the 2D spectra of fig 5.6 (black: T =300 fs, red: T=500 fs), normalized to the maximum of the respective 2D-IR spectrum. (a-d) Diagonal cuts, taken through the GSB maximum at (1241,1250) cm^{-1}. (e-h) Antidiagonal cuts taken through (1206,1206) cm^{-1}. (i-l) Antidiagonal cuts taken through the respective frequency of the newly emergent feature: (1230,1230) cm^{-1} (Na^+), (1235,1235) cm^{-1} (Ca^{2+}), and (1250,1250) cm^{-1} (Mg^{2+}). Cuts through the 2D spectrum of pure DMP (a,e,i) are shown in all other graphs as dashed lines for reference.

2D-IR spectra. The signal amplitudes of linear spectra are proportional to μ^2, those of 2D-IR spectra to μ^4, the spectral position, however, should not be affected by the spectroscopic method. The maximum of the diagonal cuts through the 2D signal is registered at 1235-1240 cm^{-1} for Ca^{2+} and 1245 cm^{-1} for Mg^{2+}. This is in agreement with the absorption maxima of $A_{complex,min}$ at 1238 cm^{-1} for Ca^{2+} and 1246 cm^{-1} for Mg^{2+} (see fig. 5.3, solid lines). When increasing the concentration $c_{complex}$ in eq. (5.2) above $c_{complex,min}$, the spectral position of $A_{complex}$ shifts towards lower frequencies. We found that for Ca^{2+} $A_{complex}$ is centered at 1233 cm^{-1} for $c_{complex} > 60$ mM ($0.3c_0$, i.e. 30% of all DMP molecules), and for Mg^{2+} at 1244 cm^{-1} for $c_{complex} > 74$ mM ($0.37c_0$). These concentrations therefore mark an upper boundary for the concentration of DMP/ion complexes, the uncertainty is on the order of 25%. An upper estimate of DMP/Na^+ complexes is not possible, due to the comparably small frequency shift.

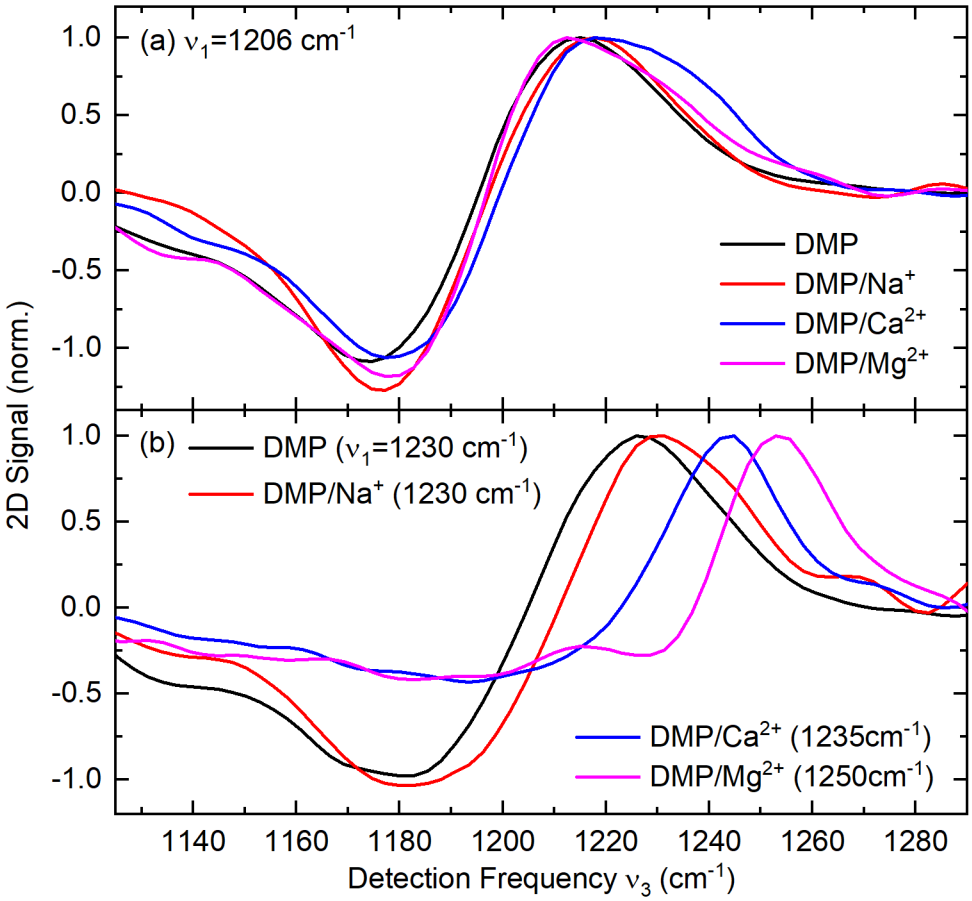

Figure 5.8: Horizontal cuts through the spectra of fig. 5.6. Cuts were taken at ν_3=1206 cm^{-1} and the respective frequency of the newly emergent feature ν_3=1230, 1235, and 1250 cm^{-1} for Na^+, Ca^{2+}, and Mg^{2+}, respectively. Horizontal cuts would disclose off-diagonal peaks, should they be present in the 2D-IR spectra.

Important to note in the 2D-IR spectra of fig. 5.6 is the absence of off-diagonal peaks in the region of $\nu_{AS}(PO_2^-)$ (cf. the off-diagonal elements in the schematic 2D-IR spectrum of fig. 3.8). A reliable indicator of this are cuts through the 2D spectrum along the detection frequency axis, shown in fig. 5.8. Fig. 5.8(a) shows these horizontal cuts for the various ions at ν_1 = 1206 cm^{-1}, the maximum of the signal for pure DMP. They reflect the positive GSB&SE signal at 1218 cm^{-1} and the negative ESA signal at 1180 cm^{-1}. Coupling between the original $\nu_{AS}(PO_2^-)$ mode at 1206 cm^{-1} and the new band would result in an additional peak at the frequency of the DMP/ion complex (1235 cm^{-1} and 1245 cm^{-1} for Ca^{2+} and Mg^{2+}, respectively). This is clearly not the case for Mg^{2+}, while Ca^{2+} shows some broadening in this frequency region.

Similarly, coupling would result in off-diagonal peaks at $\nu_3 \approx 1200$ cm^{-1} in horizontal cuts through the maximum of the emerging mode. Such cuts are displayed in fig. 5.8(b) for the different ions. The cuts for the addition of Mg^{2+} and Ca^{2+} both show a broad, but weak minimum in the frequency region around 1200 cm^{-1}. This can be attributed to the ESA signal of the original $\nu_{AS}(PO_2^-)$ mode that extends to these high frequencies. It is no sign

of coupling between the original $\nu_{AS}(PO_2^-)$ mode and the new mode due to ion interactions.

To investigate the behaviour of 2D spectra of $\nu_{AS}(PO_2^-)$ with increasing ion concentration, figure 5.9(a-d) shows 2D-IR spectra of DMP with added Mg^{2+} concentrations ranging from 0.5 to 2 M. All spectra are taken at a waiting time $T = 300$ fs and show diagonally elongated spectra for all Mg^{2+} concentrations. With the addition of 0.5 M $MgCl_2$ the peak structure of pure DMP undergoes a spectral broadening, the signal maximum shifts to (1209,1221) cm^{-1}. Upon further increase of Mg^{2+} ion concentration a shoulder develops around (1237,1253) cm^{-1}.

Cuts taken diagonally through the signal maximum at (1206,1215) cm^{-1} show the evolution of the diagonal linewidths and are presented in fig. 5.9(e). The initial spectral broadening at 0.5 M Mg^{2+} concentration gives way to a side shoulder for higher Mg^{2+} concentrations. The original DMP peak shape is conserved for 1 and 2 M of Mg^{2+} ions, its amplitude decreases by about 25%. Antidiagonal cuts (fig. 5.9(f,g)) through (1205,1205) cm^{-1} and (1250,1250) cm^{-1} depict antidiagonal linewidths for DMP and DMP/ion complexes, respectively. The lineshape of the original $\nu_{AS}(PO_2^-)$ mode at 1205 cm^{-1} is shown to be independent of Mg^{2+} concentration. The signal strength of the cut through (1250,1250) cm^{-1} increases from a negligible contribution at $c_{Mg^{2+}} = 0$ M to $\approx 1/2$ of the original peak at $c_{Mg^{2+}} = 2$ M. By rough estimate, the antidiagonal linewidth of the emergent feature is smaller by a factor of 2, illustrated by the rescaled frequency axis.

Figure 5.10(a-c) shows 2D spectra of DMP with 2 M added $MgCl_2$ for different waiting times T. While the general shape of 2D features is conserved up to $T = 750$ fs, the signal amplitudes shift with increasing waiting time. Cuts along the diagonal axis show that the signal decrease of the emergent band is far less pronounced than for the initial DMP species. The spectra at longer waiting time show a significantly stronger signal at 1250 cm^{-1} relative to the $\nu_{AS}(PO_2^-)$ mode of pure DMP. This is in good agreement with the longer lifetime measured for the emergent spectral feature in pump-probe experiments.

The qualitative analyses of the experimental 2D-IR spectra can be corroborated by a quantitative 2D spectral analysis based on Kubo lineshape theory, as described in section 3.2.4. The 2D-IR spectra are simulated by explicitly calculating the third-order response function. The frequency fluctuation correlation function (FFCF) of a given vibrational mode ν_i that gives rise to the lineshape function $g_i(t)$ is modeled using a double-exponential Kubo ansatz of the form $\frac{1}{4\pi^2}\langle\delta\omega(\tau'')\delta\omega(0)\rangle = \Delta\nu_{1i}^2 e^{-t/\tau_1} + \Delta\nu_{2i}^2 e^{-t/\tau_2}$(cf. eq. (3.13)). The two exponentials represent fluctuations in the environment of the $\nu_{AS}(PO_2^-)$ mode with the fluctuation amplitude $\Delta\nu$ that act on on two different timescales. Here, we use correlation times τ_1=300 fs and $\tau_2 = 50$ ps, in accordance with previous simulations on DNA samples, to mimic fast librations of surrounding water molecules and slower chemical rearrangements [37]. Simulations have aimed at replicating the 2D spectra of pure DMP and DMP with 2 M of added $MgCl_2$ at a waiting time T=500 fs, since these spectra offer the clearest separation of original and emerging band. The simulated spectra are shown in fig. 5.11, the corresponding parameter set is given in table 5.1.

The pure DMP spectrum is made up of two spectral components, reflecting the two conformers: *gt*-DMP at 1195 cm^{-1}, *gg*-DMP at 1215 cm^{-1}. The vibrational lifetimes of both components are set to 300 fs in accordance with the PP measurements of fig. 5.5. Fast fluc-

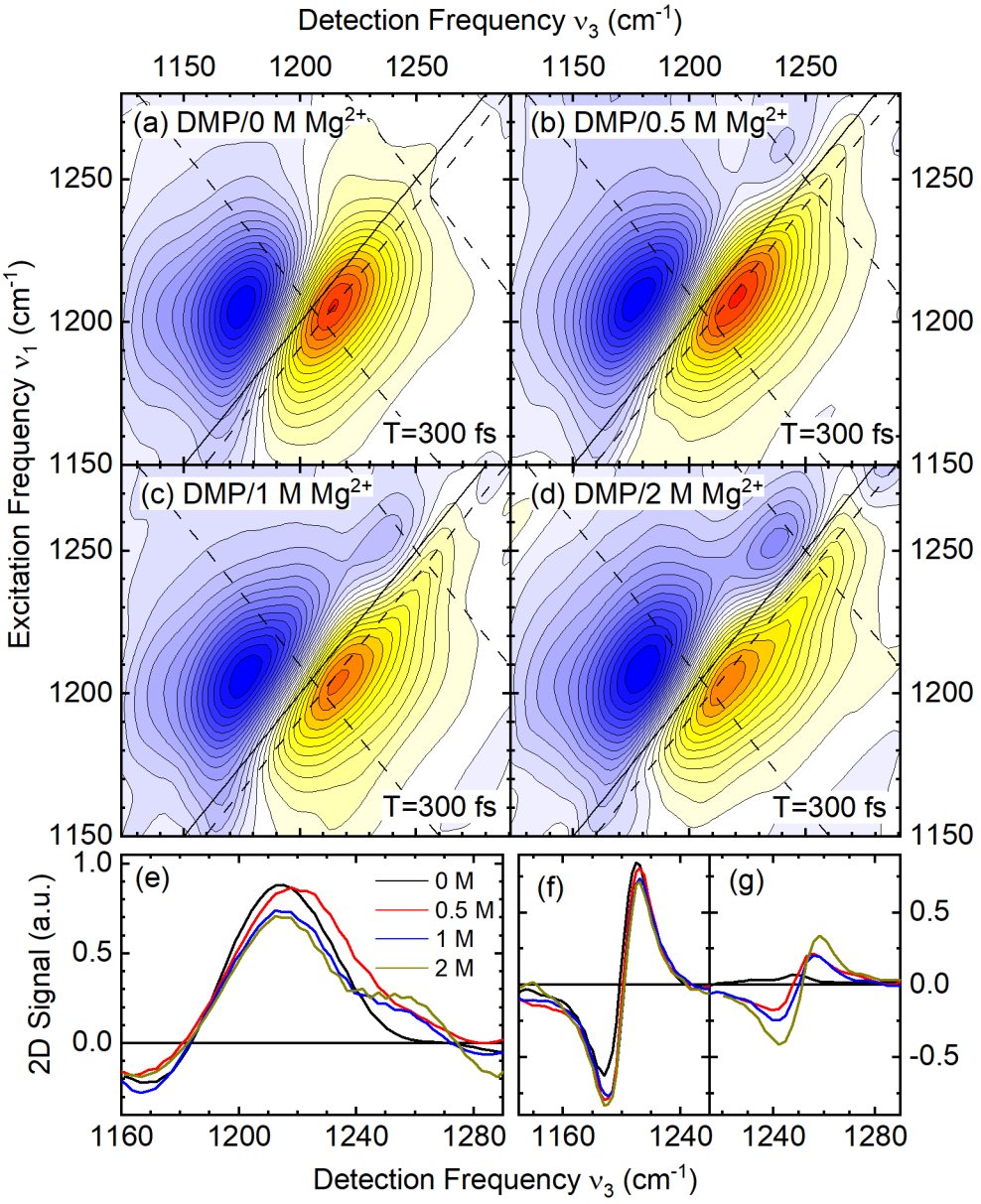

Figure 5.9: Dependence of DMP and DMP/ion species on added ion concentration. (a-d) 2D spectra of 0.2 M DMP in H_2O taken for different concentrations of added $MgCl_2$ at a waiting time of T=300 fs. (e) Diagonal cuts through the 2D spectra through (ν_1, ν_3)=(1206,1215) cm^{-1}. With increasing concentration the emergent feature at 1275 cm^{-1} can be clearly distinguished. (f) Cuts through the 2D spectra taken along the antidiagonal through (ν_1, ν_3)=(1205,1205) cm^{-1} and (g) through (ν_1, ν_3)=(1250,1250) cm^{-1}. The antidiagonal linewidth of the emergent feature is smaller by a factor of ≈2.

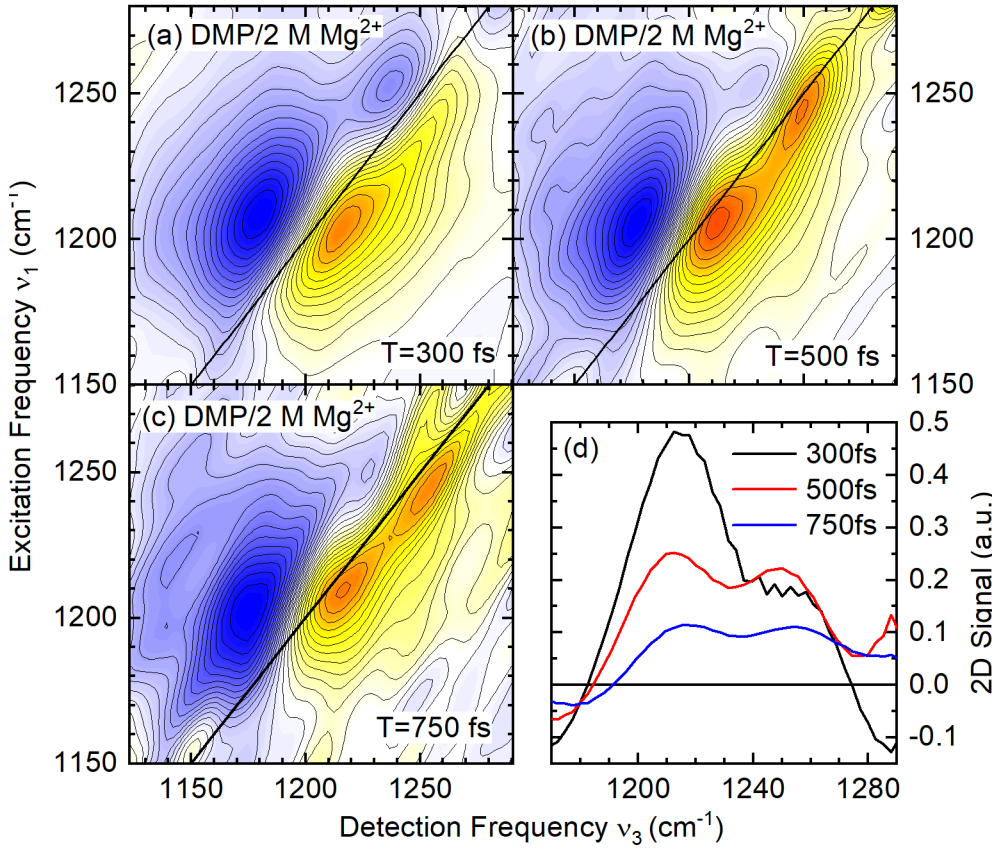

Figure 5.10: Dependence of pure DMP and DMP/ion species on waiting time. (a-c) 2D spectra of 0.2 M DMP and 2 M $MgCl_2$ in H_2O for T=300, 500, and 750 fs, respectively. (d) Cuts through the 2D spectra taken parallel to the frequency diagonal passing through (ν_1, ν_3)=(1206,1215) cm^{-1}.

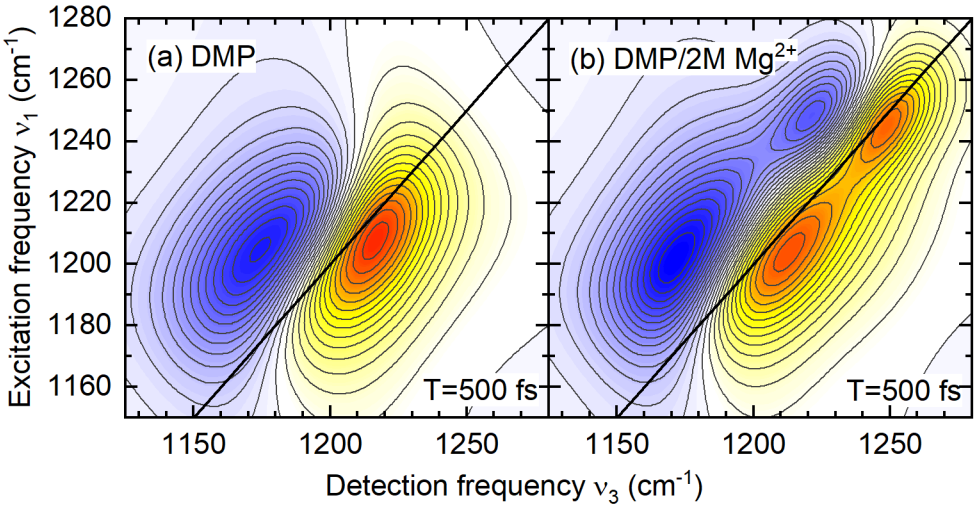

Figure 5.11: 2D spectra simulated using the Kubo formalism detailed in section 3.2.4. Simulated spectra show DMP in H_2O (a) and DMP in H_2O with added 2 M of $MgCl_2$ (b) at a waiting time of T=500 fs.

mode ν_i	relative scaling	frequency v=0→1	anharmonicity Δ	decay time T_{1i}	fluctuation amplitudes $\Delta\nu_{1i}$	$\Delta\nu_{2i}$
		cm^{-1}	cm^{-1}	fs	cm^{-1}	cm^{-1}
ν_1	90/83	1195	26/26	300	17/15	9.5/8.0
ν_2	100/100	1215	21/25	300	13.8/13.8	10.7/11.7
ν_3	0/49	1248.5	-/25	500	-/10.6	-/10.0

Table 5.1: Parameter set as used in the numerical simulation of the 2D-IR spectra of DMP with added 0/2 M $MgCl_2$ shown in figure 5.11 at a waiting time $T = 500$ fs.

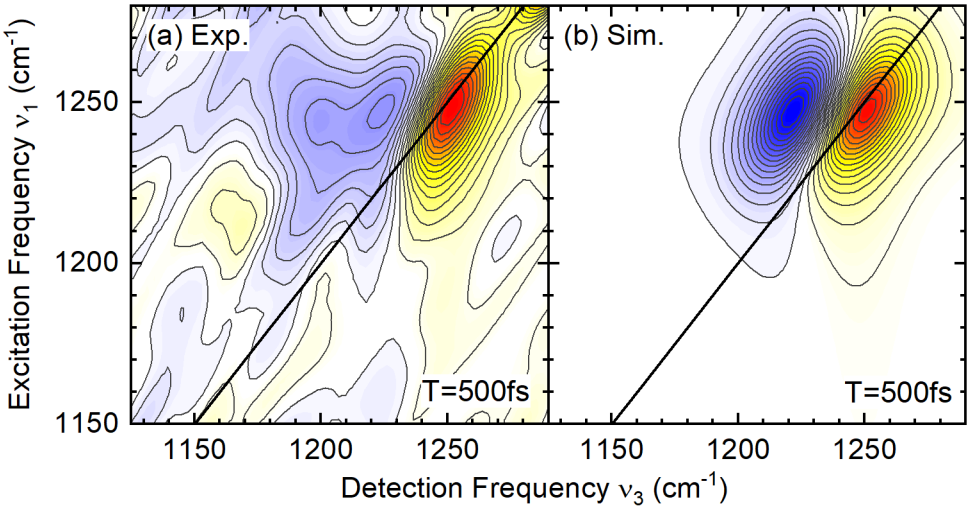

Figure 5.12: (a) Difference 2D spectrum displaying the newly emergent frequency band upon addition of ions. The spectrum was calculated by subtracting normalized 2D-IR spectra of DMP with and without 2 M Mg^{2+}. (b) Simulated 2D-IR spectrum of only the emergent component (row ν_3 of table 5.1).

tuations show higher amplitudes than slower fluctuations for both *gg* and *gt* conformers. The recovered fluctuation amplitudes allow to put the parameters into the context of the two limiting cases of Kubo lineshape analysis, discussed in section 3.2.3. In the homogeneous limit, where the lineshape is Lorentzian, $\Delta\omega \cdot \tau_c \ll 1$, where $\Delta\omega[\mathrm{fs}^{-1}] = 2\pi c \cdot \Delta\nu[\mathrm{cm}^{-1}]$. In the inhomogeneous limit, $\Delta\omega \cdot \tau_c \gg 1$ needs to be satisfied, the lineshape then is Gaussian. The fast fluctuations that act on $\nu_{AS}(PO_2^-)$ occur at timescales $\tau_{c1} = 300$ fs and show amplitudes $\Delta\nu_1 \approx 14\,\mathrm{cm}^{-1}$, yielding $\Delta\omega_1 \cdot \tau_{c1} = 0.8$. The fast fluctuations thus contribute to the homogeneous broadening of the 2D-IR spectrum, but are not significantly in the limiting region. The timescale of the slow component in the simulation is τ_{c2}=50 ps. Together with the fluctuation amplitudes $\Delta\nu_2$ ≈10 cm^{-1}, the product $\Delta\omega_2 \cdot \tau_{c2} \approx 100$, well within the inhomogeneous limit. These fluctuations then are responsible for the strong inhomogeneous broadening that we observe along the diagonal.

The emergence of the new band is simulated by an additional vibrational mode centered at 1248.5 cm^{-1} and scaled at 49% of the original *gg* vibrational mode. The lifetime was set to 500 fs (cf. PP results). Fluctuation amplitudes are 10 cm^{-1} for both fast and slow

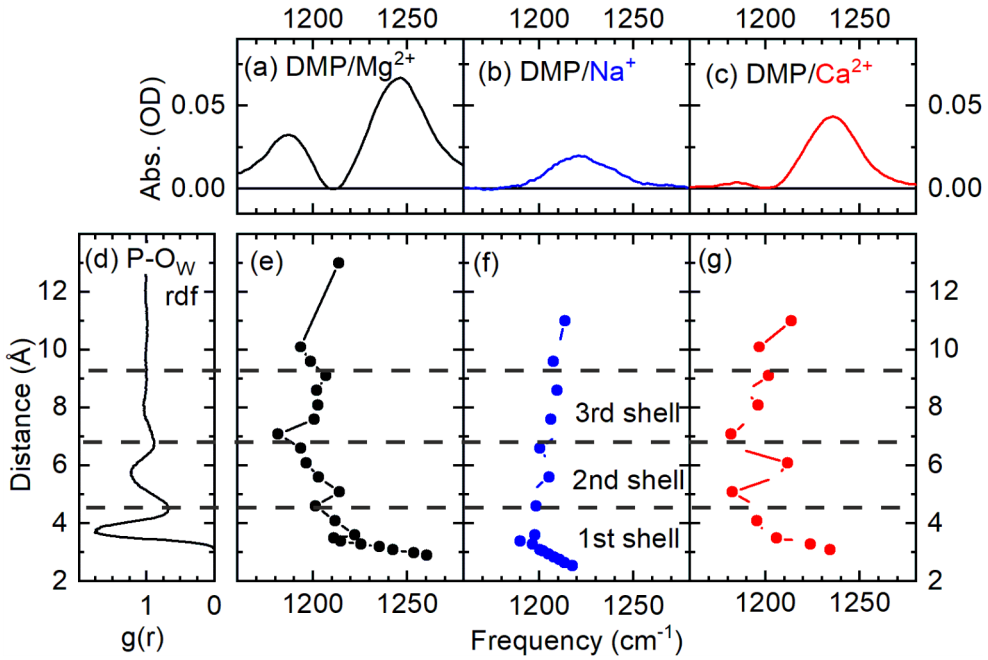

Figure 5.13: Simulated vibrational frequency as a function of P–ion distance for Mg^{2+}, Na^{+}, and Ca^{2+}. (a-c) Weighted difference spectra for DMP/Mg^{2+}, DMP/Na^{+}, and DMP/Ca^{2+} complexes at 2 M ion concentrations, depicting contributions of DMP/ion complexes to the vibrational spectrum, as shown in fig. 5.3. (d) Radial distribution function of the phosphate-water oxygen distance showing the distribution of solvation shells around the phosphate group. (from [38]) (e-g) Vibrational frequency of the asymmetric phosphate stretch vibration as a function of P–ion distance for Mg^{2+}, Na^{+}, and Ca^{2+}, respectively. Frequencies were calculated using DFT for clusters of one DMP molecule, 19 water molecules, and one respective cation.

component. Figure 5.12 isolates the emerging mode by comparing a differential 2D spectrum to a simulated 2D spectrum consisting purely of the new mode ν_3. The differential 2D-IR spectrum was computed by subtracting the normalized 2D spectrum of pure DMP from the normalized spectrum of DMP/2 M Mg^{2+}. The spectra are in good agreement.
0

5.3 Theory and Discussion

The experimental results were complemented by theoretical simulations of DMP/ion clusters in a water environment. Figure 5.13 links DFT calculations to experimentally measured spectral changes. The points in fig. 5.13(e-g) show the computed frequency of $\nu_{AS}(PO_2^-)$ as a function of ion-phosphorous distance D. For comparison, fig. 5.13(d) marks the hydration layers around fully hydrated DMP according to the minima in the radial distribution function of P–water oxygen distances [38]. Ions are initially placed at D$>$ 10Å under fully solvated conditions (N_{H_2O}=19), the equilibrium frequency is 1212 cm^{-1}. Approaching the DMP molecule leads to an initial red-shift in vibrational frequency for all ions, down to 1190 cm^{-1} for Na^{+}, 1185 cm^{-1} for Ca^{2+}, and 1180 cm^{-1} for Mg^{2+}. The clusters show distinct differences, at what distance this minimal frequency is reached. DMP/Na^{+} reaches the

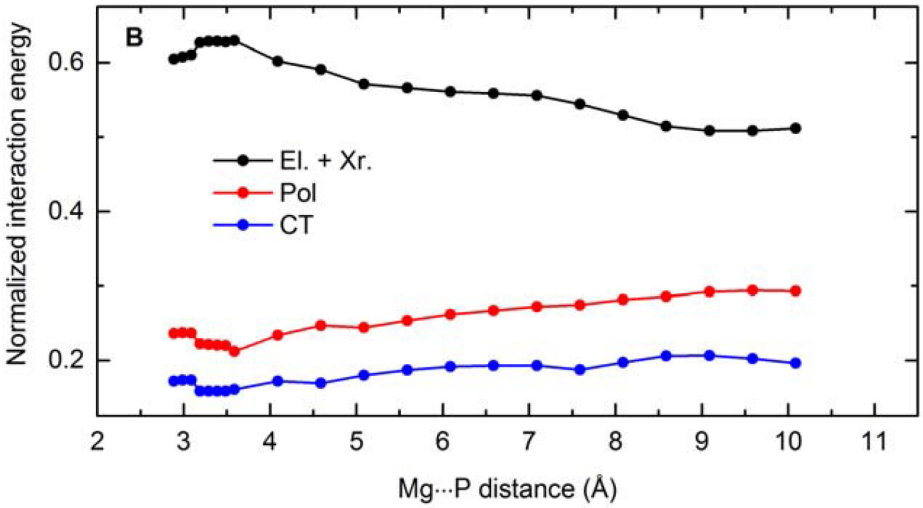

Figure 5.14: Normalized interaction energy of a $DMP^{-}(H_2O)_{19}Mg^{2+}$ cluster as a function of Mg-P distance. ALMO-EDA allows to separate the total energy into contributions from electrostatic and exchange repulsion interactions (black), polarization terms (red) and charge transfer (blue). Normalization is performed with respect to the total interaction energy at 10.09Å.

minimum at ≈3 Å, whereas the divalent ions have their turning point at significantly larger distances. Ca^{2+} shows strong fluctuations, but starts shifting to the blue again within the 2nd solvation shell, Mg^{2+} reaches its minimum at ≈7 Å. When the ions surpass this critical distance, $\nu_{AS}(PO_2^-)$ strongly shifts towards higher frequencies. Breaking into the first hydration shell of the phosphate group in particular changes the frequency significantly. The final data point records 1220 cm^{-1} at a distance of 2.5 Å for Na^+, but up to 1240 cm^{-1} for Ca^{2+} (D≈3 Å) and 1260 cm^{-1} for Mg^{2+}. These frequencies agree well with the frequency contributions emergent in the infrared absorption spectra, shown here in (a-c) (from fig. 5.2).

To investigate the microscopic origin of the frequency blue shifts, we look at the contributions to the intermolecular interaction energy using ALMO-EDA (fig. 5.14, for DMP/Mg^{2+}). The contribution of polarization and charge transfer terms decreases with decreasing Mg^{2+} phosphate distance. In turn, electrostatic and exchange repulsion terms, that are predominant to begin with, increase from ≈50% to > 60%. This change influences the molecular binding potential (fig. 5.15). At fully solvated geometries, here D= 9.0889Å, the total intermolecular interaction terms are symmetrical about the oscillator's equilibrium position. For small distances, the contributions are highly asymmetric, resulting in a deformed bonding potential. For positive displacements from the potential minimum, the dominant term is electrostatic and exchange repulsion. For negative displacements, polarization effects and charge transfer dominate, but to a reduced amount compared to electrostatics and exchange repulsion at positive elongations.

Theoretical simulations were also used to gain a geometrical insight into DMP-ion interactions. Minimal hydration geometries were constructed to this purpose for DFT calculations. Only enough water molecules were added to fill both the first hydration shell of DMP and of

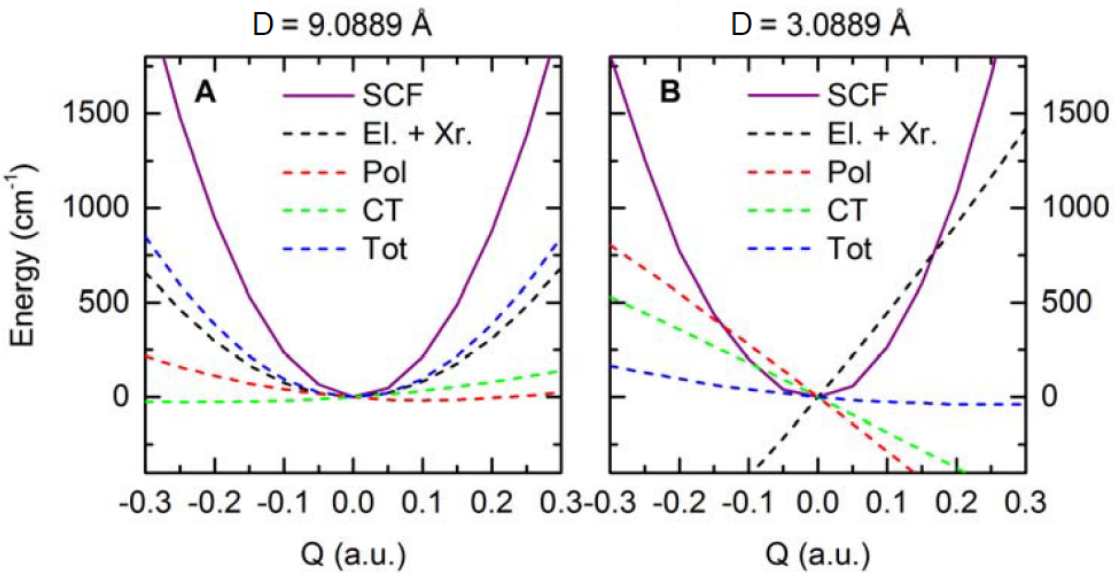

Figure 5.15: Molecular binding potential along the $\nu_{AS}(PO_2^-)$ normal coordinate Q for a $DMP^-(H_2O)_{19}Mg^{2+}$ cluster. Potentials were analyzed using ALMO-EDA at D=9.0889Å (a, solvent-separated geometry) and at D=3.0889Å (b, contact ion pair geometry). Contribution to the total intermolecular interactions (blue) come from electrostatic and exchange repulsion (black), polarization (red), and charge transfer (green). The potential was obtained by self-consistent field simulation (purple) and accounts for the geometric displacement of the cluster.

the respective ion (N=11 for Na^+ and Mg^{2+}, N=13 for Ca^{2+}). This minimal arrangement is expected to lead to CIP geometries typical for the respective ion. The corresponding geometries after constrained optimization are shown in fig. 5.16, together with the phosphate-ion distance and the angle $\alpha = \measuredangle$ P-O1...Ion. The Na^+ ion forms part of the regular hydration tetrahedron around the phosphate oxygen ($\alpha = 127.3°$), where it replaces one of the water molecules. The divalent ions arrange more in a linear extension of the P-O1 bond. In the case of Mg^{2+} the angle is 173.9°, the Ca^{2+} ion is situated between the two distinct cases with an angle $\alpha = 152.2°$. Both Ca^{2+} and Mg^{2+} disturb the tetrahedral hydration gemometry around the O1 oxygen significantly, a good reference gives the intact tetrahedron around the O2 oxygen. The solvation shell of the ions, however, is less perturbed. Mg^{2+} keeps its characteristic octahedral hydration geometry, replacing one of the water molecules by the O1 oxygen of the phosphate group. Mg^{2+} also reports the smallest distance to the phosphorous.

A broader understanding is achieved by MD simulations of the DMP-ion system. Two-dimensional potentials of mean force (PMF) from these simulations are shown in fig. 5.17. They display the relative free energy along the P...ion distance and the angle $\alpha = \measuredangle$P-O1...Ion. This illustrates the configuration space that the ion explores within the 1.59 µs of simulation time. The Na^+ ion evidently shows the strongest fluctuations, the free energy is lowest at a P–Na^+ distance ≈5 Å, with a broadly angled local minimum at ≈3.5 Å and a highly localized minimum at 3.8 Å, $\alpha = 80°$. Ca^{2+} shows the free energy minimum at 3.8 Å, larger distances are also probed but separated by a potential barrier on the order of 2000 cm^{-1}. The Mg^{2+} only probes short distances within the simulation time. Depict-

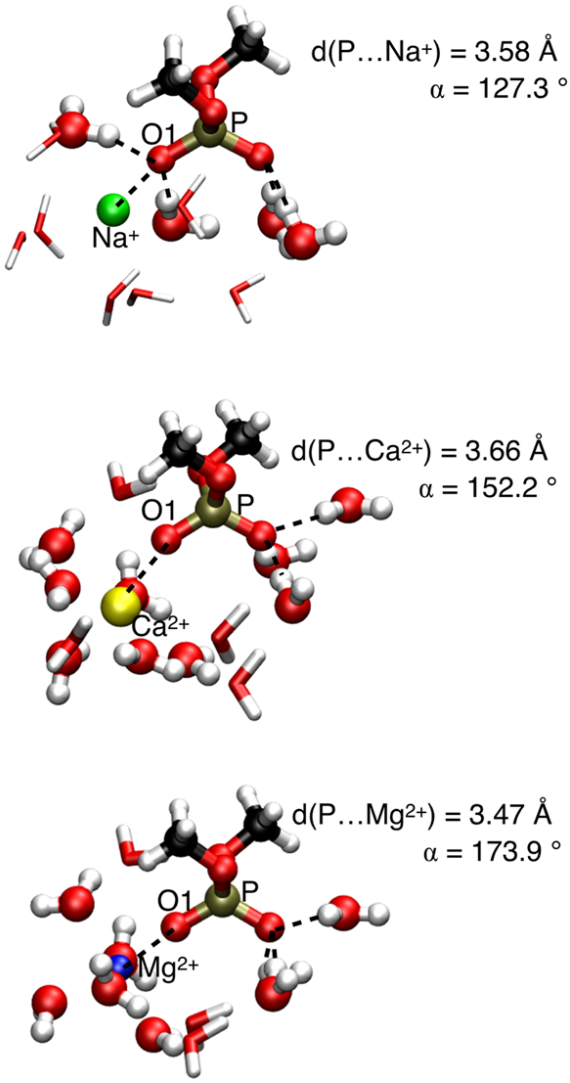

Figure 5.16: Minimum hydration geometries of DMP^-/Na^+ (a, N_{H_2O}=11), DMP^-/Ca^{2+} (b, N_{H_2O}=13), and DMP^-/Mg^{2+} (c, N_{H_2O}=11), respectively. Minimum hydration geometries show a prototypical contact pairing geometry, distance and angle are shown.

ing the minimal energy at each respective angle for distances $D < 4$Å shows the angular dependency of the minimal free energy. The singular data points represent the minimal hydration geometries from the DFT calculations in figure 5.16.

The results provided in this chapter demonstrate the sensitivity of $\nu_{AS}(PO_2^-)$ to detect the formation of phosphate-ion contact pairs. DMP samples exhibit changes of the vibrational spectrum, no matter which of the four biologically relevant cations is added. The extent of these changes differs, in hand with the distinctly different, ion-dependent geometries of CIPs.

IR spectra of pure DMP in water reflect the different conformations the molecule can adapt. The elongation of 2D-IR lineshapes along the diagonal indicates an inhomogeneous distribution of frequencies due to the structural heterogeneity of DMP molecules in solution.

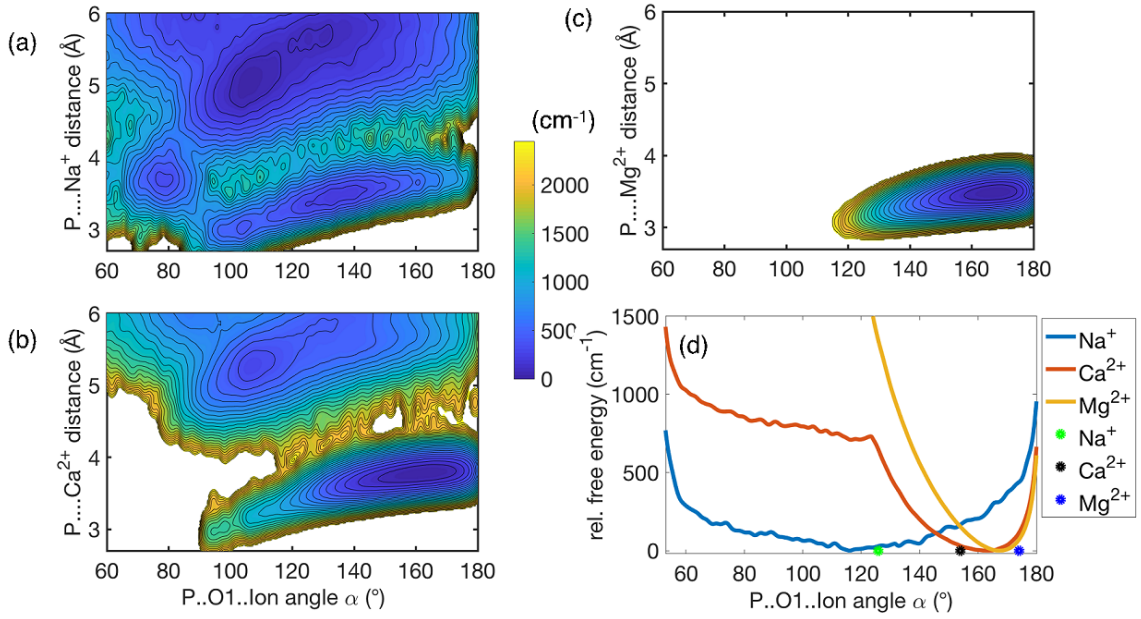

Figure 5.17: (a-c) 2D potential of mean force of DMP and, respectively, the three major cations along P-ion distance and the angular coordinate $\alpha = \measuredangle$ P-O_1...Ion. The PMF was obtained from MD simulations, white areas show unsampled configurations. (d) Angular dependence of the free energy, derived by locating the energy minimum for each α at distances $D < 4$Å. The singular data points indicate the angle of the minimal hydration geometries displayed in fig. 5.16.

Molecules are arranged either in *gg* or *gt* conformation with a surrounding fluctuating hydration shell.

The emergence of a vibrational band, blue-shifted from the original $\nu_{AS}(PO_2^-)$ has been traced by FTIR and 2D-IR spectroscopy, its dependency on ion concentration suggests an underlying interaction of the DMP molecule with the ion. The previously established sensitivity of (PO_2^-) vibrations on hydration (see sec. 2.2) points to an interaction within the first two to three hydration layers of the phosphate group. DFT calculations directly link the vibrational blue-shift to ions situated within the first hydration shell, forming a direct contact ion pair with the DMP molecule. The absence of off-diagonal elements in all measured 2D-IR spectra points to independent oscillators that do not interact on the 750 fs timescale of the experiment. Short-lived effects like energy exchange would be visible already on the timescales we work with. Chemical exchange, i.e. the breaking and rebonding of solvation geometries, particularly ion pairs, that would also induce such off-diagonal elements [132].

Mg^{2+} ions induce the strongest blue-shift ($50\,cm^{-1}$), a substantial shift is also observed for Ca^{2+} ($35\,cm^{-1}$). Monovalent ions cause a significantly weaker spectral shift, suggesting an underlying mechanism that highly depends on ion charge. DFT calculations show a dominant contribution of electrostatic and exchange repulsion interactions to the intermolecular interaction energies. The reduced distance between DMP^- and a cation in the second and

third shell leads to an increase in electrostatic interactions. Water molecules re-orient themselves along the strong electric field and increase the field strength. The simulations predict a red-shift that will be discussed momentarily. Upon breaching the first hydration layer, closing the distance between ion and DMP molecules further leads to exchange repulsion interactions on the basis of the Pauli exclusion principle. Fig. 5.15 shows the impact of this repulsion on the bonding potential: the induced asymmetry leads to the observed blue-shifted transition frequencies.

The ion-dependent behaviour can be understood by looking more closely at the geometries of the different CIPs. The minimal hydration CIP geometries in fig. 5.16 show that in the case of Mg^{2+} the phosphate oxygen O1 replaces one of the water molecules originally surrounding the Mg^{2+} ion. The rigid hydration structure around Mg^{2+} has been emphasized in section 2.1.2, the Mg^{2+}–P distance of 3.47 Å is smaller than the typical P..O_W distance in the first solvation shell evident in the radial distribution function of figure 5.13 (d(P-O_W) ≈3.8 Å). Interactions are therefore within the regime of exchange repulsion interactions (Mg..O1 distance ≈ 2.02 Å). The Mg^{2+} ion aligns almost linearly with respect to the P..O1 axis, the high rigidity of the system is reflected in the potential of mean force. Within the MD simulation time, the Mg^{2+} ion does not explore the configuration space outside of the CIP geometry, in line with the >µs residence time of first shell water molecules (cf. table 2.1). A second influence of the specific CIP geometry is found when analyzing the 2D-IR spectra. The smaller antidiagonal linewidth of the new mode is a sign of reduced fluctuations of water molecules surrounding these DMP/Mg^{2+} CIPs. The lineshape of the original band at 1220 cm^{-1} is conserved, underlining that the original vibrational mode is unaffected by the excess ions.

Ca^{2+} and Na^{+} show a higher degree of structural fluctuation around the PO_2^- moiety. The Ca^{2+} ion deviates from the almost linear geometry of the Mg^{2+}, the Na^{+} ion even embeds itself fully into the tetrahedral hydration geometry of the phosphate. Both ions are further away from the PO_2^- in the minimal geometry than Mg^{2+}, likely due to the less strict hydration structure surrounding both ions. The repulsive part of the interaction potential is probed to a lesser degree by the Ca^{2+} ion, so the blue-shift is smaller. For Na^{+} (and similarly K^{+}) the singular charge prevents as strong an electric field between the ion and the phosphate group. Frequency shifts in both directions are therefore significantly smaller, in fact only the blue-shift is distinct enough to be detected in IR spectroscopy.

The divalent ions Mg^{2+} and Ca^{2+} also perturb the relaxation mechanism of $\nu_{AS}(PO_2^-)$, leading to the observed longer lifetime of 500 fs for the new vibrational mode. Relaxation occurs via energy dissipation to lower energy modes of the phosphate group, such as bending vibrations. The shift of the vibrational frequency likely detunes the efficient resonance conditions that are responsible for the fast relaxation (300 fs) of pure DMP species.

In addition to the purely qualitative observation that the blue-shift occurs, the amplitude of the CIP band allows to draw quantitative conclusions on the population of CIPs. DMP-ion interactions are statistically distributed in first-, second-, and third-order hydration shell geometries. Pure DMP samples contain 0.2 M DMP^- and 0.2 M Na^{+}. A full hydration of the first shell requires 2.2 M H_2O, which is amply provided for by the ≈ 55 M concentration of H_2O molecules in pure water. The addition of cations requires 6 additional water molecules to solvate each ion's first hydration shell (8 for Ca^{2+}), as well as 6 water molecules for each

Cl^- anion. With up to 2 M salt concentrations used in the experiments, this adds up to 24 M of water molecules for the monovalent salts, 36 M for $MgCl_2$, and 40 M for $CaCl_2$. At these concentrations second hydration shells are bound to overlap and ions occupy positions at all levels of hydration, mimicking the distinction of CIPs and SSIPs observed in RNA hydration (see sec. 2.1.3).

A lower estimate for CIP concentration can be derived from the boundary condition that the absorbance purely due to DMP/ion complexes, as derived in eq. (5.2), must be greater than zero. The relative concentration of DMP/ion pairs is then 12% for Na^+, 6% for K^+, 20% for Ca^{2+}, and 18% for Mg^{2+}. An upper boundary can not be estimated by FTIR alone. Rather, we compare the frequency position of the CIP band from diagonal cuts through 2D-IR spectra with the increasingly red-shifted frequency maximum in absorption spectra of DMP/ion complexes $A_{complex}(\nu)$ upon tuning $c_{complex}$ (cf. fig. 5.3). This yields an upper concentration estimate of 30% for Ca^{2+} and 37% for Mg^{2+}. The blue-shifted contribution to the spectrum of DMP/Na^+ is too small to isolate its frequency position, so no upper estimate can be given in that regard.

The relative scaling parameter used in 2D Kubo analysis (cf. table 5.1) also gives concentration proportions under the assumption that the transition dipole moment μ is the same for all vibrational bands. From the spectrum of DMP in neat water the scaling factors indicate that 47% of DMP molecules are in *gt*, 53% in *gg* conformation. From the simulation with Mg^{2+}, 21% of all phosphate contributions come from the blue-shifted CIP mode, well within the estimated range.

The DFT calculations from fig. 5.13 predict not only a blue-shift of $\nu_{AS}(PO_2^-)$ once the counterion breaches the first hydration shell, but also a red-shift for the divalent ions Mg^{2+} and Ca^{2+} in the second and third hydration shell. This corresponds to a scenario where the strong electric field between PO_2^- and the ion polarizes the separating water molecules, increasing the field strength and consequently the field-dependent Stark shift of $\nu_{AS}(PO_2^-)$ to lower frequencies. In FTIR spectra this can be observed for DMP/Mg^{2+} complexes and to a lesser extent DMP/Ca^{2+} complexes. The amplitude of this SSIP band is smaller than the CIP band, even though a larger proportion of SSIP geometries is expected from the statistical considerations stated above. This lack of absorbance points to either a higher population of CIP states than expected, or to a reduced transition dipole moment for SSIPs. A reduced μ also explains the absence of red-shifted elements in the 2D-IR spectra, where the μ^4-dependency intrinsically filters out smaller contributions, like the librational water background. It is therefore the more likely scenario.

In conclusion, the data collected in this chapter show that the asymmetric phosphate stretch vibration is a reliable sensor for the formation of contact ion pairs via a blue-shift in vibrational frequency. The particularly rigid hydration shell of Mg^{2+} is responsible for a particularly strong response, which may be the origin of the special role Mg^{2+} ions play in biology.

6 RNA Melting

The previous chapter established the sensitivity of $\nu_{AS}(PO_2^-)$ to the direct ion environment. The aim of this thesis is to apply this technique to biologically relevant RNA molecules. The infrared spectrum of RNA molecules in the range of $\nu_{AS}(PO_2^-)$, however, reflects a complex solvation environment around the RNA that is not well understood, as explained in chapter 2. Since the phosphate vibration is so sensitive not only to ions in residence, but also to the water environment, any understanding of the ion problem requires a better understanding of the solvation structure in general.

The aim of this chapter is thus to discern hydration geometries present around solvated RNA and the extent to which they contribute to the IR spectrum. RNA disordering upon melting at high temperatures is used perturb the solvation structures prevailing at room temperature. Together with theoretical simulations this allows to track changes in the infrared spectrum and ultimately assign hydration geometries to spectral features.

In section 4.2.2 the structural changes accompanying dsRNA melting were discussed. Raising the temperature above the characteristic melting point $T_m \approx 328\,\mathrm{K}$ results in a separation of strands that significantly increases UV absorbance at 260 nm and transforms the spectral shape of circular dichroism spectra. As shown earlier, the phosphate vibration $\nu_{AS}(PO_2^-)$ can sensitively report changes in its environment. In this chapter, the extent to which the structural changes upon heating influence the phosphate environment will be examined. This will allow to more accurately describe the different contributions to the $\nu_{AS}(PO_2^-)$ band and, with the help of theory, to assign the different vibrational modes to specific hydration geometries present around the RNA backbone.

6.1 Phosphate Behaviour upon Heating

As a reference measurement, the model system DMP was dissolved in water and heated. This shows the influence of temperature on the phosphate mode itself. As shown in figure 6.1 heating of DMP results in an absorbance loss around $1190\,\mathrm{cm}^{-1}$ and a concomitant gain at $1222\,\mathrm{cm}^{-1}$. The relative amplitude of these changes is on the order of 10%. The steep gradient between minimum and maximum suggests a spectral overlap, that distorts the actual frequency positions. Two Gaussian functions were fitted to the difference spectrum to account for this, they yield frequency positions for the absorbance decrease at $1195\pm2\,\mathrm{cm}^{-1}$ and the absorbance increase at $1213\pm12\,\mathrm{cm}^{-1}$, for a frequency difference of $18\,\mathrm{cm}^{-1}$. The error is relatively high due to the strong overlap region.

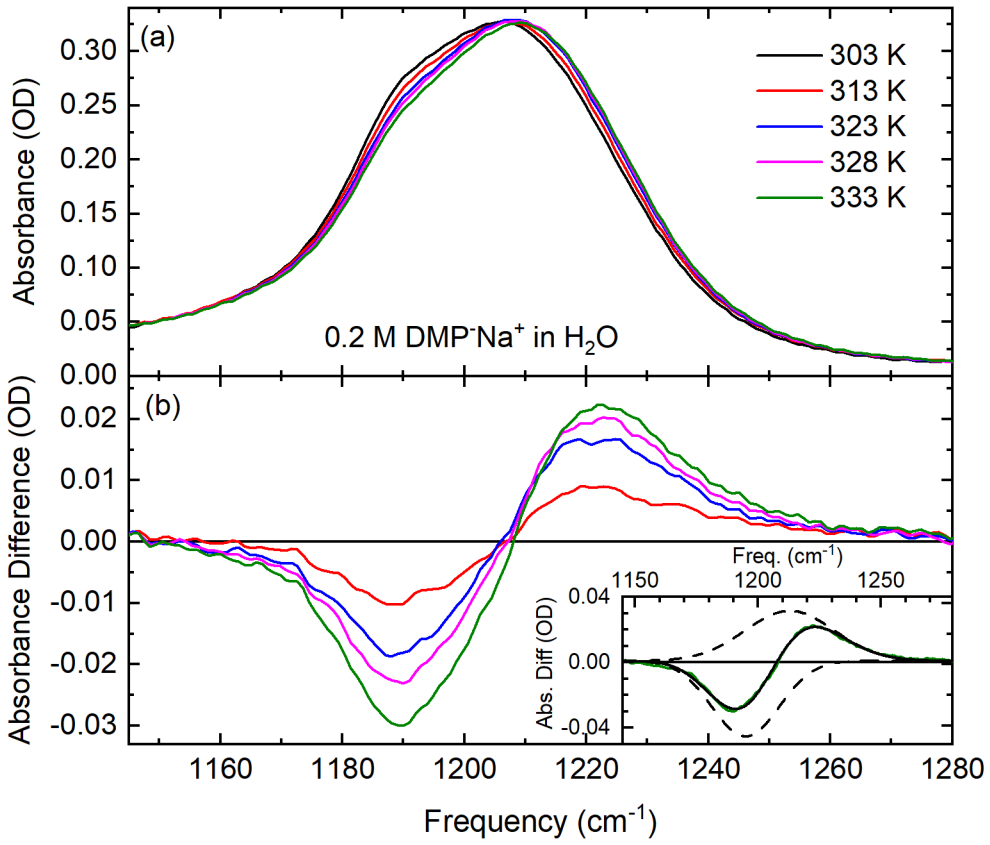

Figure 6.1: (a) FTIR spectra of 0.2 M Na^+DMP^- in water for temperatures ranging from 303 K to 333 K. (b) Differential FTIR spectra, where the absorbance at T=303 K is subtracted from all spectra in (a). Inset: Two Gaussian functions centered at 1195 and 1213 cm^{-1}, respectively, fit the difference spectrum to disclose the approximate shape of the individual contributions.

Two possible explanations present itself for the observed frequency shift. For one, this could be an indication for a population transfer from *gt* to *gg* conformers. Recent ab-initio calculations report vibrational frequencies of 1185 and 1215 cm^{-1} for *gt* and *gg* conformers, respectively [38].

A second possible explanation lies in the spatial rearrangement of the surrounding water molecules upon heating. From MD simulations Liu et al. have reported moderate spatial rearrangement of hydration waters from the first to the second solvation shell upon temperature increase [133]. This results in a redistribution of electric field amplitudes with electric field differences about 25 MV/cm. The amplitude change of ≈10% predicted in ref. [133] agrees well with the data presented here. Reported Stark shift parameters for the asymmetric phosphate stretch vibration range between 0.5 and 1.35 cm^{-1}/(MV/cm) [38, 104]. The frequency difference of 18 cm^{-1} would correspond to a Stark shift parameter of 0.72 cm^{-1}/(MV/cm), well within the range of parameters reported so far.

In all, the precise origin of the frequency shift is unclear, and will not be further discussed in this work. While a frequency shift due to rearranging water molecules would lead to a

similar signal change, an increase in *gg* conformer concentration at higher temperatures can not be fully excluded. Further thermodynamical calculations, that are beyond the scope of this work, would be necessary for further evidence. It is important however, to keep the frequency upshift in mind, when discussing spectral changes upon heating of RNA systems.

6.2 Vibrations of the RNA backbone

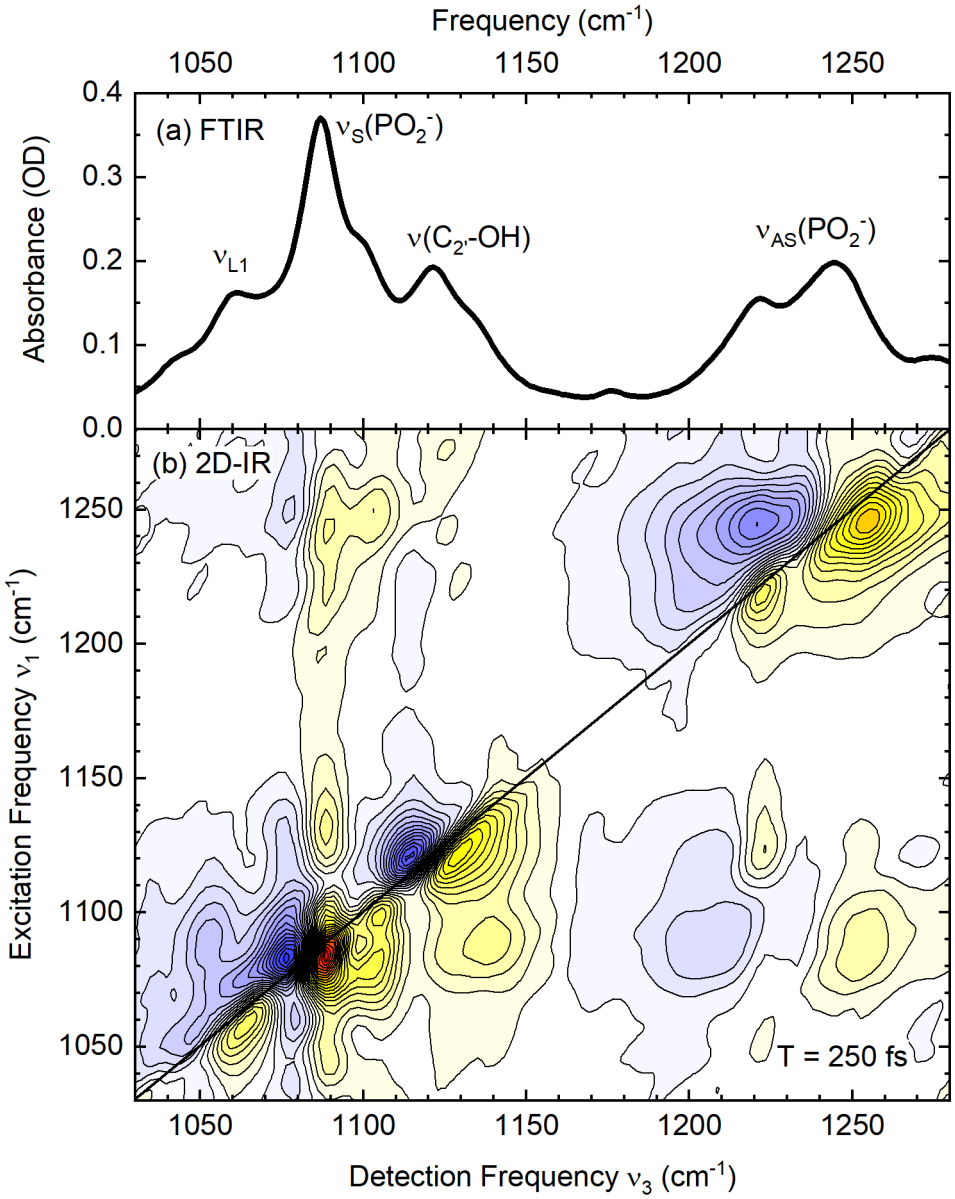

Figure 6.2: Vibrational spectra of dsAU-RNA in H_2O in the range of the phosphate stretch vibrations display the multitude of vibrational backbone modes. (a) FTIR absorption spectrum together with assignments of absorption maxima to phosphate stretch vibrations and C–O stretch vibrations. (b) 2D-IR spectrum showing the rich coupling pattern of the vibrational backbone modes at a waiting time T=250 fs.

We have talked about the backbone vibrations of RNA as carriers of energy transport within the RNA molecule, but also heavily involved in dissipation of energy from the RNA molecule to the solvent. Fig. 6.2 gives an idea of the various interactions taking place within the RNA backbone by displaying the steady-state IR absorption spectrum (a) and the 2D-IR spectrum (b) of dsRNA in water [14]. In the displayed range from 1030-1280 cm^{-1} we observe the dominant symmetric and asymmetric phosphate stretch vibrations $\nu_S(\mathrm{PO}_2^-)$ and $\nu_{AS}(\mathrm{PO}_2^-)$ at 1090 cm^{-1} and 1220-1250 cm^{-1}, respectively. Other backbone modes in this frequency region are C–O stretch vibrations either from the $\mathrm{C}_{2'}$-OH bond (1120 cm^{-1}) or from linker C-O groups that link phosphate groups and ribose rings (1060 cm^{-1}).

2D-IR spectroscopy allows to disentangle the convoluted linear spectrum. This resolves certain side shoulders as distinct vibrational modes, e.g. the peak at $(\nu_1, \nu_3) = (1100, 1105)\,\mathrm{cm}^{-1}$, that was assigned to a second C-O linker mode. The 2D-IR spectrum most prominently shows the rich coupling pattern, particularly involving the phosphate group vibrations. Coupling between $\nu_S(\mathrm{PO}_2^-)$ and $\nu_{AS}(\mathrm{PO}_2^-)$ results in cross-peaks at $(\nu_1, \nu_3) = (1240, 1100)\,\mathrm{cm}^{-1}$ and (1080,1250) cm^{-1}. The $\nu(C_{2'} - OH)$ vibration is also involved in coupling to both phosphate modes. Particularly interesting in the context if this thesis is the double-peak structure of $\nu_{AS}(\mathrm{PO}_2^-)$ at 1220/1250 cm^{-1}, that shows no intermode coupling between the two peaks. The peaks come from distinctly different phosphate sites in the RNA backbone, ref. [14] attributes the spectral separation to different local hydration geometries.

6.3 RNA behaviour upon heating

In light of these results we look at the behaviour of the $\nu_{AS}(\mathrm{PO}_2^-)$ vibration of dsRNA in water upon heating. FTIR spectra taken for different sample temperatures T_S are shown in figure 6.3. Heating the RNA sample leads to a substantial reshaping of the absorbance spectrum. At room temperature the spectrum displays three distinct peaks, centered at 1220, 1245, and 1278 cm^{-1}. These develop into a broad feature for temperatures T_S exceeding 338 K. This broad absorption band is centered around 1230 cm^{-1}, with a steep descent on the red flank and a longdrawn blue flank.

Difference spectra allow to assess the changes in more detail. In figure 6.3(b) difference spectra are computed by subtracting the FTIR spectrum at T_S=303 K from spectra at higher temperatures. The strongest decrease in absorbance is measured at 1250 cm^{-1}, with a second, significantly weaker decrease around 1282 cm^{-1}. These are accompanied by a broad absorbance increase around 1210 cm^{-1} and 1230 cm^{-1}, interrupted by a local minimum at 1220 cm^{-1}. Absorbance also increases slightly around 1265 cm^{-1}.

Insight in the ultrashort dynamics is gained from pump-probe spectra shown in fig. 6.4. The spectrum at T_S =303 K shows a strong positive absorbance change at 1210 cm^{-1} and a negative absorbance change at 1255 cm^{-1} separated by a convoluted central region (fig. 6.4(a)). The strong features are due to ESA of the 1220 cm^{-1} sidepeak and GSB&SE of the main peak at 1245 cm^{-1} (cf. FTIR spectra in fig. 6.3). The close spectral proximity of both these bands leads to an overlap of the GSB component of the 1220 cm^{-1} band and the ESA component of the 1245 cm^{-1} band, which makes the overlap region from 1210-1240 cm^{-1} difficult to interpret. Raising the sample temperature above the transition temperature T_m simplifies the appearance of the PP spectrum (fig. 6.4(b)). At T_S = 348 K the spectrum

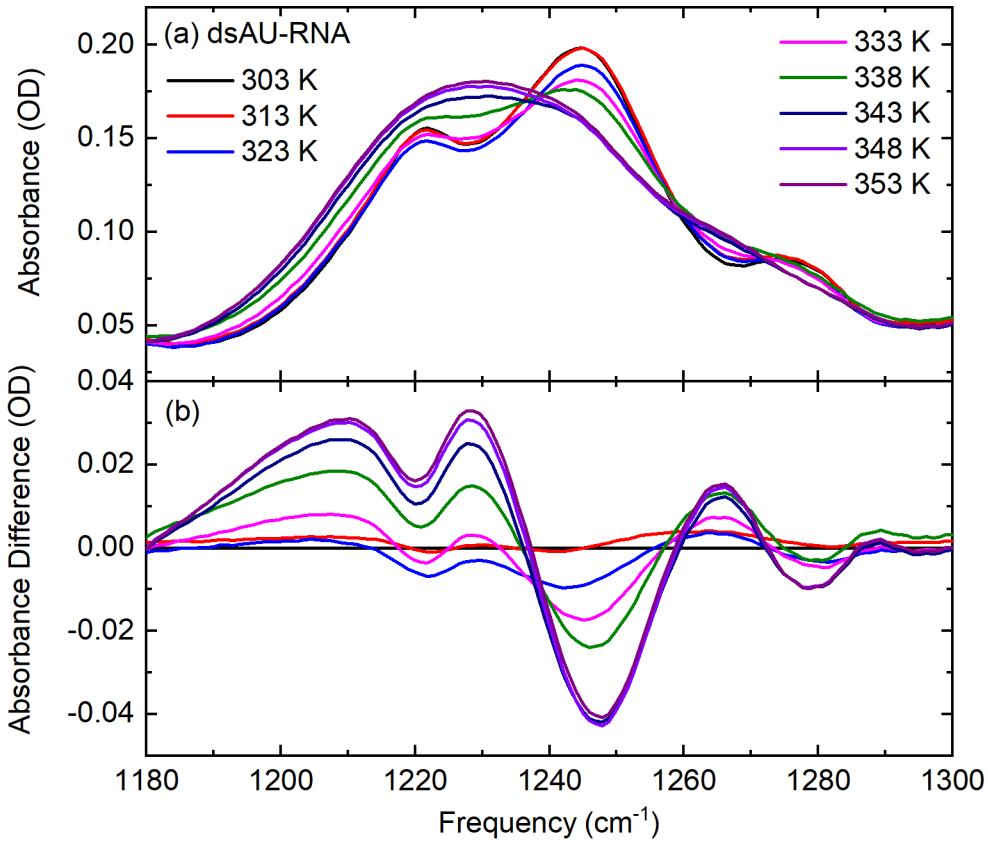

Figure 6.3: (a) Temperature-dependent FTIR spectra of 2.3 mM dsAU-RNA in water. With increasing temperature a shift in maximum absorption together with a general broadening is observed. (b) Absorbance difference spectra calculated by subtracting the absorbance at 303 K from the spectra in figure (a). Spectra show a strong decrease ($\approx$ 20%) at 1240 cm^{-1} together with a jagged increase in the range of 1170-1230 cm^{-1}.

consists of a positive absorbance change at 1200 cm^{-1} and a negative change at 1245 cm^{-1}.

Kinetic traces track the temperature dependence of the $\nu_{AS}(PO_2^-)$ vibrational lifetime. They are shown in fig. 6.4 (c) and (d) together with single-exponential fits. To avoid the overlap region, the traces were averaged over a 10 cm^{-1} region (1245-1255 cm^{-1} and 1195-1205 cm^{-1}, respectively), the single-exponential decay function is fitted for delay times $T \geq 300$ fs to avoid coherent artifacts from the sample windows (here: CaF_2). The fitted decay times were 370 and 350 fs for the ESA signal at 303 and 348 K, respectively, as well as 310 and 320 fs for the GSB&SE signal at 303 and 348 K, respectively. There is no evident dependence of the vibrational lifetime on temperature.

2D-IR spectra deconvolute the condensed overlap region by mapping the spectral response onto a two-dimensional plane. 2D-IR spectra of dsRNA at low and high sample temperature (T_S=303 and 348 K) in the frequency region of $\nu_{AS}(PO_2^-)$ are displayed in figure 6.5. The spectrum taken at room temperature shows three discernible peaks, similar to the FTIR spectrum. The strongest peak is centered around (ν_1, ν_3)=(1240,1250) cm^{-1}, two more peaks are centered around (ν_1, ν_3)=(1217,1222) cm^{-1} and (ν_1, ν_3)=(1280,1283) cm^{-1},

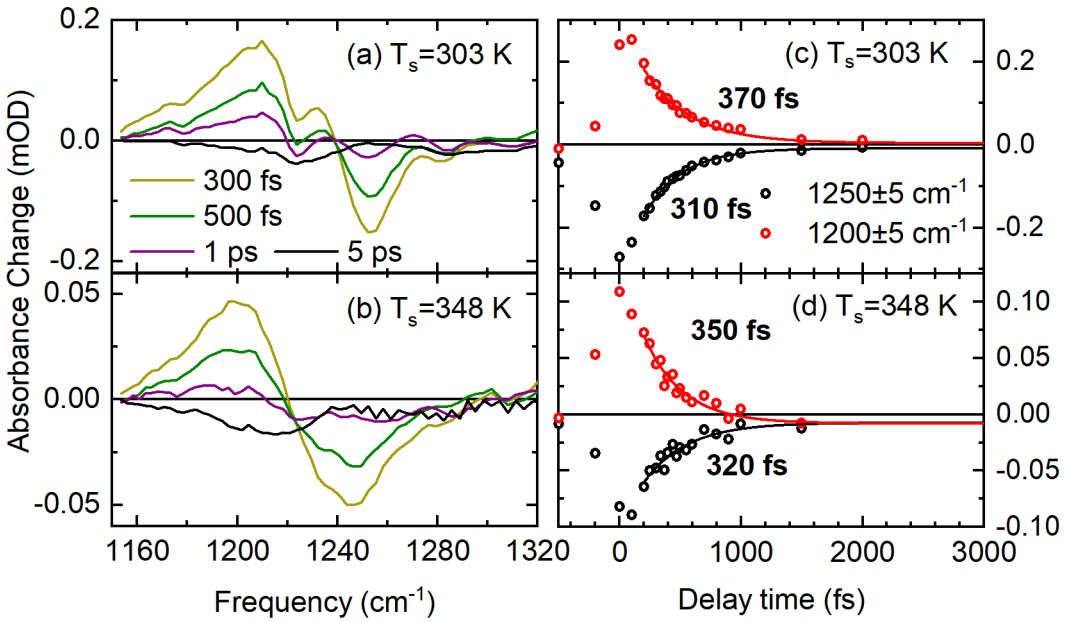

Figure 6.4: (a,b) Temperature-dependent pump-probe spectra of 4 mM dsAU-RNA in water in the range of the asymmetric phosphate stretch vibration $\nu_{AS}(PO_2^-)$. Positive contributions to the signal reflect excited state absorption (ESA) of the v=1→2 transition, negative signal shows ground-state bleach and stimulated emission (GSB& SE) on the v=0→1 transition (c,d) Temperature-dependent pump-probe signal as a function of delay time taken at maximum and minimum pump-probe signal. Data were averaged over a frequency window of 10 cm^{-1} and fitted with a single-exponential decay function. The decay time constant is indicated.

respectively. There are no discernible off-diagonal elements. Raising the temperature of the sample to T_S=348 K leads to a single, broad spectral feature elongated along the diagonal and centered around (ν_1, ν_3)=(1220,1220) cm^{-1}.
From the full spectrum it is difficult to clearly gather information on line shape and linewidths. To facilitate the analysis, cuts taken along diagonal and off-diagonal axes are displayed in figure 6.6, normalized to the absolute maximum of the respective 2D spectrum.

Diagonal cuts (figure 6.6(a)) are most sensitive to the inhomogeneous broadening of a vibrational mode. This usually reflects differences in the static environment of the molecule in question. In the case of dsRNA, cuts along the diagonal axis through the maximum of 2D signal at (ν_1, ν_3)=(1240,1250) cm^{-1} reflect the three-peak structure that is also present in the FTIR spectra of figure 6.3. The maximum of the signal is centered around ν_3=1250 cm^{-1}, with two broad shoulders at 1220 cm^{-1} and 1280 cm^{-1}, respectively. With increasing temperature the peak signal shifts to 1230 cm^{-1}, the shoulder at 1280 cm^{-1} disappears completely. The feature at high temperatures appears to have a larger spectral width due to a larger inhomogeneous broadening.

Antidiagonal cuts through the maximum of each spectral peak (figure 6.6(b)) in turn reflect the antidiagonal linewidth of the signal. It is determined mainly by fast fluctuations in the vicinity of the phosphate group. The dispersive nature of the antidiagonal cuts is

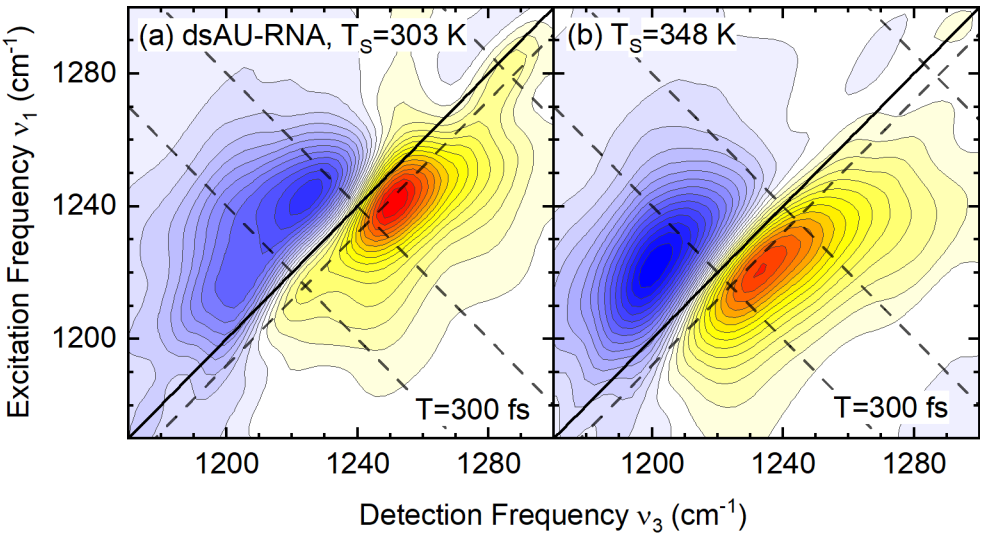

Figure 6.5: Experimental 2D-IR spectra of 4.6 mM dsAU-RNA in water at sample temperatures T_S = 303 K (a) and T_S = 348 K (b). Shown is the absorptive 2D signal normalized to the absolute maximum of the signal. Yellow-red contours represent signal due to ground-state bleach and stimulated emission on the v=0→1 transition, blue contours signalize excited state absorption on the v=1→2 transition. Neighboring contour lines are 7.5% apart. In both cases the waiting time was 300 fs. At room temperature the three-peak structure present in the FTIR spectra can be resolved. The maximum peak is centered at (ν_1, ν_3)=(1240,1250) cm^{-1}, with two side peaks at (1217,1222) cm^{-1} and (1280,1283) cm^{-1}. The absence of off-diagonal elements indicates that there is no coupling between the spectral elements. At 348 K, the spectrum consists of one broad peak centered at (ν_1, ν_3)=(1220,1220) cm^{-1}. Dashed lines indicate where cuts of the spectrum were taken for a more detailed look (figure 6.6).

due to the overlap of GSB&SE elements with ESA signal, an indication that the diagonal anharmonicity of the vibrational mode is small compared to the spectral linewidth.
The signal at 1241 cm^{-1} decreases by a small amount upon heating, a strong increase can be observed for the component at 1221 cm^{-1}. A significant broadening is evident for the 1241 cm^{-1} component, an indication of increasing fluctuations contributing to the linewidth. The 1283 cm^{-1} band disappears completely upon heating, in agreement with the diagonal cuts in (a).

A quantitative approach to 2D spectral analysis is possible using numerical density matrix simulations. As discussed in section 3.2.4, the absorptive 2D signal is calculated using a Kubo-Ansatz for the FFCF. In our case, the FFCF contains two exponentials (see eq. (3.13)), representing fluctuations on short (τ_1 = 300 fs) and long time scales (τ_2=50 ps), respectively. Fast fluctuations, such as water librations mostly affect the antidiagonal linewidth, whereas slow fluctations, due to structural differences, impact the broadening along the diagonal.

Simulated spectra for dsRNA at a waiting time T=300 fs are shown in figure 6.7 for T_S=303 K (a) and T_S=348 K (b). Simulated and experimental cuts taken along diagonal and anti-diagonal axes are shown in figure (c) and (d) to demonstrate the good agreement

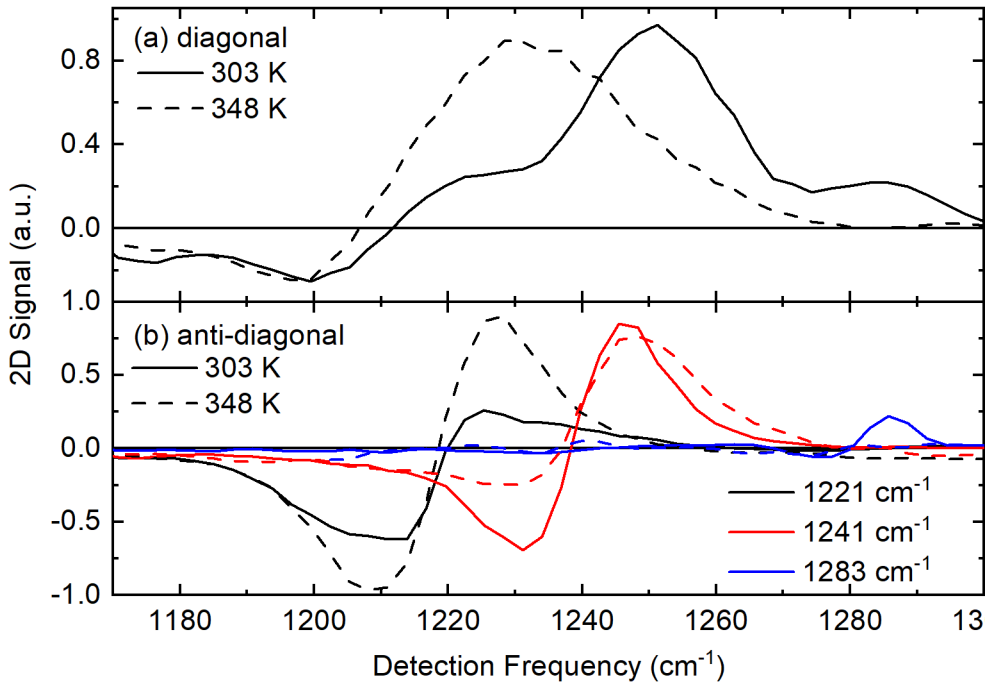

Figure 6.6: Cuts along the 2D spectra shown in figure 6.5 (solid lines: T_S=303 K, dashed lines T_S=348 K) (a) Cuts along the diagonal axis through (ν_1, ν_3)=(1240,1250) cm^{-1}. (b) Cuts along the anti-diagonal axis through (ν_1, ν_3)=(1221,1221) cm^{-1}, (1241,1241) cm^{-1}, and (1283,1283) cm^{-1}. All cuts were normalized with respect to the absolute maximum of the respective 2D spectrum. Clearly visible is the strong shift to lower frequencies with temperature.

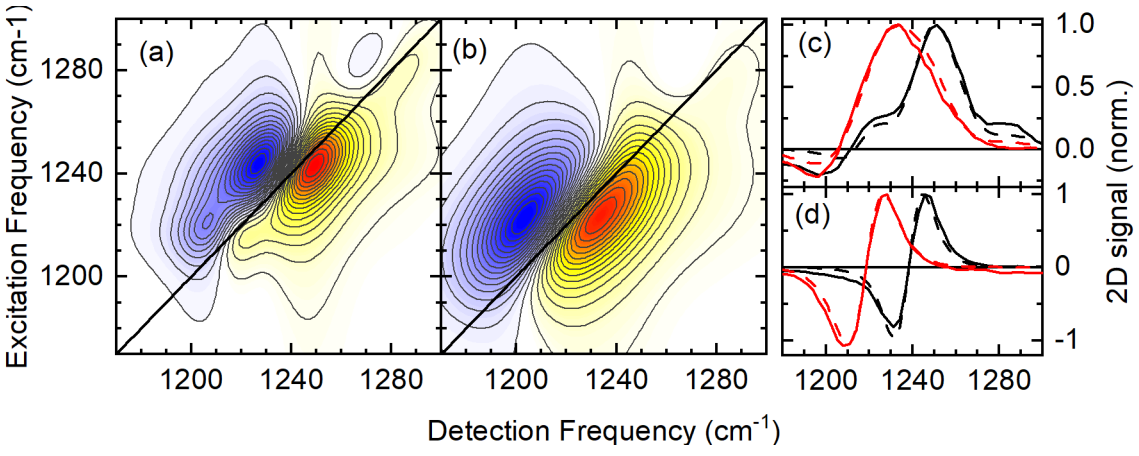

Figure 6.7: Simulated 2D spectra of dsAU-RNA for T_S=303 K (a) and T_S=348 K (b). Cuts through the 2D spectra (solid: experiment, dashed: simulation) show a good agreement with experimental spectra: (c) Cuts along the diagonal axis through (ν_1, ν_3)=(1240,1250) cm^{-1} (black: T_S=303 K, red: T_S=348 K. (d) Cuts along the anti-diagonal through (ν_1, ν_3)=(1221,1221) cm^{-1} (red, T_S=348 K) and (ν_1, ν_3)=(1241,1241) cm^{-1} (black, T_S=303 K)

with experimental results. The parameter set is provided in table 6.1. Most notable is the change in relative scaling with temperature, the ratio ν_1:ν_2 flips from ≈1:2 to 3:1. The fluctuation amplitudes show differing behaviour. The amplitude $\Delta\nu_1$ for fluctuations on a short time scale (τ_1=300 fs) increases by a factor of $\approx 2-3$ for all modes. Fluctuation amplitudes $\Delta\nu_2$ on the long timescale (τ_2=50 ps) are increasing by a factor of 2 for ν_1, but decreasing by a factor of 3 for ν_2, identical to the changes in relative scaling of the respective modes.

mode ν_i	relative scaling	frequency v=0→1	anharmonicity Δ	decay time T_{1i}	fluctuation amplitudes $\Delta\nu_{1i}$	$\Delta\nu_{2i}$
		cm^{-1}	cm^{-1}	fs	cm^{-1}	cm^{-1}
ν_1	43/100	1220	11	300	3.2/9.6	6.4/12.7
ν_2	100/36	1245	10/13	300	8.5/13.8	10.1/3.2
ν_3	22/10	1280	11/9	450	5.3/10.6	9.1/8.0

Table 6.1: Parameter set for 303/348 K as used in the numerical simulation of the 2D-IR spectra shown in figure 6.7.

It is of interest to compare the observed temperature-dependent frequency changes to absorbance changes of single-stranded RNA. Section 4.2.2 outlined that heating a single-stranded adenine RNA oligomer (ssA-RNA) is accompanied by a monotonous increase in UV absorption. This indicates a steady destacking of the bases with increasing temperature. The structural changes are expected to be less pronounced than the melting effect in dsAU-RNA.

The structural changes are reflected in the FTIR absorbance spectra displayed in figure6.8. The spectrum at room temperature is dominated by a peak at 1242 cm^{-1} with a side shoulder at ≈ 1220 cm^{-1}. With rising temperature the spectrum reforms into a single broad feature centered around 1230 cm^{-1}. The difference spectra (b) exhibit a similar behaviour to that of dsAU-RNA. A strong decrease in absorbance at 1245 cm^{-1} is flanked by increases at 1226 and 1270 cm^{-1}, respectively. The amplitude of the changes, however, is only on the order of 10 mOD, a factor of 2-3 lower than the absorbance differences for dsAU-RNA.

The 2D-IR spectra of ssA-RNA presented in fig. 6.9 also display spectral changes that are less pronounced than in the dsRNA case. The spectrum at 303 K shows a strong GSB&SE maximum at (1250,1240) cm^{-1} with an ESA contribution around (1220,1235) cm^{-1}. Both are highly elongated along the diagonal axis. The GSB peak shifts to (1245,1235) cm^{-1} at elevated temperatures, the ESA contribution to (1205,1225) cm^{-1}. Diagonal cuts are shown in fig. 6.9(c) and highlight the comparatively small frequency shift upon heating.

6.3.1 Theory and Discussion

Theoretical MD simulations in combination with QM/MM calculations were performed with the aim of understanding the origin of the frequency redshift. The results most relevant in the present context are summarized in fig. 6.10. MD simulations were run to map the 23-mer AU double helix and its hydration shell. The simulations show three charateristic types of hydration patterns, presented as snapshots in figure 6.10(a), that will be referred

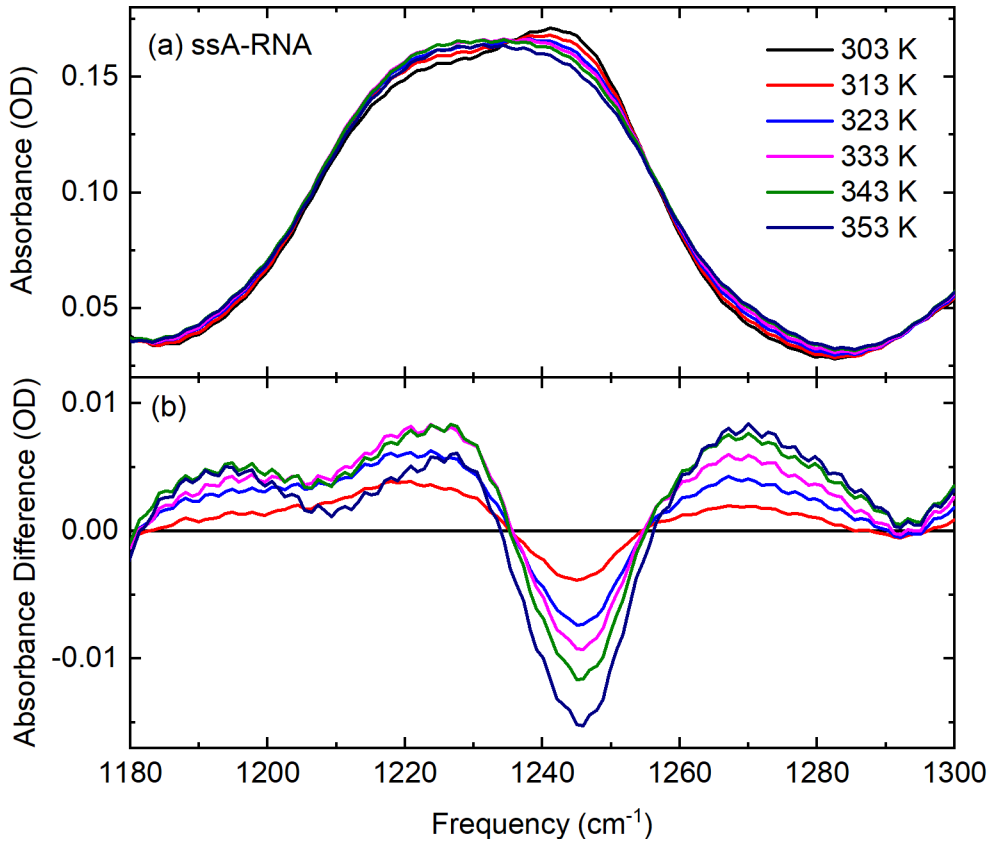

Figure 6.8: (a) Temperature-dependent FTIR spectra of 4 mM ssA-RNA in water. With increasing temperature a limited shift in maximum absorption together with a general broadening is observed. (b) Absorbance difference spectra calculated by subtracting the absorbance at room temperature from the spectra in figure (a). Spectral changes are on the order of 10% of the absolute absorption signal.

to as type-**A**/**B**/**C** hydration.

Characteristic for geometry **A** is a fully solvated hydration shell around the phosphate group. Six water molecules form a tetrahedral solvation shell around each of the two free oxygens. Geometry **B** on the other hand is characterized by an under-coordination of the phosphate group by water. Depicted is an overlap of hydration spheres between neighboring phosphates, a single water molecule bridges the comparably small phosphate-phosphate O...O distance. Type-**B** geometries are located mainly in the deep and narrow major groove and regions with particularly strict steric constraints. Type-**C** hydration is characterized by an Na^+ counterion in direct coordination with the phosphate group. It displaces one of the water molecules in the first hydration shell, leading to an undercoordinated solvation environment.

The visual difference in hydration manifests itself in a bimodal distribution of the mean number of phosphate oxygen – water hydrogen bonds (HB). Figure 6.10(c) disentangles this distribution along the lines of the hydration types introduced above. The maximum of the distribution for type-**A** hydration is at 5 HBs (4.82 statistical average) and distinctly

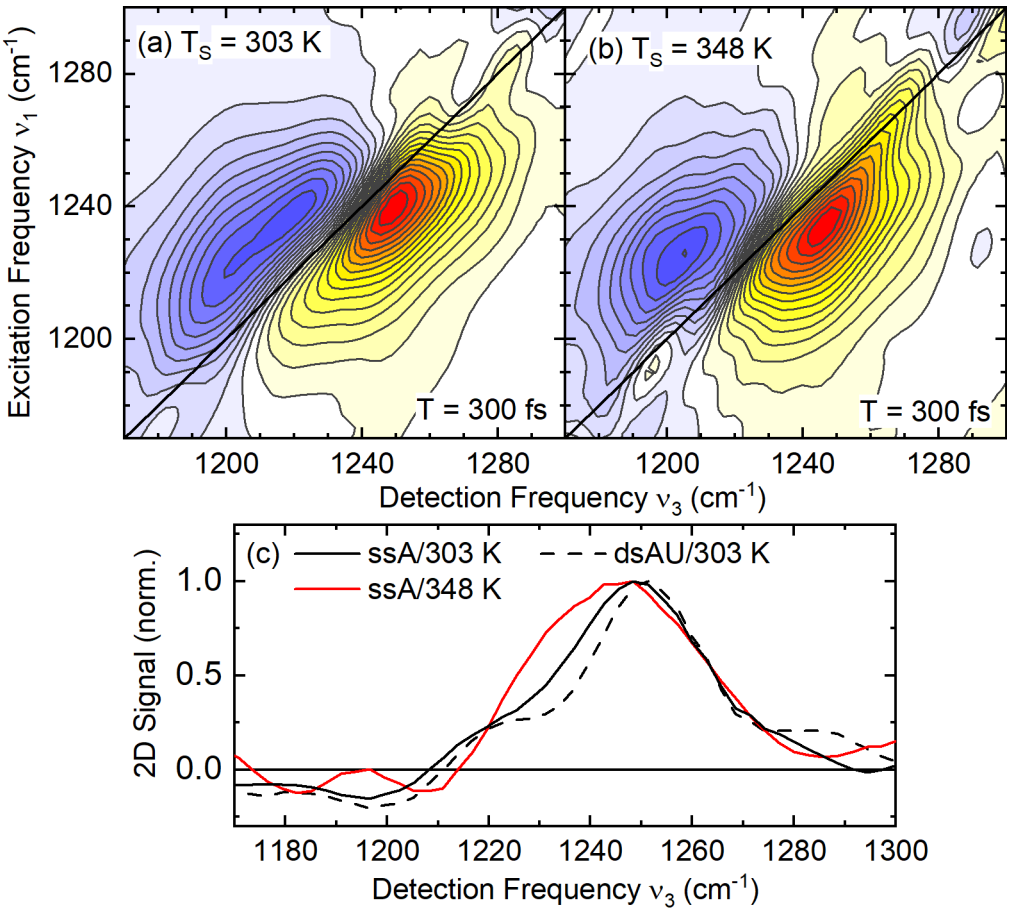

Figure 6.9: Absorptive 2D-IR spectra of 8 mM ssA-RNA in water at sample temperatures T_S = 303 K (a) and T_S = 348 K (b). (c) Diagonal cuts through the spectra at (1240,1250) cm^{-1}. normalized with respect to the absolute maximum of the respective 2D spectrum. The dashed line shows the diagonal cut through the spectrum of dsAU-RNA at 303 K for comparison.

less for **B** and **C** (on average 4.02).

The different hydration schemes are mapped to vibrational frequencies using QM/MM calculations (fig. 6.10(a)). Geometry **A** (green) contributes mainly to vibrational absorption along 1220 cm^{-1}, the vibrational mode at 1245 cm^{-1} has contributions of both **B**- and **C**-type solvation (blue and orange, respectively). Higher frequency absorption is linked only to **C**-type hydration.

The theoretical assignment of vibrational frequencies to hydration geometries now helps to understand the spectral signature observed upon RNA melting. FTIR spectra of dsRNA show a decrease in absorbance at 1250 cm^{-1} and a concomitant increase at 1220 cm^{-1}. The absence of cross peaks in the 2D-IR spectra distinguishes the vibrational modes as independent oscillators at different RNA sites. The changes of the FTIR and 2D-IR spectra with increasing T_S show a decrease in the number of type **B** geometries as sterical constraints are lifted upon strand separation. Accordingly, the number of phosphate sites with

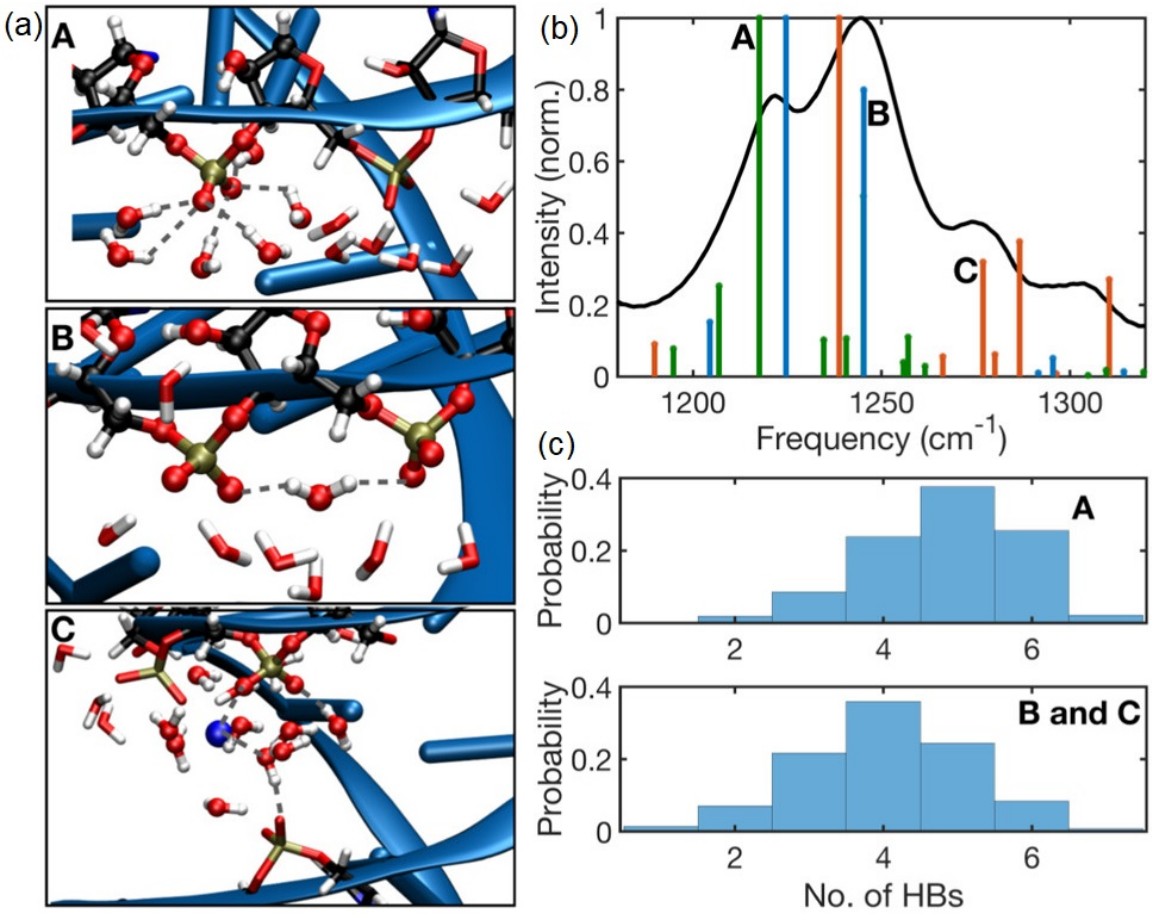

Figure 6.10: Results of MD simulations in combination with QM/MM calculations establish different hydration geometries as source of distinct $\nu_{AS}(PO_2^-)$ modes. (a) Stereotypical hydration geometries found in MD simulations of 23-mer dsAU-RNA. **A**-type hydration consists of six water molecules solvating the free phosphate oxygens in a tetrahedral arrangement. **B**-type hydration is characterized by an under-coordination of water molecules, due to sterical constraints set by the RNA molecule. The relatively small phosphate-phosphate distance allows individual water molecules to bridge the gap and act as linkers. **C**-type hydration has a positively charged counterion (blue) in direct vicinity of the phosphate group, also resulting in an under-solvated environment. (b) Stick representation of simulated IR absorption spectra in the range of the asymmetric phosphate stretch vibration from QM/MM calculations, contributions from the different hydration geometries are color-coded (green: **A**-type; blue: **B**-type; orange: **C**-type). The black spectrum gives the experimental spectrum of dsAU-RNA at room temperature as a reference. (c) Probability of hydrogen bond formation depending on geometry, taken from snapshots of MD simulations.

a full hydration shell (type **A**) increases. The results of the analysis of the 2D-IR spectra (table 6.1) allow to estimate the extent of the transfer: at room temperature the majority of phosphate groups (≈60%) contribute to **B**-type mode ν_2 at 1245 cm^{-1}, 25% to **A**-type absorption at $\nu_1 = 1220\,cm^{-1}$. At 348 K the contributions, and with it the relative concentrations of solvation geometries have shifted towards a full hydration shell (25% vs. 68%). This proportional change is also reflected in the transformation of the inhomogeneous fluctuation amplitude.

The pronounced structural rearrangement of the RNA double helix upon heating governs the relative abundance of hydration geometries. Raising the temperature above the melting temperature results in a separation of the two strands, together with a more continuous destacking of bases. This increases phosphate-phosphate distances, reducing the sterical constraints present in **B**-type geometries. Water molecules are able to reach the phosphate oxygens, so that the full hydration of the phosphate groups predominates the solvation structure at elevated temperatures.

The experimental data of single-stranded RNA underline these observations. ssA-RNA exhibits a stronger 1220 cm^{-1} side shoulder already at room temperature. It forms a single helix, as can be seen from CD measurements, but is characterized by P...P distances longer than in the double helix. Therefore, already at room temperature more phosphate groups are solvated in a full tetrahedral arrangement. Heating results in a steady destacking of bases without particular restructuring (see also the melting curves in fig. 4.2). The resultant changes both in FTIR and 2D-IR spectra are expectedly smaller.

The structural rearrangement of the double helix provides the macroscopic explanation for the observed frequency shifts. What is their underlying microscopic origin? Similar frequency shifts of $\nu_{AS}(PO_2^-)$ in DNA systems upon increasing hydration have been reported in [36, 43] and were attributed to electric fields stemming from water molecules in the first two to three hydration layers. The observed frequency shift was due to a Stark shift under electric field strengths of ≈ 50 MV/cm with a Stark shift parameter of 0.5 cm^{-1}/(MV/cm). MD simulations of dsRNA found electric fields from the water molecules of fully solvated DNA on the order of 80-150 MV/cm [134], shown in fig. 6.11 (red bars). However, the decisive part for the Stark effect was determined to be the projected electric field on the bisector axis of the O1...P...O2 phosphate group (blue bars). This is greatly reduced in RNA due to the steric constraints particular in groove regions. The difference in electric field strengths between underhydrated geometries and fully hydrated geometries amounts to ≈ 50 MV/cm, explaining the frequency difference of 25 cm^{-1} we observe.

FTIR difference spectra of ssA-RNA display a blue-shift with a frequency difference of $\Delta\nu \approx 25\,cm^{-1}$ in addition to the red-shift due to the transformation of the phosphate hydration shell. This blue-shift is in line with the observations of heated DMP systems in section 6.1. There, the shift was attributed to either a conformational preference for the *gg* conformer at higher temperatures or a structural rearrangement of the solvation shell waters.

Another solvent-induced effect can be seen in the homogeneous fluctuation amplitudes $\Delta\nu_1$ in table 6.1. They increase significantly upon heating, independent of the vibrational mode. These fluctuations occur on short time scales and are predominantly the librations of the surrounding water shell. As such, it comes as no surprise that a temperature increase in-

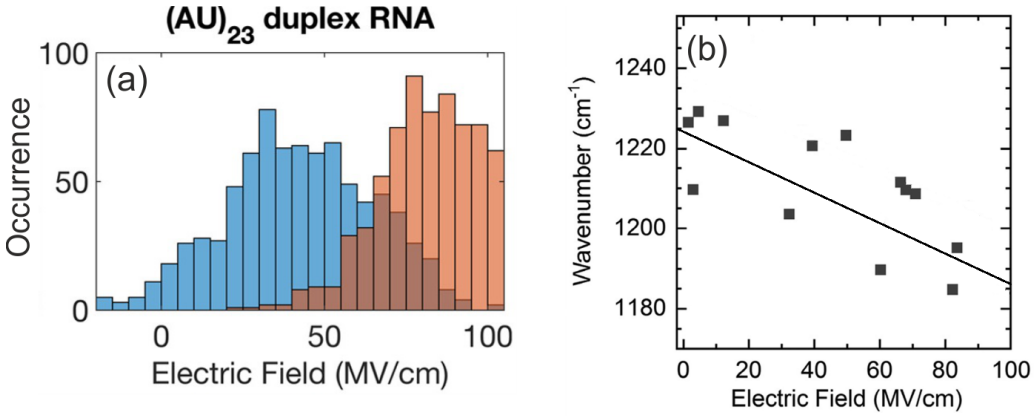

Figure 6.11: (a) Electric field strengths acting on the phosphate group. Red: Total electric field at the midpoint of the O1-P=O2 bisector . Blue: Projected electric field onto the O1-P=O2 bisector. (b) Dependence of the $\nu_{AS}(PO_2^-)$ vibrational frequency on the projected electric field from MD simulations. Frequencies were calculated using QM/MM calculations on the particular geometric arrangement responsible for the respective electric field. The solid line represents a slope of -0.38 cm^{-1}/(MV/cm).

duces stronger fluctuations.

One aspect that has not been discussed this far is the **C**-type hydration structure. It is characterized by an Na^+ counterion in the direct vicinity of the phosphate group and is predicted to be responsible for vibrational absorption at significantly blue-shifted frequencies. This blue-shifted absorbance is also observed in the counterion-dependent spectra of the DMP model system in chapter 5. The close proximity of ion and PO_2^- results in an under-hydrated phosphate group and strong exchange repulsion interactions that shift the $\nu_{AS}(PO_2^-)$ mode to higher frequencies. Its application to RNA systems is systematically investigated in the upcoming chapter. In the context of temperature-dependent experiments, we observe a decrease of this particular spectral signature, which indicates a reduced ion population in heated RNA samples. This effect has been described in ref. [135] to be a consequence of the reduced charge density upon heating. The corresponding lower electrostatic potential yields less counterions to condensate around the RNA.

In summary, this chapter investigated the hydration structures surrounding dsRNA phosphate groups. Using theoretical simulations, three major hydration geometries were established: Fully hydrated phosphate groups, phosphates with a reduced hydration coordination, and phosphates exposed to counterions. At room temperature phosphates with reduced coordination predominate, due to the steric constraints RNA geometry sets. Elevating the temperature rearranges the RNA helical structure. This leads to a distinct transformation from partially hydrated phosphate groups to full hydration, that can be followed using IR spectroscopy of the asymmetric phosphate stretch vibration.

7

Magnesium ion binding to RNA

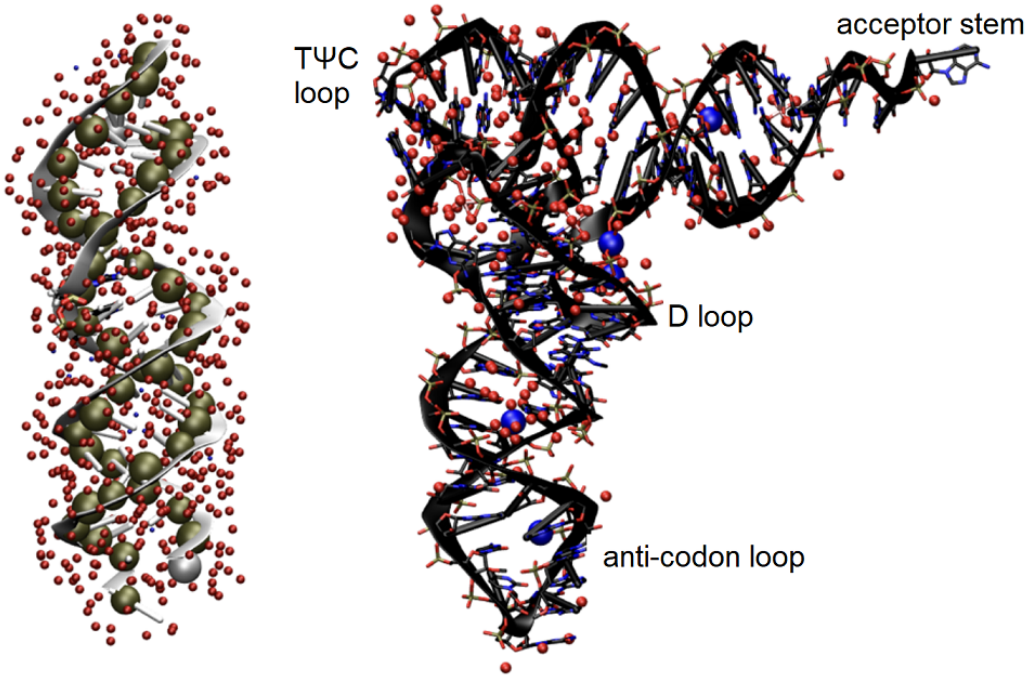

Figure 7.1: Tertiary structure of the RNA molecules used in the experiments. dsRNA (left) shows A-helix geometry stereotypical for helical RNA, tRNA (right) forms a complex functional structure.

After clearly assigning vibrational modes in the $\nu_{AS}(PO_2^-)$ region to specific hydration geometries of RNA phosphate groups, it is now possible to investigate the impact of Mg^{2+} ions on RNA. In this chapter, synthetical double-stranded RNA (dsRNA) and biologically relevant transfer RNA (tRNA) will be examined after adding controlled amounts of Mg^{2+} to an RNA aqueous solution. dsRNA with its helical structure is a good reference for the tRNA. Both molecules are shown in figure 7.1. tRNA forms a typical folded tertiary structure to fulfil its functional role of linking mRNA codons to their respective amino acid counterpart. The tRNA molecule contains regions with particularly high phosphate density, such as the D loop or the TΨC loop, as well as regions that more closely resemble the helical structure of dsRNA, such as the anti-codon loop. For our experiments we employed two different tRNA samples, as explained in section 4.2. Phenylalanine specific $tRNA^{phe}$ from yeast, as well as tRNA extracted from *E.coli* that represents a variety of different anti-codon sequences. All samples were dialyzed using the Mg^{2+} chelating agent EDTA to remove Mg^{2+}

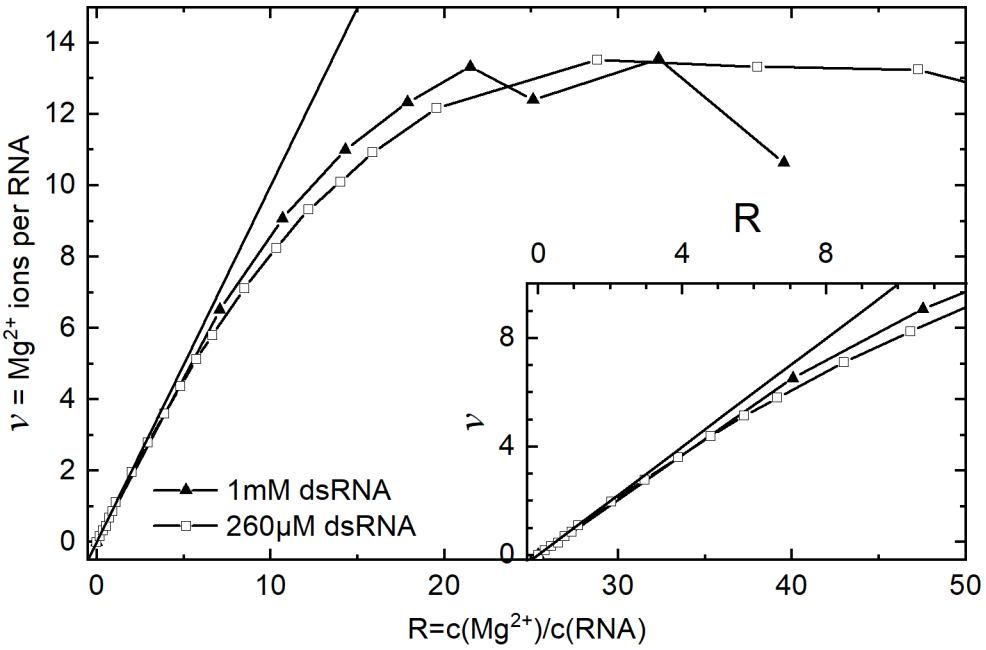

Figure 7.2: Mg^{2+} binding for double-stranded RNA at 1 mM (black triangles) and 260 µM (hollow squares) as determined by fluorescence titration measurements. The graph displays the average number v of Mg^{2+} ions bound per dsRNA molecule as a function of the added Mg^{2+} per RNA. The main graph captures the saturation behaviour of Mg^{2+} binding, whereas the inset focuses on the behaviour for R< 12. The solid line corresponds to full Mg^{2+} uptake, i.e. every Mg^{2+} ion added also interacts with the RNA sample.

ions initially present (cf. chapter 4). The thus treated tRNA molecules are characterized by a counterion environment consisting almost entirely of sodium ions, as revealed by ICP-OES measurements. Analytic methods allow to quantitatively evaluate Mg^{2+}-RNA interactions that can be interpreted with the help of theoretical simulations.

7.1 Experimental Results

It is helpful to quantify the ion atmosphere in the system at hand before focusing on ions in the more direct vicinity of the RNA sample. Figures 7.2 and 7.3 show the results of fluorescence titration measurements for dsRNA and tRNA, as explained in section 3.1. Briefly, $MgCl_2$ is added to a solution of RNA and 8-HQS. Binding to 8-HQS increases the measured fluorescence intensity, binding to RNA inhibits fluorescence. The method allows to quantify the number of Mg^{2+} ions associated with RNA, but can not specify whether the interactions occur in a direct binding geometry or via the diffuse ion atmosphere. The number of Mg^{2+} ions associated with the RNA molecule is plotted against the ratio R of their concentrations. This ratio R=c(Mg^{2+})/c(RNA) gives the amount of Mg^{2+} added per RNA and allows to compare experiments with different concentrations of RNA. The curve initially follows the solid line where every added Mg^{2+} interacts with RNA. Deviation from this behaviour sets in at around R≈3 for dsRNA, so that e.g. at R=10 only 8-9 of the added ions interact. Binding saturates at R≈20 reaching values of 14±2 Mg^{2+} ions per dsRNA molecule. In the case of tRNA, we see a dependence of Mg^{2+} binding on the tRNA sample used. $tRNA^{phe}$

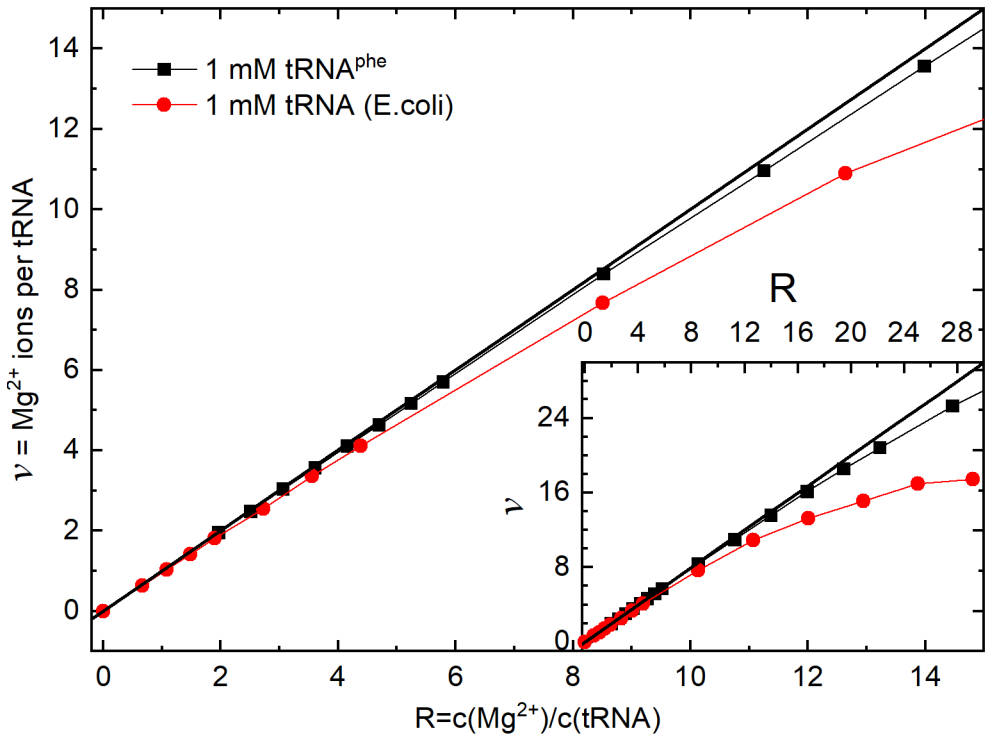

Figure 7.3: Mg^{2+} binding by dialyzed $tRNA^{phe}$ (black squares) and *E.coli* tRNA (red circles) as determined by fluorescence titration measurements. The graph displays the average number of Mg^{2+} ions bound per tRNA molecule as a function of the added Mg^{2+} per tRNA. The main graph focuses on the behaviour for R< 15, whereas the inset captures the differing saturation behaviour of the two tRNA samples. The solid line corresponds to full Mg^{2+} uptake, i.e. every Mg^{2+} ion added also interacts with the RNA sample.

follows the linear reference closely up to R=15 and deviates from it by ≈3 Mg^{2+} ions at R=28. In contrast, *E.coli* tRNA with different specificities deviates from the linear trend already at R≈4 and saturates at ≈18 Mg^{2+} ions per tRNA molecule.

It is important to emphasize that the RNA samples initially contain negligible amounts of Mg^{2+}. In the case of tRNA, Mg^{2+} ions in the supplied samples were removed using a dialysis procedure detailed in section 4.2.3 and replaced by Na^{+} ions. ICP-OES measurements confirmed that the dominant counterion before measurements was Na^{+} both in dsRNA and tRNA samples.

After quantifying general interactions of RNA with Mg^{2+} ions, infrared absorption experiments were performed over a range of Mg^{2+} concentrations. The aim is to discern the blue-shift characteristic for contact-ion pairs established in chapter 5 for DMP. Fig. 7.4(a) shows measured absorption spectra of dsRNA in the range of the asymmetric phosphate stretch vibration $\nu_{AS}(PO_2^-)$ for different values of R, figures 7.5 and 7.6 show spectra of $tRNA^{phe}$ and *E.coli* tRNA, respectively. All spectra show the previously noted double peak structure with absorption maxima at 1220 cm^{-1} and 1244 cm^{-1}. These peaks are characteristic for a fully hydrated and an undercoordinated solvation shell, as was shown in chapter 6 by observing a transformation of the spectrum upon melting of the double

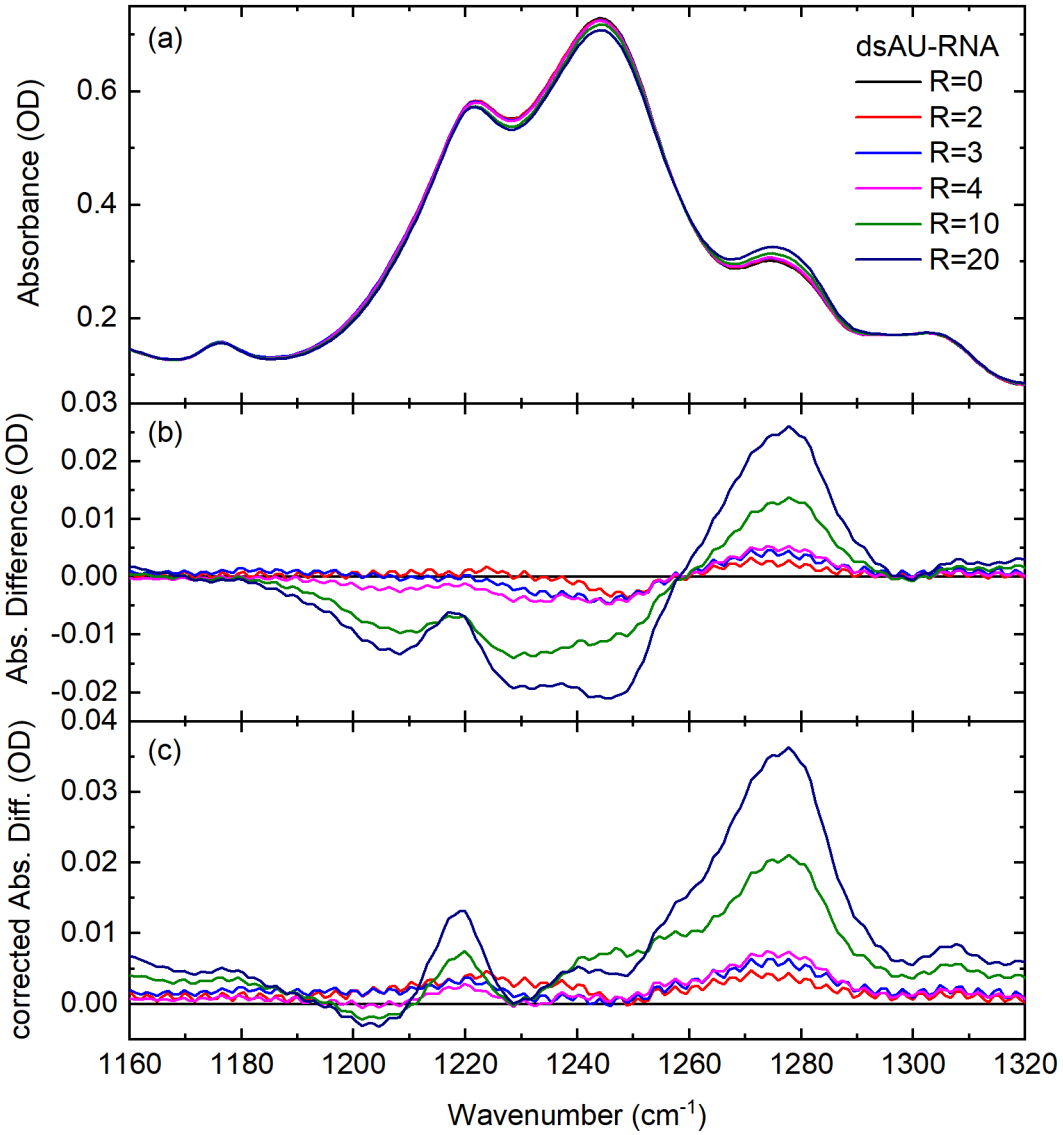

Figure 7.4: FTIR spectra of 6.9 mM dsAU-RNA in water with added $MgCl_2$. Mg^{2+} concentration is given in terms of the RNA concentration in the sample by the ratio R=c(Mg^{2+})/c(RNA). This parameter R is crucial to compare the wide ranges of RNA and Mg^{2+} concentrations used throughout. (a) Linear absorption spectra for R=0-20. Absorption from the librational water background (including the respective solvated $MgCl_2$) was subtracted for all spectra. (b) Difference spectra computed by subtracting the spectrum A(R=0) from all spectra in (a). (c) Absorbance difference spectra corrected to account for the loss of regular phosphate species according to equation (7.1). Thus, these difference spectra illustrate the absorption exclusively of backbone phosphate groups affected by the added Mg^{2+}.

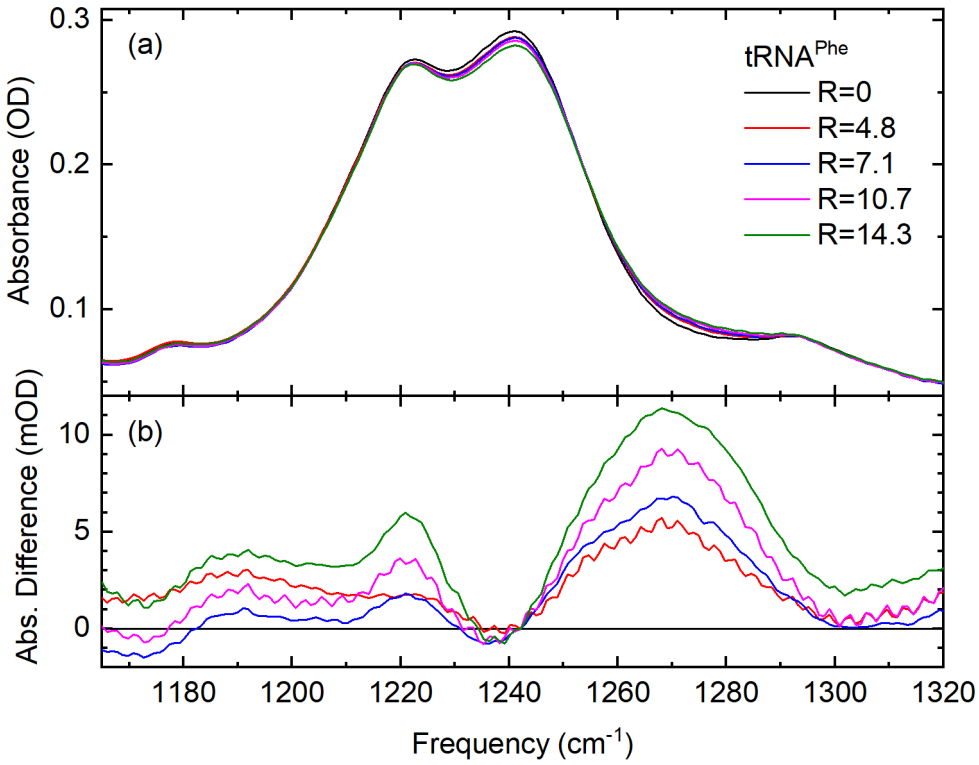

Figure 7.5: FTIR spectra of 4.2 mM $tRNA^{phe}$ in water with added $MgCl_2$. Mg^{2+} concentration is given in terms of the RNA concentration in the sample by the ratio R=c(Mg^{2+})/c(RNA). (a) Linear absorption spectra for R=0-14.3. Absorption from the librational water background (including the respective solvated $MgCl_2$) was subtracted for all spectra. (b) Absorbance difference spectra corrected to account for the loss of regular phosphate species according to equation (7.1).

helix. dsRNA shows an additional peak at 1278 cm^{-1} which was shown to be the result of an ion perturbed solvation shell. The side shoulder around 1300 cm^{-1} is in the range of N-H and C-N base vibrations. The absorption spectra show an increase in absorbance at 1277 cm^{-1} upon addition of Mg^{2+}. This is accompanied by a decrease in absorbance of the two dominant vibrational bands at 1220 and 1245 cm^{-1}. These absorption changes show up prominently in the difference spectrum given in fig. 7.4(b), where the absorbance spectrum at R=0 was subtracted from all spectra in (a). Figure 7.4(c) focuses on the absorbance of phosphates interacting with ions, similarly to the weighted difference spectra shown in fig. 5.3. These weighted difference spectra are calculated by subtracting a weighted spectrum of dsAU-RNA without added Mg^{2+} to reflect the depletion of the original phosphate species that does not interact with Mg^{2+} ions. This is done by factoring in a normalization term χ into the differential absorption

$$\Delta A(R,\nu) = A(R,\nu) - \chi \cdot A(R=0,\nu), \tag{7.1}$$

$$\text{with} \qquad \chi = \frac{A(R,\nu = 1245\text{cm}^{-1})}{A(R=0,\nu = 1245\text{cm}^{-1})}.$$

This normalization term takes into account the decrease in concentration of phosphate groups contributing to the major absorption band at 1245 cm^{-1}. This weighted absorbance

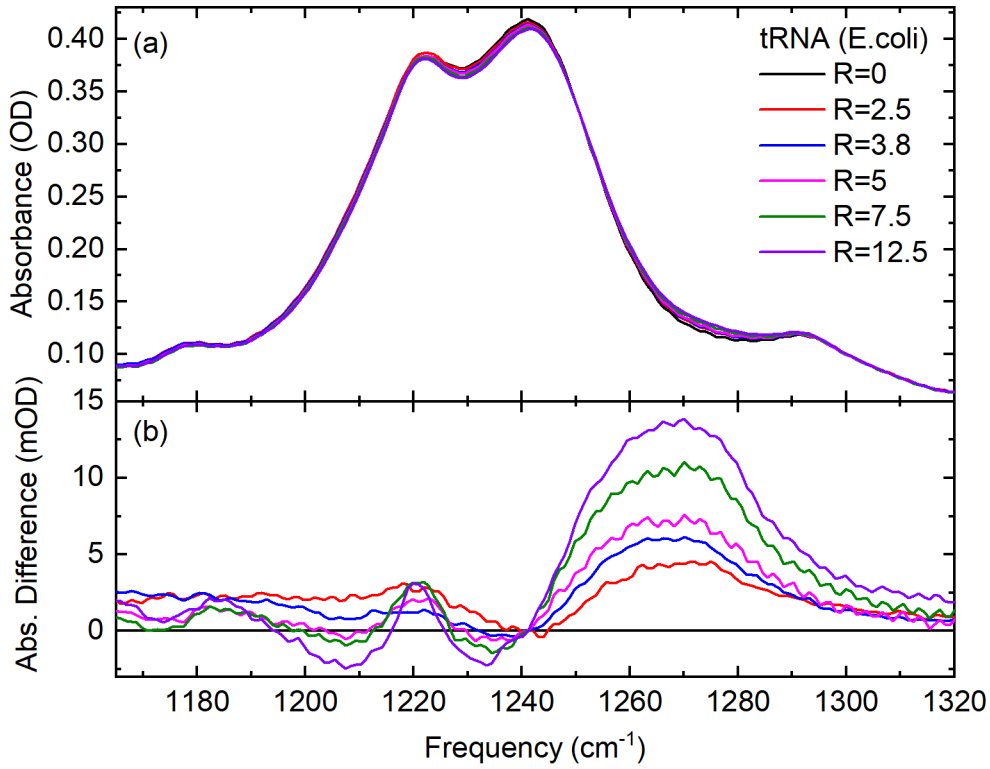

Figure 7.6: FTIR spectra of 4 mM *E.coli* tRNA in water with added $MgCl_2$. Mg^{2+} concentration is given in terms of the RNA concentration in the sample by the ratio R=c(Mg^{2+})/c(RNA). (a) Linear absorption spectra for R=0-12.5. Absorption from the librational water background (including the respective solvated $MgCl_2$) was subtracted for all spectra. (b) Absorbance difference spectra corrected to account for the loss of regular phosphate species according to eq.(7.1).

difference spectrum shows a maximum signal at 1277 cm^{-1}, with a weaker feature ($\approx 1/3$) around 1220 cm^{-1}. Weighted absorbance difference spectra for $tRNA^{phe}$ and *E.coli* tRNA are shown in fig. 7.5(b) and 7.6(b). They show the same qualitative behaviour, with the blue-shifted component centered around 1270 cm^{-1}. The maximum absorbance change for $tRNA^{phe}$ at R=14 amounts to 11 mOD, $\approx 4\%$ of the maximum absorbance at 1240 cm^{-1}. In the case of *E.coli* tRNA, the peak reaches 13 mOD at R=12.5, 3.3% of the maximum absorption.

A total of eight measurement series at various dsRNA/tRNA and Mg^{2+} concentrations were performed to investigate the systematic behaviour of the 1270 cm^{-1} band. Curves plotting the maximum of weighted absorption spectra against the Mg^{2+} concentration show a systematic increase of the 1270 cm^{-1} band upon addition of Mg^{2+}. Samples differ in RNA concentration by up to 20%, so data were normalized to the respective absorbance maximum at R=0 for each measurement series according to $\Delta A_{norm}(R,\nu) = \frac{\Delta A(R,1277\mathrm{cm}^{-1})}{A(R=0,\nu_{max})}$. ν_{max} denotes the peak position of $\nu_{AS}(PO_2^-)$ and is 1245 cm^{-1} for dsRNA samples and 1240 cm^{-1} for tRNA samples.

Such a curve for the two measurement series of dsRNA is plotted in fig.7.7, and in fig. 7.8

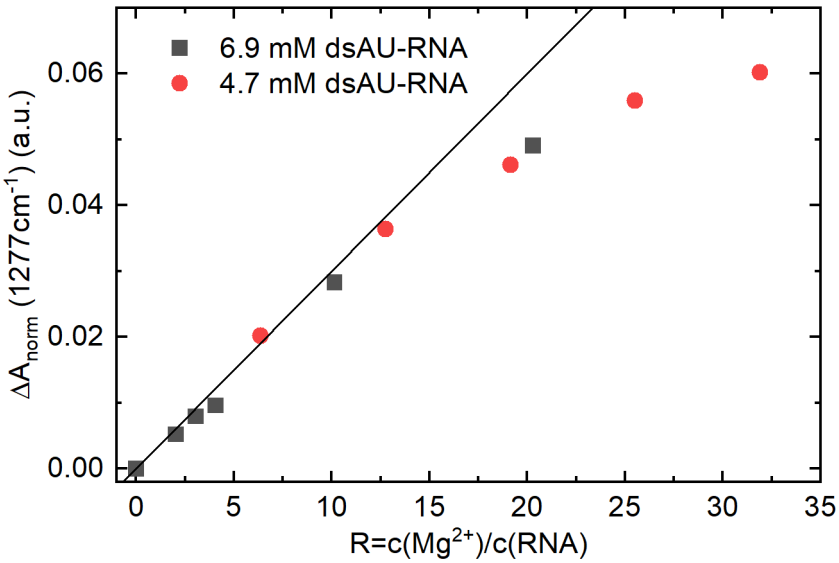

Figure 7.7: Normalized absorbance difference of the newly emergent $\nu_{AS}(PO_2^-)$ mode of dsAU-RNA at 1277 cm^{-1} as a function of R. Data of two measurement series are shown with differing RNA concentration and normalized to the respective absorbance maximum (1245 cm^{-1}) at R=0 for each series. The solid line is extrapolated from the data at R< 10 to illustrate the saturation behaviour.

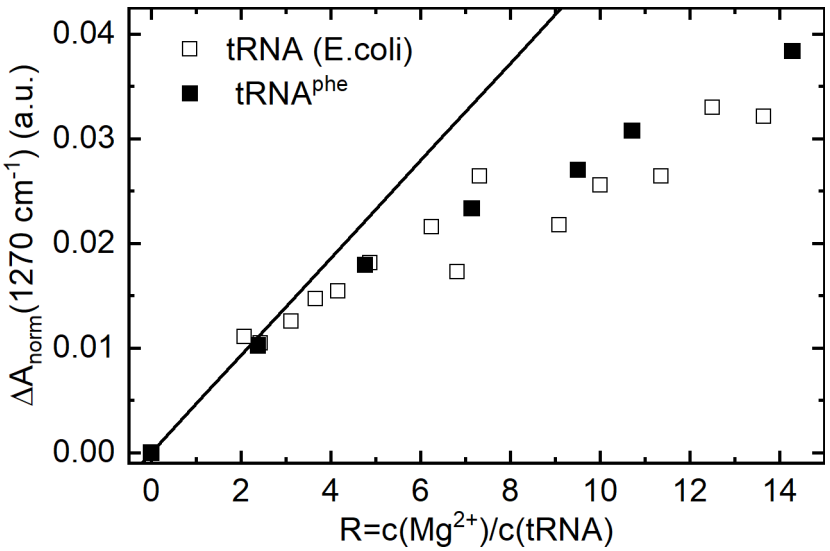

Figure 7.8: Normalized absorbance difference of the newly emergent $\nu_{AS}(PO_2^-)$ mode of $tRNA^{phe}$ (black squares) and *E.coli* tRNA (hollow squares) at 1270 cm^{-1} as a function of R. Data of six measurement series (four for *E.coli* tRNA, two for $tRNA^{phe}$) are shown normalized to the respective absorbance maximum (1240 cm^{-1}) at R=0 for each measurement series. The solid line is extrapolated from the data at R=2 to illustrate the saturation behaviour.

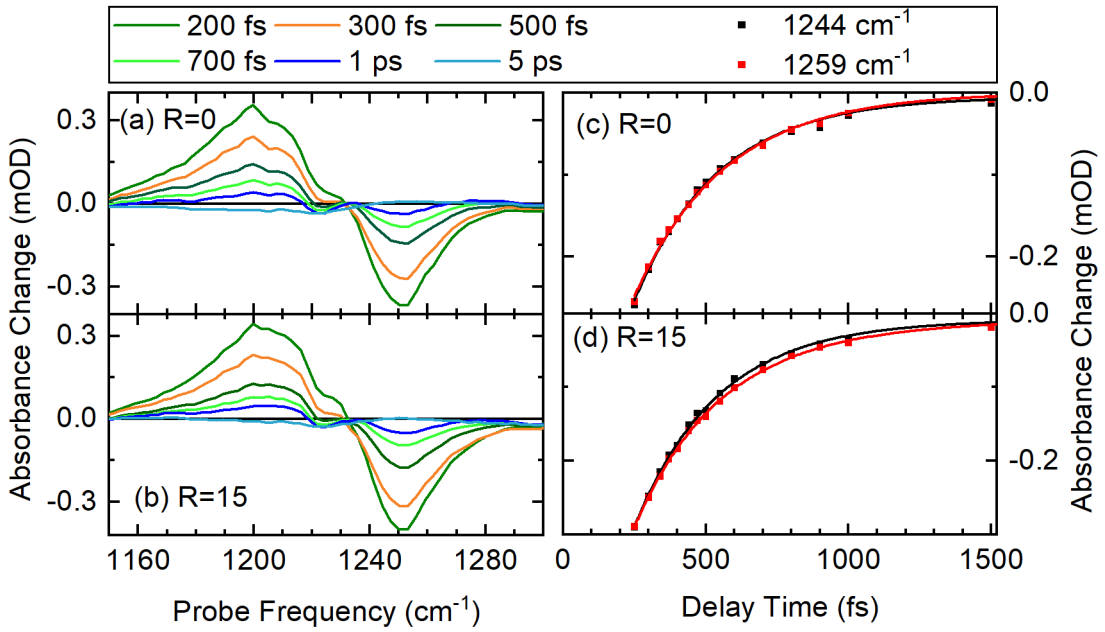

Figure 7.9: Pump-probe spectra of 4 mM $tRNA^{phe}$ in water for R=0 (a) and R=15 (b) show the absorbance change as a function of probe frequency. (c,d) Kinetic pump-probe traces taken at 1244 cm^{-1} and 1259 cm^{-1}, i.e. blue and red flank of the ground-state bleach signal, show the influence of the added Mg^{2+} as a slight increase in decay time. An exponential function was fitted to the data for $T \geq 250$ fs and yielded decay constants of 290 fs at 1244 cm^{-1}. At 1259 cm^{-1} the time constant was 290 fs as well, but an additional exponential component with t_2=700 fs was required to adequately fit the curve for R=15.

for all six tRNA measurements. The solid line is chosen to represent the approximately linear initial increase of the CIP band with Mg^{2+}. A saturation from this linear behaviour for dsRNA sets in at R≈12. At R=20, the additional CIP band amounts to 5% of the original absorbance maximum. Assuming a similar molar absorption coefficient ε, an initial quantitative estimate for CIP population is 1-2 contact ion pairs per RNA molecule.
The tRNA data show a steady increase that immediately deviates from the initial linear trend. In this behaviour tRNA differs from dsRNA. In contrast to the general uptake of Mg^{2+}, where the different tRNA samples showed different saturation behaviour, the emergent CIP band follows the same course for both $tRNA^{phe}$ and *E.coli* tRNA. At R=14 we reach relative absorbance differences of 4% for an initial estimate of 3 CIPs per tRNA.

Pump probe experiments with both tRNA species were performed to uncover lifetime dynamics of the different $\nu_{AS}(PO_2^-)$ modes, results are shown in figs. 7.9 and 7.10. Fig. 7.9 (a,b) displays the pump probe spectrum of $tRNA^{phe}$ without and with added Mg^{2+}. Both spectra show a positive absorbance change centered at 1190 cm^{-1} that reflects excited state absorption, as well as a negative absorbance change centered around 1250 cm^{-1} due to ground-state bleach and stimulated emission. The close spectral proximity makes it impossible to differentiate the two different contributions to $\nu_{AS}(PO_2^-)$ that have been established in chapter 6. It is also not possible to visibly discern an impact from the addition of Mg^{2+} in the region of the CIP peak ≈ 1270 cm^{-1}. However, kinetic traces taken at different frequency positions reveal deviating relaxation behaviour upon Mg^{2+} uptake. These traces are

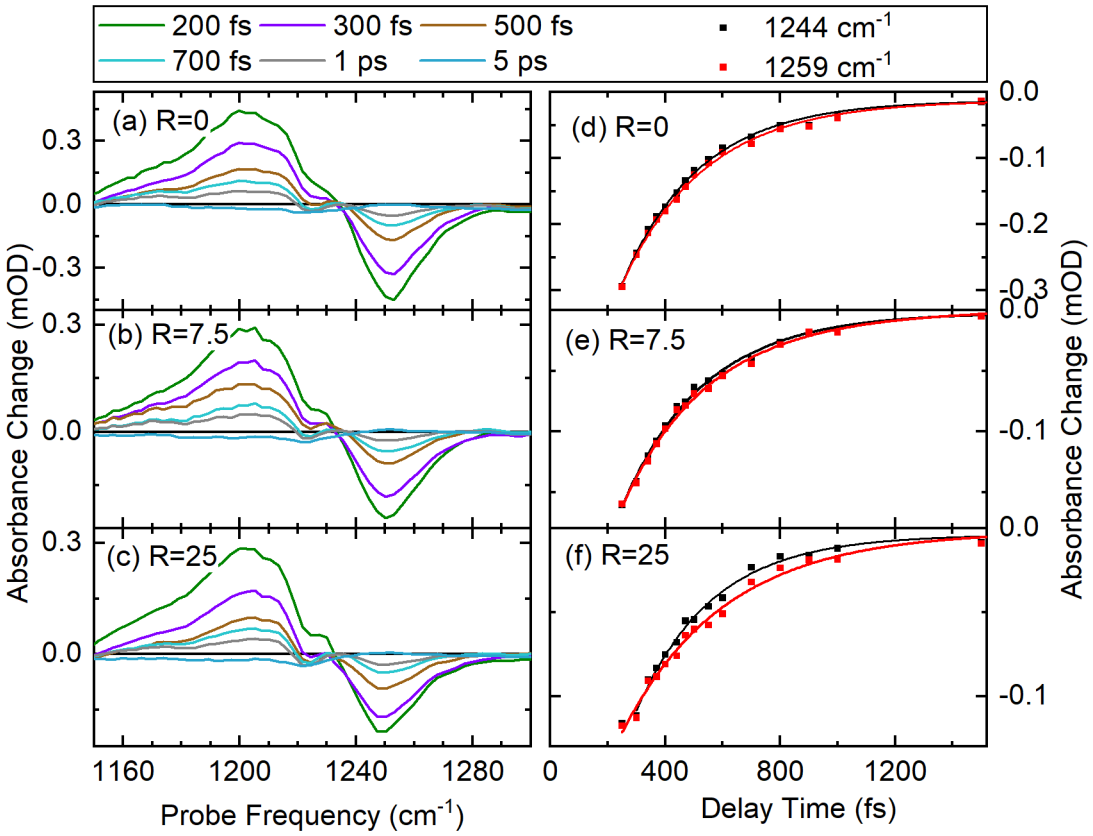

Figure 7.10: (a-c) Pump-probe spectra of 4 mM *E.coli* tRNA in water for R=0-25 show the absorbance change as a function of probe frequency. (d-f) Kinetic pump-probe traces taken at 1244 cm^{-1} and 1259 cm^{-1}, i.e. blue and red flank of the ground-state bleach signal, show the influence of the added Mg^{2+} as a slight increase in decay time. An exponential function was fitted to the data for $T \geq$250 fs and yielded decay constants of 290 fs at 1244 cm^{-1}. At 1259 cm^{-1}, single-exponential fits yielded time constants of 290, 315, and 360 fs for R=0, 7.5, and 25, respectively. This corresponded to a double-exponential decay with a primary decay time of t_1=290 fs and an additional exponential component with t_2=700 fs.

shown in fig. 7.9(c) and (d) and follow the delay-dependent absorbance change at 1244 cm^{-1} and 1259 cm^{-1}, i.e., the low- and high-frequency flank of the GSB signal, respectively. At R=0 both curves overlap, whereas at R=15 the curve at 1259 cm^{-1} shows a slowed decay. Data were fit to exponential functions, displayed as solid lines. Single-exponential functions with a time constant T =290 fs capture the decay for R=0, as well as the curve taken at 1244 cm^{-1} for R=15. The kinetic trace at 1259 cm^{-1} for R=15 was fitted using a double-exponential decay with time constants t_1 = 290 fs and t_2=700 fs.

This slowing down is more pronounced in pump-probe data of *E.coli* tRNA, fig. 7.10. Again, the pump-probe spectra show ESA, as well as GSB&SE of the spectrally overlapping $\nu_{AS}(PO_2^-)$ vibrational modes at 1200 cm^{-1} and 1250 cm^{-1}, respectively. The kinetic traces taken at 1244 cm^{-1} and 1259 cm^{-1} show different relaxation for the samples with added Mg^{2+}. Single-exponential fits reveal a stable time constant of $\approx$ 290 fs for the component at 1244 cm^{-1}. However the time constant of the 1259 cm^{-1} contribution increases with added

Mg^{2+}. Fits show single-exponential decay constants of 290, 315, and 360 fs for R=0, 7.5, and 25, respectively, all time constants carry an error of ≈30 fs both from measurement and fitting. As was the case for $tRNA^{phe}$, the kinetic trace at 1259 cm^{-1} can be similarly fitted using a double-exponential decay function with time constants t_1=290 fs and t_2=700 fs.

2D-IR spectra of RNA with and without added Mg^{2+} allow to disentangle the different contributions to the vibrational response. Figure 7.11 presents such spectra for dsAU-RNA. The absorptive 2D signal, i.e. the real part of rephasing and non-rephasing signal added up, is plotted as a function of detection frequency and excitation frequency. The spectrum reflects the three types of local hydration structure discussed in the previous chapter. The strongest vibrational GSB&SE signal at (ν_1, ν_3)=(1240,1250) cm^{-1} originates from phosphate groups with an underhydrated solvation shell due to the sterical constraints of the RNA molecule. The corresponding ESA signal is shifted to (1240,1225) cm^{-1}. The shoulder at (1217,1222) cm^{-1} reflects a second $\nu_{AS}(PO_2^-)$ mode from phosphate groups surrounded by a full hydration shell. The third peak in the 2D-IR spectrum at (1280,1283) cm^{-1} was attributed to phosphate groups with an ion perturbed solvation shell in chapter 6. Adding Mg^{2+} results in a change of the relative heights of the three peaks and a rearrangement of contour lines around (1285,1278) cm^{-1}. Diagonal cuts taken through the maximum of the GSB signal at (1240,1250) cm^{-1} show the increase of nonlinear signal around (1280,1280) cm^{-1} upon addition of Mg^{2+} more clearly and are displayed in fig. 7.12.

Absorptive 2D-IR spectra of $tRNA^{phe}$ are shown in fig. 7.13 for c(Mg^{2+})/c(tRNA) ratios up to R=15. The spectrum at R=0 shows two particularly strong features: a positive, yellow-red contoured signal centered at (1250,1240) cm^{-1} due to GSB&SE, and a negative, blue-contoured signal, shifted towards lower detection frequencies (1208,1230) cm^{-1}. This signal stems from ESA, and is blue-shifted due to the diagonal anharmonicity of the $\nu_{AS}(PO_2^-)$ vibrational mode. The diagonal anharmonicity also results in a steep overlap region along the $\nu_1 = \nu_3$ axis. Both major signals are elongated diagonally, with a certain asymmetry favoring lower frequencies. At higher frequencies, the signal appears compressed. A second, less pronounced feature is registered at (1295,1290) cm^{-1} as a yellowish peak, its ESA counterpart is centered at (1280,1285) cm^{-1}. Both components are elongated along the diagonal. The addition of Mg^{2+} to the tRNA results in the extension of the major peak towards higher frequencies. At R=7.5 the extension connects with the minor feature mentioned above. Further addition continuously increases the signal strength in the frequency region ≈(1275,1270) cm^{-1}, as can be seen in the contour lines adopting increasingly yellow shades. The red flank of the 2D-IR spectrum ≈(1225,1210) cm^{-1} does not react in any particular way to the addition of Mg^{2+}.
Cuts parallel to the diagonal are shown in fig. 7.14 and follow the emergence of the new band at $\nu_3 \approx 1289\,cm^{-1}$ via the development of a spectral shoulder. There is no shoulder around 1220 cm^{-1}, in contrast to the diagonal cuts of dsRNA. Generally, the behaviour around 1220 cm^{-1} is very irregular with added Mg^{2+} concentration.

2D-IR spectra of *E.coli* tRNA show a very similar behaviour, they are displayed in fig. 7.15. Spectra initially report a strong and a weak GSB&SE feature at (1250,1240) cm^{-1} and (1290,1285) cm^{-1}, respectively. They are complemented by ESA contributions at (1210,1230) cm^{-1} and (1275,1285) cm^{-1}. Addition of Mg^{2+} ions increases signal around (1280,1270) cm^{-1} that can be perceived as a weak shift in contour lines for R≤5.6 and manifests in a shoulder for R≥8.3. Again, the signal at lower frequencies appears to remain

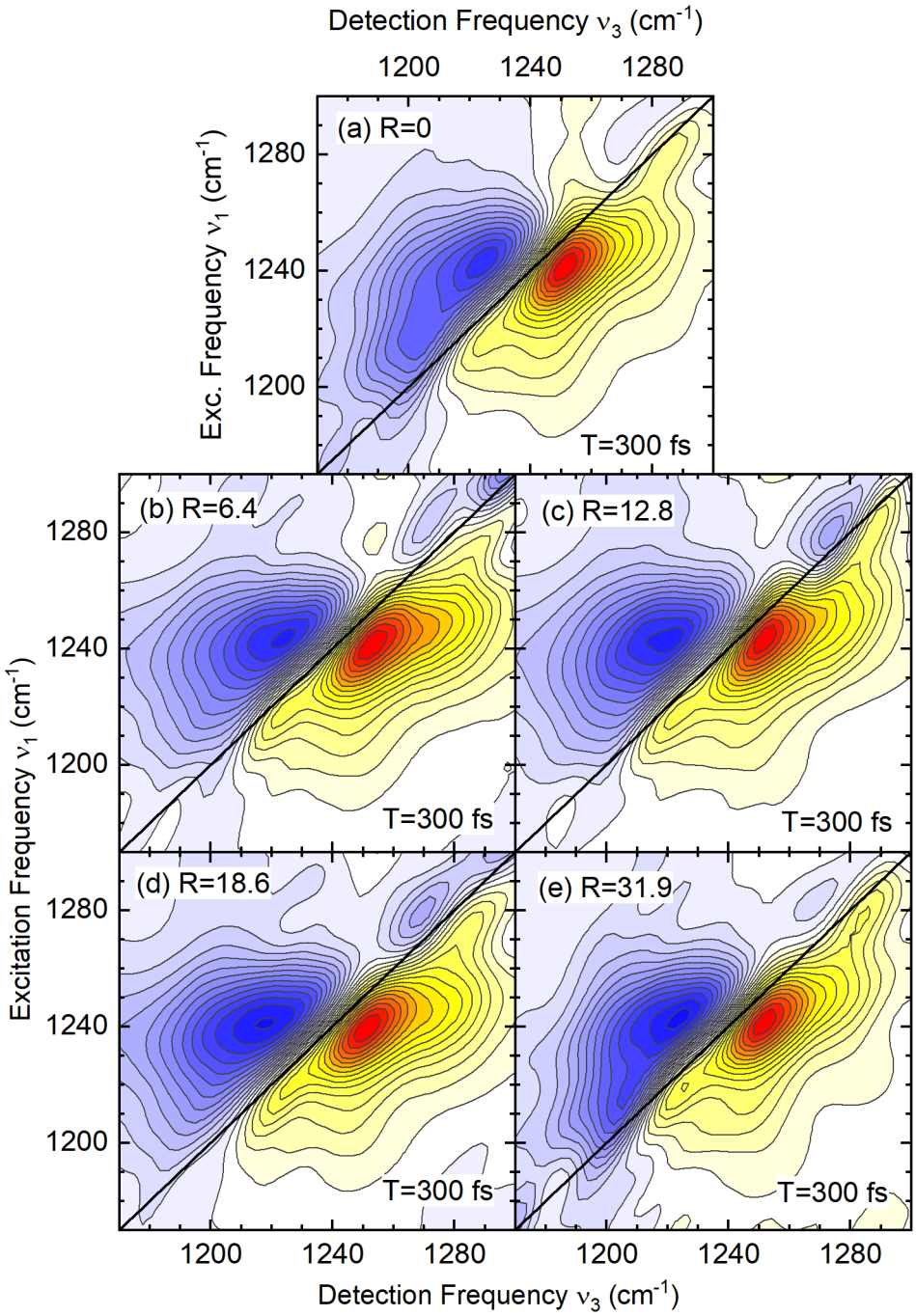

Figure 7.11: Experimental 2D-IR spectra of 4.7 mM dsAU-RNA in water for increasing Mg^{2+} concentrations, given here in terms of the total RNA concentration as R=c(Mg^{2+}/c(RNA)). The absorptive 2D signal is plotted as a function of excitation frequency ν_1 and detection frequency ν_3. Blue contour lines indicate signal due to ESA of the v=1 $\rightarrow$ 2 transition of $\nu_{AS}(PO_2^-)$, yellow-red contours show GSB&SE on the v=0 $\rightarrow$ 1 transition. Signal change between neighbouring contour lines is 7.5%.

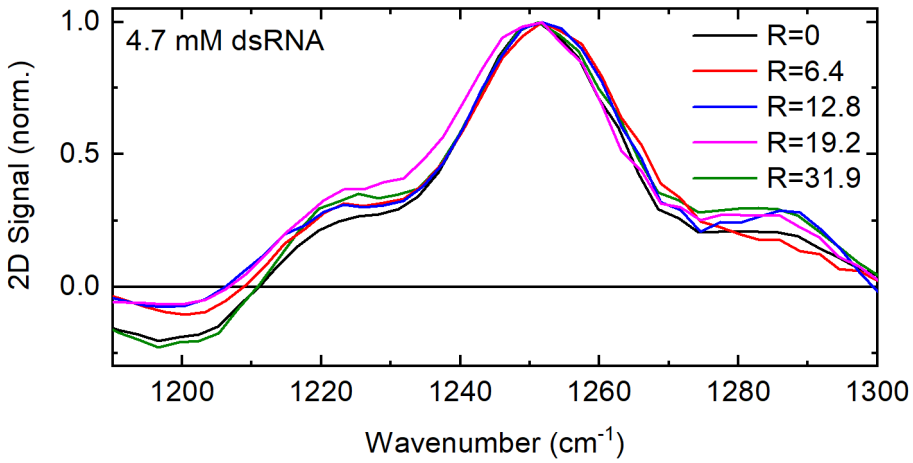

Figure 7.12: Diagonal cuts through the spectra of dsAU-RNA shown in figure 7.11 for the different Mg^{2+} concentrations. Cuts are taken parallel to the diagonal axis $\nu_1 = \nu_3$ and pass through (ν_1, ν_3)=(1240,1250) cm^{-1}.

unaffected. Cuts along the diagonal are presented in fig. 7.16 to underline these findings. The particularly elongated red flank forms a shoulder for all Mg^{2+} concentrations, the CIP mode increases the 2D signal around ν_3=1275 cm^{-1}.

The 2D Kubo simulations introduced in chapter 3 allow for a quantitative analysis of the experimental spectra. Figure 7.17(a-c) display the simulated spectra of dsAU-RNA together with anti-diagonal cuts (d-f). The cuts demonstrate the good agreement of simulation and experiment.

mode ν_i	relative scaling	frequency v=0→1	anharmonicity Δ	decay time T_{1i}	fluctuation amplitudes $\Delta\nu_{1i}$	$\Delta\nu_{2i}$
		cm^{-1}	cm^{-1}	fs	cm^{-1}	cm^{-1}
ν_1	43/44/39	1218	11/14/14	300	3.2/3.2/4.2	6.4/9/6.4
ν_2	100	1242.5	10/7/7	300	8.5/8.5/8	10.1/10.1/10.1
ν_3	0/13/15	1274	-/8/10	600	-/9.6/9.6	-/5.3/4.2
ν_4	22/21/17	1282	11/6.5/5	450	5.3/5.3/3.7	9.1/5.8/4.2

Table 7.1: Parameter set as used in the numerical simulation of the 2D-IR spectra of dsAU-RNA for R=0/19/32 shown in figure 7.17.

The parameters used in the simulation are given in Table 7.1. Four vibrational modes were considered for the simulations: ν_1 at 1220 cm^{-1} represents phosphate groups with fully coordinated hydration shell, ν_2 at 1242 cm^{-1} (1243 for *E.coli*) those with an under-coordinated shell, predominant in RNA. ν_3 at 1276 cm^{-1}(*E.coli*: 1269) represents the initially non-existent contribution to the spectrum due to Mg^{2+}-PO_2^- contact ion pairs, and ν_4 at 1290 cm^{-1} (*E.coli*: 1281) the initial signal observed in the 2D spectrum in the range of N-H base vibrations. The decay time of the first two modes is assumed to be 290 fs, that of the last two modes 700 fs (*E.coli*: 800 fs), in line with results from pump-probe measurements. Contributions to the Kubo lineshape come from a fast component τ_1=300 fs and a

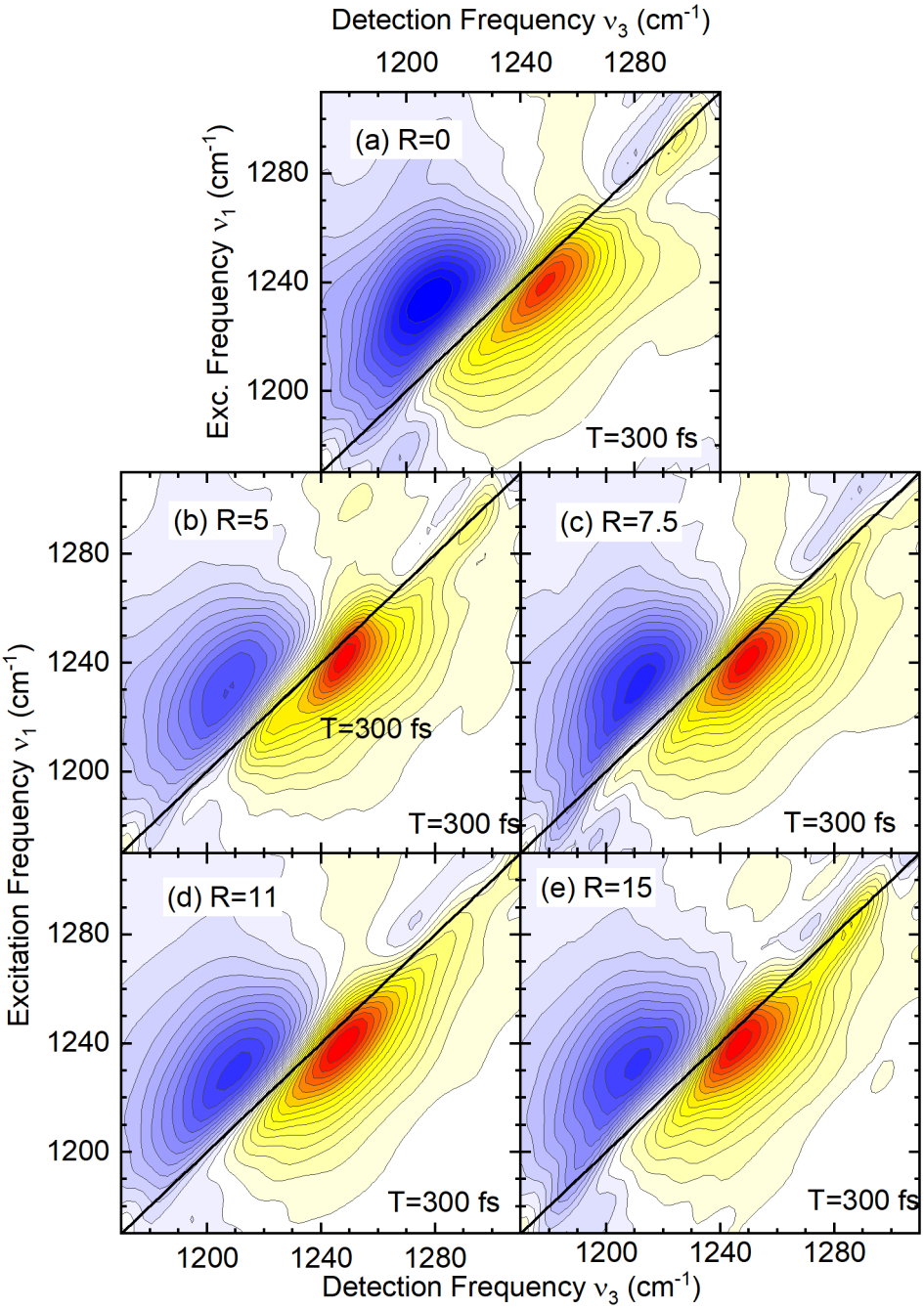

Figure 7.13: Experimental 2D-IR spectra of 4 mM $tRNA^{phe}$ in water for increasing Mg^{2+} concentrations given by the ratio R. The absorptive 2D signal is plotted as a function of excitation frequency ν_1 and detection frequency ν_3. Blue contour lines indicate signal due to excited state absorption of the v=1 $\rightarrow$ 2 transition of $\nu_{AS}(PO_2^-)$, yellow-red contours show ground-state bleach and stimulated emission. Signal change between neighbouring contour lines is 7.5%.

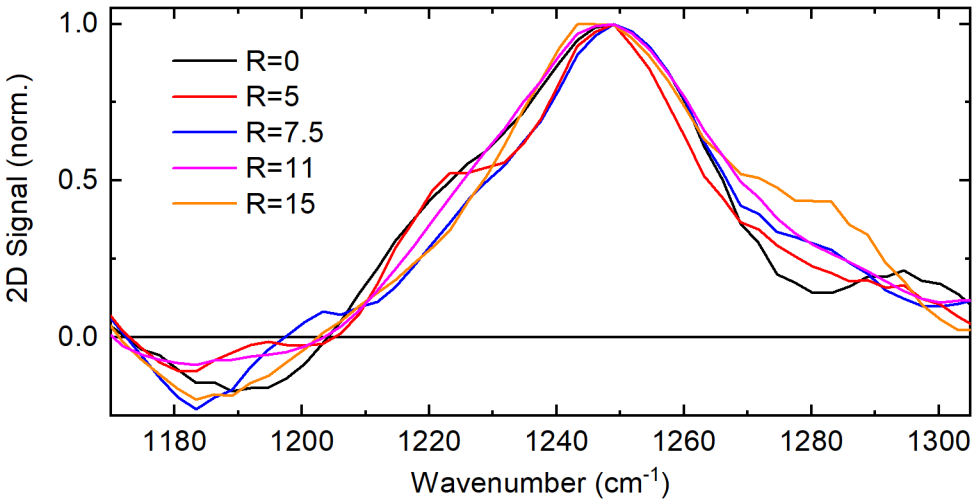

Figure 7.14: Diagonal cuts through the spectra of tRNA^{phe} shown in figure 7.13 for the different Mg^{2+} concentrations. Cuts are taken parallel to the diagonal axis $\nu_1 = \nu_3$ and pass through (ν_1, ν_3)=(1240,1250) cm^{-1}.

slow component τ_2=50 ps, that contribute with the fluctuation amplitudes $\Delta\nu_1$ and $\Delta\nu_2$. For R=20 the relative scaling of the CIP band amounts to roughly 10% of all phosphate contributions, or 4-5 Mg^{2+} contact ions per RNA molecule.

Simulated spectra for tRNA^{phe} and *E.coli* tRNA are shown in figs. 7.18 and 7.19, respectively, together with cuts along diagonal and anti-diagonal axes. The cuts illustrate the accuracy of the simulation, the parameters used in each simulation are summarized in tables 7.2 and 7.3 for tRNA^{phe} and *E.coli* tRNA, respectively. The relative scaling of the CIP mode at 1276 cm^{-1} rises with addition of Mg^{2+} from 0 to 16 (18 for *E.coli*) for the given ratios of R=0→15. The rise is particularly pronounced for small R≈ 5. In that concentration range simulated spectra show a relative scaling of ≈ 6% of all phosphate modes, corresponding to 5 phosphate groups in CIP geometries.

Fluctuation amplitudes show no particular dependence on Mg^{2+} concentration, nor is there a strong difference between fast and slow fluctuations. However, we observe that amplitudes are strongest for the dominant vibrational mode ν_2 and smallest for the two weaker modes ν_3 and ν_4. The simulated parameters agree with the Kubo simulation results in chapter 6 for dsRNA at different temperatures.

7.2 Theoretical Results

Theoretical simulations were performed on the RNA/Mg^{2+} systems to help interpret the experimental results. Figure 7.20(a,b) compares the experimentally measured IR spectrum of dsRNA and tRNA^{phe} to QM/MM simulation results in the range of the asymmetric phosphate stretch vibration $\nu_{AS}(PO_2^-)$. The vibrational density of states (DOS) allows to map Mg^{2+}-PO_2^- distances to vibrational frequencies. The DOS exhibits a clear spectral separation between contact ion pairs (CIP, 1250-1300 cm^{-1}, blue) and unaffected phosphate

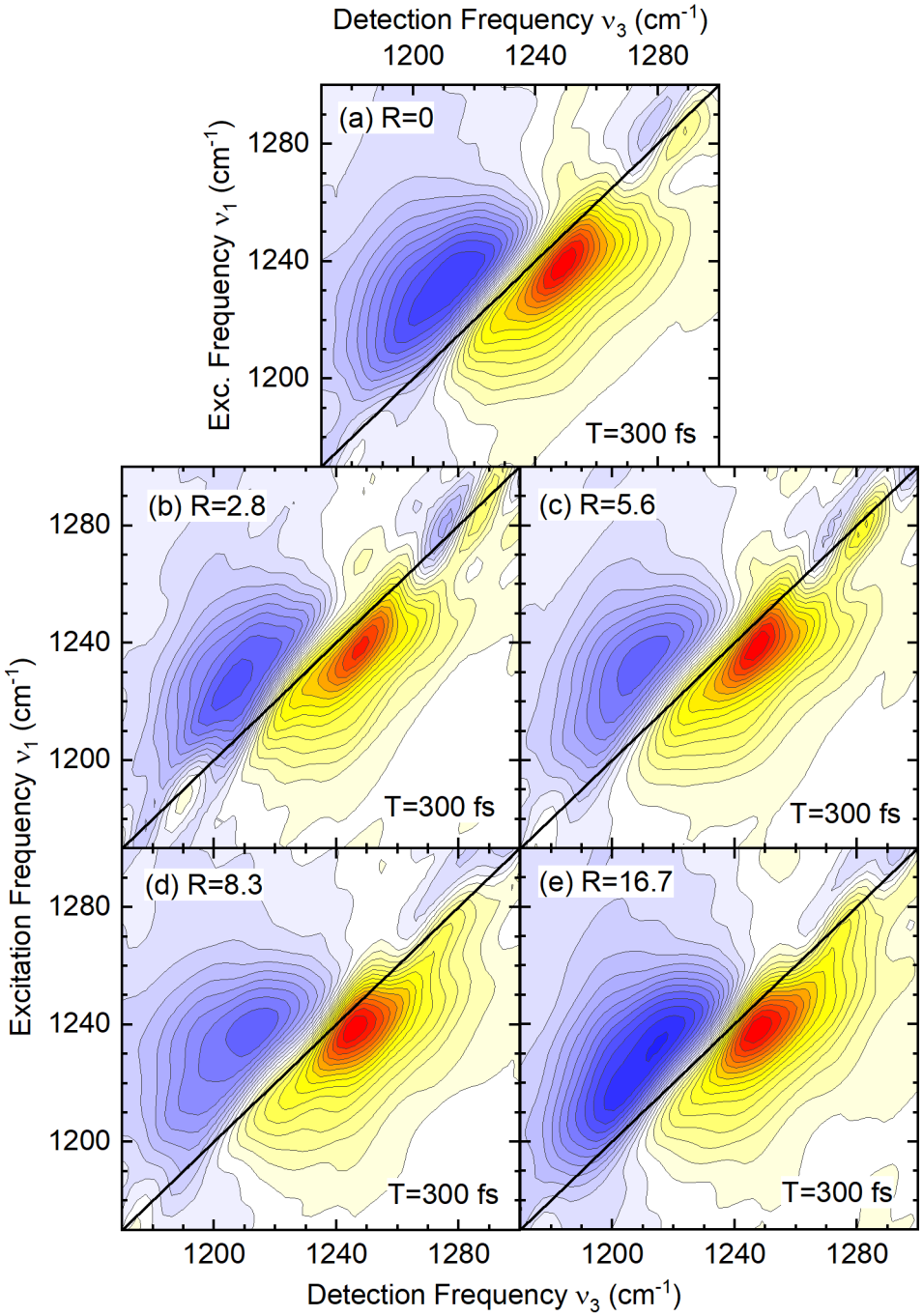

Figure 7.15: Experimental 2D-IR spectra of 3.6 mM *E.coli* tRNA in H_2O for increasing Mg^{2+} concentrations given by the ratio R. The absorptive 2D signal is plotted as a function of excitation frequency ν_1 and detection frequency ν_3. Blue contour lines indicate signal due to ESA of the v=1 $\rightarrow$ 2 transition of $\nu_{AS}(PO_2^-)$, yellow-red contours show GSB&SE on the v=0 $\rightarrow$ 1 transition. Signal change between neighbouring contour lines is 7.5%.

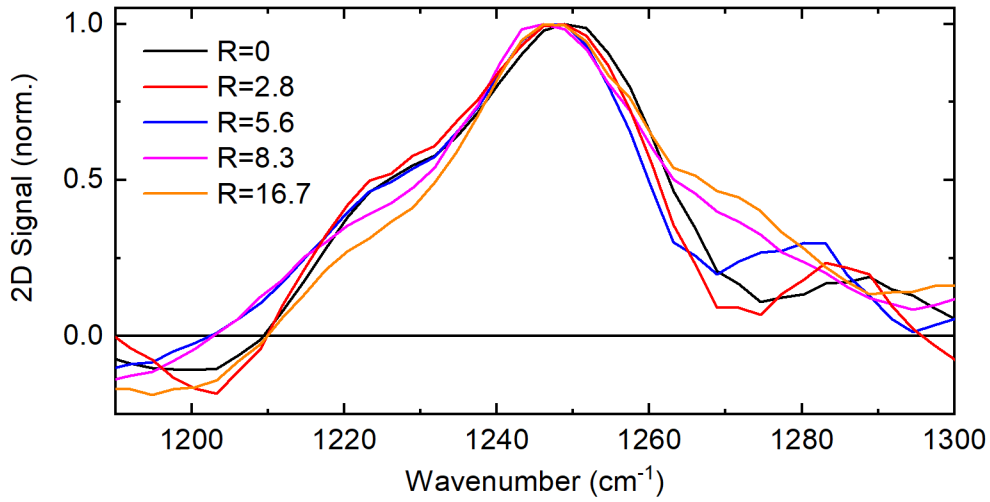

Figure 7.16: Diagonal cuts through the spectra of *E.coli* tRNA shown in figure 7.15 for the different Mg^{2+} concentrations. Cuts are taken parallel to the diagonal axis $\nu_1 = \nu_3$ and pass through (ν_1, ν_3)=(1240,1250) cm^{-1}.

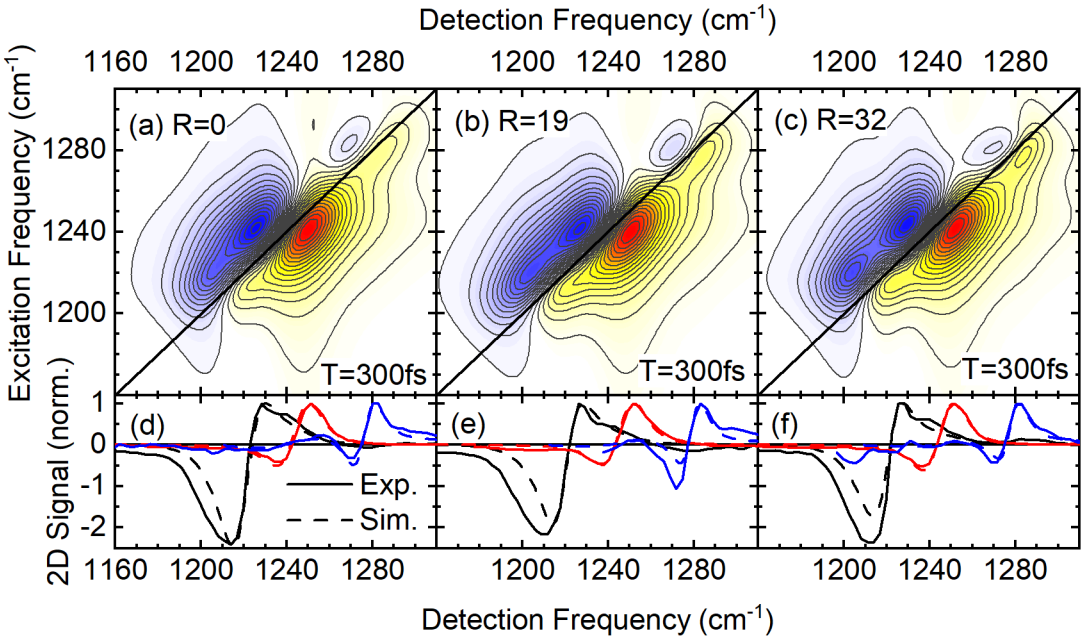

Figure 7.17: (a-c) Simulated 2D-IR spectra of dsAU-RNA with added Mg^{2+}. Spectra were obtained by calculating the third-order response function with the help of the Kubo lineshape model. The parameters used are summarized in table 7.1. (d-f) Anti-diagonal cuts taken through (ν_1, ν_3)=(1223,1223) cm^{-1} (black), (1246,1246) cm^{-1} (red), and (1277,1277) cm^{-1} (blue) normalized to the respective signal maximum. Dashed lines show the simulated signal, solid lines the experimental data.

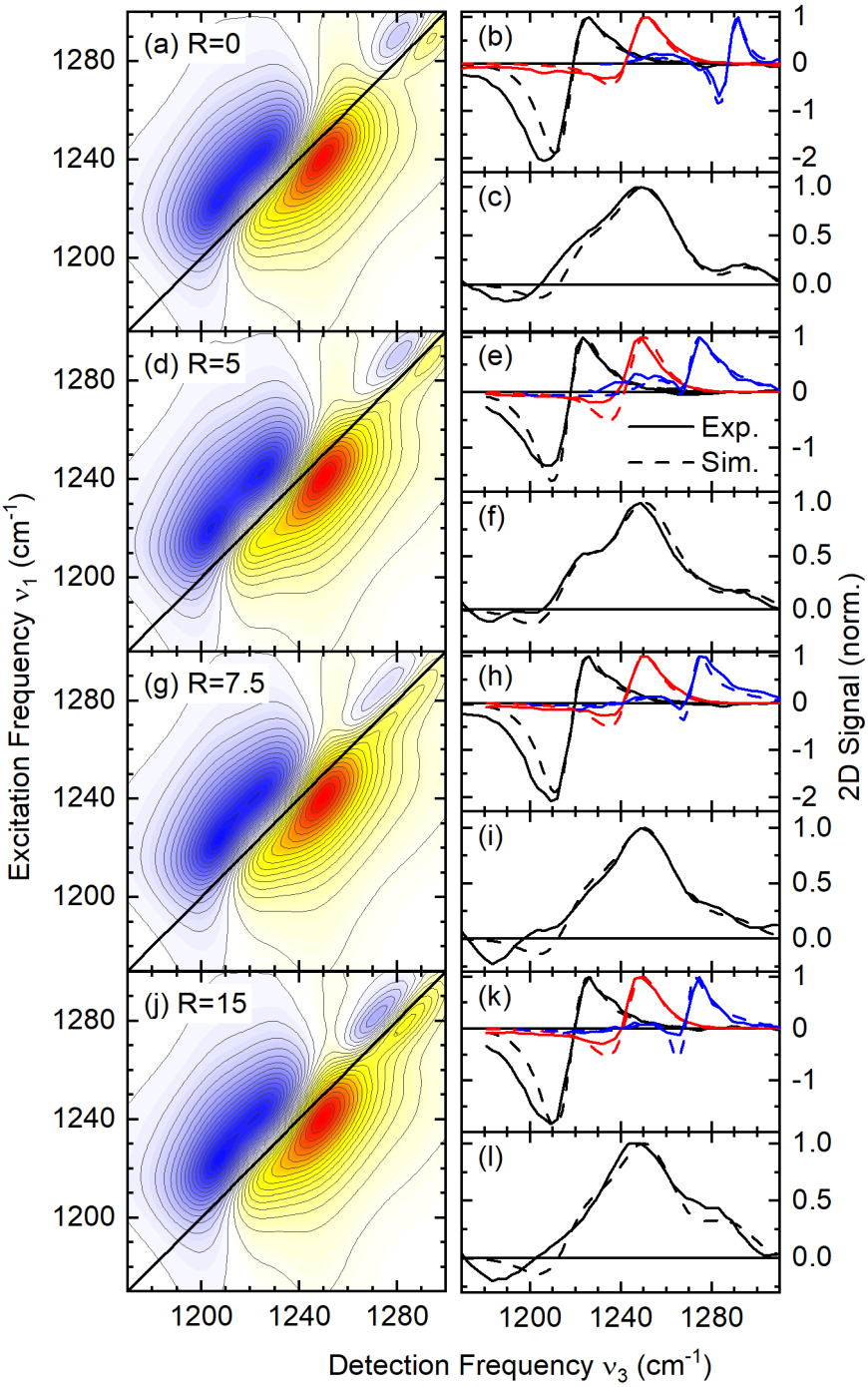

Figure 7.18: (a,d,g,j) Simulated 2D-IR spectra of $tRNA^{phe}$ with added Mg^{2+}. Spectra were obtained by calculating the third-order response function with the help of the Kubo lineshape model. The parameters used are summarized in table 7.2. (b,e,h,k) Anti-diagonal cuts taken through (ν_1, ν_3)=(1219,1219) cm^{-1} (black), (1246,1246) cm^{-1} (red), and (1270,1270) cm^{-1} (blue, (ν_1, ν_3)=(1288,1288) cm^{-1} for R=0) normalized to the respective signal maximum. (c,f,i,l) Diagonal cuts through (ν_1, ν_3)=(1240,1250) cm^{-1}, as in fig. 7.14, dashed lines show the simulated signal, solid lines the experimental data.

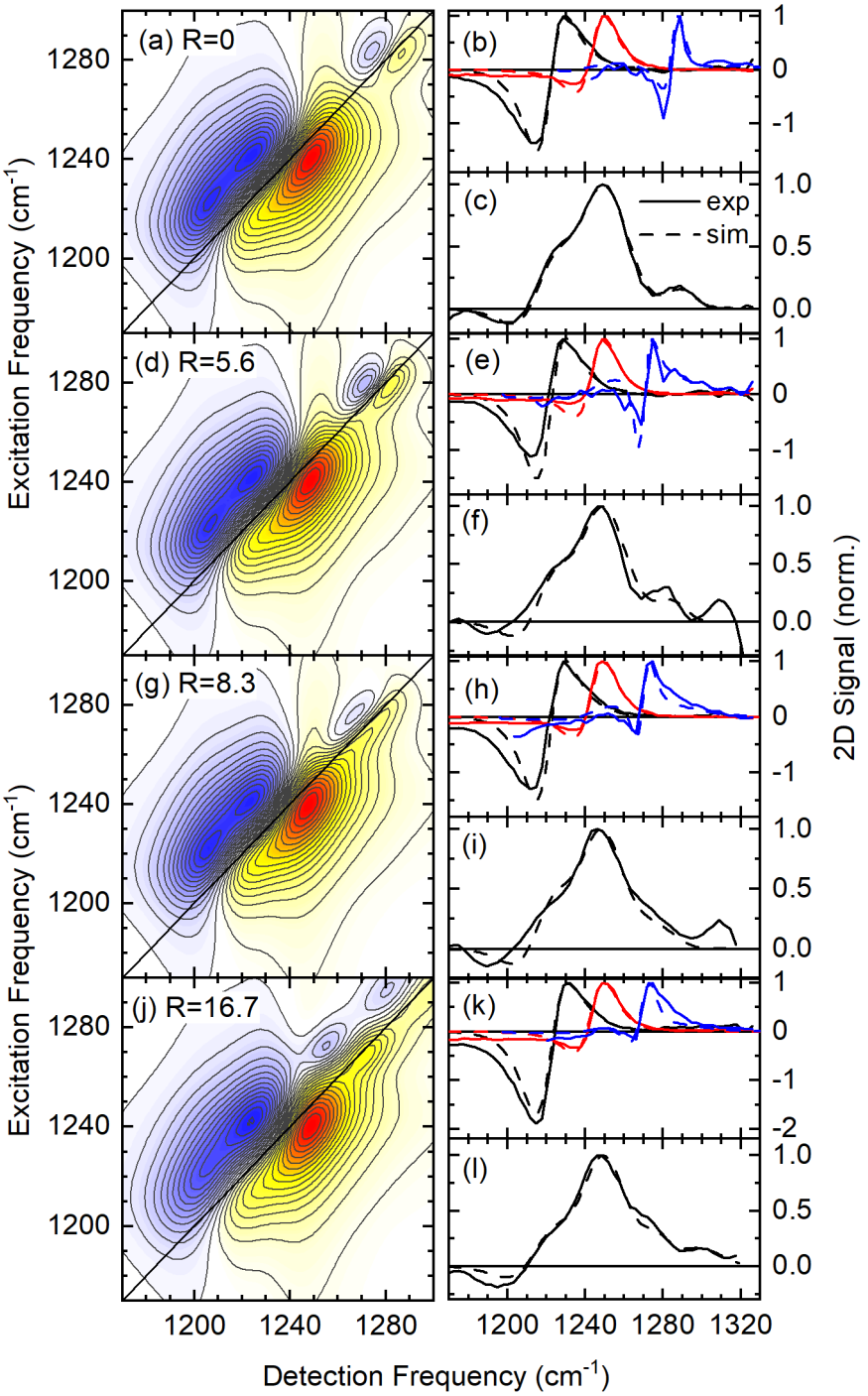

Figure 7.19: (a,d,g,j) Simulated 2D-IR spectra of *E.coli* tRNA with added Mg^{2+}. Spectra were obtained by calculating the third-order response function with the help of the Kubo lineshape model. The parameters used are summarized in table 7.3. (b,e,h,k) Antidiagonal cuts taken through (ν_1, ν_3)=(1224,1224) cm^{-1} (black), (1245,1245) cm^{-1} (red), and (1270,1270) cm^{-1} (blue, (1285,1285) cm^{-1} for R=0) normalized to the respective signal maximum. (c,f,i,l) Diagonal cuts through (ν_1, ν_3)=(1240,1250) cm^{-1}, as in fig. 7.16, dashed lines show the simulated signal, solid lines the experimental data.

mode ν_i	relative scaling	frequency v=0→1	anharmonicity Δ	decay time T_{1i}	fluctuation amplitudes $\Delta\nu_{1i}$	$\Delta\nu_{2i}$
		cm^{-1}	cm^{-1}	fs	cm^{-1}	cm^{-1}
ν_1	57	1220	12	290	6.9	6.9
ν_2	100	1242	11	290	9	11.1
ν_3	0/10/12/16	1276	12.5	700	5.3	6.4
ν_4	17/16/15/17	1290	8	700	6.4	7.4

Table 7.2: Parameter set as used in the numerical simulation of the 2D-IR spectra of $tRNA^{phe}$ for R=0/5/7.5/15 shown in figure 7.18.

mode ν_i	relative scaling	frequency v=0→1	anharmonicity Δ	decay time T_{1i}	fluctuation amplitudes $\Delta\nu_{1i}$	$\Delta\nu_{2i}$
		cm^{-1}	cm^{-1}	fs	cm^{-1}	cm^{-1}
ν_1	67/71/71/70	1219.5	12	290	6.9	7.4
ν_2	100	1243	11	290	8	8.5
ν_3	0/9/15/18	1269	8	800	5.3	5.3
ν_4	16/15/10/18	1281	8.5	800	6.4	5.8

Table 7.3: Parameter set as used in the numerical simulation of the 2D-IR spectra of *E.coli* tRNA for R=0/5.6/8.3/16.7 shown in figure 7.19.

groups (1190-1260 cm^{-1}, black). Phosphate groups in solvent-separated ion pairing (SSIP) overlap with unaffected phosphates to a large degree, spectral outliers exist both for CIPs and SSIPs, resulting from singular, specific interaction geometries. The simulated spectrum captures the broad spectral contributions to the linear absorption spectrum, albeit signal intensities diverge from the measured experimental absorption. Fig. 7.20(c) projects the frequency shifted phosphate groups onto the three-dimensional tRNA structure. The mapping shows the general proximity that CIPs and SSIPs share.

MD simulation results on dsRNA (runtime 0.6 µs) presented in fig. 7.21 give an insight into particularities of the system. The snapshot in (a) shows a distribution of Mg^{2+} ions predominantly in the deep, but narrow major groove of the helix. Both CIP and SSIP geometries can be observed, the insets show typical geometries of Mg^{2+} ions (CIP: middle, SSIP: bottom). The middle inset also shows the parallel occurence of CIP and SSIP: direct contact is only the case for the phosphate group to the top left, whereas contact to the lower phosphate group is mediated by a water molecule in the first hydration shell of the Mg^{2+} ion.
The interaction potential of the RNA/Mg^{2+} system as a function of Mg^{2+}...PO_2^- distance d and interaction angle $\alpha = \measuredangle Mg^{2+}$...O1-P is displayed in a 2D potential of mean force depicted in fig. 7.21(b). Both coordinates are illustrated in the top inset. The distinction lines between CIP (d<4Å) and SSIP (4Å<d< 6Å) follow the radial distribution of water molecules around DMP^- shown in figure 5.13. Two distinct, steep minima in the PMF are observed for CIPs at $\alpha \approx 5°$ and $\alpha \approx 11°$. The energy landscape for SSIPs is more even. It shows symmetry along the bisector of the phosphate group ($\alpha \approx 56°$), where a local

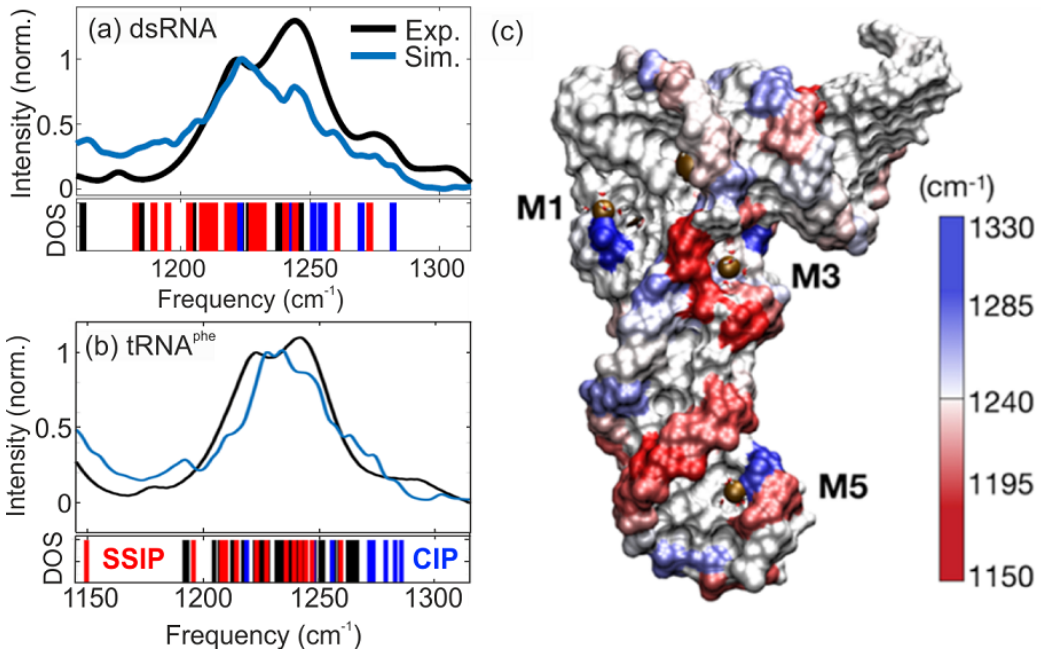

Figure 7.20: (a,b) Simulated (blue) and experimental (black) linear infrared absorption spectra in the frequency range of $\nu_{AS}(PO_2^-)$. QM/MM simulations are compared to the experimentally measured FTIR spectra of dsAU-RNA (a) and $tRNA^{phe}$ (b) in water. The bottom panel shows the respective vibrational density of states (DOS) of the $\nu_{AS}(PO_2^-)$ band. Frequency positions of $(PO_2^-)/Mg^{2+}$ CIPs are color coded in blue, SSIPs in red. Unaffected PO_2^- are shown in black. (c) Vibrational frequencies of phosphate groups mapped onto the tertiary structure of $tRNA^{phe}$.

minimum is recorded.

The trajectory of a $tRNA^{phe}$ molecule was simulated for 1 µs, the results are summarized in figs. 7.22-7.24. Fig. 7.22 shows the simulated Mg^{2+} distribution around $tRNA^{phe}$ along isodensity contour lines of 0.005 $Å^{-3}$ (grey) and the instantaneous ion positions from a snapshot at the end of the simulation time (gold). The majority of Mg^{2+} ions cluster in regions of high charge density, particularly the $T\Psi C$ and D loop. Snapshots of selected local Mg^{2+} geometries show the variety of interactions. The ion **M1** in the TΨC loop links two neighbouring phosphate groups via direct interactions. In contrast, **M5** is situated in the helical region of the anti-codon loop. It forms a contact pair with one (PO_2^-), but interacts with the neighbouring phosphate in a solvent-separated geometry. Fig. (c) illustrates the hydration pattern of the bound Mg^{2+} ions using the example of **M8**. One water molecule from the tetrahedral first hydration shell is replaced by one of the phosphate oxygens. Contact geometries form a linear P-O..Mg^{2+} arrangement observable in all snapshots, similar to the findings for dsRNA (cf. fig.7.21). Radial distribution functions (rdf) are shown in fig. 7.23 to illustrate the distance-dependent probability distributions for various phosphate-atom/ion interactions. Divalent ions (c) are particularly pronounced around 2 Å from the phosphate oxygen, significantly below typical phosphate-water distances in the first hydration shell (a). Na^+ ions, intrinsically present both in experiment and MD simulation, also accumulate within the first phosphate hydration shell, but additionally reflect solvation be-

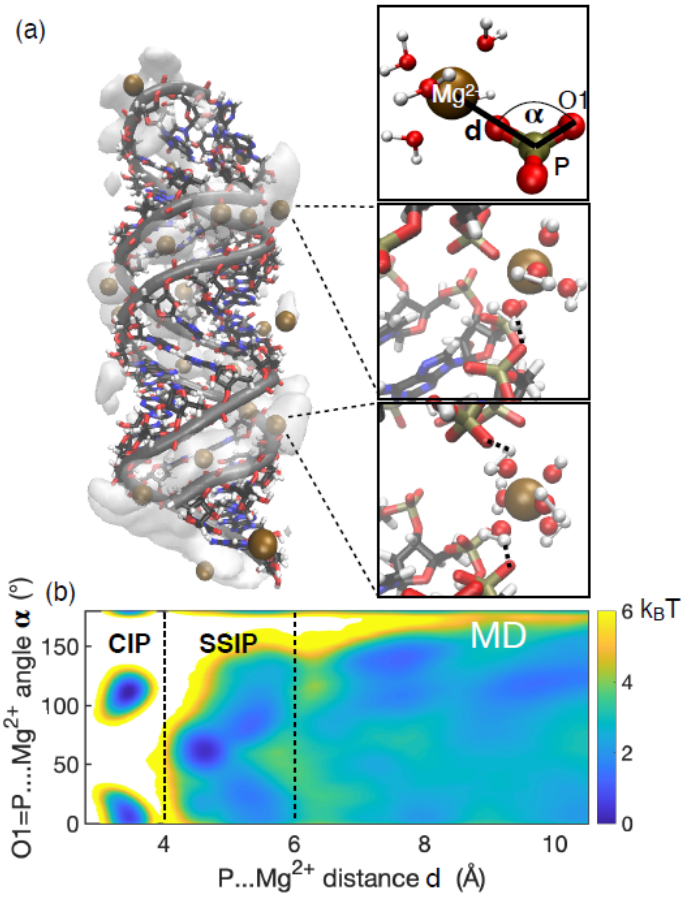

Figure 7.21: Molecular structure of AU double helical RNA and its surrounding Mg^{2+} ions, snapshot taken at 0.6 µs of MD simulation. Mg^{2+} ions are shown in ochre, oxygen atoms in red, nitrogen atoms in blue, carbon atoms in black and phosphorous atoms in yellow. The grey contour lines represent an isodensity line for a Mg^{2+} concentration of $0.02\,Å^{-3}$. The inlays show the distance coordinate d and the angular coordinate α (top), a contact ion pair (CIP, middle) and a solvent separated ion pair (SSIP, bottom) of phosphate groups and Mg^{2+} ions together with water molecules in the first solvation shell of the Mg^{2+} ion. Hydrogen bonds of H_2O with the (PO_2^-) group are indicated with dashed lines. (b) Potential of mean force in the plane of (PO_2^-) groups, as experienced by Mg^{2+} ions.

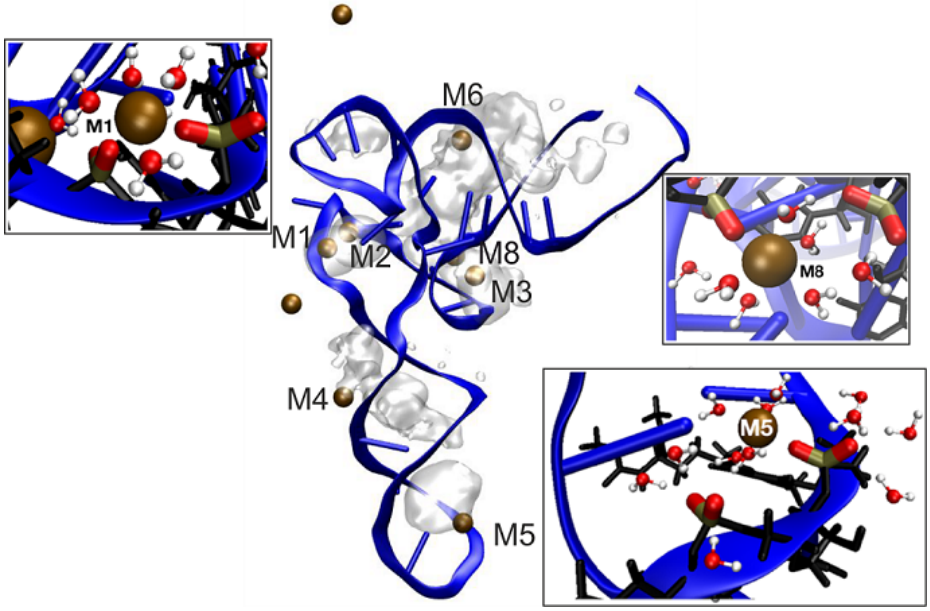

Figure 7.22: Tertiary structure of $tRNA^{phe}$ (blue) with Mg^{2+} ion positions. Mg^{2+} ions in ochre show instantaneous positions after 1 µs of MD simulations. Grey contour lines represent regions with the same concentration density of 0.005 $Å^{-3}$, averaged over 2500 equidistant snapshots. A singular Mn^{2+} ion was included in the simulation on the basis of x-ray diffraction measurements, it is situated above the M6 Mg^{2+} ion. Exemplary local geometries are shown for three contact ion pairs in different regions of the $tRNA^{phe}$ molecule. Oxygen atoms are shown in red, hydrogen atoms in white and phosphorus atoms in yellow. Uninvolved atoms of the tRNA molecule are shown in black.

yond the 9Å shown here, indicating their role in the formation of the diffuse ion atmosphere.

The effect of Mg^{2+} ions on the surface electrostatic potential is shown in fig. 7.24(c). The negative charge of the PO_2^- groups is unsurprisingly responsible for a high negative potential for the majority of the tRNA molecule. However, regions that harbour Mg^{2+} ions show a more neutral potential (anti-codon loop) or even revert to a net-positive potential (particularly D and $T\Psi C$ loop). This impact on electric properties is also observed in fig.7.24(a,b), where the electric field on the mid-point of the O1-P-O2 bisector is displayed for both CIPs and solvent-surrounded phosphate groups. The ion contribution to the electric field for CIPs reaches around 150 MV/cm and is mediated by water molecules to a total field strength of ≈100 MV/cm. The electric field on solvent exposed phosphate groups is significantly lower (40 MV/cm, up to 60 MV/cm) and stems mainly from the surrounding water molecules in the first shell. Contributions from surrounding ions, present from the second shell outwards, amount to no more than 15 MV/cm.

Fig. 7.25 shows the radial distribution of Mg^{2+} ions surrounding the RNA double helix at R=20. Three peaks can be distinguished at 3Å, 8Å, and 11Å, respectively. The concentration tails off up until ≈20Å. Quantitative information on the formation of CIPs was gathered by performing multiple simulations for varying ratios R of Mg^{2+} to RNA concentration. The result is shown in the inset of figure 7.25 and shows an initially linear increase that saturates at $R \approx 20$. It must be noted that the population of CIPs strongly depends on

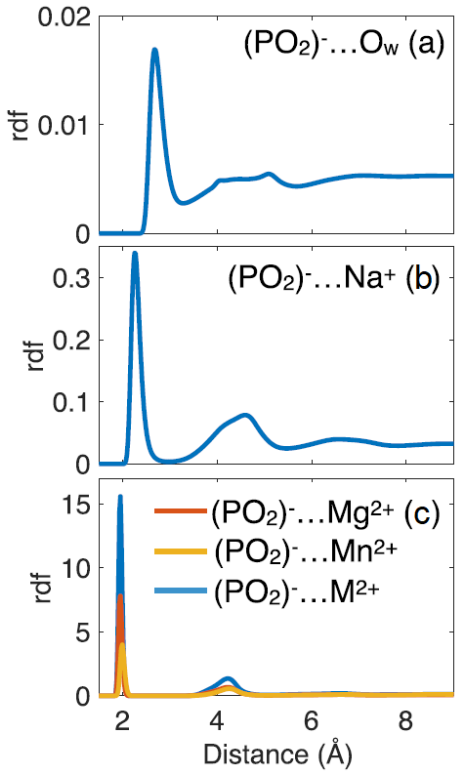

Figure 7.23: Radial distribution functions (rdf) show the probability of finding two atoms at a specific distance from one another. This is shown here for the phosphate groups of $tRNA^{phe}$ and the constituents of its hydration shell, namely water oxygens (a), Na^+ counterions (b), and divalent counterions (c). Contributions of divalent ions are further separated by Mg^{2+} (red) and manganese ions (Mn^{2+}, yellow).

the applied force fields. The presented force-field combination TIP4P-FB/12-6-4-J captures the saturation behaviour accurately and is therefore considered to be the most reliable in the context of the experiments. 10±1 CIPs per RNA molecule are predicted, a factor of ≈ 2 more than found in the experiments. Simulations run with other force field parameters predict significantly higher CIP numbers or none at all. These considerations overextend the scope of this work but are discussed in detail in [136].

7.3 Discussion

Chapter 5 established the asymmetric phosphate stretch vibration as a marker mode for contact-ion pair formation in the phosphate model system DMP. Here, the impact of excess Mg^{2+} concentration on $\nu_{AS}(PO_2^-)$ of double-helical RNA (dsRNA) and two different samples of dialysed transfer RNA ($tRNA^{phe}$ and *E.coli* tRNA) was examined. All RNA systems show an emerging vibrational mode around 1270 cm^{-1} with increasing Mg^{2+} concentration. This frequency shift is comparable to frequency shifts in DMP and can be linked to the formation of CIPs by QM/MM calculations. Exchange repulsion interactions were established in chapter 5 as the origin of the shift in the model system DMP. This appears to also be the case for RNA. The 2D-PMF in fig. 7.21(b) shows that CIPs occur

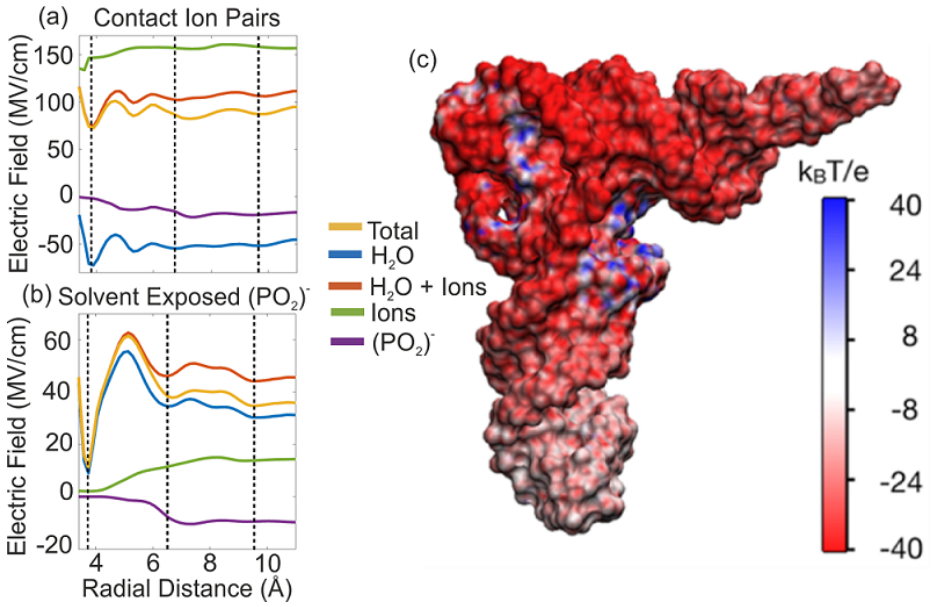

Figure 7.24: (a,b) Electric fields acting on the bisector of the $tRNA^{phe}$ phosphate group sorted by their origin shown here for phosphate groups in contact ion pairs (a), and phosphate groups where the first solvation shell consists exclusively of water molecules (solvent exposed phosphates, b). Contributions of water molecules are shown in blue, ion contributions in green. Contributions from other phosphate groups are shown in purple to add up to the total electric field (yellow). (c) Surface electrostatic potential of $tRNA^{phe}$, calculated from MD simulations.

at Mg^{2+}–P distances $d < 4$Å, thus intruding on the first hydration shell of the phosphate. Radial distribution functions show that these interactions of Mg^{2+}-phosphate oxygen pairs are significantly closer than for phosphate oxygen-water oxygens.

The combination of fluorescence measurements with IR spectroscopy allows to quantitatively put the formation of CIPs into the context of the general ion environment of the RNA molecules. The initial ion environment, as measured in ICP-OES experiments, consists almost exclusively of Na^+ counterions. In the case of tRNA this is the result of dialysis with EDTA. Added Mg^{2+} interacts with the RNA as either a part of the diffuse ion atmosphere, in a direct binding geometry, or not at all. The number of Mg^{2+} ions associated with dsRNA saturates at about 13 Mg^{2+} ions for R≥15, that for *E.coli* tRNA at 18 Mg^{2+} per RNA for R≥24, reflecting the higher number of negatively charged phosphate groups. $tRNA^{phe}$ deviates little from the linear trend.

The IR absorbance changes around 1270 cm^{-1} show a saturation behaviour for all RNA molecules. The increase in CIP feature follows an initially linear trend for dsRNA, but deviates from it for tRNA. This is in agreement with the observed Mg^{2+} localization in the homogeneous major groove, whereas Mg^{2+} binds to tRNA at distinct, highly different binding pockets. Quantitative information on contact binding can be drawn from linear IR absorption spectra, where the relative absorbance change predicts a rough estimate of 1-2 dsRNA-Mg^{2+} contact pairs at R=19 and ≈ 3 Mg^{2+}-tRNA contact pairs at R=14. A more sophisticated reporter of CIP population are the presented 2D-IR spectra. Their elliptical

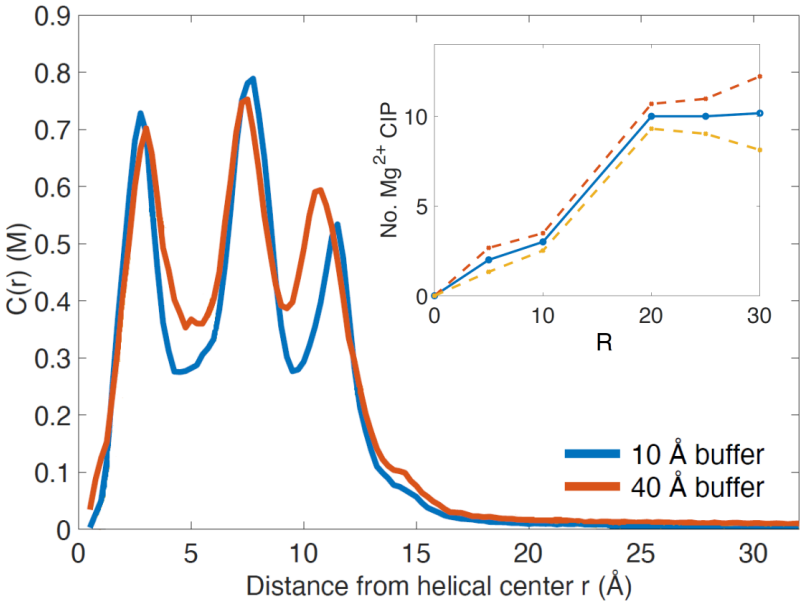

Figure 7.25: Radial profile of Mg^{2+} ion concentration from the helical center of dsRNA at R=20, as determined by MD simulations. Three peaks show CIP& SSIP binding, the ion atmosphere sets in around 15Å. Results are given for simulation cell sizes with a 10 Å buffer region (blue) and a 40 Å buffer region (red). Inset: Number of recorded contact ion pairs after 0.6 µs simulation time as a function of Mg/RNA concentration ratio R. The solid lines show the average over the last 50 ns of the simulations, dashed lines illustrate the standard deviation.

lineshape reflects the inhomogeneous environment of RNA phosphate groups, the absence of cross peaks shows that the vibrational response originates from independent oscillators at different RNA sites. The CIP mode around (1275,1275) cm^{-1} emerges as a result of excess Mg^{2+}. Kubo analysis of the dsRNA 2D-IR spectrum at R=19 estimates 4-5 CIPs per RNA from the relative amplitude of the emergent CIP mode,and 7-8 CIPs per tRNA molecule at R≈15. This latter number is in good agreement with the observed Mg^{2+} binding sites in x-ray diffraction [4], for the first time confirming CIP formation also in aqueous solution. All in all, up to 35% of the interacting Mg^{2+} ions detected in fluorescence titration measurements are found in CIP geometries.

The corresponding binding sites were analyzed using MD simulations. Simulations of dsRNA predict up to 10 CIPs per RNA distributed predominantly in the major groove of the double helix, twice as many as found in experiments. This disagreement is due to current force fields overestimating the strength of the Coulomb interaction. The deep and narrow major groove with its high negative charge density is the predominant location of CIPs because it allows for a self-stabilizing effect: counterions bridge the interstrand phosphate-distances, negate the electrostatic repulsion and thus allow for even further contraction. In tRNA, Mg^{2+} contact ions preferentially populate specific locations with high negative charge density. Those tRNA-Mg^{2+} CIPs shown in isodensity plot of fig. 7.22 were stable throughout the 1 µs simulation time, matching the >µs residence time of water molecules in the first hydration shell of Mg^{2+}. This confirms the findings of previous

simulations with DMP, that Mg^{2+}-(PO_2^-) contact geometries form particularly stable arrangements (see fig. 5.17). It provides evidence as to why magnesium plays such a vital role in biomolecular processes.

It was shown that the majority of Mg^{2+} ions is located in condensed regions of the tRNA molecule. There, the positive charge enables the ions to link phosphate groups, which manifests in the parallel formation of CIP and SSIP geometries (see the local geometries in figs. 7.21 and 7.22). The small relative absorbance increase at $1220\,cm^{-1}$ (fig. 7.4) seems to reflect the formation of SSIPs, similar to the red-shifted feature observed in DMP^-/Mg^{2+} systems in fig. 5.3. The structural rigidity of the binding pockets is corroborated by the fluctuation amplitudes used to simulate the 2D-IR spectra. The amplitude of short timescale fluctuations, $\Delta\nu_1$, is ≈50% lower for the CIP vibrational mode (see tables 7.3 and 7.2). This reflects reduced water librations compared to the main vibrational modes at 1220 and $1242\,cm^{-1}$, i.e. a higher rigidity in the CIP pockets. Double helical RNA on the other hand does not show these effects (table 7.1), likely because the binding along the major groove does not stabilize the phosphate solvation shells to the same extent. Solvation geometries are still largely accessible by water outside the groove, which is less the case for the D and $T\Psi C$ loop in tRNA.

The biophysical importance of these binding pockets is seen in the surface electrostatic potential, fig. 7.24. Mg^{2+} ions lead to a (over)compensation of the originally highly negative potential. Coulomb repulsion, the major hindrance in achieving the condensed tertiary folding, is overcome by the ions placed in these strategic locations. In addition, the counterions situated in the anti-codon loop effectively neutralize the electrostatic potential at the anti-codon. This may be a vital step in protein synthesis, as it reduces Coulomb repulsion in tRNA-mRNA interactions [30]. It is important to note that the electrostatic potential predicted by Poisson-Boltzmann calculations, e.g. in [33], is about one order of magnitude lower. This results from the inherent assumption that it is long-range electrostatic interactions that govern Mg^{2+}/RNA interactions. An extensive theoretical analysis of shortcomings of PB theory versus MD simulations in the context of RNA molecules is given in [136]. In our results, direct interactions of Mg^{2+} ions with the phosphate groups of the backbone are most important in the electrostatic stabilization of the tRNA tertiary structure. The comparably small contribution of the ion atmosphere to the electrostatic environment is also visible in the contributions to the electric field. The electric field due to positive counterions in solvent-exposed phosphates amounts to ≈ 14 MV/cm, an order of magnitude lower than the contributions in contact-ion pairs. It is overshadowed by the electric field due to local water molecules, an aspect disregarded in the continuum solvent model of PB theory.

The radially dependent Mg^{2+} concentration in fig. 7.25 gives a global idea of how directly bound ions (CIP&SSIP) are distributed in helical RNA with respect to the ion atmosphere. The first major peak, at a distance of ≈ 3Å from the helical center stems mostly from Mg^{2+} ions that cluster at the ends of the helical axes. As such, these Mg^{2+} ions are a result of the inherent nature of short double-stranded RNA. The ions in the major groove, as discussed in CIP or SSIP geometries (or both), show a concentration maximum at ≈ 8Å. A smaller portion of similar ion pairs is situated at ≈ 11Å, where interaction occurs mainly in SSIP geometries (cf. the 13Å radius of an RNA double helix, fig. 1.3). MD simulations predict a decaying concentration tail up to ≈ 20Å , contributions of the ion atmosphere to the overall

Mg^{2+} concentration are small. This contrasts our experimental findings, where $\geq 70\%$ of all associated Mg^{2+} ions are associated in non-CIP geometries. But it agrees with the general overestimation of CIPs by MD simulations.

In summary, this chapter investigated the effect of Mg^{2+} on the $\nu_{AS}(PO_2^-)$ vibrational mode of several RNA systems. Added excess Mg^{2+} resulted in a significant frequency upshift of the asymmetric phosphate stretching mode that was assigned to the formation of RNA-Mg^{2+} contact ion pairs. This assignment together with theoretical simulations allowed to predict up to 30% of bound Mg^{2+} ions to form CIPs, predominantly in regions of high negative charge density, i.e. the major groove of dsRNA, and the congested loop regions of tRNA. More generally, phosphate group vibrations were shown to be sensitive reporters of the ion environment in biologically relevant RNA systems.

8

Conclusion and Summary

This thesis addresses the structure and interactions of hydrated biomolecular systems. Of particular interest are electric interactions of RNA with a water environment containing ions, and their impact on RNA structure and dynamics. Vibrations of the RNA backbone serve as noninvasive probes of local electric fields and interaction geometries. Their response is mapped by femtosecond two-dimensional infrared (2D-IR) spectroscopy and analyzed by theoretical calculations.

In particular, we employed the asymmetric phosphate stretch vibration $\nu_{AS}(PO_2^-)$ as a most sensitive reporter to investigate the binding of Mg^{2+} to phosphate groups of the RNA backbone in an aqueous environment. These phosphate groups constitute the major hydration site of RNA, yet the complex interactions with surrounding solvent molecules are still poorly understood on a local level. Additionally, Coulomb repulsion from proximate phosphate groups is a significant impediment to the formation of a functional tertiary structure in RNA. To what extent positively charged counterions compensate these repulsive Coulomb interactions on a molecular level has been controversially discussed in literature. Exploiting the surface sensitivity of phosphate vibrations, we demonstrated a new approach to detect the formation of RNA/Mg^{2+} contact ion pairs (CIP) and interpret their role in stabilization of complex folded RNA structure. We used ultrafast 2D-IR spectroscopy to investigate the response of the dimethyl phosphate anion (DMP), a common model system for the RNA backbone phosphate group, to a variety of positively charged counterions. With the reference of the model system we studied hydration structure and ion environment of more complex systems, namely a synthetical RNA double helix, as a model for helical regions of complex RNA structures, and two kinds of biologically relevant transfer RNA. The following results have been obtained:

Dimethyl phosphate anion

The dimethyl phosphate anion with its central phosphate group is a common model system for phosphate groups in the nucleic acid backbone. Here, we dissolved the anion in aqueous solutions containing the alkali and alkaline earth metals Na^+, K^+, Ca^{2+}, or Mg^{2+}. Vibrational spectra in the spectral region of $\nu_{AS}(PO_2^-)$ show a distinct frequency blue-shift upon exposure to ions. The new spectral feature originates from independent oscillators, confirmed by the absence of cross-peaks in 2D-IR spectra, and exhibits a longer lifetime than the original $\nu_{AS}(PO_2^-)$ mode. The extent of the blue-shift depends on valency and size of the respective cation, the strongest frequency shift was observed for Mg^{2+}. Theoretical simulations determined the origin of the shift to arise from exchange repulsion interactions upon formation of a contact ion pair. CIPs are arranged in a linear Mg^{2+}...O1-P arrangement, with Mg^{2+}...O

distances characteristically below 2.1Å. A weaker shift towards lower frequencies could also be observed, albeit for divalent ions only, and assigned to solvent-separated ion pairs. The identified characteristic frequency shifts upon contact pair formation with the phosphate group form the basis for the quantitative investigations of CIP formation in more complex RNA systems.

Melting experiments of synthetical dsRNA

The heating of synthetical double helical RNA (dsRNA) is accompanied by a structural transition at the melting temperature of $T_m \approx 328\,K$. This transition is captured by vibrational spectra of $\nu_{AS}(PO_2^-)$ as a re-scaling of the major absorption peaks. 2D-IR spectroscopy could discern three independent spectral components contributing to the vibrational spectra of $\nu_{AS}(PO_2^-)$, attributed to three different kinds of phosphate hydration environments. 2D-IR peaks have an elliptical lineshape, reflecting the inhomogeneous environment around the RNA backbone. Solvating water molecules generate electrical field strengths on the order of tens of MV/cm that act on the phosphate group. As a result, $\nu_{AS}(PO_2^-)$ is subject to a vibrational Stark shift, the vibrational frequency highly depends on the local solvation structure. With increasing hydration, the $\nu_{AS}(PO_2^-)$ vibrational frequency shifts to lower frequencies. MD simulations and QM/MM calculations assigned the particular local geometries to their spectral position:

- Fully hydrated phosphate groups, i.e. surrounded by around six water molecules that form a tetrahedral solvation shell, contribute at $1220\,cm^{-1}$. Such phosphate groups are generally situated at the RNA surface.
- Phosphate groups with an under-coordinated hydration shell, where single water molecules bridge the small distance between neighbouring phosphate groups, contribute at $1245\,cm^{-1}$. These are mostly present in the deep and narrow major groove of dsRNA where solvent accessibility is substantially reduced.
- Phosphate groups directly interacting with the Na^+ counterions are further shifted to the blue and contribute at $1280\,cm^{-1}$.

The structural transition observed upon heating reduces sterical constraints in the RNA double helix and allows a higher degree of hydration. Vibrational spectra thus report the transition from predominantly under-hydrated phosphate groups to predominantly fully hydrated local geometries.

Mg^{2+} binding to RNA

To investigate RNA-ion interactions, synthetical dsRNA and biological tRNA were dissolved in aqueous solution containing varying amounts of Mg^{2+} counterions. We observed a similar frequency blue-shift upon exposing RNA to Mg^{2+}, as with DMP. The changes in the vibrational spectra could be attributed to a newly emerging vibrational mode assigned to the formation of RNA/Mg^{2+} contact ion pairs using QM/MM calculations. Upon adding $\approx$ 20 Mg^{2+} ions per RNA molecule, up to 10% of phosphate groups contributed to the CIP signal in each of the RNA systems. This is in line with the 7-9 directly bound ions observed in crystallographic x-ray diffraction measurements of $tRNA^{phe}$. The 2D-IR measurements confirmed for the first time that CIP formation is an important structural element also in aqueous environment. MD simulations show that CIPs form predominantly

in the major groove of dsRNA, as well as in condensed loop regions of the tRNA molecule. They (over)compensate locally the electrostatic Coulomb repulsion of the negatively charged phosphate groups and thus stabilize the formation of RNA tertiary structure.

Concluding Remarks

Our work demonstrated the potential of vibrational excitations as sensitive, non-invasive probes of biomolecular hydration environments. Together with a theoretical description on the molecular level, time-resolved vibrational spectroscopy helps to understand the manifold of RNA interactions with its surrounding water molecules and counterions. The approach could be used further to study the role of water molecules and (contact) ions in more complex scenarios, e.g., the highly dynamical folding process of complex RNA molecules.

9 Zusammenfassung

Diese Dissertation betrachtet Struktur und Wechselwirkungen hydratisierter biomolekularer Systeme. Von besonderem Interesse sind elektrische Interaktionen von RNA mit Wassermolekülen und Ionen der näheren Umgebung, sowie deren Einfluss auf Struktur und Dynamik der RNA. Schwingungen des RNA-Zuckerphosphat-Rückgrats fungieren als nichtinvasive Sonden lokaler elektrischer Felder und Wechselwirkungsgeometrien. Ihre Antwort wird durch zweidimensionale Infrarotspektroskopie (2D-IR) im Femtosekundenbereich erfasst und durch theoretische Berechnungen analysiert.

Wir verwenden insbesondere die asymmetrische Phosphatstreckschwingung $\nu_{AS}(PO_2^-)$ als äußerst empfindlichen Sensor, um die Bindung von Magnesium-Ionen (Mg^{2+}) an Phosphatgruppen des RNA Rückgrats in wässriger Umgebung zu untersuchen. Diese Phosphatgruppen sind maßgebliche Hydratationspunkte der RNA. Die komplexen Wechselwirkungen mit Wassermolekülen der Umgebung sind jedoch auf lokaler Ebene nur schlecht verstanden. Zusätzlich ist die Coulombabstoßung benachbarter Phosphatgruppen ein signifikantes Hindernis bei der Bildung einer funktionellen Tertiärstruktur der RNA. In welchem Umfang positiv geladene Gegenionen diese repulsiven Coulombwechselwirkungen auf molekularer Ebene kompensieren, wird in der wissenschaftlichen Literatur kontrovers diskutiert. Unter Ausnutzung der Empfindlichkeit der Phosphatschwingungen auf ihre Solvatationsumgebung demonstrieren wir einen neuen Ansatz, um die Bildung von RNA/Mg^{2+} Kontaktionenpaaren (CIP) zu detektieren und deren Beitrag zur Stabilisierung komplex gefalteter RNA Strukturen auszuwerten. Wir verwenden ultrakurze 2D-IR Spektroskopie, um die Antwort des Dimethylphosphat-Anions (DMP), eines verbreiteten Modellsystems der RNA-Phosphatgruppe, auf unterschiedliche, positiv geladene Gegenionen zu untersuchen. Mit dem Modellsystem als Referenz studieren wir die Hydratationsstruktur und die Ionenumgebung verschiedener RNA-Systeme: zum Einen eine synthetische RNA-Doppelhelix als Modell für helix-ähnliche Regionen komplexer RNA-Strukturen, zum Anderen zwei Arten biologisch relevanter Transfer-RNA (tRNA). Die Hauptergebnisse sind im Folgenden zusammengetragen:

Dimethylphosphat-Anion

Das Dimethylphosphat-Anion mit seiner zentalen Phosphatgruppe ist ein verbreitetes Modellsystem für Phosphatgruppen im Rückgrat von Nukleinsäuren. Hier lösen wir das Anion in wässrigen Lösungen, die die Alkali- und Erdalkalimetalle Na^+, K^+, Ca^{2+}, oder Mg^{2+} beinhalten. Schwingungsspektren in der spektralen Region von $\nu_{AS}(PO_2^-)$ zeigen eine ausgeprägte Blauverschiebung, wenn die Phosphatgruppe den Ionen ausgesetzt ist. Die neue spektrale Bande stammt von unabhängigen Oszillatoren, wie die Abwesenheit von Kreuzsignalen im

2D-IR Spektrum belegt, und zeigt eine längere Lebensdauer als die ursprüngliche $\nu_{AS}(PO_2^-)$-Mode. Der Umfang der Blauverschiebung hängt von Valenz und Größe des jeweiligen Kations ab. Die stärkste Frequenzverschiebung wurde für das zweifach positiv geladene Mg^{2+} beobachtet. Theoretische Simulationen konnten den Ursprung der Verschiebung ermitteln, sie entsteht durch repulsive Austauschwechselwirkungen bei der Bildung von Kontaktionenpaaren. CIPs sind in einer linearen Mg^{2+}...O1-P Geometrie angeordnet, mit charakteristischen Mg^{2+}...O Abständen unter 2.1 Å. Eine schwächere Frequenzverschiebung hin zu niedrigeren Frequenzen konnte ebenso beobachtet werden, jedoch nur für divalente Ionen. Sie konnte Lösemittel-separierten Ionenpaaren zugeordnet werden. Die ermittelten charakteristischen Frequenzverschiebungen bei Entstehung von Kontaktpaaren mit der Phosphatgruppe bilden die Basis für quantitative Untersuchungen der CIP-Bildung in komplexeren RNA-Systemen.

Schmelzexperimente synthetischer dsRNA

Das Erhitzen synthetischer Doppelstrang-RNA (dsRNA) wird von einem strukturellen Übergang an der Schmelztemperatur $T_m \approx 328\,\mathrm{K}$ begleitet. Dieser Übergang wird in Schwingungsspektren von $\nu_{AS}(PO_2^-)$ als Reskalierung der wichtigsten Absorptionsmaxima erfasst. 2D-IR Spektroskopie erlaubt es, drei unabhängige spektrale Komponenten zu unterscheiden, die zu Schwingungsspektren von $\nu_{AS}(PO_2^-)$ beitragen. 2D-IR Banden haben eine elliptische Linienform, was die inhomogene Umgebung der Phosphatgruppen als Teil des RNA-Rückgrats widerspiegelt. Diese lassen sich auf drei unterschiedliche Hydratationsumgebungen der Phosphatgruppe zurückführen. Solvatisierende Wassermoleküle generieren elektrische Feldstärken in der Größenordnung von bis zu 100 MV/cm, die auf die Phosphatgruppe wirken. Im Ergebnis ist die $\nu_{AS}(PO_2^-)$ Schwingung einer Stark-Verschiebung ausgesetzt, die Schwingungsfrequenz hängt stark von der lokalen Solvatationsstruktur ab. Mit zunehmender Hydratisierung verschiebt sich die Schwingungsfrequenz zu niedrigeren Frequenzen. MD-Simulationen und QM/MM-Berechnungen können die spezifischen lokalen Konfigurationen der jeweiligen spektralen Position zuordnen:

- Vollständig hydratisierte Phosphatgruppen, umgeben von sechs Wassermolekülen, die eine tetraedrische Solvatationshülle bilden, tragen zu 2D-IR Signal um $1220\,\mathrm{cm}^{-1}$ bei. Solche Phosphatgruppen befinden sich für gewöhnlich an der Oberfläche des RNA-Moleküls.

- Phosphatgruppen mit einer unterkoordinierten Hydratationshülle, bei der einzelne Wassermoleküle die geringe Entfernung zwischen benachbarten Phosphatgruppen überbrücken, tragen zu 2D-IR Signal um $1245\,\mathrm{cm}^{-1}$ bei. Diese befinden sich hauptsächlich in der tiefen, schmalen *großen Furche* der dsRNA, in der die Verfügbarkeit von Wassermolekülen stark reduziert ist.

- Phosphatgruppen, die direkt mit Na^+ Gegenionen interagieren, sind zusätzlich blauverschoben und tragen zu 2D-IR Signal um $1280\,\mathrm{cm}^{-1}$ bei.

Der strukturelle Übergang beim Erhitzen verringert sterische Beschränkungen in der RNA-Doppelhelix und erlaubt eine stärkere Hydratation. Schwingungsspektren zeigen dann den Übergang von hauptsächlich unter-hydratisierten Phosphatgruppen zu vornehmlich hydratisierten lokalen Geometrien.

Mg^{2+} Bindung an RNA

Um RNA-Ionen-Wechselwirkungen zu untersuchen, wurde synthetische dsRNA und biologische tRNA in wässriger Lösung mit unterschiedlichen Mengen an Mg^{2+} Gegenionen gelöst. Wir beobachten eine ähnliche Blauverschiebung wie bei DMP, wenn RNA Mg^{2+} ausgesetzt ist. Die Veränderungen in den Schwingungsspektren gehen auf eine neu entstehende Schwingungsmode zurück, die mithilfe von QM/MM-Berechnungen der Bildung von RNA/Mg^{2+} Kontaktionenpaaren zugeordnet wurde. Bei Zugabe von ≈20 Mg^{2+}-Ionen pro RNA-Molekül tragen bis zu 10% aller Phosphatgruppen zum CIP-Signal bei, dies für alle betrachteten RNA-Systeme. Dies deckt sich mit den 7-9 direkt gebundenen Ionen, die in kristallografischen Röntgenbeugungsmessungen von $tRNA^{phe}$ beobachtet wurden. Die 2D-IR Messungen bestätigen zum ersten Mal, dass die Bildung von Kontaktionenpaaren auch in wässriger Lösung ein wichtiges strukturelles Element ist. MD-Simulationen zeigen, dass sich CIPs vordergründig in der *großen Furche* der dsRNA bilden, sowie in verdichteten Schleifenstrukturen der tRNA. Dort (über)kompensieren CIPs die elektrostatische Coulombabstoßung der negativ geladenen Phosphatgruppen auf lokaler Ebene und stabilisieren so die Bildung der RNA-Tertiärstruktur.

Abschließende Bemerkungen

Unsere Arbeit demonstriert das Potential von Schwingungsanregungen als sensitive, nichtinvasive Sonden biomolekularer Hydratationsumgebungen. Zusammen mit einer theoretischen Beschreibung auf molekularer Ebene hilft zeitaufgelöste Schwingungsspektroskopie beim Verständnis der vielfältigen Wechselwirkungen zwischen RNA und den sie umgebenden Wassermolekülen und Gegenionen. Der Ansatz könnte weiter genutzt werden, um die Rolle von Wassermolekülen und (Kontakt)Ionen in komplexeren Szenarien zu untersuchen, z.B. dem hochdynamischen Faltungsprozess komplexerer RNA-Moleküle.

Publications

Peer Reviewed Articles

Related to this work:

- E. M. Bruening, J. Schauss, T. Siebert, B. P. Fingerhut, and T. Elsaesser, "Vibrational Dynamics and Couplings of the Hydrated RNA Backbone: A Two-Dimensional Infrared Study", *J. Phys. Chem. Letters* 9 (2018), 583–587
- J. Schauss, F. Dahms, B. P. Fingerhut, and T. Elsaesser, "Phosphate-Magnesium Ion Interactions in Water Probed by Ultrafast Two-Dimensional Infrared Spectroscopy", *J. Phys. Chem. Letters* 10 (2019), 238–243
- J. Schauss, A. Kundu, B. P. Fingerhut, and T. Elsaesser, "Contact Ion Pairs of Phosphate Groups in Water: Two-Dimensional Infrared Spectroscopy of Dimethyl Phosphate and ab Initio Simulations", *J. Phys. Chem. Letters* 10 (2019), 6281–6286
- B. P. Fingerhut, J. Schauss, A. Kundu, and T. Elsaesser, "Aqueous Contact Ion Pairs of Phosphate Groups with Na^+, Ca^{2+} and Mg^{2+} - Structural Discrimination by Femtosecond Infrared Spectroscopy and Molecular Dynamics Simulations", *Zeitschrift für Physikalische Chemie*, vol. 234, issue 7-9 (2020), 491–495
- A. Kundu, J. Schauss, B. P. Fingerhut, and T. Elsaesser, "Change of Hydration Patterns upon RNA Melting Probed by Excitations of Phosphate Backbone Vibrations", *J. Phys. Chem. B* 124 (2020), 2132–2138
- J. Schauss, A. Kundu, B. P. Fingerhut, and T. Elsaesser, "Magnesium Contact Ions Stabilize the Tertiary Structure of Transfer RNA: Electrostatics Mapped by Two-Dimensional Infrared Spectra and Ab-Initio Simulations", *J. Phys. Chem. B* 125 (2021), 740–747
- B.P. Fingerhut, J.Schauss, A. Kundu, and T. Elsaesser, "Contact pairs of RNA with magnesium ions - electrostatics beyond the Poisson-Boltzmann equation", *Biophysical Journal* 120 (2021), 5322–5332
- T. Elsaesser, J. Schauss, A. Kundu, and B.P. Fingerhut, "Phosphate Vibrations Probe Electric Fields in Hydrated Biomolecules: Spectroscopy, Dynamics, and Interactions", *J. Phys. Chem. B* 125 (2021), 3899–3908

Other:

- A. Feist, K. Priebe, J. Schauss, S. V. Yalunin, S. Schaefer, and C. Ropers, "Quantum Coherent Optical Phase Modulation in an Ultrafast Transmission Electron Microscope" *Nature* 521(7551):200-203 (2015)

Bibliography

[1] B. Alberts, A. Johnson, J. Lewis, D. Morgan, M. Raff, K. Roberts, and P. Walter. *Molecular Biology of the Cell*. Garland Science, 5th edition, 2008.

[2] J. S. Turner, J. A. O'Halloran, E. Kalaidina, W. Kim, A. J. Schmitz, J. Q. Zhou, T. Lei, M. Thapa, R. E. Chen, J. B. Case, F. Amanat, A. M. Rauseo, A. Haile, X. Xie, M. K. Klebert, T. Suessen, W. D. Middleton, P.-Y. Shi, F. Krammer, S. A. Teefey, M. S. Diamond, R. M. Presti, and A. H. Ellebedy. SARS-CoV-2 mRNA vaccines induce persistent human germinal centre responses. *Nature*, 596:109–113, 2021.

[3] E. Bettini and M. Locci. SARS-CoV-2 mRNA Vaccines: Immunological Mechanism and Beyond. *Vaccines*, 9:147, 2021.

[4] H. Shi and P. B. Moore. The crystal structure of yeast phenylalanine tRNA at 1.93Å resolution: A classic structure revisited. *RNA*, 6:1091–1105, 2000.

[5] L. Huang, S. Ishibe-Murakami, D. J. Patel, and A. Serganov. Long-range pseudoknot interactions dictate the regulatory response in the tetrahydrofolate riboswitch. *PNAS*, 108:14801–14806, 2011.

[6] A. Bashan, I. Agmon, R. Zarivach, F. Schluenzen, J. Harms, R. Berision, H. Bartels, F. Franceschi, T. Auerbach, H. A. Hansen, E. Kossoy, M. Kessler, and A. Yonath. Structural Basis of the Ribosomal Machinery for Peptide Bond Formation, Translocation, and Nascent Chain Progression. *Molecular Cell*, 11:91–102, 2003.

[7] H. Hori. Methylated nucleosides in tRNA and tRNA methyltransferases. *Frontiers in genetics*, 5-144:1–26, 2014.

[8] W. Saenger. *Principles of Nucleic Acid Structure*. Springer, 1984.

[9] M. Brandl, M. Meyer, and J. Sühnel. Water-Mediated Base Pairs in RNA: A Quantum-Chemical Study. *The Journal of Physical Chemistry A*, 104:11177–11187, 2000.

[10] E. C. Friedberg. *DNA Repair*. W.H. Freeman and Company, 1984.

[11] A. Baudrimont, S. Voegeli, E. C. Viloria, F. Stritt, M. Lenon, T. Wada, V. Jaquet, and A. Becskei. Multiplexed gene control reveals rapid mRNA turnover. *Sci. Adv.*, 3:e1700006, 2017.

[12] A. K. Hopper. Transfer RNA Post-Transcriptional Processing, Turnover, and Subcellular Dynamics in the Yeast *Saccharomyces cerevisiae*. *Genetics*, 194:43–67, 2013.

[13] M. E. Allentoft, M. Collins, D. Harker, J. Haile, C. L. Oskam, M. L. Hale, P. F. Cmapos, J. A. Samaniego, M. T. P. Gilbert, E. Willerslev, G. Zhang, R. P. Scofield, R. N. Holdaway, and M. Bunce. The half-life of DNA in bone: measuring decay kinetics in 158 dated fossils. *Proc. R. Soc. B*, 279:4724–4733, 2012.

[14] E. M. Bruening, J. Schauss, T. Siebert, B. P. Fingerhut, and T. Elsaesser. Vibrational Dynamics and Couplings of the Hydrated RNA Backbone: A Two-Dimensional Infrared Study. *Journal of Physical Chemistry Letters*, 9:583–587, 2018.

[15] M. Egli, S. Portmann, and N. Usman. RNA Hydration: A Detailed Look. *Biochemistry*, 35:8489–8494, 1996.

[16] P. Auffinger and E. Westhof. Water and Ion Binding Around RNA and DNA (C,G) Oligomers. *J. Mol. Biol.*, 300:1113–1131, 2000.

[17] J. R. Arias-Gonzalez. Single-molecule portrait of DNA and RNA double helices. *Integr. Biol.*, 6:904–925, 2014.

[18] K. Miura, I. Fujii, M. Fuke, and S. Kawase. Double-stranded Ribonucleic Acid from Cytoplasmic Polyhedrosis Virus of the Silkworm. *Fournal of Virology*, 2:1211–1222, 1968.

[19] R. B. Wickner. Double-stranded RNA Viruses of *Saccharomyces cerevisiae*. *Microbiological Reviews*, 60:250–265, 1996.

[20] S. J. Poynter and S. J. DeWitte-Orr. Understanding Viral dsRNA-Mediated Innate Ummune Responses at the Cellular Level Using a Rainbow Trout Model. *Fornt. Immunol.*, 9:829, 2018.

[21] A. L. Feig and O. C. Uhlenbeck. The Role of Metal Ions in RNA Biochemistry. In R. F. Gesteland and J. F. Atkins, editors, *The RNA World, Second Edition*, chapter 12. Cold Spring Harbor Laboratory Press, 1999.

[22] S. A. Woodson. Compact Intermediates in RNA Folding. *Annu. Rev. Biophys.*, 39:61–77, 2010.

[23] D. Crothers, P. Cole, C. Hilbers, and R. Shulman. The Molecular Mechanism of Thermal Unfolding of *Eschericia coli* Formylmethionine Transfer RNA. *J.Mol.Biol.*, 87:63–88, 1974.

[24] J. Pan, M. L. Deras, and S. A. Woodson. Fast Folding of a Ribozyme by Stabilizing Core Interactions: Evidence for Multiple Folding Pathways in RNA. *J. Mol. Biol.*, 296:133–144, 2000.

[25] A. Tissières, J. D. Watson, D. Schlessinger, and B. Hollingworth. Ribonulceoprotein Particles from *Eschericia coli*. *J. Mol. Biol.*, 1:221–233, 1959.

[26] K. Fuwa, W. E. Wacker, R. Druyan, A. F. Bartholomay, and B. L. Vallee. Nucleic Acids and Metals, II: Transition Metals as Determinants of the Conformation of Ribonucleic Acids. *PNAS*, 46:1298–1307, 1960.

[27] P. Cole, S. Yang, and D. Crothers. Conformational Changes of Transfer Ribonucleic Acid. Equilibrium Phase Diagrams. *Biochemistry*, 11:4358–4368, 1972.

[28] R. Schroeder, A. Barta, and K. Semrad. Strategies for RNA Folding and Assembly. *Nature Reviews Molecular Cell Biology*, 5:908–919, 2004.

[29] D. Thirumalai, N. Lee, S. A. Woodson, and D. Klimov. Early Events in RNA Folding. *Annu. Rev. Phys. Chem.*, 52:751–762, 2001.

[30] B. P. Fingerhut. The mutual interactions of RNA, counterions and water - quantifiying the electrostatics at the phosphate-water interface. *Chem. Commun.*, 57:12880–12897, 2021.

[31] M. Chaplin. Do we underestimate the importance of water in cell biology? *Nat. Rev. Mol. Cell Biol.*, 7:861–866, 2006.

[32] Y. Levy and J. N. Onuchic. Water Mediation in Protein Folding and Molecular Recognition. *Annu. Rev. Biophys. Biomol. Struct.*, 35:389–415, 2006.

[33] V. K. Misra and D. E. Draper. Mg^{2+} Binding to tRNA Revisited: The Nonlinear Poisson-Boltzmann Model. *J. Mol. Biol.*, 299:813–825, 2000.

[34] D. J. Klein, P. B. Moore, and T. A. Steitz. The contribution of metal ions to the structural stability of the large ribosomal subunit. *RNA*, 10:1366–1379, 2004.

[35] A. S. Petrov, J. C. Bowman, S. C. Harvey, and L. D. Williams. Bidentate RNA-magnesium clamps: On the origin of the special role of magnesium in RNA folding. *RNA*, 17:291–297, 2011.

[36] M. Falk, K. A. Hartman, Jr., and R. Lord. Hydration of Deoxyribonucleic Acid. II. An Infrared Study. *J. Am. Chem. Soc.*, 85:387–391, 1963.

[37] T. Siebert, B. Guchhait, Y. Liu, R. Costard, and T. Elsaesser. Anharmonic Backbone Vibrations in Ultrafast Processes at the DNA-Water Interface. *J. Phys. Chem. B*, 119:9670–9677, 2015.

[38] B. P. Fingerhut, R. Costard, and T. Elsaesser. Predominance of short range Coulomb forces in phosphate-water interactions - a theoretical analysis. *The Journal of Chemical Physics*, 145,115101, 2016.

[39] R. A. Friedman and B. Honig. A Free Energy Analysis of Nucleic Acid Base Stacking in Aqueous Solution. *Biophysical Journal*, 69:1528–1535, 1995.

[40] D. Laage, T. Elsaesser, and J. T. Hynes. Water Dynamics in the Hydration Shells of Biomolecules. *Chem. Rev.*, 117:10694–10725, 2017.

[41] V. A. Bloomfield, D. M. Crothers, and I. Tinoco Jr. *Nucleic Acids: Structures, Properties, and Functions* . University Science Books, first edition, 2000.

[42] S. K. Pal and A. H. Zewail. Dynamics of Water in Biological Recognition. *Chem. Rev.*, 104:2099–2123, 2004.

[43] T. Siebert, B. Guchhait, Y. Liu, B. P. Fingerhut, and T. Elsaesser. Range, Magnitude, and Ultrafast Dynamics of Electric Fields at the Hydrated DNA Surface. *J. Phys. Chem. Letters*, 7:3131–3136, 2016.

[44] F. Bruni, S. Imberti, R. Mancinelli, and M. A. Ricci. Aqueous solutions of divalent chlorides: Ions hydration shell and water structure. *The Journal of Chemical Physics*, 136, 064520, 2012.

[45] F. Jalilehvand, D. Spångberg, P. Lindqvist-Reis, K. Hermansson, I. Persson, and M. Sandström. Hydration of the Calcium Ion. An EXAFS, Large-Angle X-ray Scattering, and Molecular Dynamics Simulation Study. *J. Am. Chem. Soc.*, 123:431–441, 2001.

[46] O. Andersen, H. Ingolfsson, and J. Lundbæk. Ion Channels. In H. Bohr, editor, *Handbook of molecular biophysics*, pages 557–592. Wiley-VCH, 2009.

[47] R. Mancinelli, A. Botti, F. Bruni, M. Ricci, and A. Soper. Hydration of Sodium, Potassium, and Chloride Ions in Solution and the Concept of Structure Maker/Breaker. *The Journal of Physical Chemistry B*, 111:13570–13577, 2007.

[48] H. J. Bakker, M. F. Kropman, and A. W. Omta. Effect of ions on the structure and dynamics of liquid water. *J. Phys.: Condens. Matter*, 17:S3215–S3224, 2005.

[49] S. Friesen, G. Hefter, and R. Buchner. Cation Hydration and Ion Pairing in Aqueous Solutions of $MgCl_2$ and $CaCl_2$. *J. Phys. Chem. B*, 123:891–900, 2019.

[50] H. T. Nguyen and D. Thirumalai. Charge density of cation determines inner versus outer shell coordination to phosphate in RNA. *The Journal of Physical Chemistry B*, 124:4114–4122, 2020.

[51] V. K. Misra and D. E. Draper. On the Role of Magnesium Ions in RNA Stability. *Biopolymers*, 48:113–135, 1998.

[52] J. Wyman and S. J. Gill. *Binding and Linkage*. University Science Books, 1990.

[53] R. Römer and R. Hach. tRNA Conformation and Magnesium Binding: A Study of Yeast Phenylalanine-Specific tRNA by a Fluorescent Indicator and Differential Melting Curves. *Eur. J. Biochem.*, 55:271–284, 1975.

[54] G. Scatchard. The Attractions of Proteins for Small Molecules and Ions. *Annaly New York Academy of Sciences*, 51:660–672, 1949.

[55] D. Grilley, A. M. Soto, and D. E. Draper. Direct quantitation of Mg^{2+}-RNA interactions by use of a fluorescent dye. *Methods Enzymol.*, 455:71–94, 2009.

[56] D. Stigter. Evaluation of the Counterion Condensation Theory of Polyelectrolytes. *Biophysical Journal*, 69:380–388, 1995.

[57] S. Kirmizialtin, A. R. J. Silalahi, R. Elber, and M. O. Fenley. The Ionic Atmosphere around A-RNA: Poisson-Boltzmann and Molecular Dynamics Simulations. *Biophysical Journal*, 102:829–838, 2012.

[58] G. S. Manning. Limiting Laws and Counterion Condensation in Polyelectrolyte Solutions I. Colligative Properties. *J. Chem. Phys.*, 51,3:924–933, 1969.

[59] G. S. Manning. Limiting Laws and Counterion Condensation in Polyelectrolyte Solutions 8. Mixtures of Counterions, Species Selectivity, and Valence Selectivity. *J. Phys. Chem.*, 88:6654–6661, 1984.

[60] M. Gebala and D. Herschlag. Quantitative Studies of an RNA Duplex Electrostatics by Ion Counting. *Biophysical Journal*, 117:1116–1124, 2019.

[61] K. A. Sharp and B. Honig. Calculating Total Electrostatic Energies with the Nonlinear Poisson-Boltzmann Equation. *J. Phys. Chem*, 94:7684–7692, 1990.

[62] S. W. Chen and B. Honig. Monovalent and Divalent Salt Effects on Electrostatic Free Energies Defined by the Nonlinear Poisson-Boltzmann Equation: Application to DNA Binding Reactions. *J. Phys. Chem. B*, 101:9113–9118, 1997.

[63] Z.-J. Tan and S.-J. Chen. RNA Helix Stability in Mixed Na^+/Mg^{2+} Solution. *Biophysical Journal*, 92:3615–3632, 2007.

[64] The Amber Homepage. `https://ambermd.org/`. Accessed: 11.01.2022.

[65] CHARMM. `https://www.charmm.org//`. Accessed: 11.01.2022.

[66] A. Pérez, I. Marchán, D. Svozil, J. Šponer, T. E. C. III, C. A. Laughton, and M. Orozco. Refinement of the AMBER Force Field for Nucleic Acids: Improving the Description of α/γ Conformers. *Biophysical Journal*, 92:3817–3829, 2007.

[67] I. Yildirim, H. A. Stern, S. D. Kennedy, J. D. Tubbs, and D. H. Turner. Reparameterization of RNA χ Torsion Parameters for the AMBER Force Field and Comparison to NMR Spectra for Cytidine und Uridine. *J. Chem. Theory Comput.*, 6:1520–1531, 2010.

[68] J. Šponer, M. Otyepka, P. Banáš, K. Réblová, and N. Walter. Molecular Dynamics Simulations of RNA Molecules. In T. Schlick, editor, *Innovations in Biomolecular Modeling and Simulations: Volume 2*, chapter 6. The Royal Society of Chemistry, 2012.

[69] P. Auffinger. Molecular Dynamics Simulations of RNA Systems. In R. Hartmann, A. Bindereif, A. Schön, and E. Westhof, editors, *Handbook of RNA Biochemistry, Volume Two, Second Edition*, chapter 32. Wiley-VCH, 2014.

[70] E. Duboué-Dijon, P. E. Mason, H. E. Fischer, and P. Jungwirth. Hydration and Ion Pairing in Aqueous Mg^{2+} and Zn^{2+} Solutions: Force-Field Description Aided by Neutron Scattering Experiments and Ab Initio Molecular Dynamics Simulations. *J. Phys. Chem. B*, 122:3296–3306, 2018.

[71] E. Duboué-Dijon, M. Javanainen, P. Delcroix, P. Jungwirth, and J. Martinez-Seara. A practical guide to biologically relevant molecular simulations with charge scaling for electronic polarization. *J. Chem. Phys.*, 153:050901, 2020.

[72] S. Kirmizialtin and R. Elber. Computational Exploration of Mobile Ion Distributions around RNA Duplex. *J. Phys. Chem. B*, 114:8207–8220, 2010.

[73] K. Xi, F.-H. Wang, G. Xiong, Z.-L. Zhang, and Z.-J. Tan. Competitive Binding of Mg^{2+} and Na^+ Ions to Nucleic Acids: From Helices to Trtiary Structures. *Biophysical Journal*, 114:1776–1790, 2018.

[74] N. M. Fischer, M. D. Polêto, J. Steuer, and D. van der Spoel. Influence of Na^+ and Mg^{2+} ions on RNA structures studied with molecular dynamics simulations. *Nucleic Acids Research*, 46:4872–4882, 2018.

[75] S. Cruz-León and N. Schwierz. Hofmeister Series for Metal-Cation-RNA Interactions: The Interplay of Binding Affinity and Exchange Kinetics. *Langmuir*, 36:5979–5989, 2020.

[76] F. Hofmeister. Zur Lehre von der Wirkung der Salze. *Archiv f. experiment. Pathol. und Pharmakol*, 24:247–260, 1888.

[77] Y. S. Choi and C. W. Carr. Ion-binding Studies of Ribonucleic Acid and *Eschericia coli* Ribosomes. *J. Mol. Biol*, 25:331–345, 1967.

[78] R. E. Benesch, R. Benesch, and G. Macduff. Subunit Exchange and Ligand Binding: A new Hypothesis for the mechanism of Oxygenation of Hemoglobin. *Biochemistry*, 54:535–542, 1965.

[79] M. M. Rubin and J.-P. Changeux. On the Nature of Allosteric Transitions: Implications of Non-exclusive Ligand Binding. *J. Mol. Biol.*, 21:265–274, 1966.

[80] D. E. Draper. A guide to ions and RNA structure. *RNA*, 10:335–343, 2004.

[81] D. Leipply and D. E. Draper. The dependence of RNA tertiary structure stability on Mg^{2+} concentration: interpretation of the Hill equation and coefficient. *Biochemistry*, 49:1843–1853, 2010.

[82] D. Leipply and D. E. Draper. Effects of Mg^{2+} on the Free Energy Landcsape for Folding a Purine Riboswitch RNA. *Biochemistry*, 50:2790–2799, 2011.

[83] D. Leipply and D. E. Draper. Evidence for a Thermodynamically Distinct Mg^{2+} Ion Associated with Formation of an RNA Tertiary Structure. *JACS*, 133:13397–13405, 2011.

[84] L. Pollack. SAXS Studies of Ion-Nucleic Acid Interactions. *Annu. Rev. Biophys.*, 40:225–242, 2011.

[85] Y. Chen and L. Pollack. SAXS studies of RNA: structures, dynamics, and interactions with partners. *WIREs RNA*, 7:512–526, 2016.

[86] S. Kirmizialtin, S. A. Pabit, S. P. Meisburger, L. Pollack, and R. Elber. RNA and Its Ionic Cloud: Solution Scattering Experiments and Atomically Detailed Simulations. *Biophysical Journal*, 102:819–828, 2012.

[87] J. Lipfert, S. Doniach, R. Das, and D. Herschlag. Understanding Nucleic Acid-Ion Interactions. *Annu. Rev. Biochem.*, 83:813–841, 2014.

[88] Y. Bai, M. Greenfeld, K. J. Travers, V. B. Chu, J. Lipfert, S. Doniach, and D. Herschlag. Quantitative and Comprehensive Decomposition of the Ion Atmosphere around Nucleic Acids. *J. Am. Chem. Soc.*, 129:14981–14988, 2007.

[89] S. R. Holbrook, J. L. Sussman, R. W. Warrant, G. M. Chruch, and S.-H. Kim. RNA-ligand interactions: (I) magnesium binding sites in yeast $tRNA^{Phe}$. *Nucleic Acids Research*, 4:2811–2820, 1977.

[90] A. Jack, J. Ladner, D. Rhodes, R. Brown, and A. Klug. A Crystallographic Study of Metal-binding to Yeast Phenylalanine Transfer RNA. *J. Mol. Biol.*, 111:315–328, 1977.

[91] M. C. Erat and R. K. Sigel. Methods to Detect and Characterize Metal Ion Binding Sites in RNA. In A. Sigel, H. Sigel, and R. K. Sigel, editors, *Metal Ions in Life Sciences*, volume 9, pages 37–100. Royal Society of Chemistry, 2011.

[92] D. E. Draper. On the Coordination Properties of Eu^{3+} bound to tRNA. *Biophysical Chemistry*, 21:91–101, 1985.

[93] C. R. Jones and D. R. Kearns. Investigation of the Structure of Yeast $tRNA^{Phe}$ by Nuclear Magnestic Resonance: Paramagnetic Rare Earth Ion Probes of Structure. *PNAS*, 71:4237–4240, 1974.

[94] D. E. Draper, D. Grilley, and A. M. Soto. Ions and RNA Folding. *Annu. Rev. Biophys. Biomol. Struct.*, 34:221–243, 2005.

[95] C. Schildkraut and S. Lifson. Dependence of the Melting Temperature of DNA on Salt Concentration. *Biopolymers*, 3:195–208, 1965.

[96] J. W. Lyons and L. Kotin. The Effect of Magnesium Ion on the Secondary Structure of Deoxyribonucleic Acid. *JACS*, 87:1781–1785, 1965.

[97] Y. Guan, C. J. Wurrey, and G. J. T. Jr. Vibrational Analysis of Nucleic Acids I. The Phosphodiester Group in Dimethyl Phosphate Model Compounds: $(CH_3O)_2PO_2^-$, $(CD_3O)_2PO_2^-$, and $(^{13}CH_3O)_2PO_2^{-*}$. *Biophys. J*, 66:225–235, 1994.

[98] J. Florián, V. Baumruk, M. Štrajbl, L. Bednárová, and J. Štěpánek. IR and Raman Spectra, Conformational Flexibility, and Scaled Quantum Mechanical Force Fields of Sodium Dimethyl Phosphate and Dimethyl Phosphate Anion. *J. Phys. Chem.*, 100:1559–1568, 1996.

[99] B. Jayaram, G. Ravishanker, and D. L. Beveridger. Conformational Preferences of Phosphodiester Torsion Angles in Dimethylphosphate Anion in Free Space and Water: Quasi-Harmonic Monte Carlo and Hydratoin Shell Calculations. *J. Phys. Chem.*, 92:1032–1034, 1988.

[100] R. Costard, I. A. Heisler, and T. Elsaesser. Structural Dynamics of Hydrated Phospholipid Surfaces Probed by Ultrafast 2D Spectroscopy of Phosphate Vibrations. *J. Phys. Chem. Lett.*, 5:506 – 511, 2014.

[101] R. Costard, T. Tyborski, B. P. Fingerhut, and T. Elsaesser. Ultrafast phosphate hydration dynamics in bulk H_2O. *J. Chem. Phys.*, 142:212406, 2015.

[102] L. Szyc, M. Yang, and T. Elsaesser. Ultrafast Energy Exchange via Water-Phosphate Interactions in Hydrated DNA. *J. Phys, Chem. B*, 114:7951–7957, 2010.

[103] J. Schauss. Ultrafast vibrational spectroscopy of dimethylphosphate in an aqueous environment. Master's thesis, Karlsruhe Institute of Technology, 2018.

[104] N. M. Levinson, E. E. Bolte, C. S. Miller, S. A. Corcelli, and S. G. Boxer. Phosphate Vibrations Probe Local Electric Fields and Hydration in Biomolecules. *Journal of the American Chemical Society*, 133:13236–13239, 2011.

[105] G. M. Blackburn and M. J. Gait. *Nucleic acids in chemistry and biology.* Oxford University Press, second edition, 1996.

[106] J. A. Bishop. Complex Formation and Fluorescence 1. Complexes of 8-Hydroxyquinoline-5-Sulfonic Acid. *Analytica Chimica Acta*, 29:172–177, 1963.

[107] S.-Y. Park, P. Gosh, S. O. Park, Y. M. Lee, S. K. Kwak, and O.-H. Kwon. Origin of ultraweak fluorescence of 8-hydroxyquinoline in water: photoinduced ultrafast proton transfer. *RSC Advances*, 6:9812–9821, 2016.

[108] P. M. Morse. Diatomic Molecules According to the Wave Mechanics. II. Vibrational Levels. *Physical Review*, 34:57–64, 1929.

[109] P. Hamm and M. Zanni. *Concepts and Methods of 2D Infrared Spectroscopy.* Cambridge University Press, 2011.

[110] R. Kubo. A Stochastic Theory of Line Shape. *Stochastic Processes in Chemical Physics*, 15:101–127, 1969.

[111] S. Mukamel. *Principles of Nonlinear Optical Spectroscopy.* Number 6. Oxford University Press on Demand, 1999.

[112] R. W. Boyd. *Nonlinear Optics.* Academic Press, 2008.

[113] Y. Shen. *The Principles of Nonlinear Optics.* Wiley, 1984.

[114] R. Costard. *Ultrafast Dynamics of Phospholipid-Water Interfaces Studied by Nonlinear Time-Resolved Vibrational Spectroscopy.* Springer, 2015.

[115] F. Dahms. *The Hydrated Excess Proton Studied by Nonlinear Time-Resolved Vibrational Spectroscopy.* dissertation, Humboldt-Universität Berlin, 2018.

[116] J. Schauss, F. Dahms, B. P. Fingerhut, and T. Elsaesser. Phosphate-Magnesium Ion Interactions in Water Probed by Ultrafast Two-Dimensional Infrared Spectroscopy. *The Journal of Physical Chemistry Letters*, 10:238–243, 2019.

[117] J. Schauss, A. Kundu, B. P. Fingerhut, and T. Elsaesser. Contact Ion Pairs of Phosphate Groups in Water: Two-Dimensional Infrared Spectroscopy of Dimethyl Phosphate and ab Initio Simulations. *The Journal of Physical Chemistry Letters*, 10:6281–6286, 2019.

[118] M. Valiev, E. Bylaska, N. Govind, K. Kowalski, T. Straatsma, H. van Dam, D. Wang, J. Nieplocha, E. Apra, T. Windus, and W. de Jong. NWChem: A Comprehensive and Scalable Open-Source Solution for Large Scale Molecular Simulations. *Comput. Phys. Commun.*, 181:1477–1489, 2010.

[119] J. Liquier, A. Akhebat, E. Taillandier, F. Ceolin, T. Huynh Dinh, and J. Igolen. Characterization by FTIR spectroscopy of the oligoribonucleotide duplexes r(A-U)$_6$ and r(A-U)$_8$. *Spectrochimica Acta*, 47A:177–186, 1991.

[120] M. J. Nowak, L. Lapinski, J. S. Kwiatkowski, and J. Lesczcyński. Molecular Structure and Infrared Spectra of Adenine. Experimental Matrix Isolation and Density Functional Theory Study of Adenine ^{15}N Isotopomers. *J. Phys. Chem.*, 100:3527–3534, 1996.

[121] S. Lee, A. Anderson, W. Smith, R. Griffey, and V. Mohan. Temperature-dependent Raman and infrared spectra of nucleosides. Part I - adenosine. *Journal of Raman Spectroscopy*, 31:891–896, 2000.

[122] Appendix: UV Spectroscopy for the Quantitation of RNA. In R. Hartmann, A. Bindereif, A. Schön, and E. Westhof, editors, *Handbook of RNA Biochemistry, Volume Two, First Edition.* Wiley-VCH, 2005.

[123] M. J. Cavaluzzi and P. N. Borer. Revised UV extinction coefficients for nucleoside-5'-monophosphates and unpaired DNA and RNA. *Nucleic Acids Research*, 32, 2004.

[124] Oligo extinction coefficient calculator. `https://www.fechem.uzh.ch/MT/links/ext.html`. Accessed: 15.12.2021.

[125] A. O. Nwokeoji, P. M. Kilby, D. E. Portwood, and M. J. Dickman. Accurate Quantification of Nucleic Acids Using Hypochromicity Measurements in Conjunction with UV Spectrophotometry. *Analytical Chemistry*, 89:13567–13574, 2017.

[126] P. Dumas, E. Ennifar, F. Disdier, and P. Walter. UV Melting Studies with RNA. In R. Hartmann, A. Bindereif, A. Schön, and E. Westhof, editors, *Handbook of RNA Biochemistry, Volume One, Second Edition*, chapter 22. Wiley-VCH, 2014.

[127] J. Kypr, I. Kejnovská, D. Renčiuk, and M. Vorlíčková. Circular dichroism and conformational polymorphism of DNA. *Nucleic Acids Research*, 37:1713–1725, 2009.

[128] W. C. Johnson. Nucleic Acids . Spectroscopic and Kinetic Data. Physical Data I. In W. Saenger, editor, *Landolt Boernstein New Series - Group VII Biophysics*, volume 1c. Springer-Verlag Berlin Heidelberg, 1990.

[129] A. D. Blum, O. C. Uhlenbeck, and I. T. Jr. Circular Dichroism Study of Nine Species of Transfer Ribonucleic Acid. *Biochemistry*, 11:3248–3256, 1972.

[130] G. Arena, S. Musumeci, and R. Purrello. Calcium- and Magnesium-EDTA Complexes. Stability constants and their Dependence on Temperature and Ionic Strength. *Thermochimica Acta*, 61:129–138, 1983.

[131] S. Ashihara, N. Huse, A. Espagne, E. Nibbering, and T. Elsaesser. Vibrational Couplings and Ultrafast Relaxation of the O–H Bending Mode in Liquid H_2O. *Chemical Physics Letters*, 424:66–70, 2006.

[132] J. Zheng, K. Kwak, J. Asbury, X. Chen, I. R. Piletic, and M. Fayer. Ultrafast Dynamics of Solute-Solvent Complexation Observed at Thermal Equilibrium in Real Time. *Science*, 309:1338–1343, 2005.

[133] Y. Liu, B. Guchhait, T. Siebert, B. P. Fingerhut, and T. Elsaesser. Molecular couplings and energy exchange between DNA and water mapped by femtosecond infrared spectroscopy of backbone vibrations. *Structural Dynamics*, 4:044015–1–044015–15, 2017.

[134] T. Elsaesser, J. Schauss, A. Kundu, and B. P. Fingerhut. Phosphate Vibrations Probe Electric Fields in Hydrated Biomolecules: Spectroscopy, Dynamics, and Interactions. *The Journal of Physical Chemistry B*, 125:3899–3908, 2021.

[135] J. Völker, H. H. Klump, G. S. Manning, and K. J. Breslauer. Counterion Association with Native and Denatured Nucleic Acids: An Experimental Approach. *J. Mol. Biol.*, 310:1011–1025, 2001.

[136] B. P. Fingerhut, J. Schauss, A. Kundu, and T. Elsaesser. Contact Pairs of RNA with magnesium ions - electrostatics beyond the Poisson-Boltzmann equation. *Biophysical Journal*, 120:5322–5332, 2021.

Danksagung

Da sich der Moment der Abgabe nähert, ist es Zeit, den Menschen zu danken, ohne die diese Arbeit wohl nicht zustande gekommen wäre.

Zuerst gilt mein Dank Professor Thomas Elsässer für die Möglichkeit, an diesem spannenden Projekt zu arbeiten, für die vielen Diskussionen und Fragen, die mir mit jedem Mal mehr Einblick in die Materie gewährt haben, und für die Geduld bei der Betreuung dieser Arbeit.

Dr. Benjamin Fingerhut kann ich nicht genug danken, für unzählige Gespräche über Wissen und Nicht-Wissen und sein offenes Ohr zu wirklich jeder Zeit.

Dr. Fabian Dahms und Dr. Achintya Kundu, für die erlebnisreiche Zeit im 2D-IR-Labor. Die Tiefen ließen sich am Ende noch alle überwinden, sodass die Höhen in dieser Arbeit Erscheinung finden können.

Janett Feickert für die super Zusammenarbeit wenn es um irgendetwas chemikalisch-biologisches ging. Und das ging es im Laufe des Projektes ziemlich häufig...deine Hilfe war Gold wert.

Regina Lendt und Dr. Eva-Maria Brüning, für die ersten Einweisungen in Chemielabor und RNA-Handling und das ein oder andere Stück Kuchen. Peter Scholze, für alles Werkstättliche und den einen oder anderen Konzertbesuch. Heike Nikolenko, für die Möglichkeit CD-Messungen durchzuführen, auch noch sehr, sehr kurzfristig. Dr. Tobias Goldhammer für die ICP-OES Messungen, noch kurzfristiger.

Alle Menschen, mit denen Mittagspausen eine spannende Zeit mit einer unendlichen Vielfalt an Themen wurden. Vielen Dank, Andrei, Mara, Roman, Martin, Nirmalendu, Erik, Carlo, Debkumar, Peng, Zoey, und natürlich Marc-Oliver für die entspannte Büroatmosphäre.

Mein größter Dank gilt aber meiner Familie. Mami, Papi, Franka, Natalie, Austin, Victoria und natürlich Luca. Ohne euch als Rückzugsort wäre diese Arbeit nie fertig geworden, ohne eure Liebe und Unterstützung wäre, hätte, könnte, so vieles nie geschehen können. Ich bin wahnsinnig froh, dass ich euch habe.

Selbständigkeitserklärung

Ich erkläre, dass ich die Dissertation selbständig und nur unter Verwendung der von mir gemäß §7 Abs. 3 der Promotionsordnung der Mathematisch-Naturwissenschaftlichen Fakultät, veröffentlicht im Amtlichen Mitteilungsblatt der Humboldt-Universität zu Berlin Nr. 42/2018 am 11.07.2018 angegebenen Hilfsmittel angefertigt habe.

Berlin, den 01.02.2022